



Proceedings of the International Conference  
**Instabilities and Control of Excitable Networks:**  
*From Macro- to Nano-Systems*

Dolgoprudny, Russia

May 25-30, 2012

УДК 001:004.7:007.5:519.1:573:576.3:65.  
ББК 28.071+28.91+32.97

Instabilities and Control of Excitable Networks / Moscow: MAKS-Pess, 2012, 133 p.

The present book contains the proceedings of the International Conference “Instabilities and Control of Excitable Networks: From Macro- to Nano-Systems” (ICENet-2012) hosted by Moscow Institute of Physics and Technology in Dolgoprudny, Russia, on 25-30 May, 2012. The conference was devoted to the problems of complex excitable network dynamics in physiology, biomedicine, physics, chemistry and social systems.

Неустойчивости в возбудимых сетях и возможности управления ими / Москва: МАКС-Пресс, 2012. — 133 с.

В сборник вошли труды участников международной конференции “Instabilities and Control in Excitable Networks: From Macro- to Nano-Systems” (Неустойчивости в возбудимых сетях и возможности управления ими: от макро- к нано-системам), проходившей в Московском физико-техническом институте (г. Долгопрудный, Россия) в период с 25 по 30 мая 2012. Конференция была посвящена изучению сложного возбудимого динамического поведения систем, организованных по сетевому принципу, в физиологии, биомедицине, физике, химии и социальной сфере.

# Organizing Committee

K.I. Agladze — co-chairman

G.Th. Guria — co-chairman

A.A. Muraviev

D.V. Goldshtein

A.M. Pertsov

*K.E. Zlobina — scientific secretary*

*A.R. Gagarina — secretary*

# Acknowledgments



Moscow Institute of Physics and Technology



National Research Centre for Haematology



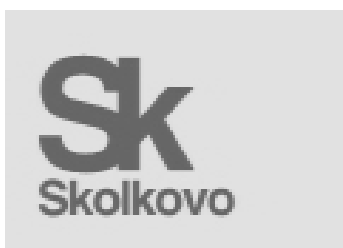
Russian Foundation for Basic Research



Conference Management System



Moscow Center of Technology Transfer



Skolkovo Innovation Center

# Preface

## International Conference "Instabilities and Control of Excitable Networks: From Macro- to Nano-Systems"

was held in Dolgoprudny, Russia in May 25-30 and devoted to the problems of complex excitable network dynamics in physiology, biomedicine, physics, chemistry and social systems. The main topics were:

- Instabilities in far-from-equilibrium excitable network dynamics;
- Pattern formation in network-organized systems;
- Control of threshold and kinetic cascade avalanche-like phenomena;
- Conceptual items and their application to natural and social systems.

The main goal of the conference was to advance interdisciplinary research and develop new cross-disciplinary links in Russia and abroad. The Conference was attended by a few vibrant groups of researchers at different stages of their academic careers. The participating scholars have studied problems related to self-organization in various systems, engineering of excitable biological tissues and control of excitable networks. We believe that this conference was foster new contacts and an exchange of exciting ideas. Presented in this issue collection of the papers to some degree reflects the present state of art in the area.

Sincerely Yours,  
Co-Chairs,  
*Konstantin Agladze*  
and  
*Georgy Guria*

# Conference Program

<i>N.N. Agladze, N.I. Doronina, K.I. Agladze</i> Cardiac tissue engineering with the aid of polyhydroxybutyrate membranes and nanofibers . . . . .	1
<i>V.N. Biktashev, D. Barkley, I.V. Biktasheva, G.V. Bordyugov, H. Dierckx, A.J. Foulkes, S.W. Morgan, G. Plank, N.A. Sarvazyan, O. Selsil, H. Vershelde</i> Asymptotic dynamics and control of spiral and scroll waves . . . . .	8
<i>O.A. Dudchenko, G.Th. Guria</i> Self-Sustained Peristaltic Transport in Biological Systems: A Theoretical Study . . . . .	19
<i>W. Ebeling, A.P. Chetverikov, M.G. Velarde</i> Solitonic excitations and control in nonlinear chains and networks . . . . .	28
<i>E.V. Gasnikova</i> One way to generate Lyapunov function for the chemical kinetic equations . . . . .	40
<i>M.A. Herrero</i> Mathematical Models in Social Dynamics . . . . .	43
<i>A.E. Kaplan, S.N. Volkov</i> “Locitons” in self-interacting atomic nanolattices . . . . .	53
<i>A.V. Khalyavkin</i> From macro- to nano-systems and back in search of the primary cause and control of aging . . . . .	69
<i>A.S. Kholodov, S.S. Simakov, Y.N. Soe, T.M. Gamilov</i> Computational Model of Blood Flow Optimization in Lower Extremities during Intensive Exercise . . . . .	77
<i>A.V. Leonidov, E.L. Rumyantsev</i> Russian interbank networks: main characteristics and stability with respect to contagion . . . . .	83
<i>V.A. Malyshev, A.A. Zamyatin</i> Mathematics for some classes of networks . . . . .	90
<i>A.A. Polezhaev, M.Yu. Borina</i> Spatial-Temporal Patterns Arising in Active Media in the Vicinity of the Wave Bifurcation . . . . .	104
<i>A.S. Rukhlenko, K.E. Zlobina, G.Th. Guria</i> Threshold activation of blood coagulation cascade in intensive flow and formation of fibre-like fibrin polymer networks . . . . .	113

# Cardiac tissue engineering with the aid of polyhydroxybutyrate membranes and nanofibers

N.N. Agladze<sup>1</sup>, N.I. Doronina<sup>2</sup> and K.I. Agladze<sup>1,3,\*</sup>

<sup>1</sup>*Moscow Institute of Physics and Technology, Dolgoprudny 141700, Russia*

<sup>2</sup>*Institute of Biochemistry and Physiology of Microorganisms, Pushchino 142290, Russia*

<sup>3</sup>*Institute for Integrated Cell-Material Sciences (iCeMS), Kyoto University, Kyoto 606-8501, Japan*

\**e-mail address: agladze@yahoo.com*

## 1 Introduction

A rapid development of tissue engineering in the last decade has caused an increased demand for materials that can serve as scaffolds for the tissue constructs. The major common requirements for these materials are biocompatibility (non-toxicity), matching mechanical and elastic properties to a specific type of tissue, and safe biodegradation of the scaffold in the body. However, highly specialized cells, such as cardiomyocytes, are most demanding to the scaffold materials and in a cardiac tissue engineering to the above requirements is added necessity to ensure functional electrophysiological unity of cells, i.e. besides only survival and growth, the engineered tissue should be able transmitting electrical signals and contracting synchronously. In recent years, with varying degrees of success, various polymer materials were used to achieve this goal [1–3].

Previously, it was shown that one of the promising materials for tissue engineering is polyhydroxybutyrate (PHB). It was successfully used for cultivation of dermoblasts and fibroblasts [4], connective tissue [5], it was used as a supporting scaffold for differentiating stem cells [6]. Moreover, PHB was successfully used for the preparation of substitute pericardial patches and thus demonstrated its full compatibility with cardiac tissue [7, 8].

In the present study, we investigated the use of PHB for the cardiac tissue engineering. The PHB was prepared either in the form of thin membranes, or in the form of polymer fibers obtained by electrospinning. Isolated neonatal rat cardiomyocytes were seeded either on fibers matrices or membranes and cultured to form confluent cardiac monolayers. Functioning of obtained tissue patches was tested by visual observation of contractions and with the aid of optical mapping [9] i.e. registration of excitation waves with fluorescent markers. The latter one allowed ensuring the fact that cultured cells represented electrophysiological syncytium. We have shown that both primary culture neonatal cardiomyocytes and immortalized HL-1 cells, successfully attached to the polymer surface to form a contracting, electrophysiologically unified monolayer.

## 2 Materials and methods

### 2.1 Cell culture

#### 2.1.1 Primary culture of cardiomyocytes

The isolation protocol was used as in [10]. Briefly, hearts isolated from neonatal 2-3 day-old rats were minced and left overnight in a trypsin solution. Next morning they were dispersed in a collagenase type 2 solution. To remove the fibroblasts after centrifugation,

the isolated cells were suspended in Dulbecco's modified Eagle's Medium (DMEM with 10% fetal bovine serum, 1% penicillin-streptomycin) and kept in a tissue culture dish for 1 h. Non-adherent cells were collected and plated on a polymer substrate coated with human plasma fibronectin (Gibco) and incubated at 37°C under humidified 5% CO<sub>2</sub> conditions for 1 day. After incubation, the medium was replaced with a minimum essential medium (MEM) containing 5% fetal bovine serum, 1% penicillin-streptomycin, and the incubation continued for a minimum 3 days until confluent monolayers were formed, up to 8 days.

### 2.1.2 HL-1 and HL-1 ChR2 cells

HL-1 cell (immortalized cardiomyocytes of atrial tumor mouse heart) and HL1ChR2 cells (HL-1 cells transfected with the gene rhodopsin R 2) were obtained from Dr. Philippe Sasse (Institut für Physiologie 1 Universität Bonn Life and Brain Center) at passage #77 and passage #98 respectively. Cells were grown in Claycomb medium according to the original protocols [11].

## 2.2 Polymeric membranes and fibers

The polymer membranes were manufactured from the class of biodegradable polymers polyhydroxybutyrate (PHB) / oxovalerate (PGBV) with different molecular weights.

The polymer was synthesized in the Institute of Biochemistry and Physiology of Microorganisms, RAS, Pushchino, Moscow Region.

Membrane size: strip width of 2-3 mm and a length of 10-25 mm, flaps 10 to 15 × 13-18 mm, with a thickness of 80-120 microns.

For the experiments, membranes were numbered:

- 1 — PHB, MM = 278 kDa
- 2 — PHB, MW = 4600 kDa
- 3 — PGBV, MM = 900 kDa
- 4 — PHB, MM = 280 kDa
- 5 — PHB porous, MM = 280 kDa
- 7 — PHB, MM = 400 kDa

Nanofibers (diameter 5-10 microns) were obtained by the electrospinning of 8-10% solution of PHB in chloroform in NANON setup. As a collector, we used either whole plates of 10% of the polydimethylsiloxane (PDMS), or PDMS plates with pre-cut circular holes in them with a diameter of 10 mm. The conditions of the electrospinning were optimized for the maximal alignment of fibers on the collector.

## 2.3 Optical Mapping

Excitation waves were monitored using the Ca<sup>2+</sup>-sensitive fluorescent dye Fluo-4 (Invitrogen). The dye was added at a final concentration of 10 μM into standard Tyrode's solution (Sigma) for 60 min before the onset of the experiments. Images were acquired using EM-CCD camera (iXon3, Andor) connected to a macro-view MVX10, Olympus microscope. The data were acquired at 50 frames per sec in 128 × 128 pixels resolution which correspond to 18 × 18 mm<sup>2</sup> area of the dish. The fluorescence of the dye was excited at  $\lambda = 490$  nm using the microscope light source unit outfitted with a mercury lamp and a blue bandpass filter.

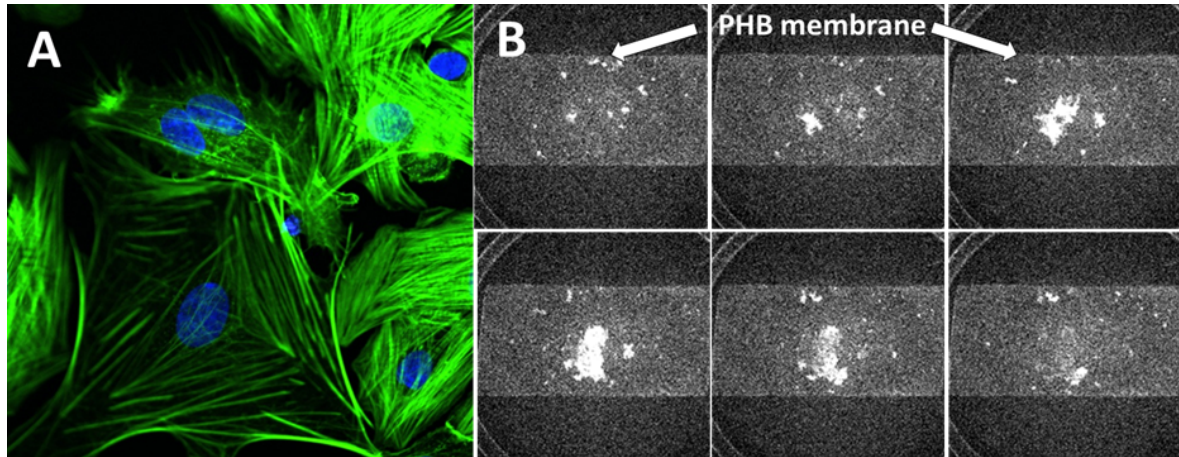


**Figure 1: Localized excitation in premature tissue culture.**

Primary 2-day old culture of neonatal rat cardiomyocytes grown on PHBV membrane #3 with M.W. = 900 kDa. A) Immunostaining: Alexa Fluor 488 phalloidin (green) — f-actin, DAPI (blue) — nuclear. B) Foci of excitation recorded with the optical mapping. Time between frames 100 msec.

At the end of the optical mapping of the control samples were treated with immunofluorescent dyes Alexa Fluor 488 phalloidin to identify the distribution of F-actin in cells, DAPI to visualize cell nuclei.

In some experiments, in order to distinguish between different types of cells, the labeling dye Cell Tracker Red was used cell. Photomicrographs were performed on LSM 710 confocal microscope

### 3 Results and discussion

#### 3.1 Culture of neonatal cardiomyocytes different dates grown on membranes with different molecular weight

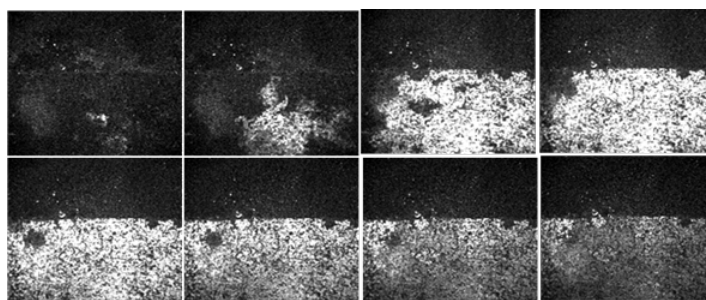


**Figure 2: Propagation of excitation in a 3 days — old culture.**

Primary 3-day old culture of cardiomyocytes grown on PHB membrane #1 with M.W. = 278 kDa. The boundary of the membrane is clearly seen in the upper part of the image. Time interval is 10 msec.

Excitation pattern was changed on the third day, a typical example represented in Fig. 2. The series of images shows that the excitation, originated in spontaneous pacemaker cells spread

Isolated cardiomyocytes were seeded and cultured on all 7 types of PHB membranes with different molecular weight. All of them exhibited vivid beating culture and demonstrational examples are described below. Fig. 1 demonstrates the culture of neonatal cardiomyocytes grown on PHBV membrane #3 on the second day after seeding. Optical mapping revealed that in spite of the ability of individual clusters of cells to spontaneous periodic activity, the excitation is localized, waves do not propagate through the entire culture and consequently, the cells do not form an excitable network. However, exci-

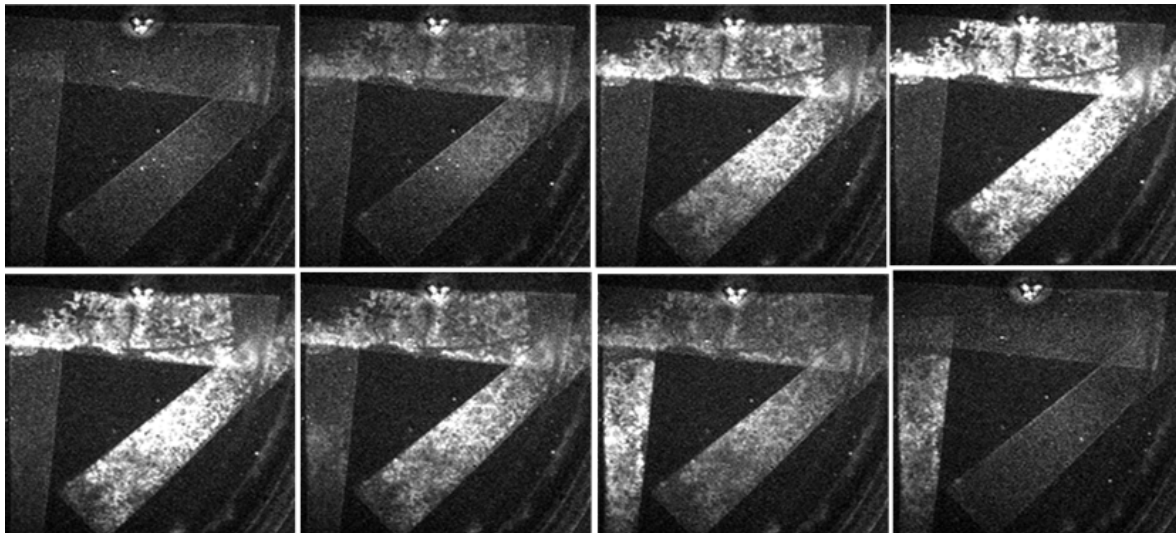


**Figure 3: Excitation propagation in 5-days old culture.**

Neonatal cardiomyocytes were seeded on the stripes of PHB membrane #3 with M.W. = 900 kDa. Excitation propagates through the arrangement of the stripes.

to the whole culture area. The recorded frames show section of the membrane with the attached cells, and a boundary between the membrane and the bottom of the Petri dish, not covered by a layer of cardiomyocytes is clearly visible.

Figure 3 illustrates the propagation of excitation waves in the five-day culture. PHB membrane was cut into strips, which were then coated with fibronectin and seeded with cells. The excitation waves propagated in the area of PHB strips.

In our experiments, cardiac tissue grown on PHB/PHBV membranes similar to other substrates [3] may reach functional maturity 3-4 days after cell seeding, and is able to effectively

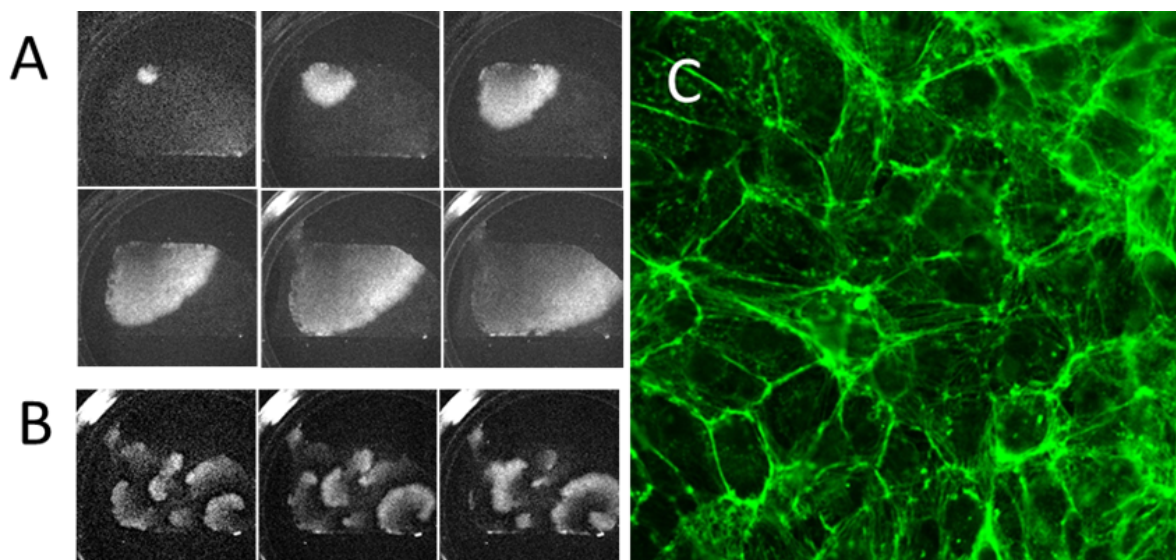


**Figure 4: 7 days-old culture of cardiomyocytes H11-ChR2 grown on PHB membrane #1 with M.W. = 278 kDa.**

A) Propagation of single wave. B) Rotating reentry waves. C) Alexa 488 Fluor Phalloidin staining of the culture.

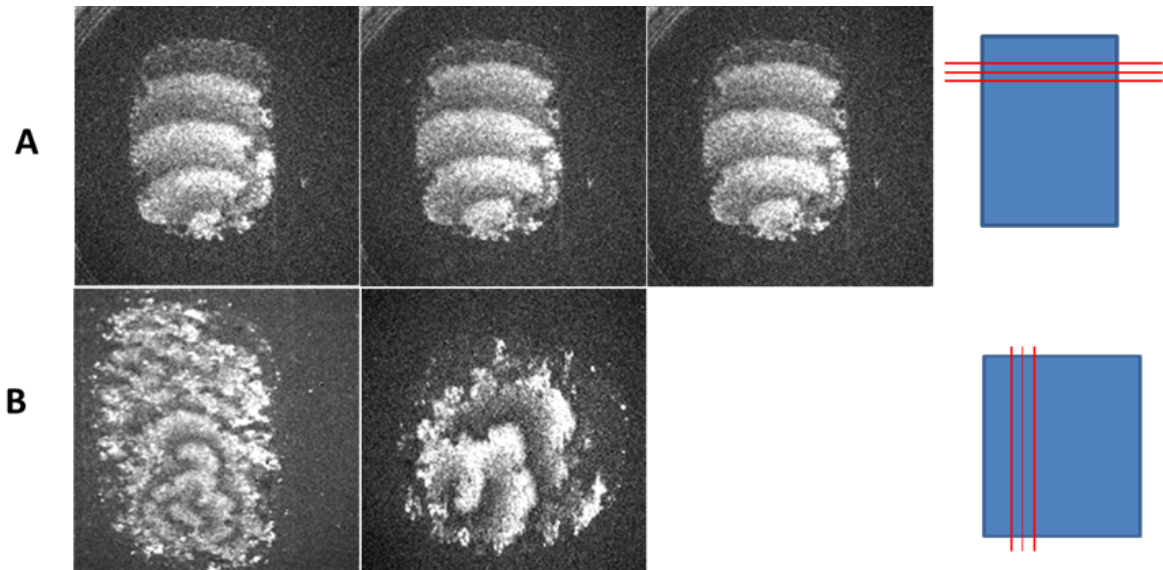


**Figure 5: Tissue culture HL1 grown on PDMS plate with applied PHB nanofibers.**  
A) 4-days old. B) 5-days old.

sustain excitation waves.

### 3.2 Cell culture HL-1 ChR2

Similarly to the primary cardiac culture, it was shown that the cells from the cell line HL-1 ChR2 can attach, grow and form the excitable interconnected network on PHB membranes. Figure 4 shows the propagation of excitation waves in HL-1 ChR2 cell culture. 4A represents the series of frames illustrating propagation of the single wave, and 4B — formation of rotating waves (reentry) at later stages of the activity in the culture.

### 3.3 Anisotropic culture obtained by using PHB nanofibers

We investigated the possibility of using PHB nanofibers for the forming of anisotropic layer of cardiac cells, as in [3]. In contrast to the previously used PMGI fibers, polyhydroxybutyrate fibers cannot be transferred to the glass using thermal printing. The adhesion of the fibers to the glass substrate is not sufficient to form a stable structure to serve as the substrate for cell culturing. For this reason, PHB nanofibers after electrospinning were transferred to the polydimethylsiloxane (PDMS) plate, and PDMS substrate with the fibers was used for seeding and culturing cells. Figure 5 shows the propagation of excitation waves in the 5-day old culture of HL-1 cells grown on PDMS plate with PHB nanofibers. As in the case of the PMGI fibers, PHB fibers are orienting factor for the cells, and they are extended in the direction of the fibers. As a result, anisotropy of propagation was observed: the wave speed along the direction of fibers was greater than in the direction perpendicular to the fibers orientation.

### 3.4 Cell culture on suspended PHB fibers

An important property of the nanofibers is that they can be used not only as a guiding factor for the cells growing on a solid substrate, but also substitute the solid support itself. This property of polymer fibers is especially important for assembling multilayered patches of tissue. We checked the ability of PHB fibers to serve as the carrier elements for cultured cells; it was found that the strength and elasticity of PHB fibers are sufficient for growing cells directly on them, without solid support. Figure 6 illustrates the propagation of excitation in the strip-like area of cultured tissue grown on suspended PHB fibers during 5 days. The excitation started at the left edge of the tissue and propagated through the area of most dense

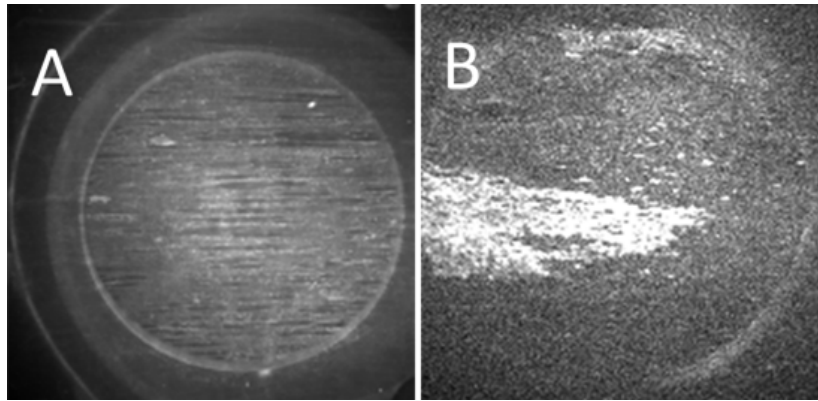


**Figure 6: Propagation of excitation in the tissue culture grown on suspended PHB nanofibers.** A) PHB nanofibers suspended in a circular frame. The direction of alignment is horizontal on the picture. B) Propagation of excitation from the left edge of the tissue culture.

fibers and cells, from left to right. Eventually, it spread on entire tissue area (not shown).

## 4 Conclusion

Our results show that cardiac cells of various origins can be successfully grown on polyhydroxybutyrate substrates, in both forms: membrane and nanofiber matrix. Apparently, the choice of the structure of the substrate is determined by its purpose: polymer membranes are convenient from a mechanical point of view, as a structural element that can be easily placed in the desired location. At the same time, the membrane bears isotropically arranged cells whereas nanofibers can create patches of cultured tissue with the desired degree of anisotropy [3]. In terms of development of electrophysiological syncytium, polyhydroxybutyrate scaffold showed its full compatibility with the excitability of cardiac cells.

The authors are grateful to A. Teplenin for the help with electrospinning setup and to I. Erofeev for the help with optical mapping.

## References

- [1] S. K. Bhatia. Tissue engineering for clinical applications. *Biotechnology Journal*, 5(12):1309–1323, 2010.
- [2] K. L. Christman and R. J. Lee. Biomaterials for the treatment of myocardial infarction. *Journal of the American College of Cardiology*, 48(5):907–913, 2006.
- [3] Y. Orlova, N. Magome, L. Liu, Y. Chen, and K. Agladze. Electrospun nanofibers as a tool for architecture control in engineered cardiac tissue. *Biomaterials*, 32(24):5615–5624, 2011.
- [4] X. T. Li, J. Sun, S. Chen, and G. Q. Chen. In vitro investigation of maleated poly(3-hydroxybutyrate-co-3-hydroxyhexanoate) for its biocompatibility to mouse fibroblast L929 and human microvascular endothelial cells. *Journal of Biomedical Materials Research Part A*, 87A(3):832–842, 2011.
- [5] S. Rathbone, P. Furrer, J. Lübben, M. Zinn, and S. Cartmell. Biocompatibility of polyhydroxyalkanoate as a potential material for ligament and tendon scaffold material. *Journal of Biomedical Materials Research Part A*, 93A(4):1391–1403, 2010.
- [6] L. Wang, Z. H. Wang, C. Y. Shen, M. L. You, J. F. Xiao, and G. Q. Chen. Differentiation of human bone marrow mesenchymal stem cells grown in terpolyesters of 3-hydroxyalkanoates scaffolds into nerve cells. *Biomaterials*, 31(7):1691–1698, 2010.

- [7] O. Duvernoy, T. Malm, J. Ramström, and S. Bowald. A biodegradable patch used as a pericardial substitute after cardiac surgery: 6- and 24-month evaluation with CT. *Thoracic and Cardiovascular Surgeon*, 43(5):271–274, 1995.
- [8] T. Malm, S. Bowald, A. Bylock, T. Saldeen, and C. Busch. Regeneration of pericardial tissue on absorbable polymer patches implanted into the pericardial sac. An immunohistochemical, ultrastructural and biochemical study in the sheep. *Scandinavian Journal of Thoracic and Cardiovascular Surgery*, 26(1):15–21, 1992.
- [9] A. Isomura, M. Hörning, K. Agladze, and K. Yoshikawa. Eliminating spiral waves pinned to an anatomical obstacle in cardiac myocytes by high-frequency stimuli. *Physical Review E*, 78(6):066216, 2008.
- [10] K. Agladze, M. W. Kay, V. Krinsky, and N. Sarvazyan. Interaction between spiral and paced waves in cardiac tissue. *Am J Physiol Heart Circ Physiol*, 293(1):H503–H513, 2007.
- [11] Dr. W. Claycomb. *HL-1 Cardiac Cell Line*. Multi Channel Systems MCS GmbH, 2004.

# Asymptotic dynamics and control of spiral and scroll waves

V. N. Biktashev<sup>1,2,\*</sup>, D. Barkley<sup>3</sup>, I. V. Biktasheva<sup>1</sup>, G. V. Bordyugov<sup>1,4</sup>,  
H. Dierckx<sup>1,5</sup>, A. J. Foulkes<sup>1,6</sup>, S. W. Morgan<sup>1</sup>, G. Plank<sup>7</sup>,  
N. A. Sarvazyan<sup>8</sup>, O. Selsil<sup>1</sup> and H. Verschelde<sup>5</sup>

<sup>1</sup>*University of Liverpool, UK*

<sup>2</sup>*University of Exeter, UK*

<sup>3</sup>*Warwick University, UK*

<sup>4</sup>*Humboldt University, Berlin, Germany*

<sup>5</sup>*Ghent University, Belgium*

<sup>6</sup>*Manchester University, UK*

<sup>7</sup>*Graz University, Austria*

<sup>8</sup>*George Washington University, Washington DC, USA*

\**e-mail address: v.n.biktashev@exeter.ac.uk*

## 1 Introduction

Spiral waves in two spatial dimensions (2D), and scroll waves in three dimensions (3D), are regimes of self-organization observed in physical, chemical and biological dissipative systems, where wave propagation is supported by a source of energy stored in the medium [1–9]. A spiral wave is a remarkably stable solution: it only reacts to perturbations if they are sufficiently close to its “core”. The result of that is that when only relatively small perturbations are concerned, dynamics of spiral waves is phenomenologically similar to that of “particles”, despite the fact that a spiral wave is in no way a localized object, but tends to fill up all the available medium. This macroscopic “wave-particle duality” [10] extends to three dimensions: scroll waves can be described as “string-like” objects [11].

This article is a retelling of a conference presentation which reviewed a few selected papers, dedicated to exploring this particle- and string-like dynamics and possibilities of exploiting it for the purposes of their control. A particular importance of control may be in cardiac tissue, where spiral and scroll waves underlie dangerous arrhythmias.

## 2 An outline of the theory

Here we briefly overview the key results of the asymptotic theory of spiral wave dynamics, more details of which can be found *e.g.* in [10, 12, 13] This theory centers on reaction-diffusion systems,

$$\partial_t \mathbf{u} = \mathbf{f}(\mathbf{u}) + \mathbf{D} \nabla^2 \mathbf{u} + \varepsilon \mathbf{h}, \quad \mathbf{u}, \mathbf{f}, \mathbf{h} \in \mathbb{R}^\ell, \quad \mathbf{D} \in \mathbb{R}^{\ell \times \ell}, \quad \ell \geq 2.$$

Here  $\ell$  is the number of reacting components,  $\mathbf{u} = \mathbf{u}(\vec{r}, t)$  is the column-vector of reagent concentrations,  $\vec{r} \in \mathbb{R}^2$  or  $\mathbb{R}^3$  is the position vector in the physical space,  $\mathbf{D}$  is the matrix of diffusion coefficients,  $\mathbf{f}$  is the column-vector describing the reaction rates, and  $\varepsilon \mathbf{h} = \varepsilon \mathbf{h}(\mathbf{u}, \nabla \mathbf{u}, \vec{r}, t)$ ,  $\varepsilon \ll 1$ , is a small perturbation. The rationale of considering  $\varepsilon \mathbf{h}$  separately from  $\mathbf{f}$  is that at  $\varepsilon = 0$ , the system has a symmetry with respect to translations and

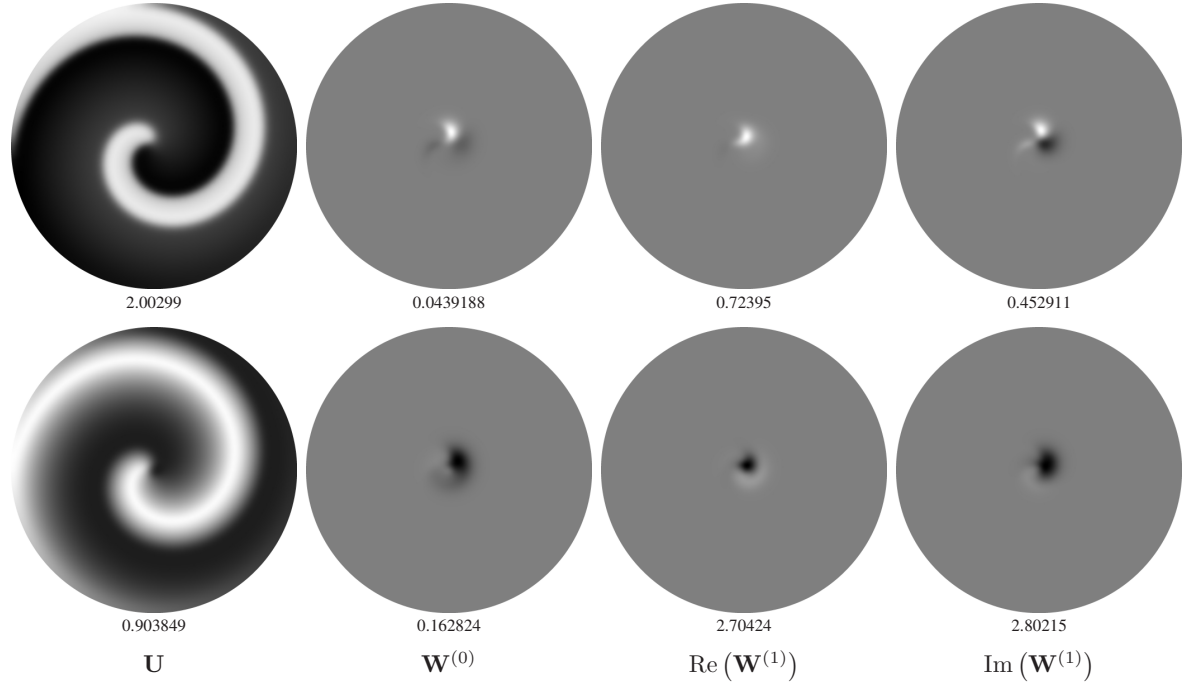


**Figure 1:** Response functions for FitzHugh-Nagumo system [14].

rotations of the  $\vec{r}$  space and translations in time  $t$ , so  $\varepsilon \mathbf{h}$  is a generic symmetry-breaking perturbation.

We assume existence of steadily rotating spiral wave solutions at  $\varepsilon = 0$ :

$$\mathbf{u}(\vec{r}, t) = \mathbf{U}(\rho(\vec{r} - \vec{R}), \vartheta(\vec{r} - \vec{R}) + \omega t - \Phi),$$

where  $\vec{r} = (x, y)$ ,  $\rho(\cdot)$  and  $\vartheta(\cdot)$  are polar coordinates,  $\vec{R} = (X, Y) = \text{const}$ ,  $\Phi = \text{const}$ , and  $\omega$  is an eigenvalue, *i.e.* there are only discrete values of  $\omega$  possible for any given reaction diffusion system; typically just one (up to the sign). This is not always the case with spiral waves: in some systems they “meander”, that is rotate unsteadily; this case is not considered here.

If  $\varepsilon$  is nonzero but small enough, the spiral drifts: solution remains approximately as above, but with  $\vec{R}$  and  $\Phi$  no longer constant but changing with time,  $d\vec{R}/dt = \mathcal{O}(\varepsilon)$ ,  $d\Phi/dt = \mathcal{O}(\varepsilon)$ .

The velocity of the drift caused by the perturbation is given by

$$\dot{R} = \varepsilon \int_{\phi-\pi}^{\phi+\pi} e^{-i\xi} \langle \mathbf{W}, \tilde{\mathbf{h}}(\mathbf{U}; \rho, \theta, \xi) \rangle \frac{d\xi}{2\pi} + \mathcal{O}(\varepsilon^2),$$

where  $(\rho, \theta)$  are corotating polar coordinates,  $\phi$  and  $\xi$  measure the rotation phase,  $\phi = \omega t - \Phi(t)$ , and the angular brackets denote an inner product in the functional space, that is an integral of the form

$$\langle \mathbf{w}, \mathbf{v} \rangle = \int_{\mathbb{R}^2} \mathbf{w}^+(\vec{r}) \mathbf{v}(\vec{r}) d^2\vec{r} = \int_0^\infty \int_0^{2\pi} \mathbf{w}^+(\rho, \theta) \mathbf{v}(\rho, \theta) \rho d\rho d\theta.$$

These expressions use the so called response function  $\mathbf{W}(\rho, \theta) = \mathbf{W}^{(1)}(\rho, \theta) \in \mathbb{C}$ : eigenfunction of the adjoint linearized operator, corresponding to eigenvalue  $i\omega$ . More precisely, this is “translational” eigenfunction as it describes drift (translation) of spiral centre  $\vec{R}$

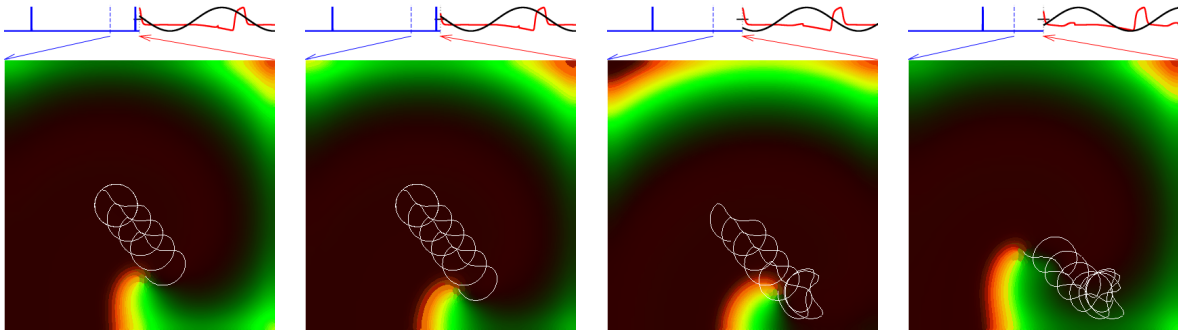


**Figure 2:** Resonant drift and resonant repulsion of a spiral wave in FitzHugh-Nagumo system. Graphs on top: the record of the action potential in the top right corner, vs the sinusoidal representing the clock that controls periodic stimulation. Change of relative position of action potential with respect to the clock means change of the direction of the drift. [13, 15]

through space; there is also “rotational” eigenfunction  $\mathbf{W}^{(0)}(\rho, \theta)$ , which describes the drift of the spiral’s fiducial rotation phase  $\Phi$ ; this is of a lesser interest in this review. Figure 1 illustrates the spiral wave solution and the response functions in a popular simple model of excitable media, the FitzHugh-Nagumo system. The pictures represent density plots of the corresponding solutions at a selected moment of time; they rotate clockwise as time progresses. The crucial feature of the response functions is that they quickly approach zero beyond the “core” area near to the rotation centre. This is the mathematical basis for the “particle-like” behaviour of spiral waves: the response functions show how an instantaneous and infinitesimal perturbation of a particular component will affect the spiral wave position, so the grey area outside the core means that any perturbation there will have virtually no long-term effect of the spiral, whereas perturbation into the lighter or darker areas within the core can cause a shift of the spiral wave rotation centre.

The simplest sort of spiral wave drift is a “resonant drift” of spirals, theoretically predicted by Davydov *et al.* [16] and first experimentally observed by Agladze *et al.* [17]. It occurs in response to perturbation explicitly depending on time,  $\mathbf{h} = \mathbf{h}(\mathbf{u}, t)$ , so violating the time shift symmetry. This dependence on time is periodic, with a period equal to the period of the spiral wave, thus “resonant”. The idea is illustrated in figure 2. The perturbation has a form of periodic pulses; the clock that controls these pulses is represented by the sinusoidal curve on top of the pictures. The result of one pulse is a displacement of the scroll by a certain distance in the direction, depending on the orientation of the spiral wave at the moment of the pulse delivery. The subsequent pulses are delivered with the period equal to the period of the spiral, hence they fall at the same orientation of the spiral and cause its displacements in the same direction again and again. The direction of this drift thus depends on the relative phase of the stimulation clock and the spiral wave phase, which is represented by the action potential, recorded at the top right corner, also shown on top of the pictures. However, the period of the spiral wave changes as its core approaches the boundary of the medium. Hence the phase relationship between the spiral and the stimulation changes, as can be seen by the change of the relative position of the action potential and the stimulation clock. Change of the phase difference means change of the direction of the drift, which will continue until the spiral moves far enough from the boundary, so the resonance restores and the drift proceeds at a straight line away from the boundary. This appears as a “repulsion” of the spiral from the boundary. An asymptotic description of this resonant repulsion mechanism can be found in [12, 15]. Since spiral waves underlie cardiac arrhythmias, their elimination by forcing them to drift to an inexcitable boundary can be a viable anti-arrhythmic strategy. In this

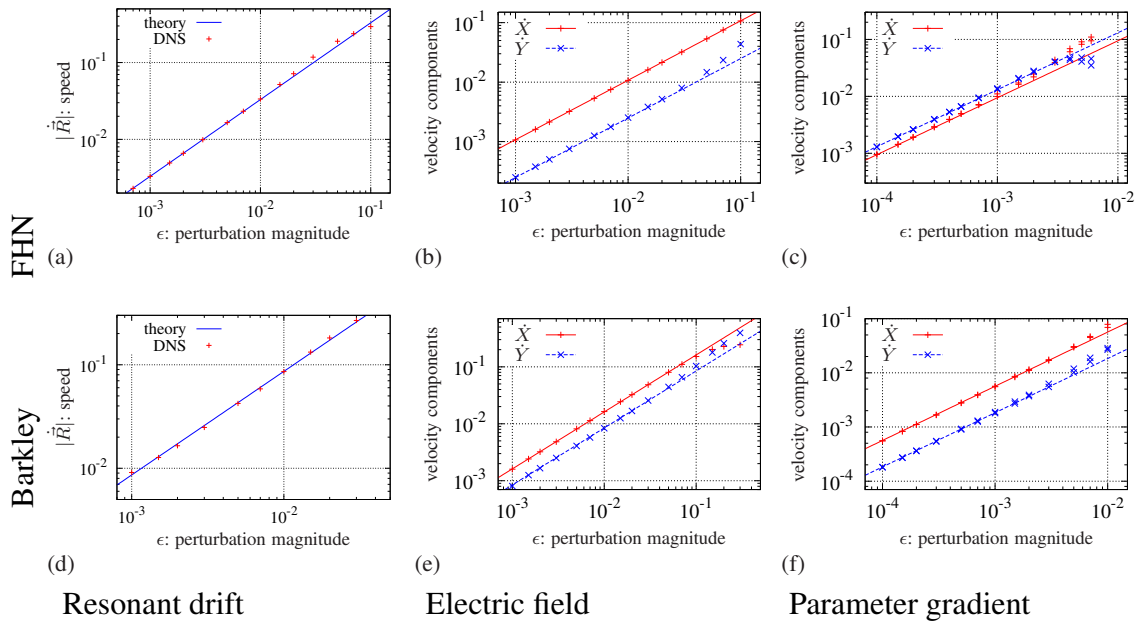


**Figure 4:** Drift speed: asymptotics (“theory”) vs direct numerical simulations (“DNS”) [13].

context, the resonant repulsion is an undesirable effect. It can, however, be easily overcome by using a feed-back, to synchronize the stimulation with the rotation of the spiral wave and thus ensure the resonance [12, 18].

Another well known sort of drift happens when the perturbation violates the spatial translation symmetry,  $\mathbf{h} = \mathbf{h}(\mathbf{u}, \vec{r})$ . This means, that the right-hand sides of the reaction-diffusion system depend on space coordinates, or, in physical language, the medium is spatially inhomogeneous. Within the perturbation theory, this results in an oscillating perturbation, applied by the spiral wave “onto itself”, as it rotates through points of the medium with different properties, so the perturbation is periodic and always resonant. This sort of drift is illustrated in figure 3, where the blue component of the colour represents one of the parameters of the reaction kinetics, so the right and left halves of the medium are slightly different in their properties, which causes the spiral to drift.

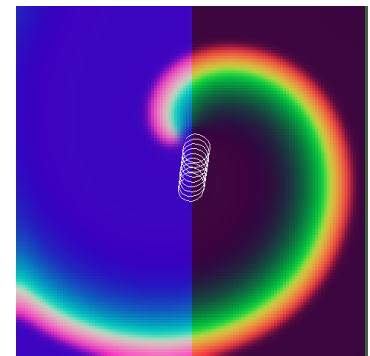


**Figure 3:** Drift of a spiral wave caused by stepwise parametric inhomogeneity in FitzHugh-Nagumo system [12, 13, 19].

The speed and direction of the drift caused by a stepwise inhomogeneity, as in figure 3, depend on the position of the spiral’s instant rotation centre relative to the step. If the inhomogeneity is in the form of a slight linear gradient spreading over a long distance, then the spiral can drift with the same speed in the same direction throughout that distance. A yet another sort of perturbation that can cause drift is the one that breaks the rotational symmetry of the problem:  $\mathbf{h} = \mathbf{h}(\mathbf{u}, \nabla \mathbf{u})$ . For instance, if the molecules of the reacting species are electrically charged and an external electric field is applied, then  $\mathbf{h} = \mathbf{A} \nabla \mathbf{u}$  where diagonal matrix  $\mathbf{A}$  represents electrophoretic mobilities of the reagents.

Knowing the response functions, the velocities of these types of drift: resonant, electrophoretic and inhomogeneity-induced, can be predicted. Figure 4 compares these predictions with direct numerical simulations, for the FitzHugh-Nagumo system, and for the Barkley system, which is a very popular variation of the FitzHugh-Nagumo, particularly convenient for conceptual simulations.

Theoretical predictions based on the response functions showed that the dependence of the inhomogeneity-induced drift on the relative location of the spiral wave and inhomogeneity sometimes may be not straightforward: attraction at some distances may change to repulsion at other distances. For the case of a localized inhomogeneity, this may lead to the situation that there is a stable distance between the spiral and the inhomogeneity, so a spiral wave starting from a wide range of initial conditions launches into a circular “orbital motion” around the inhomogeneity, as shown in figure 5.

In the figure, the circular green spot in the middle represents the inhomogeneity, *i.e.* the site where the parameters of the reaction kinetics slightly differ. The spiral wave is depicted by the red/blue colour palette, with red component representing the “excitation” variable of the Barkley system and the blue component representing the “recovery” variable. The thin white line depicts the trajectory of the tip of that spiral wave, which is defined as an intersection of selected isolines of the two components. This trajectory was averaged over every period of rotation, and the corresponding instant rotation centres are represented by blue (earlier time moments) and yellow (later time moments) small circles. At the selected parameters, the inhomogeneity is repelling at small distances and attracting at larger distances. Correspondingly, the spiral wave that started near the local inhomogeneity, departs away from it, but only until it reaches the distance beyond which the repulsion changes to attraction. The spiral then continues to drift along the circle of the radius at which the radial component of the drift force generated by the inhomogeneity vanishes. The radius and the velocity of this orbital drift are in good agreement with predictions based on the response functions.

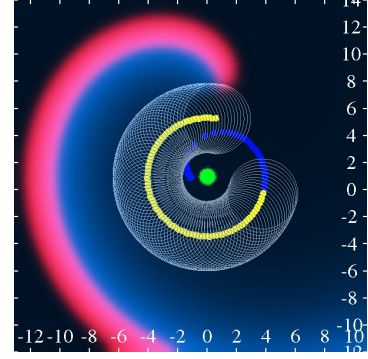


**Figure 5:** Orbital movement of a spiral wave in Barkley system around a localized inhomogeneity [20].

### 3 Application in 2D: drift of spirals in an ischaemic border zone

In the asymptotic theory described above, the drift velocity  $\dot{\vec{R}}$  linearly depends on the perturbation  $\mathbf{h}$ . This immediately implies that when several different types of perturbations are applied simultaneously, their effects add up. Thus we have a superposition principle: a superposition of various perturbations

$$\varepsilon \mathbf{h} = \sum_j \varepsilon_j \mathbf{h}_j,$$

has additive effect on the drift velocity

$$\dot{\vec{R}} \approx \sum_j \varepsilon_j \gamma_j,$$

where the “specific forces” are

$$\gamma_j = \int_{\phi-\pi}^{\phi+\pi} e^{-i\xi} \langle \mathbf{W}, \tilde{\mathbf{h}}_j \rangle \frac{d\xi}{2\pi}.$$

This has been used to explain some phenomena observed in a computational model, describing experiments with cultures of cardiac cells, which in turn mimic events that happen at a boundary of an ischemic zone that gradually recovers during reperfusion ([21], see figure 6). In the experiments and in the simulations, a certain combination of variations in

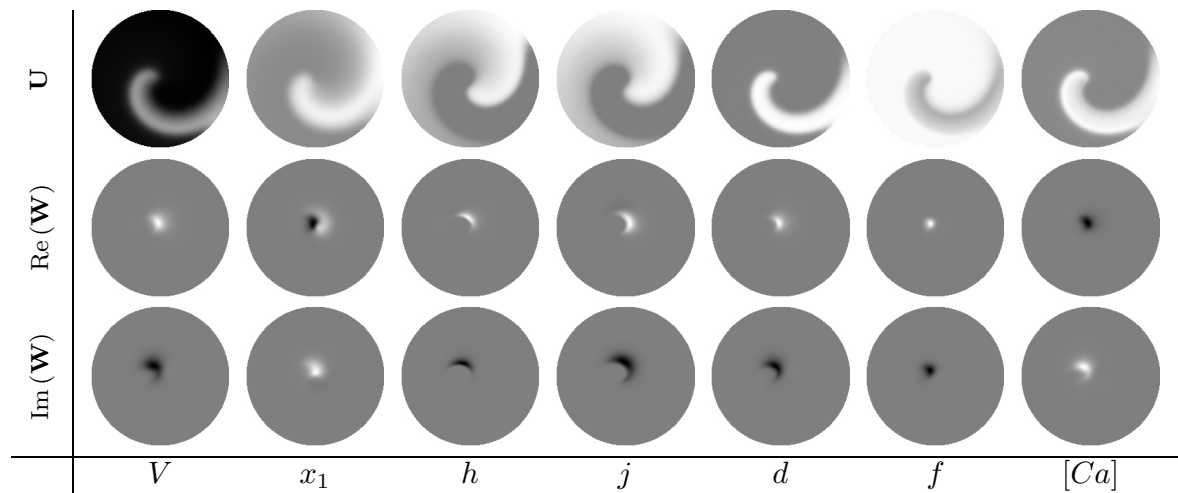


**Figure 7:** Translation response functions for Beeler-Reuter-Pumir model [22].

cell excitability/automaticity and in strength of their electric coupling with each other created conditions in which spontaneous activity of individual cells created propagating waves which broke up creating microscopic-scale spiral wave activity. One notable feature of these spiral waves was their drift, which would often temporarily stop, or “pin” at local heterogeneities. This feature was essential for the arrhythmogeneity of the ischemic border zone, as the pinned spiral waves had the chance to be not dragged together with the border zone, but survive its passage, after which they develop into macroscopic scale re-entrant waves.

The asymptotic theory has been applied to analyse and explain these phenomena. Figure 7 illustrates the response functions calculated for the particular ionic model of cardiac excitability that was used in the simulations of [21]. The figure shows the spiral wave solution and the components of the translational response function, in the same format as in figure 1, only this model has  $\ell = 7$  components. As before, a prominent feature is the localization of all the components of the response function, which justifies the particle-like description of spiral waves in this system.

Indeed, comparison of the predictions of the asymptotic theory with standard numerical simulations, such as electrophoretic drift,

showed a good agreement. In simulations more specific for the electrophysiological setting described above, one deals with a combination of perturbations: localized heterogeneities, smooth gradients of excitability and of cell-to-cell coupling strength, *i.e.* diffusion coefficient. In realistic simulations, the strength of these perturbations is not necessarily small

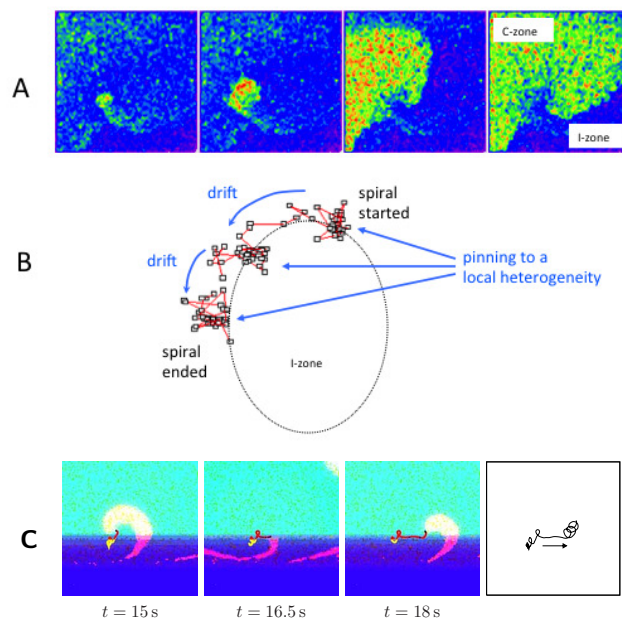


**Figure 6:** Start/stop drift of spiral wave in (A,B) a culture of neonatal rat cells, (C) in simulations using Pumir’s modification of Beeler-Reuter model [21].

enough for quantitative correspondence, still the asymptotic theory has been able to explain, on the qualitative level, some of the observed phenomena.

Figure 8 presents comparison of asymptotic theory with direct numerical simulation. Panel (a) is a fragment of simulation where the drifting spiral wave (the trajectory of the tip is shown by a thin white line) is temporarily stopped at a dark spot and then resumed the drift afterwards. A small puzzle was that the experimental data suggested that such temporary stopping could happen both near spots of higher excitability, as well as spots of lower excitability, whereas asymptotic theory predicts that if a localized perturbation of one sign is attracting then a perturbation of the opposite sign must be repelling.

A hypothetical explanation that repulsion may change to attraction at different distances (see discussion of “orbital motion” above), did not work for this case as the response functions in this system did not show the sign-changing character required for that. Figure 8(b) describes a hypothetical mechanism of temporary pinning at a repulsive inhomogeneity, which is consistent with the present system. In this case, the spiral drift slows down near an unstable equilibrium point, where the drift forces due to localized inhomogeneity and due to the smooth gradients equilibrate each other. Panel (c) illustrates another possibility, where two repelling circular local inhomogeneities are arranged in such a way that a stable equilibrium between now three forces exists, where the spiral can pin indefinitely (or in reality, until the smooth gradients move away due to reperfusion). Panel (d) shows for comparison the more straightforward case of pinning to an attracting heterogeneity. In panels (b–d), green dots in the middle represent the local heterogeneities, the red cyloidal line is the trajectory of the tip in the numerical simulations, the small black arrows are the direction field of the drift according to the asymptotic theory and blue open circles are the trajectories of the drift calculated based on the asymptotic theory.

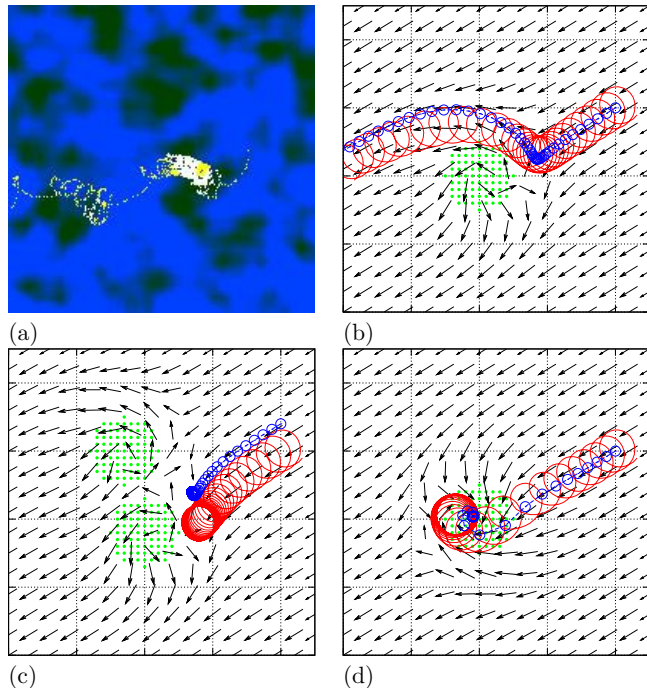


**Figure 8:** Pinning of drifting spiral wave to local heterogeneity.

#### 4 Applications in 3D: resonant drift of scrolls and filament tension

The asymptotic theory of spiral waves in 2D can be extended to scroll waves in 3D. The instantaneous rotation center of a spiral wave becomes the filament of a scroll in 3D. So equations of motion for the spiral position  $\vec{R}(t)$  and phase  $\Phi(t)$  are transformed to equations of motions of the scroll wave filament  $\vec{R}(\sigma, t)$  and the corresponding phase distribution  $\Phi(\sigma, t)$ , where  $\sigma$  is a coordinate along the filament. Thus we have new degrees of freedom in 3D: the filament can be curved, and the phase may vary along the filament.

Variation of scroll phase along its filament is called twist. Remember that the direction of the resonant drift of a spiral wave depends on the phase of that spiral. So if resonant forcing is applied to a twisted scroll, then “spiral waves” in different cross-sections of this scroll will have different phases and drift in different directions. This will lead to formation of a scroll with a filament of a helical shape, illustrated in figure 9(a). The picture shows a snapshot of

a wavefront, defined as an isosurface of the excitation variable, more precisely its part where the recovery variable is less than a certain constant, so only the front of the excitation wave is shown but not the back. Note that as a result, the scroll as a whole does not drift anywhere, as its different parts tend to go into different directions.

The twist of the scroll in figure 9(a) was created artificially by using appropriate initial and boundary conditions. In cardiac tissue, twist may occur spontaneously due to inherent inhomogeneities of the electrophysiology of cells and anisotropy of the structure of tissue. This may result in a failure of the resonant forcing to eliminate scrolls in heart tissue. A snapshot of a simulation of resonant forcing of a fibrillatory activity in an anatomically realistic model of heart ventricles is shown in figure 9(b). Unlike panel (a), here are shown only parts of the wavefronts that are close to the filament. Technically, the wavefront is defined as an isosurface of the variable representing transmembrane voltage, which is usually understood as the excitation variable. One of the other 6 variables was chosen as the recovery variable that is often used to distinguish wavefronts from wave backs. Here the selection of the voltage isosurface pieces for visualization was done by selecting only intermediate (neither the front, nor the back) values of the recovery variable. So we may assume that depicted are the “lines of singularity”, which correspond to the tips of the spiral waves in 2D, and which rotate around the scroll filaments. Besides, we can see variations of the phase of the filament, as change of orientation of the visualized stripe of the front surface. Twist of the filament correlates with its helical shape.

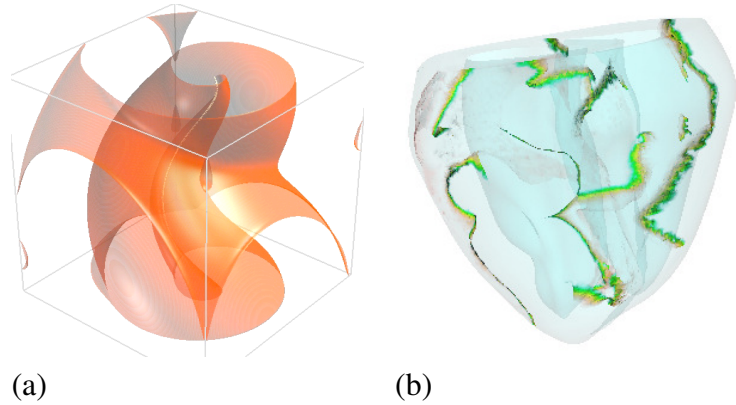


**Figure 9:** Twisted scroll with helical filament caused by resonant stimulation, (a) in Barkley system, (b) in the rabbit ventricle anatomical model with modified Beeler-Reuter kinetics [23].

Dynamics of the filament position can be interesting in itself even without effects of twist or resonant forcing. The asymptotic motion equation can be written in terms of the Frenet-Serret frame, see figure 10, where  $\vec{T}$  is the tangent vector,  $\vec{N}$  is the principal normal vector and  $\vec{B}$  is the binormal vector at a point of the filament with coordinate  $\sigma$  along the filament.

Then in the lowest order, the filament equation of motion is [26]

$$(\vec{N} + i\vec{B}) \cdot \vec{R} = (b_2 + ic_3) \kappa \quad (1)$$

where  $\kappa = |\partial_s \vec{T}|$  is the filament curvature,  $s$  is the arclength coordinate, so  $ds = |\partial_\sigma \vec{R}| d\sigma$ , and the coefficients  $b_2$  and  $c_3$  can be calculated using the response function. A simple property of this equation of motion is that, neglecting boundary effects, the total length of the filament satisfies

$$\frac{d}{dt} \int ds = - \int b_2 \kappa^2 ds,$$

that is, if the coefficient  $b_2 > 0$ , then the filament shrinks unless it is straight; and if  $b_2 < 0$ , then it will lengthen, and the straight filament is unstable. Thus this coefficient is sometimes called filament “tension”.

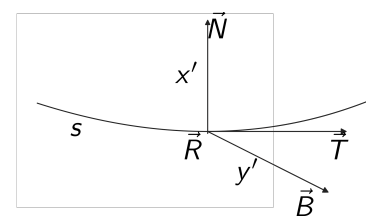


**Figure 10:** Frenet-Serret frame at a point of the scroll filament.

Instability of the straight filament, in a large enough volume of excitable medium, leads to constant lengthening through curving, and multiplication through break-up of scroll filaments, and can result in “scroll wave turbulence”, see figure 11(a). The apparently chaotic character of this regime, and the “critical mass” phenomenon, in that a large enough volume is required for it, make it similar to cardiac fibrillation, hence a possibility that negative tension may play a role in some forms or stages of cardiac fibrillation.

Notably scroll wave turbulence occurs in 3D in the same equations which in 2D render perfectly stable spiral waves.

Hence it is interesting, how transition from a stable 2D rotation to a 3D turbulence happens in thin sheets of excitable media, like some cardiac muscles, including human atria. Figure 11(b) illustrates one such regime, where the filament bends but only slightly, and a result of that bend is precession, showing up on the surface of the medium as a meandering spiral, whose tip describes a flower-like trajectory. A similar phenomenon was observed in a model of heart tissue [27]. This regime can be described using response functions, but higher-order asymptotics compared to those in equation (1) are required [25]. The key role in restabilizing a filament with negative tension belongs to a coefficient called “filament rigidity”. There is an analogy here with mechanics of an elastic beam, so that the negative tension of the scroll filament corresponds to the compressive stress of the beam, the filament rigidity corresponds to the beam’s stiffness, and the regime illustrated in figure 11(b) is similar to “Euler’s buckling” of the beam.

The theory of arrhythmogenicity of retracting ischemic border zone, briefly described above, was 2D, as were the cell culture experiments on which it was based. However some real cardiac muscles, including human ventricles, are essentially 3D. The concept of filament tension is useful for consideration of possible 3D aspects, which cannot be studied in cell culture experiments, but can be simulated numerically. Two snapshots from such numerical experiments are shown in figure 12. The settings in these two experiments were exactly the same except for the value of an excitability parameter for the bulk of the recovered tissue above the retracting ischaemic boundary zone. On the left panel, the excitability is low, so that the filament tension is negative. After transition of the boundary zone, there is a scroll wave in the recovered tissue, *i.e.* in the cardiac muscle we would see a macroscopic re-entry. On the right panel, on the contrary, the excitability is higher and the filament tension is positive. As a result, since all the newly born scroll waves have filaments ending within the chaotic activ-

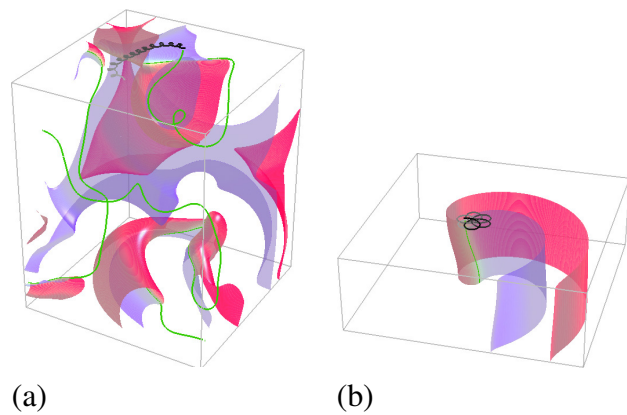


**Figure 11:** Effects of negative filament tension: (a) scroll wave turbulence in a big volume, (b) buckled scroll in a thin volume, Barkley system [24, 25].

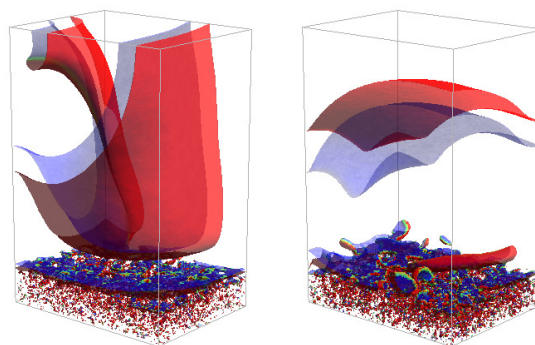


**Figure 12:** Effect of filament tension on arrhythmogenicity of retracting ischemic border zone. Left: negative tension. Right: positive tension [22].

ity of the moving boundary zone, these filaments are dragged down together with that zone by that tension. In the simulation in the right panel, after the passage of the boundary zone, the medium returns to the resting state, which would correspond to no re-entrant activity in the cardiac muscle.

## 5 Conclusion

Mathematically, the localization of the response functions of spiral waves is a special feature of the corresponding linearization operator, when the eigenfunctions of the operator and of its adjoint have very different properties and belong to different spaces. Physically this localization means that spiral waves behave like point objects, and scroll waves behave like string objects, despite their wave appearance. Asymptotic theory based on that is (within its limits) in good quantitative agreement with direct simulations. This asymptotic theory can successfully predict new qualitative phenomena (orbital motion, pinning to repelling inhomogeneity, scroll turbulence, buckling). This theory is applicable to cardiac excitation models and may have impact on clinically relevant problems.

## Acknowledgements

Studies described in this mini-review have been supported through the years by: Wellcome Trust grants 03881712, 045192, EPSRC grants GR/S75314/01, EP/S016391/1, EP/D500338/1, EP/D074789/1, EP/D074746/1, EP/I029664/1 (UK), Royal Society grant 2005/R4 (UK), NIH grants HL076722, HL095828 (USA), Austrian Science Fund FWF grant F3210-N18 and a travel grant of FWO-Flanders (Belgium). Experimental results shown in figure 6 were obtained in collaboration with A. Arutyunyan.

## References

- [1] A. M. Zhabotinsky and A. N. Zaikin. Spatial phenomena in the auto-oscillatory system. In E. E. Selkov, A. A. Zhabotinsky, and S. E. Shnol, editors, *Oscillatory processes in biological and chemical systems*, page 279. Nauka, Pushchino, 1971.
- [2] M. A. Allesie, F. I. M. Bonke, and F. J. G. Schopman. Circus movement in rabbit atrial muscle as a mechanism of tachycardia. *Circ. Res.*, 33:54–62, 1973.
- [3] F. Alcantara and M. Monk. Signal propagation during aggregation in the slime mold *Dictyostelium Discoideum*. *J. Gen. Microbiol.*, 85:321–334, 1974.
- [4] N. A. Gorelova and J. Bures. Spiral waves of spreading depression in the isolated chicken retina. *J. Neurobiol.*, 14:353–363, 1983.
- [5] B. F. Madore and W. L. Freedman. Self-organizing structures. *Am. Sci.*, 75:252–259, 1987.
- [6] S. Jakubith, H. H. Rotermund, W. Engel, A. von Oertzen, and G. Ertl. Spatiotemporal concentration patterns in a surface reaction — propagating and standing waves, rotating spirals, and turbulence. *Phys. Rev. Lett.*, 65(24):3013–3016, 1990.
- [7] J. Lechleiter, S. Girard, E. Peralta, and D. Clapham. Spiral calcium wave propagation and annihilation in *Xenopus Laevis* oocytes. *Science*, 252(5002), 1991.
- [8] T. Frisch, S. Rica, P. Coulet, and J. M. Gilli. Spiral waves in liquid crystal. *Phys. Rev. Lett.*, 72(10):1471–1474, 1994.
- [9] M. C. Cross and P. C. Hohenberg. Pattern formation outside of equilibrium. *Rev. Mod. Phys.*, 65(3):851–1123, 1993.
- [10] I. V. Biktasheva and V. N. Biktashev. On a wave-particle dualism of spiral waves dynamics. *Phys. Rev. E*, 67:026221, 2003.

- [11] H. Verschelde, H. Dierckx, and O. Bernus. Covariant stringlike dynamics of scroll wave filaments in anisotropic cardiac tissue. *Phys. Rev. Lett.*, 99:168104, 2007.
- [12] V. N. Biktashev and A. V. Holden. Resonant drift of autowave vortices in 2d and the effects of boundaries and inhomogeneities. *Chaos Solitons & Fractals*, 5(3,4):575–622, 1995.
- [13] I. V. Biktasheva, D. Barkley, V. N. Biktashev, and A. J. Foulkes. Computation of the drift velocity of spiral waves using response functions. *Phys. Rev. E*, 81(6):066202, 2010.
- [14] I. V. Biktasheva, D. Barkley, V. N. Biktashev, G. V. Bordyugov, and A. J. Foulkes. Computation of the response functions of spiral waves in active media. *Phys. Rev. E*, 79(5):056702, 2009.
- [15] V. N. Biktashev and A. V. Holden. Resonant drift of an autowave vortex in a bounded medium. *Phys. Lett. A*, 181(3):216–224, 1993.
- [16] V. A. Davydov, V. S. Zykov, A. S. Mikhailov, and P. K. Brazhnik. Drift and resonance of spiral waves in a distributed excitable medium. *Radiofizika*, 31:574–582, 1988.
- [17] K. I. Agladze, V. A. Davydov, and A. S. Mikhailov. The observation of the spiral wave resonance in a distributed excitable medium. *JETP Letters*, 45(12):601–605, 1987.
- [18] V. N. Biktashev and A. V. Holden. Design principles of a low-voltage cardiac defibrillator based on the effect of feed-back resonant drift. *J. Theor. Biol.*, 169(2):101–113, 1994.
- [19] A. M. Pertsov and E. A. Ermakova. Mechanism of the drift of a spiral wave in an inhomogeneous medium. *Biofizika*, 33(2):338–342, 1988.
- [20] V. N. Biktashev, D. Barkley, and I. V. Biktasheva. Orbital motion of spiral waves in excitable media. *Phys. Rev. Lett.*, 104(5):058302, 2010.
- [21] V. N. Biktashev, A. Arutunyan, and N. A. Sarvazyan. Generation and escape of local waves from the boundary of uncoupled cardiac tissue. *Biophys. J.*, 94:3726–3738, 2008.
- [22] V. N. Biktashev, I. V. Biktasheva, and N. A. Sarvazyan. Evolution of spiral and scroll waves of excitation in a mathematical model of ischaemic border zone. *PLoS ONE*, 6(9):e24388, 2011.
- [23] V. N. Biktashev, I. V. Biktasheva, G. Plank, and S. W. Morgan. Resonant drift of scroll waves. In preparation.
- [24] V. N. Biktashev. A three-dimensional autowave turbulence. *Int. J. of Bifurcation and Chaos*, 8(4):677–684, 1998.
- [25] H. Dierckx, H. Verschelde, Ö. Selsil, and V. N. Biktashev. Buckling of scroll waves. *Phys. Rev. Lett.*, 109(17):174102, 2012.
- [26] V. N. Biktashev, A. V. Holden, and H. Zhang. Tension of organizing filaments of scroll waves. *Phil. Trans. Roy. Soc. Lond. ser. A*, 347:611–630, 1994.
- [27] S. Alonso and A. V. Panfilov. Negative filament tension in the Luo-Rudy model of cardiac tissue. *Chaos*, 17:015102, 2007.

# Self-Sustained Peristaltic Transport in Biological Systems: A Theoretical Study

O.A. Dudchenko<sup>1</sup> and G.Th. Guria<sup>1,2,\*</sup>

<sup>1</sup>*Moscow Institute of Physics and Technology, Dolgoprudny, Russia*

<sup>2</sup>*National Research Centre for Haematology, Moscow, Russia*

\**e-mail address: guria@blood.ru*

Human body can be viewed as a collection of systems, each playing a specific role in the function of the body as a whole [1]. Transporting systems – gastro-intestinal, cardiovascular, lymphatic, urinary, etc., – are important constituents of this collection.

Similar in functional attributes transporting systems share many common features in their structural organization: each can be regarded as a hollow tubular organ which relies (to a different extent) on peristaltic motility driven by muscle cells from within the wall of the conducting tube.

Coordinating contractile muscle activity of the adjacent tube segments is crucial for achieving efficient transport. Mechanisms that ensure the required coordination in different physiological transport systems have been the subject of many experimental and theoretical studies [2–10]. These studies have shown that the stimuli, which control the muscle cell activity, are to a large extent autonomous, independent of central nervous system input. Instead, the contractions are coordinated locally, by the so-called enteric nervous system.

A wonderful illustration to the autonomous, self-sustainable nature of peristaltic motility can be found, for example, in the work conducted by Prof. G.W. Mawe and his co-workers at the University of Vermont College of Medicine. Their research involves filming peristaltic motility of an isolated guinea-pig colon. The colon segment is kept vital by placing it into an

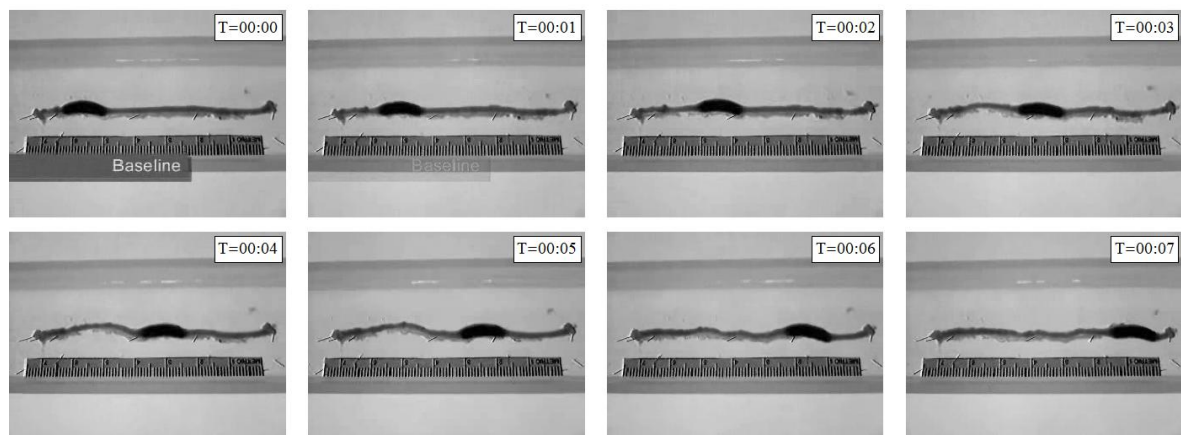


**Figure 1:** Image sequence illustrating the self-sustainable nature of peristaltic motility: a rigid pellet is being propelled by an isolated guinea-pig colon. See [11] for a detailed account of the experimental procedure. Courtesy of Prof. Gary W. Mawe, Department of Anatomy and Neurobiology, University of Vermont College of Medicine.

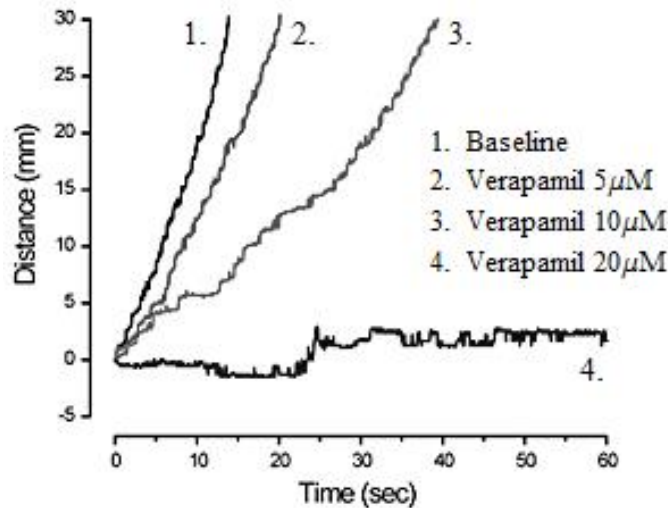


**Figure 2:** Dose-dependent reduction of peristaltic propulsion rate. Data are reproduced with permission of Dr. Gerald Herrera of Catamount Research and Development ([www.catamountresearch.com](http://www.catamountresearch.com)).

oxygenated organ bath. Figure 1 gives a sequence of images from one of their experimental videos showing a rigid pellet being propelled along the isolated colon segment.

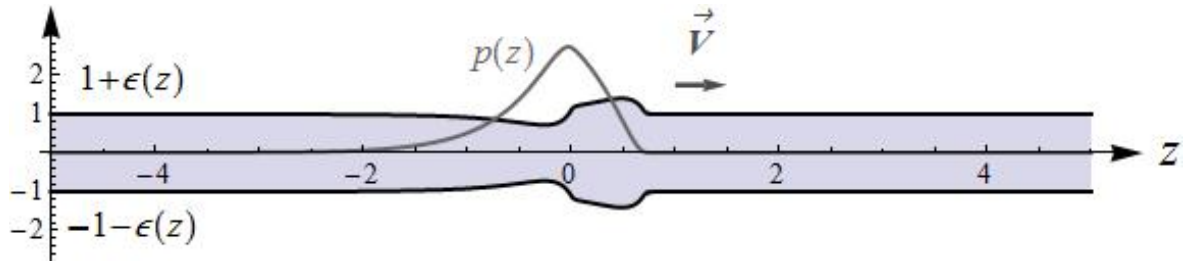
The analysis of experimental data shows that the velocity of the pellet remains fairly constant along the conducting vessel (see Fig. 2). Motility rates in the same preparation are consistent in sequential trials (see [12] for raw motility data recorded in a single specimen from a total of 8 experiments). The consistency of the results allows one to use the described experimental setup to monitor the response of the transporting system to various influences, in particular, pharmacological agents [12]. Figure 2 demonstrates the dose-dependent decline of peristaltic wave velocity caused by verapamil — a common drug for treating high blood pressure.

Assessing the adverse reaction of transporting organs to drugs is an important problem that relies on our understanding of the relationship between the motility rate and the state of the transporting system: the Young’s modulus of the vessel, sensitivity to electrical and mechanical stimuli, etc. In our recent paper [13] we have tried to elucidate the abovementioned relationship by suggesting a mathematical model of self-sustained peristaltic motility.

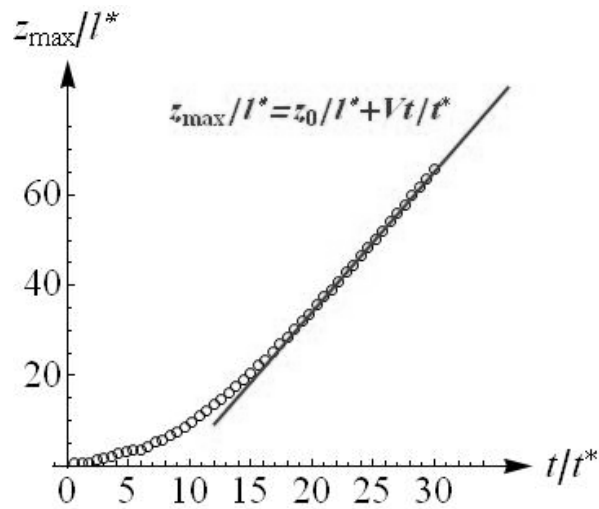
The model relies on phenomenological representation of contraction control: we simulated the enteric nervous system with a chain of excitable elements [7, 8]. The excitable elements have been suggested to be sensitive to mechanical stretch. The ability of a transporting system to perform autonomous peristaltic pumping was interpreted in terms of the model as the ability to propagate sustained waves of wall deformation.

Figure 3 shows a typical example of a solution of the model equations: a stationary peristaltic wave with a lumen deformation profile given by  $\varepsilon(z)$  and a (non-dimensional) pressure profile given by  $p(z)$ . Fig. 4 plots the position of the wave’s crest over time to illustrate the establishment of a stationary regime of propagation in numerical experiments (compare to Fig. 2).

The analysis of the model allows one to conclude, among other things, that local sensitivity to radial stretch is, in fact, sufficient to organize contractions into a self-sustained propagating deformation wave even in the absence of “horizontal” control from within the enteric network. The mechanism of propagation is as follows. The transported fluid bolus results in the dilation of the tube segment, which, being sufficiently large, causes the vessel segment to contract. Contraction pushes the fluid bolus into the adjacent segment where it,



**Figure 3:** A mathematical representation of a self-sustained travelling peristaltic wave. The position of the lumen is given by  $1 + \varepsilon(z)$  and  $-1 - \varepsilon(z)$  lines. The associated pressure wave is denoted with  $p(z)$ . The arrow with a letter “V” above it denotes the direction in which the wave is moving.



**Figure 4:** The result of a typical numerical experiment: distance from the vessel boundary to the crest of the wave  $z_{\max}$  plotted over time  $t$ .  $l^*$  and  $t^*$  denote characteristic length and time scales. Fitting of data to a straight line is shown for points distant from the vessel boundary. Compare to Fig. 2.

in turn, causes dilation. If the dilation reaches a threshold value, contraction is triggered and the sequence of events repeats itself.

In this paper we are trying to advance our understanding of coupling through mechanosensitive control circuits by asking whether other mechanical stimuli, beside radial stretch, are capable of coordinating peristaltic motility. In particular we focus our attention on shear stress, as shear stress is known to be a potent regulator of muscle cell activity. It is especially important in blood vessel physiology [15–17] where it is suspected to play an important role in coordinating the propagation of waves of vasorelaxation [18–22].

### Mathematical model

For the purpose we formulate a simple phenomenological model of a shear stress-sensitive muscular vessel. The equations of the model are as follows:

$$(1 + \varepsilon) \frac{\partial \varepsilon}{\partial t} = \frac{R_0^2}{16\mu} \frac{\partial}{\partial z} \left( (1 + \varepsilon)^4 \frac{\partial p}{\partial z} \right) \quad (1)$$

$$p + \tau_s \frac{\partial p}{\partial t} = E \left( \varepsilon + \tau_c \frac{\partial \varepsilon}{\partial t} \right) + p_a, \quad (2)$$

$$\frac{\partial p_a}{\partial t} = S(\sigma) - \beta(p_a - p_1)(p_a - p_2)(p_a - p_3). \quad (3)$$

Eq. (1) results from applying lubrication theory approximations to the equations of motion of an incompressible Newtonian fluid of viscosity  $\mu$  in a tube undergoing axisymmetric deformation [23–25]. The variables introduced are wall deformation  $\varepsilon = \varepsilon(z, t)$  and transmural pressure  $p = p(z, t)$ .  $R_0$  denotes the radius of the lumen at rest, when the vessel wall is unstrained and unstimulated.

Eq. (2) arises from circumferential stress-strain relationship given by the standard 4-element linear solid model of viscoelastic wall material [26, 27]. Parameters  $\tau_s$ ,  $\tau_c$  define the characteristic time-scales of stress relaxation and creep of an unstimulated vessel.  $E$  is the measure of wall stiffness ( $E \simeq Yh_0/R_0$  where  $Y$  denotes the Young's modulus of the vessel wall material). The  $p_a$ -term is added to the linear solid model to account for contractile forces that arise in response to regulatory stimuli.

Eqs. (1) and (2) have been used to describe, respectively, the fluid flow and the vessel wall dynamics in our previous work [13] dedicated to the analysis of regulatory potential of stretch-induced stimuli. The novel Eq. (3) models the ability of the vessel wall to relax when the shear stress  $\sigma$  on the luminal surface increases. As in [13] we suggest that, as a first approximation, the local response to a regulatory stimuli can be described as threshold «switching» from a «relaxed» state (with  $p_a = p_1$ ) to a «stressed» one (with  $p_a = p_3 > p_1$ ) and vice versa. A cubic reaction term is used to describe threshold behavior.

The term  $S(\sigma)$  represents a mechanosensitive stimulus associated with local shear stress  $\sigma$ . One can easily show that within the bounds of lubrication theory approximation the shear stress  $\sigma$  is given by the following expression:

$$\sigma = -\frac{R_0(1 + \varepsilon)}{2} \frac{\partial p}{\partial z}.$$

Suggesting  $S(\sigma)$  to be independent of the direction of the flow [17] and linear with respect to the absolute value of the shear stress (as a first approximation) one comes to the following expression for  $S(\sigma)$ :

$$S(\sigma) = -\alpha(1 + \varepsilon) |\partial p / \partial z|, \quad \alpha = const > 0. \quad (4)$$

We focus on solving the following basic problem: finding traveling-wave solutions of wall relaxation from the «stressed» state  $p_a = p_3$  ( $\varepsilon = 0$ ) into the «relaxed» state  $p_a = p_1$  ( $\varepsilon = 0$ ).

Assuming

$$p(z, t) = p(\xi), \quad \varepsilon(z, t) = \varepsilon(\xi), \quad p_a(z, t) = p_a(\xi), \quad (5)$$

where  $\xi = z - Vt$  and  $V$  ( $V > 0$ ) denotes the velocity of the traveling wave, one derives from Eqs. (1)-(4):

$$-16\mu V(1 + \varepsilon)\varepsilon' = R_0^2 \left( (1 + \varepsilon)^4 p' \right)', \quad (6)$$

$$p - V\tau_s p' = E(\varepsilon - V\tau_c \varepsilon') + p_a, \quad (7)$$

$$-Vp'_a = -\alpha(1 + \varepsilon) |p'| - \beta(p_a - p_1)(p_a - p_2)(p_a - p_3). \quad (8)$$

(The prime denotes differentiation with respect to  $\xi$ .)

To simplify the analysis let us introduce an analytically tractable approximation of Eqs. (6)-(8). For the purpose we restrict our analysis to small deformation values<sup>1</sup> so that nonlinear terms in Eq. (6) can be neglected (see [13] for details). Also, we replace the cubic reaction term in Eq. (8) with a piecewise linear analogue.

After introducing the following dimensionless quantities ( $\Upsilon = p_3 - p_2$ ):

$$\begin{aligned} \tilde{\xi} = \xi \left( \frac{R_0}{4\Upsilon} \sqrt{\frac{E}{\beta\mu}} \right)^{-1}, \quad \tilde{p} = \frac{p - p_1}{\Upsilon}, \quad \tilde{\varepsilon} = \frac{E\varepsilon}{\Upsilon}, \quad \tilde{p}_a = \frac{p_a - p_1}{\Upsilon}, \quad \tilde{V} = V \left( \frac{R_0\Upsilon}{4} \sqrt{\frac{\beta E}{\mu}} \right)^{-1}, \\ \tilde{\tau}_s = \Upsilon^2 \beta \tau_s, \quad \tilde{\tau}_c = \Upsilon^2 \beta \tau_c, \quad \tilde{\alpha} = \alpha \left( \frac{R_0\Upsilon}{4} \sqrt{\frac{\beta E}{\mu}} \right)^{-1}, \quad \tilde{p}_a^{thr} = \frac{p_2 - p_1}{\Upsilon}, \end{aligned} \quad (9)$$

the approximate model equations take the form:

$$-\tilde{V}\tilde{\varepsilon} = \tilde{p}', \quad (10)$$

$$\tilde{p} - \tilde{V}\tilde{\tau}_s\tilde{p}' = \tilde{\varepsilon} - \tilde{V}\tilde{\tau}_c\tilde{\varepsilon}' + \tilde{p}_a, \quad (11)$$

$$-\tilde{V}\tilde{p}'_a = -\tilde{\alpha}|\tilde{p}'| - \tilde{p}_a + H(\tilde{p}_a - \tilde{p}_a^{thr}). \quad (12)$$

We look for traveling wave solutions of (10)-(12) which satisfy the following boundary conditions:

$$\{\tilde{p}, \tilde{\varepsilon}, \tilde{p}_a\} \rightarrow \{1, 0, 1\}, \text{ at } \tilde{\xi} \rightarrow +\infty, \quad (13)$$

$$\{\tilde{p}, \tilde{\varepsilon}, \tilde{p}_a\} \rightarrow \{0, 0, 0\}, \text{ at } \tilde{\xi} \rightarrow -\infty. \quad (14)$$

Note that in view of (13)-(14) one can set  $|\tilde{p}'| = \tilde{p}'$  in Eq. (12).<sup>2</sup>

## Results

The procedure we follow to approach the problem (10)-(14) is described, for example, in [28–31]. We construct a traveling front out of two pieces: the leading edge where  $\tilde{p}_a > \tilde{p}_a^{thr}$  and the trailing edge of the wave corresponding to  $\tilde{p}_a < \tilde{p}_a^{thr}$ . (Thanks to the piecewise linear character of the model the solutions for each piece are the sums of three exponentials — the general solution of the related homogeneous equation — and a particular solution.) The composite solution is subject to boundary conditions (13)-(14) and a matching condition (continuity) at  $\tilde{p}_a = \tilde{p}_a^{thr}$ .

Finding a composite solution that satisfies both the boundary and the matching conditions results in an eigenvalue problem [32–34]. The eigenvalues (the velocities  $\tilde{V}$  of the traveling wave) are defined by the following implicit equation:

$$(1 - \tilde{p}_a^{thr})k_1(k_1 - k_2 - k_3) = 1/\tilde{V}^2 + \tilde{p}_a^{thr}k_2k_3 - (k_2 + k_3)/\tilde{V}. \quad (15)$$

<sup>1</sup>Note that deriving Eq. (10) requires integration of Eq. (6) prior to linearization. Integrating Eq. (6) is done assuming  $\{p', p, \varepsilon\} \rightarrow \{0, 0, 0\}$  as  $\tilde{\xi} \rightarrow \pm\infty$ .

<sup>2</sup>Rigorously speaking replacing  $|\tilde{p}'|$  with  $\tilde{p}'$  requires us to suppose that pressure distribution  $\tilde{p}(\tilde{\xi})$  is monotonous. The analysis of solutions with non-monotonous pressure profiles is beyond the scope of the present paper. Also, note that, given Eq. (10), the following equations are true:  $S(\sigma) \equiv -\alpha|p'| = -\alpha p' = \alpha V\varepsilon = \hat{\alpha}\varepsilon$ . Therefore, from a mathematical viewpoint, the regulatory stimuli due to shear-stress variation are equivalent to those induced by radial stretch in the small deformation limit.

Here  $k_n$ ,  $n = 1, 2, 3$  represent the roots of the of the differential system's characteristic equation  $L(k) = 0$ :

$$L(k, \tilde{V}) = c_3(\tilde{V})k^3 + c_2(\tilde{V})k^2 + c_1(\tilde{V})k + c_0(\tilde{V}),$$

where

$$\begin{aligned} c_3(\tilde{V}) &= \tilde{\tau}_c \tilde{V}^2, & c_2(\tilde{V}) &= \tilde{\tau}_s \tilde{V}^3 - (1 + \tilde{\tau}_c) \tilde{V}, \\ c_1(\tilde{V}) &= 1 + \tilde{\alpha} \tilde{V} - (1 + \tilde{\tau}_s) \tilde{V}^2, & c_0(\tilde{V}) &= \tilde{V}. \end{aligned}$$

Numerical analysis of Eq. (15) indicates that, in general, two different solutions can be found for each set of governing parameters  $\{\tilde{\tau}_s, \tilde{\tau}_c, \tilde{\alpha}, \tilde{p}_a^{thr}\}$ . Stability analysis shows that solutions with a smaller propagation velocity are unstable. The eigenfunctions corresponding to particular solutions of Eq. (15) define the profile of deformation and pressure along the wave. A typical stable solution is presented in Figure 5. The solutions resemble waves that were hypothesized to propagate in vessels with Bayliss regulation of myogenic activity [35].

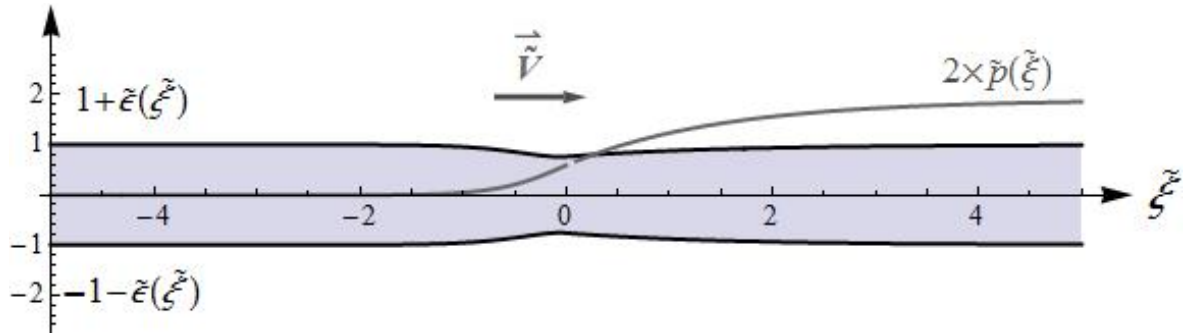


**Figure 5:** An example of a traveling wave of vasorelaxation-type of solution ( $\tilde{\tau}_s = 0.08$ ,  $\tilde{\tau}_c = 0.08$ ,  $\tilde{\alpha} = 2.5$ ,  $\tilde{p}_a^{thr} = 0.5$ ). The non-dimensional velocity is equal to  $\tilde{V} = 1.97$ .

Qualitative understanding of the solution's behavior can be obtained by analyzing the model with a quasi-steady state approximation of Eq. (12). Introducing

$$\tilde{\alpha} \tilde{p}' = -\tilde{p}_a + H(\tilde{p}_a - \tilde{p}_a^{thr}) \quad (16)$$

instead of Eq. (12) one can easily obtain the following explicit expression for the velocity of the wave<sup>3</sup> from an analogue of Eq. (15) :

$$\tilde{V}_{\pm} = \frac{(\tilde{\alpha} \pm \eta) + \sqrt{(\tilde{\alpha} \pm \eta)^2 + 4\tilde{\tau}_s}}{2\tilde{\tau}_s}. \quad (17)$$

Here  $\eta = \sqrt{\tilde{\alpha}^2 / (1 - \tilde{p}_a^{thr})^2 - 4\tilde{\tau}_c}$ . (Note that the asymptotic profiles corresponding to explicit solutions given by (17) are no longer continuous. See [13] for a more comprehensive

<sup>3</sup>It is worth noting that, in addition to the quasi-stationary limiting case described in the main text, there is another special set of parameters at which the problem can be explicitly solved:  $\tilde{\tau}_s = \tilde{\tau}_c \equiv 0$ ,  $\tilde{p}_a^{thr} = 0.5$ . The case therefore describes a system with a wall characterized by fast stress and strain relaxation and a «symmetric» mechanosensitive response. The velocity in such a system is given by:

$$\tilde{V}_{\pm} = \frac{\tilde{\alpha} \pm \sqrt{\tilde{\alpha}^2 - 4}}{2}.$$

The existence condition is  $\tilde{\alpha} > 2$ .

discussion of an analogous asymptotic analysis in the case of stretch-induced mechanosensitivity.) The explicit solutions corresponding to (17) exist provided that

$$\tilde{\alpha} > 2 \left( 1 - \tilde{p}_a^{thr} \right) \sqrt{\tilde{\tau}_c}. \quad (18)$$

It is interesting to note that the analysis of Eqs. (10)-(12) conducted above allows one to conclude that shear-stress sensitivity can mediate self-sustained propagation of another type of waves, namely waves of vasoconstriction in vessels with a “positive” contractile reaction to augmenting stress (with  $\alpha < 0$ , see Eq. (4)). Experiments indicate that such “positive” reaction to shear stress is characteristic to the blood vessels of the brain [36, 37].

To prove their existence one can make use of the fact that the system (10)-(12) is invariant with respect to the following substitution:

$$\begin{aligned} \tilde{V} &\rightarrow -\tilde{V}, & \tilde{\alpha} &\rightarrow -\tilde{\alpha}, & \tilde{p}(\tilde{\xi}) &\rightarrow 1 - \tilde{p}(-\tilde{\xi}), & \tilde{\varepsilon}(\tilde{\xi}) &\rightarrow -\tilde{\varepsilon}(-\tilde{\xi}), \\ \tilde{p}_a(\tilde{\xi}) &\rightarrow 1 - \tilde{p}_a(-\tilde{\xi}), & \tilde{p}_a^{thr} &\rightarrow 1 - \tilde{p}_a^{thr}. \end{aligned} \quad (19)$$

## Conclusions

We presented a simple mathematical model (1)-(3) of a shear-stress sensitive vessel. The model was used to analyze whether shear-stress sensitivity can serve as a factor securing peristaltic motility coordination.

The ability to coordinate motility was interpreted as the ability to ensure sustained propagation of deformation waves. The problem therefore was reduced to searching for traveling-wave solutions of the model equations.

To simplify the search a piecewise-linear approximation (10)-(12) of the model was introduced. The approximate model is analytically tractable. We used it to demonstrate the existence of sustained solutions, in particular traveling waves of vessel relaxation. We proceeded with developing an asymptotic quasi-steady state modification of the model and managed to derive the explicit formula for the velocity of the wave in a quasi-steady state model (see Eq. (17)) and the explicit condition securing their existence (18).

The authors thank Prof. A.I. Vorob'ev for his valuable comments concerning the medical aspects of the problem. We also appreciate the helpful suggestions of Prof. Yu.M. Romanovsky and Dr. V.A. Vasiliev. O.D. is grateful to *Codeminders Ltd* and in particular to A. Voloshin for technical assistance. Authors acknowledge financial support from the Schlumberger Foundation (Faculty for the Future program) and the International Science and Technology Center (grant #3744).

## References

- [1] R. F. Schmidt and G. Thews, *Human physiology*. Berlin: Springer-Verlag, 1989.
- [2] A. A. Gashev, “Lymphatic vessels: pressure- and flow-dependent regulatory reactions,” *Ann. N. Y. Acad. Sci.*, vol. 1131, pp. 100–109, 2008.
- [3] P. Santicioli and C. A. Maggi, “Myogenic and neurogenic factors in the control of pyeloureteral motility and ureteral peristalsis,” *Pharmacol. Rev.*, vol. 50, no. 4, pp. 683–722, Dec. 1998.
- [4] N. J. Spencer, G. W. Hennig, and T. K. Smith, “A rhythmic motor pattern activated by circumferential stretch in guinea-pig distal colon,” *J. Physiol. (Lond.)*, vol. 545, no. Pt 2, pp. 629–648, Dec. 2002.
- [5] J. D. Huizinga and W. J. Lammers, “Gut peristalsis is governed by a multitude of cooperating mechanisms,” *Am. J. Physiol. Gastrointest. Liver Physiol.*, vol. 296, no. 1, pp. G1–8, Jan. 2009.
- [6] N. P. Reddy, T. A. Krouskop, and P. H. Newell, “A computer model of the lymphatic system,” *Comput. Biol. Med.*, vol. 7, no. 3, pp. 181–197, Jul. 1977.

- [7] A. Bertuzzi, R. Mancinelli, M. Pescatori, and S. Salinari, "An analysis of the peristaltic reflex," *Biological Cybernetics*, vol. 35, no. 4, pp. 205–212, 1979.
- [8] V. A. Vasiliev, Y. M. Romanovskii, D. S. Chernavskii, and V. G. Yakhno, *Autowave Processes in Kinetic Systems: Spatial and Temporal Self-Organisation in Physics, Chemistry, Biology and Medicine*, 1st ed. Dordrecht: D. Reidel, 1987.
- [9] V. A. Vasiliev, S. D. Drendel', and O. L. Notova, "Autowave phenomena in gastrointestinal smooth muscle organs," in *Collective dynamics of excitation and pattern formation in biological tissues*, Gorky: IPF, 1988, pp. 137–145.
- [10] R. N. Miftakhov, G. R. Abdusheva, and J. Christensen, "Numerical Simulation of Motility Patterns of the Small Bowel. 1. Formulation of a Mathematical Model," *Journal of Theoretical Biology*, vol. 197, no. 1, pp. 89–112, 1999.
- [11] J. M. Hoffman, E. M. Brooks, and G. M. Mawe, "Gastrointestinal Motility Monitor (GIMM)," *Journal of Visualized Experiments*, no. 46, Dec. 2010.
- [12] G. Herrera, "In vitro assay for assessing gastrointestinal side effects," <http://www.catamountresearch.com/products/gimm-preclin.htm>. [Online]. Available: <http://www.catamountresearch.com/products/gimm-preclin.htm>.
- [13] O. A. Dudchenko and G. T. Guria, "Self-sustained peristaltic waves. Explicit asymptotic solutions," *PRE*, vol. 85, p. 020902(R) 1–5, 2012.
- [14] A. S. Mikhailov, *Foundations of synergetics I: Distributed active systems*, vol. 51. Berlin: Springer-Verlag, 1990.
- [15] A. M. Melkumyants, S. A. Balashov, A. N. Klimachev, S. P. Kartamyshev, and V. M. Khayutin, "Nitric oxide does not mediate flow induced endothelium dependent arterial dilatation in the cat," *Cardiovasc. Res.*, vol. 26, no. 3, pp. 256–260, Mar. 1992.
- [16] I. L. Chernyavsky and N. A. Kudryashov, "A Mathematical Model for Autoregulation of the Arterial Lumen by Endothelium-Derived Relaxing Factor," *Advanced Science Letters*, vol. 1, no. 2, pp. 226–230, 2008.
- [17] S. A. Regirer and N. K. Shadrina, "A simple model of a vessel with a wall sensitive to mechanical stimuli," *Biofizika*, vol. 47, no. 5, pp. 908–913, Oct. 2002.
- [18] S. M. Hilton, "A peripheral arterial conducting mechanism underlying dilatation of the femoral artery and concerned in functional vasodilatation in skeletal muscle," *J. Physiol. (Lond.)*, vol. 149, pp. 93–111, Dec. 1959.
- [19] B. R. Duling and R. M. Berne, "Propagated vasodilation in the microcirculation of the hamster cheek pouch," *Circ. Res.*, vol. 26, no. 2, pp. 163–170, Feb. 1970.
- [20] M. E. Burrows and P. C. Johnson, "Arteriolar responses to elevation of venous and arterial pressures in cat mesentery," *Am. J. Physiol.*, vol. 245, no. 5 Pt 1, pp. H796–807, Nov. 1983.
- [21] A. Colantuoni, S. Bertuglia, and M. Intaglietta, "Variations of rhythmic diameter changes at the arterial microvascular bifurcations," *Pfluegers Archiv European Journal of Physiology*, vol. 403, no. 3, pp. 289–295, Mar. 1985.
- [22] B.-B. Lee, J. Bergan, and S. G. Rockson, Eds., *Lymphedema: A Concise Compendium of Theory and Practice*. Springer, 2011.
- [23] S. A. Regirer, "Viscid fluid motion in a tube with deforming walls," *Fluid Dynamics*, vol. 3, no. 4, pp. 141–142, 1968.
- [24] Y.-C. Fung, "Peristaltic pumping: A bioengineering model," in *Urodynamics of the Ureter and Renal Pelvis*, Academic Press., New York: , 1971, pp. 177–198.

- [25] E. O. Carew and T. J. Pedley, "An active membrane model for peristaltic pumping: Part I—Periodic activation waves in an infinite tube," *J Biomech Eng*, vol. 119, no. 1, pp. 66–76, Feb. 1997.
- [26] S. A. Regirer, I. M. Rutkevich, and P. I. Usik, "Model of vascular tonus," *Mechanics of Composite Materials*, vol. 11, no. 4, pp. 502–505, 1975.
- [27] I. P. Herman, *Physics of the human body*. Berlin Heidelberg: Springer-Verlag, 2007.
- [28] H. P. McKean, "Nagumo's equation," *Advances in Mathematics*, vol. 4, pp. 209–223, 1970.
- [29] J. Rinzel and J. B. Keller, "Traveling wave solutions of a nerve conduction equation," *Biophys. J.*, vol. 13, no. 12, pp. 1313–1337, 1973.
- [30] M. A. Livshits, G. T. Gurija, B. N. Belintsev, and M. V. Volkenstein, "Positional differentiation as pattern formation in reaction-diffusion systems with permeable boundaries. Bifurcation analysis," *J. Math. Biology*, vol. 11, no. 3, pp. 295–310, Mar. 1981.
- [31] E. P. Zemskov and K. Kassner, "Analytically solvable models of reaction–diffusion systems," *Eur. J. Phys.*, vol. 25, no. 3, pp. 361–367, May 2004.
- [32] Y. B. Zel'dovich and D. A. Frank-Kamenetskiy, "On the theory of steady flame propagation," *Doklady Akademii Nauk*, vol. 19, pp. 693–698, 1938.
- [33] I. M. Gel'fand, "Some problems in the theory of quasi-linear equations," *Uspekhi Mat. Nauk*, vol. 14, no. 2(86), pp. 87–158, 1959.
- [34] G. I. Barenblatt, *Scaling*. Cambridge University Press, 2003.
- [35] B. N. Klochkov, A. M. Reiman, and Y. A. Stepanyants, "Unsteady flows in a fluid in pipes made of viscoelastic active material," *Fluid Dynamics*, vol. 20, no. 3, pp. 416–423, 1985.
- [36] R. M. Bryan Jr, S. P. Marrelli, M. L. Steenberg, L. A. Schildmeyer, and T. D. Johnson, "Effects of luminal shear stress on cerebral arteries and arterioles," *Am. J. Physiol. Heart Circ. Physiol.*, vol. 280, no. 5, pp. H2011–2022, May 2001.
- [37] R. M. Bryan Jr, M. L. Steenberg, and S. P. Marrelli, "Role of endothelium in shear stress-induced constrictions in rat middle cerebral artery," *Stroke*, vol. 32, no. 6, pp. 1394–1400, Jun. 2001.

# Solitonic excitations and control in nonlinear chains and networks

W. Ebeling<sup>1,\*</sup>, A.P. Chetverikov<sup>2</sup> and M.G. Velarde<sup>3</sup>

<sup>1</sup>*Institute of Physics, Humboldt University, Newtonstr. 15, 12489 Berlin, Germany*

<sup>2</sup>*Saratov State University, Faculty of Physics, Astrakhanskaya 83, Saratov 410012, Russia*

<sup>3</sup>*Universidad Alfonso X el Sabio, E-28691 Villanueva de la Cañada, and Instituto Pluridisciplinar, Universidad Complutense Madrid, Paseo Juan XXIII, 1, 28040 Madrid, Spain*

*\*e-mail address: ebeling@physik.hu-berlin.de*

## 1 Examples of solitonic excitations

Besides the commonly observable transverse or longitudinal, linear, harmonic waves (water waves in a pond, musical notes in a string or a diapason, compression-expansion, dilatational waves in elastic rubber) many examples of nonlinear, pulse-like waves of translation are also known in nature and technology [1–4]. In modern times, the first report on so-called solitary waves was published by J. S. Russell (a naval engineer-architect), around mid-XIXth century. In the Physics school laboratory, students may recall having observed running pulses in chains of balls. Indeed an array of balls in close contact offers a wave transmission line. It suffices to kick the ball at an extreme to see pulse propagation along the array as a consequence of hard-sphere (impulsive) interactions. The momentum/energy given by the kick is transported by local compressions (and expansions). Tsunami (in Japanese, waves in harbors) is also a typical consequence of waves of translation initiated by a sudden kick originated by a seaquake or a huge underwater landslide. They have been observed traveling thousand of kilometers at speeds of hundreds of kilometers per hour. Initially the kick may create an apparently innocuous wave of meter amplitude. Yet as its wavelength may reach a hundred kilometers or more on ocean waters over many kilometers of front, and a few kilometers depth, it can carry unaltered, huge running powers of more than several hundred kilowatts per square meter of front that eventually reach shore thus becoming highly devastating at shore. Nice and pleasant surf waves near shore also belong to the tsunami type and often a periodic array of such waves can be seen off-shore. Bores in rivers, also denoted hydraulic jumps (in French, mascarets) are like shock waves in gases or in crystalline matter (kinks which are not strictly shocks are also observed in such materials). They are also typical nonlinear waves moving upstream while the river flows downstream. They are generated by tides in specific rivers, like in the Amazonas in Brazil or in the Severn in England. Bore transport was used several centuries ago by Chinese peasants and merchants to trade over hundreds of kilometers. Hydraulic jumps also occur as internal waves in Straits like in the Gibraltar or in the Messina in the Mediterranean Sea. Similar internal waves have also been observed in the Atmosphere like the Morning Glory cloud in the Gulf of Carpentaria in northern Australia. In technology pulse waves are used to propagate light along optical fibers where the nonlinearity of the material is dynamically balancing electromagnetic diffraction along the path. Also worth mentioning is the report of unexpected behavior in electric power grids [5]. A few years ago the breakdown of a power line in Bremen in Germany apparently resulted in the sudden collapse of electric current in Spain, quite a long

distance apart. Something similar happened in the grid linking France to Italy via Switzerland, due to a failure in the latter. Other typical pulse-like waves are the action potential in nerves [6]. They are responsible of the functioning of our brain and our body movements. They are consequence of the interplay between nerve (axon) membrane features and ionic electric motions across the membrane due to the brine (about 70 % or more inside our skull) surrounding the neurons. Recently, in connection with microelectronics problems great interest has aroused in studying electrical networks at the nanoscale. The electric circuits of the future may very well consist of grids or networks of quantum dots connected to appropriate conducting edges. This would require a mechanism transporting electrons from one dot to another distant one. Today this is usually done by imprinting wafer masks prescribing the path along which electrons can go. But this is not the only way. An alternative is to obtain electron surfing on acoustic (hence longitudinal) waves of translation like recently achieved in piezoelectric GaAs layered structures [7–9].

Electron surfing is not alien to surf near shore or on river bores, as the underlying mathematical framework is the same. Indeed soon after the above mentioned report published by Russell, theory was developed already in the XIXth century, by Boussinesq, Lord Rayleigh and Korteweg and de Vries, among others, culminating in the soliton concept introduced by Zabusky and Kruskal in the sixties of XXth century. The universality of the soliton concept embraces Mathematics, Physics, Chemistry, Engineering, Ecology, Neurodynamics, Population Dynamics, etc. Originally solitary waves (and, subsequently, solitons) were shown to be a consequence of the dynamical balance between nonlinearity (wave speed depends on amplitude) and dispersion (wave speed depends on color or wave length). This is typical of waves eventually becoming tsunami and surf waves (very much like Sech forms). Shocks are rather attributed to the dynamical balance between nonlinearity and (viscous and heat) dissipation (very much like Tanhs forms; note that its derivative brings to the Sech). In both cases this is just an oversimplification to understand wave phenomena occurring in nature and technology. Toda was first in solving exactly a soliton problem in a model lattice he invented. He was able to analytically obtain the consequences of strong compressions. This together with the finding of some other exactly solvable models has led to a huge development of applied mathematics, computational simulations, basic science and applications. Initially the interest was placed on integrable Hamiltonian systems (with one too many, infinite integrals of motion) but his was later on considered as the ideal case.

## 2 Solitonic excitations on chains and rings

As we mentioned already a breakthrough was an exact solution obtained by Toda for chains of nonlinear springs with exponential repulsion  $U(r) = (\kappa/b)\exp(-br)$  and periodic b.c. [1, 2]. Toda solved the following system of equations:

$$\frac{dx_n}{dt} = v_n, \quad m \frac{dv_n}{dt} = -\nabla_n U(x_1, \dots, x_n) \quad (1)$$

( $U$ -potential energy). The exact Toda solution reads [1] for the compression  $\rho_n = x_{n-1} - x_n$ :

$$\rho_n = \frac{1}{b} \ln \left[ 1 + \frac{sh^2(qa)}{ch^2(q(na \pm v_s t))} \right], \quad v_s = v_0 \frac{sh(qa)}{qa} \quad (2)$$

where  $v_0 = a\sqrt{\kappa/m}$  is the sound velocity. In the long-wave limit the compression density may be expressed by

$$\rho(x, t) \simeq \rho_0 sech^2(\kappa\xi), \quad \xi = (x(t) - x(0) \pm v_s t) / \sigma, \quad (3)$$

This function is a solution of the Bussinesq equation and of the corresponding Korteweg-deVries equation. Note that  $x(t) = x(0) \pm v_s t$  is the actual position of the right- or left-moving soliton at time  $t$ ,  $v_s$  is the (supersonic) soliton velocity. Further  $q$  is the reciprocal width of the soliton, which is in the strongly supersonic case proportional to the soliton velocity [10, 11]. The expression (3) can be applied to a wide variety of potentials, in particular to FPU-3 and Morse potentials.

Circuit implementations of Toda rings were described by Singer, Oppenheim and others [12].

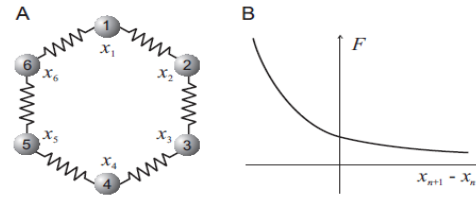


**Figure 1:** Schema of a ring of Toda springs connecting 6 nodes which are driven by Rayleigh energy sources (left). Exponentially decaying Toda forces.

The Toda ring described so far is conservative. In order to compensate the losses in physical rings of elements we developed in related work with Valeri Makarov, and Ezequiel Del Rio a driven electrical network with Toda connections [13–15]. The dynamics of the nodes was supported by Rayleigh- Van der Pol- type energy sources. The schema is demonstrated in Fig. 1. The typical excitations on this electrical network are quasi-stationary periodic electric pulses. The modes of the driven Toda ring were realized in hardware by electrical circuits, so that the excitations can be seen on a screen [13, 14].

More interesting topologies of the excitations and useful applications may be reached by twisting the ring as shown in Fig. 2. This electrical network found a valuable application for controlling the legs of hexapod robots which indeed have the same dynamic symmetries as our twisted Toda ring [15, 16]. In order to understand the essence of this application let us make a little excursion to the control of the legs of animals [16].

Animal locomotion is driven by a central pattern generator (CPG), which is an intraspinal network of neurons capable of generating a rhythmic output required for the limb control. The study of CPGs is crucial for understanding both the global animal behaviour and particular functions of such neural networks. Besides it is also important for designing neuro-inspired robots capable to move in an efficient manner like the living organisms do. The architecture of CPGs is seldom observable in vivo. However, important aspects of their structure can be inferred from observation of gait features such as the phase of the gait cycle at which a given limb hits the ground. Then phenomenological models reproducing these features can be introduced and used for the robot design. To solve the problem of dynamical pattern formation and robust transition among several types of gaits the use of oscillatory neural networks with different architectures has been proposed. In our approach we used the fact, that most animal gaits possess a degree of symmetry and universal features not far from the behavior of rings of coupled oscillators. It has been shown that coupled nonlinear oscillators can be considered as possible models for locomotor CPGs in insects and other animals.

Then transitions between different gaits can be modeled as a symmetry breaking bifurcation, leading to the switch between different activity patterns in a ring. In this paper we approach the problem of control of locomotion from the nonlinear dynamics viewpoint. We make remarkable parallels between waves observed in coupled nonlinear oscillators and the symmetries found in animal gaits. We describe how this observation might impose constraints on the general structure of a neural circuit controlling locomotion. To demonstrate the approach we considered a ring of coupled oscillators whose nonlinear elements are drawn from works of Lord Rayleigh and Toda. We proposed a method of combination of hamiltonian Toda inter-particle nonlinearity with the Rayleigh active friction. We showed theoretically and numerically existence and stability of propagating wave including solitons in such a hybrid system. Further several hardware implementations of the six-units model were developed and tested [13, 14]. We have demonstrated that the repulsive exponential forces which appear in the Toda system may be easily implemented with the help of ordinary junction diodes. The excitation patterns in a ring of coupled Toda-Rayleigh oscillators have the same symmetries as the common forward-walking gaits adopted by six-legs insects. In most earlier works gaits have been considered as fixed oscillatory rhythms. However, insects (and other animals e.g. crustaceans) apply free gaits, changing rhythms according to the environment. We propose a method how to incorporate the actuator (motor) dynamics in the CPG based on the Toda- Rayleigh circuit, hence closing the loop CPG – environment – CPG. Thus extensive calculations during locomotion over a nonhomogeneous environment are naturally done on the low CPG level with no direct participation of the robot “brain”. Animal locomotion typically employs several distinct periodic patterns of leg movements, known as gaits. Most of the gaits possess some degree of symmetry. This way we have shown in our work how the

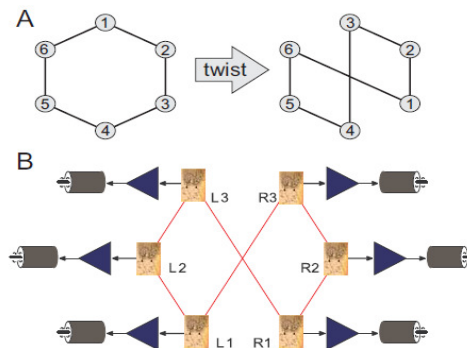


**Figure 2:** Schema of a twisted Toda network consisting of 6 nodes which are driven by Rayleigh energy sources. The upper left schema shows the original ring structure and the upper right schema the twisted network configuration which is used for controlling a hexapod robot sketched below.

symmetries of the gaits of hexapod animals and the corresponding robots can be modelled by the soliton dynamics of twisted Toda rings sustained by Rayleigh energy sources [16].

### 3 Solitonic excitations on two-dimensional networks

So far we studied 1d - networks where all nodes were arranged on a line or ring or on a twisted ring. Now we are going to study 2d lattices, where the nodes are atoms or electrical elements and the connections are defined by intermolecular forces or wires etc. As an example we study a two-dimensional triangular (equilateral) lattice of atoms connected by intermolecular forces or a corresponding electrical network.

In the two-dimensional case no closed soliton theory exists so far. A generalization of the

Boussinesq and Korteweg-de Vries equations to the two-dimensional case is the Kadomtsev - Petviashvili equation which has two known analytical solutions [17, 18]. The first one is a planar soliton

$$\rho(x, y, t) = \rho_0 \operatorname{sech}^2(\kappa \xi), \quad \xi = (x - v_s t) / \sigma, \quad (4)$$

which does not depend on  $y$ . Its profile reduces to the 1d solution. The second solution is the so-called "lump solution"

$$\rho(x, y, t) = \frac{v_s y^2 - 3v_s - (x - v_s t)^2}{[v_s y^2 - 3v_s + (x - v_s t)^2]^2} \quad (5)$$

This is a true two-dimensional solution of the Kadomtsev - Petviashvili equation which is most relevant for our problems. It has the form of a lump or a moving hill of the compression density. The lump solution, shown in Fig. 3 is normalized to unity (like a wave function) and the amplitude is given by  $\rho_0 = \frac{12}{9} v_s$ .

For studies of solitons in atomic 2d-layers we used the model of equilateral triangular

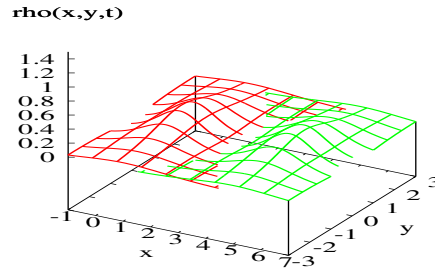


**Figure 3:** Lump-like soliton solution of the KP-equation moving in  $x$ -direction at two subsequent times.

lattices [19, 20]. For technical reasons we used a complex writing introducing the variable  $Z_n = x_n + iy_n$ . Then the equations of motion read

$$\frac{d^2 Z_n}{dt^2} = \sum_k F_{nk}(|Z_n|) z_{nk} \quad (6)$$

Solitonic excitations were excited in equilateral triangular Morse lattices by kicks in the direction of crystallographic axes. The solitons are able to move with supersonic velocity along the crystallographic axes and are rather stable [19, 20]. For experimental studies on solitonic excitations in two-dimensional lattices we refer to the work of Nayanov [7].

We mention also lattices of Lotka-Volterra type which were studied by Popov, who proved by simulations the existence of solitonic excitations [21].

#### 4 Surfing on solitons on chains and in 2d-lattices

The simplest case is when the charges follow a classical dynamics as well as the particles in the chain. An electric realization with 6 circuits on a ring was studied in detail in [14, 15] and discussed in the previous section. Instead of the exponential repulsive Toda forces we used in the mentioned work semiconductor elements with exponential characteristics. The running pulses of the voltage on the ring with crossed geometry were applied to controlling

the gaits of a hexapod [16]. The gaits are so to say "surfing" on the solitons running on the crossed six-ring.

A few analytical results are also known which describe the interaction of supersonic solitons with electrons which require a quantum description [10]. The atoms in a lattice generate - in the presence of charges - a potential well as long ago studied already by Landau and Pekar and in the supersonic case by Davydov and Zolotaryuk [10]. According to these authors, the wave function of this moving bound state reads

$$\Phi_0(x,t) \simeq C \operatorname{sech}(\kappa \xi'), \quad \xi' = (x(t) - x(0) \pm v_{se}t)/\sigma. \quad (7)$$

Accordingly the electrical density created by a supersonic lattice soliton along the coordinate  $x$  is equal to the compression density  $\rho_e(x) = \rho(x)$ . Under more general conditions the equality does not hold but still the deformation density and the electrical density are near to each other. In applying these formulae to a two-dimensional system, the  $x$ -coordinate has to be oriented along one of the crystallographic axes. The moving ground state is bell-shaped and  $v_{se}$  is the velocity of the solectron. According to the original Davydov theory the solectron velocity agrees with the soliton velocity. However this is only asymptotically true, in the case that  $v_s$  is only slightly above the sound velocity, the solectron velocity occurs to be always slower than the soliton velocity and may be even below the sound velocity [31]. In other words, a solectron can be formed only by a supersonic lattice soliton, the resulting bound state however, may be slower and can be supersonic or slightly subsonic [31].

A microscopic 1d-realization with quantum electrons was used for controlling the path of electrons [22]. We have shown that solitons are able to form bound states with the electrons and take over control. This way solitons are even able to catch electrons lying on their way, this effect has been called "vacuum-cleaning effect" (see Fig. 4) [23–26].

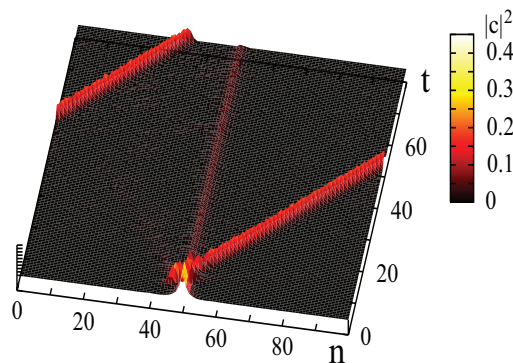


**Figure 4:** Vacuum-cleaning effect: A soliton which started here at position  $n = 40$  is able to bind an electron (initially located at  $n = 50$ ) and both move then together.

These effects exist also in the two-dimensional case. The surfing of electrons on non-linear sound waves was experimentally studied in several quite recent papers [8, 9]. For simulations of electron surfing on solitons in triangular lattices see [27].

## 5 Influence of noise - Langevin and Pauli models

According to Langevin the simplest approach of including noise is to add a white noise term to Newtons equation. In units with  $m = 1$  and introducing  $D_v$  as the strength of noise leads to the following Langevin equation with Gaussian white noise  $\xi(t)$ :

$$\frac{d\mathbf{r}}{dt} = \mathbf{v}; \quad \frac{d\mathbf{v}}{dt} = -\nabla U(\mathbf{r}) - \gamma_0 \mathbf{v} + \sqrt{2D_v} \xi(t) \quad (8)$$

In the 2d-case we add similar terms to eq.(6). This is the basis for our simulations of chains and lattices. In order to simulate the dynamics of electrons the simplest approach is to assume (see ref. [30, 31]) that the occupation probabilities of electrons  $p_n$  of the state  $n$ , characterized by a position  $\mathbf{r}_n$  and an energy  $E_n$ :. satisfy a master equation:

$$\frac{dp_n}{dt} = \sum_{n'} [W_{nn'} p_{n'} - W_{n'n} p_n]. \quad (9)$$

The basic assumption is that the electrons follow a hopping dynamics with quantum mechanical transition probabilities for the transition from site  $n$  to site  $n'$  given by

$$W(n, n') = \frac{V_0^2}{\hbar} \exp[-2\alpha_h |\mathbf{r}_n - \mathbf{r}_{n'}|] E(n, n', \beta). \quad (10)$$

Here the first factor models an exponential decay of the transition probabilities with the spatial distance of the atoms. Further  $E(n, n', \beta)$  is some symmetrical function which is in the Pauli theory a delta function  $E \sim \delta(E_n - E_{n'})$ . Several other approximations are known which take into account the influence of the heat bath, as e.g. the Lorentz profile . We use a standard approximation which is the Monte Carlo algorithm for the transition probabilities [30, 31]). The master equation is a useful tool for computer simulations of irreversible (non-coherent) electron hopping processes. Since the detailed balance is obeyed, it is guaranteed that in thermal equilibrium an H-theorem is valid and any initial distribution converges to the canonical distribution. The Pauli system of equations provides a rather fast tool for the simulations of the electron dynamics

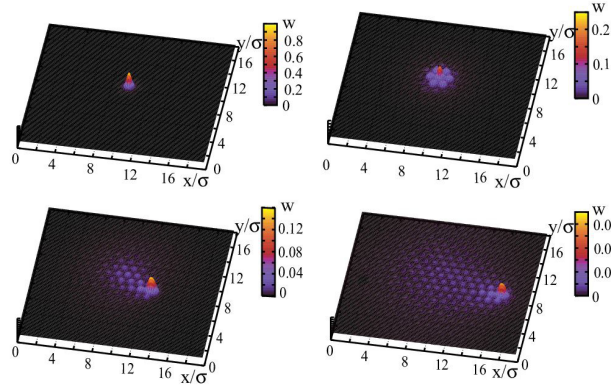


**Figure 5:** 2d Morse lattice. Soliton and electron placed near to each other but at different rows. The traveling soliton along the crystallographic axis,  $x$ , interacts with the electron being able to gather the electron probability density around itself, in kind of "vacuum cleaning" process [22, 27], eventually forming a solectron bound state and hence bringing the electron to the boundary of the lattice. The four pictures correspond to successive time instants. Parameter values:  $N = 400$ ,  $b\sigma = 4$ , and  $T = 0.01$  (measured in units  $2D$  where  $D$  is the depth of the Morse well).

## 6 Influence of electrical fields on solectrons - Fokker-Planck models

Since the fluctuative source is a Gaussian white noise, the distribution density  $f(\mathbf{r}, \mathbf{v}, \mathbf{t})$  obeys a Fokker-Planck equation [32–34]. A quantum-statistical derivation of a Fokker-Planck equation for solectrons was given by Gogolin [35, 36]. Instead of the complicated expression derived by Gogolin we use a semi-phenomenological Ansatz which reflects correctly the physics of the solectron formation:

$$\frac{\partial f(v,t)}{\partial t} + \frac{eE}{m_s} \frac{\partial f(v,t)}{\partial v} = \frac{\gamma_s}{m_s} \frac{\partial}{\partial v} \left[ \frac{\partial \mathcal{E}(v)}{\partial v} f + k_B T \frac{\partial f}{\partial v} \right]. \quad (11)$$

The essential point is that the electron is kept by the soliton in a potential well and that the solectron is hold near to the soliton velocity. To say it with Gogolin: "The field does not perturb an electron in a well; it simply accelerates the polaron to velocities  $v \simeq v_s$ , without causing its destruction". For the effective energy of driven solectrons we will use an ansatz borrowed from the the theory of driven Brownian motion [33, 34]:

$$\varepsilon(v) = \frac{m_s}{2}[v^2 - q \log(1 - a|v| + dv^2)]. \quad (12)$$

Here  $m_s$  is the effective mass and  $\gamma_s$  the effective friction due to the linear phonon-type excitations in the medium of the solectron,  $a, d, q$  are some constants also characterizing the medium. Note that the original ansatz from [33, 34] was extended by a linear term  $a|v|$ , which leads in  $v = 0$  to a Landau-like linear behavior. The soliton velocity  $v_s$  corresponds to the side minima of  $\varepsilon(v)$  (see Fig. 6). Note that the structure with side minima reminds us the roton minimum discussed in Landau's theory of superfluidity. The stationary solution of the Fokker-Planck equation is in our approximation given by

$$f(v) = Z^{-1} \exp \left[ -\frac{\varepsilon(v)}{k_B T} + \frac{eE v}{\gamma_s k_B T} \right]. \quad (13)$$

Note that the partition function is field-dependent  $Z(v_T, v_s, v_d)$ , where  $v_d$  is the Drude drift velocity, which is the classical approximation for drifting electrons and the  $v_{sd}$  the soliton driven velocity in the field

$$v_d = \frac{eE}{m_s \gamma_s}, \quad v_{sd} = k_B T \frac{\partial}{\partial v_d} \log Z(v_T, v_s, v_d) \quad (14)$$

The normalization integral  $Z$  may be numerically integrated, the drift can be estimated by

$$v_{sd} \simeq v_s \tanh \left[ \frac{v_d v_s}{v_T^2} \right] \quad \text{if} \quad v_s > v_d \quad (15)$$

The resulting curve for the drift velocity in an electrical field is shown in Fig. 6 b. The drift velocity at small fields increases quickly, up to fields when the soliton velocity is reached. This corresponds to a high differential conductivity. We note that the slope at small fields gets steeper with lowering of temperature  $T$  and corresponding thermal velocity  $v_T$ . This is studied in detail in Fig. 7. Here we show a set of decreasing thermal velocities (decreasing temperatures). Further we show that the slope, the derivative at low fields gives the static conductivity, is possibly much higher than the Drude conductivity. We presented in Fig. 7 one example with  $v_T = 0.1v_s$  where the conductivity is 10 times higher than the Drude value. With increasing temperature, if the thermal velocity approaches the thermal velocity, the conductivity converges to the Drude conductivity. We note a close relation of these findings to the results of numerical simulations of the drift velocity [15, 23, 24].

We give the drift velocity related to the soliton velocity as a function of the Drude-velocity (which is proportional to the electrical field) to the soliton velocity. For comparison the linear Drude approximation is shown. We presented in Fig. 7 is a theoretical curves for 3 temperatures  $v_T \gg v_{se}$  (straight line),  $v_T = .5v_s$ ,  $v_T = .1v_s$ . The lowest temperature correspond to about room temperature and gives the steepest derivative in the zero pint. We note that  $T = 0$ , which is out of the range of this approximation, formally corresponds to a large derivative in the zero point. Most interesting from the physical point of view is that solectrons are very fast in comparison to normal conduction electrons. Denoting the solectron density in a sample by  $n_{se}$  the electric conductivity is  $\sigma_{se} \simeq n_{se} e v_{sd}$ . That means,

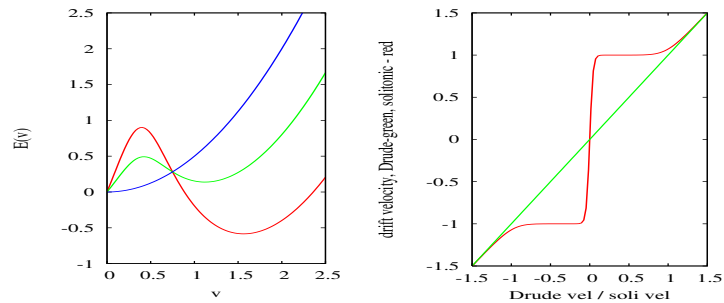


**Figure 6:** Energy functional of solitons in dependence on velocity  $m_s = 1; v_0 = 1; v_s = 1.5$  (left panel) and mean velocity of drift  $v_{sd}$  related to the Drude velocity  $v_d$  (straight line) in dependence on the dimensionless electrical field (measured in Drude velocity related to sound velocity).

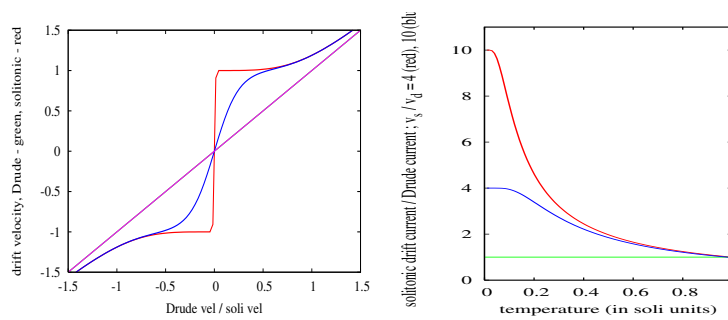


**Figure 7:** Non-Ohmic drift velocity against the dimensionless field (left panel) for the parameter set  $v_s \ll v_T$  and  $v_s = 2v_T$  (blue) and  $v_s = 10v_T$  (red). In the right panel we show the corresponding low-field conductivities as a function of the root of the temperature given as  $v_T/v_s$ .

if one could succeed to create samples with larger solectron densities  $n_{se} > 10^{20} \text{ cm}^{-3}$  then the solectronic conductivity could be higher than the conductivity of copper. Ultra-high non-Ohmic drift velocities in dependence on the field were observed experimentally in [28] and treated theoretically in several papers [15, 23, 35–38]. The supersonic velocity is in physical units around  $\text{\AA}/ps$  which corresponds to  $km/s$ . This is a rather fast electron motion in comparison to the standard velocity of conducting electrons which is usually in the range of  $cm/s$  or  $m/s$ . The conduction electrons in copper have velocities of about  $0.5 \text{ m/s}$  at  $1 \text{ V/cm}$ , solectrons are about 1000 - 10000 times faster. We note that the low-field drift corresponds to a high conductivity which may be orders of magnitude above the Drude conductivity. The shape of the curve shown in Fig. 7 is typical and agrees qualitatively with the results of the experiments and simulations [15, 23, 24, 28, 38].

## 7 Conclusions

We have shown that solitonic excitations at networks play an important role for processes in nature and technology. Here we discussed mainly the coupling between solitons and charges moving on one and two-dimensional networks. In particular we discussed several prospective applications as the control of robot by twisted rings of electric circuits, the control of elementary charges on the micro- and nanoscale and perspectives for the development of future high-conducting wires based on solectronic currents. Candidates for the development of materials with ultra-high solectron-mediated mobility are polyacetylene and polydiacetylene.

## Acknowledgment

The authors would like to thank A.S. Alexandrov (deceased), and L. Cruzeiro, E. Del Rio, V. Lakhno, V.A. Makarov, G. Röpke, S. Trigger and E.G. Wilson for discussions and correspondence. One of the authors (W. E.) expresses sincere thanks to the organizers for supporting to attend the Conference ICENET-2012. The research was supported by the Spanish Ministerio de Economía y Competividad under grant MAT2011-26221, and by the Ministry of Education and Science of the Russian Federation within FTP "Scientific and scientific-pedagogical personnel of the innovative Russia", 2009-2013, grant 14.B37.21.0751.

## References

- [1] M. Toda, *Nonlinear Waves and Solitons* (KTK Scientific Publishers, Tokyo, 1989)
- [2] N. Zabusky. Fermi-Pasta-Ulam, solitons and the fabric of nonlinear and computational science: History, synergetics, and visiometrics. *Chaos* **15**, 015102 (2005)
- [3] M. Remoissenet, *Waves Called Solitons. Concepts and Experiments*, Springer, Berlin 2010.
- [4] A.A. Nepomnyashchy, M.G. Velarde, P. Colinet, *Interfacial Phenomena and Convection*, Chapman & Hall, CRC, London, 2002.
- [5] P.J. Menck, J. Kurths. Topological identification of weak points in power grids. *Proc. Conf. NDES-2012*, 144-148, 2012.
- [6] T. Heimburg, A.D. Jackson, On soliton propagation in biomembranes and nerves, *Proc. Natl. Acad. Sci. U.S.A.* **102** (2): 9790, 2005.
- [7] V.I. Nayanov, *JETP Phys. Lett.* **44**, 314–316 (1986)
- [8] S. Hermelin, S. Takada, M. Yamamoto, S. Tarucha, A.D. Wieck, L. Saminadayar, C. Bäuerle, T. Meunier T. Electrons surfing on a sound wave as a platform for quantum optics with flying electrons, *Nature* **477**, 435-438 (2011)

- [9] R.P.G. McNeil, M. Kataoka, C. Ford, C. Barnes, D. Anderson, G. Jones, I. Farrer, D. Ritchie. On-demand single-electron transfer between distant quantum dots. *Nature* **477**, 439–442, 2011.
- [10] A.S. Davydov. *Solitons in Molecular Systems*. Kiev, 1984. 2nd Engl. edn., Reidel, Dordrecht, 1991.
- [11] A.V. Zolotaryuk, K.H. Spatschek, A.V. Savin, *Phys. Rev. B* **54**, 266 (1996).
- [12] A.C. Singer and A.V. Oppenheim. Circuit implementation of soliton systems. *Int. J. Bifurcation Chaos* **9**, 571, 1999.
- [13] V.A. Makarov, E. Del Rio, W. Ebeling, and M.G. Velarde. Dissipative Toda-Rayleigh lattice and its oscillatory modes. *Physical Review E* **64**, 0366601–36615, 2001.
- [14] E. Del Rio, V.A. Makarov, M.G. Velarde, and W. Ebeling. Mode transitions and wave propagation in a driven-dissipative Toda-Rayleigh ring. *Physical Review E* **67**, 056208–056217, 2003.
- [15] V.A. Makarov, M.G. Velarde, A.P. Chetverikov, W. Ebeling. Anharmonicity and its significance to non-Ohmic electric conduction. *Phys. Rev. E* **73**, 066626-1-12, 2006.
- [16] V.A. Makarov, E. Del Rio, M.G. Bedia, M.G. Velarde, and W. Ebeling. Central pattern generator incorporating the actuator dynamics for a hexapod robot”, *Trans. Engn., Computing Tech.* 15, 19-24 (2006) [Reprinted in *Int. J. Applied Maths. Computer Sci.* 3, 97-102 (2007)].
- [17] B.B. Kadomtsev, V.I. Petviashvili. On the stability of solitary waves in weakly dispersive media. *Sov. Phys. Dokl.* 15, 539-541 (1970)
- [18] A. A. Minzoni, N. F. Smyth. Evolution of lump solutions for the KP equation. *Wave Motion* **24**, 291 – 305, 1996.
- [19] A.P. Chetverikov, W. Ebeling, M.G. Velarde. Properties of nano-scale soliton-like excitations in two-dimensional lattice layers. *Physica D* **240**, 1954–1959, 2011.
- [20] A.P. Chetverikov, W. Ebeling, M.G. Velarde. Localized nonlinear, soliton-like waves in two-dimensional anharmonic lattices. *Wave Motion* **48**, 753–760, 2011.
- [21] S.P. Popov. Numerical modelling of solitons in simple two-dimensional lattices. *Math. Modelling* **21**, 27 – 33, 2009.
- [22] M.G. Velarde, W. Ebeling, A.P. Chetverikov, D. Hennig. Electron trapping by solitons, *Int. J. Bifurcation Chaos* **18**, 521-526, 2008.
- [23] D. Hennig, A. Neissner, M.G. Velarde, W. Ebeling. Effect of anharmonicity on charge transport in hydrogen-bonded systems, *Phys. Rev. E* **73**, 024306, 2006.
- [24] D. Hennig, A.P. Chetverikov, M.G. Velarde, W. Ebeling. Electron capture and transport mediated by lattice solitons, *Phys. Rev. E* **76**, 046602, 2007.
- [25] D. Hennig, A.P. Chetverikov, M.G. Velarde, W. Ebeling, Compounds of paired electrons and lattice solitons moving with supersonic velocity, *Phys. Rev. E* **78**, 066605, 2008.
- [26] O.G. Cantu Ros, L. Cruzeiro, M.G. Velarde, W. Ebeling. On the possibility of electric transport mediated long living intrinsic localized soliton modes, *Eur. Phys. J. B*, **80**, 545 , 2011.
- [27] A.P. Chetverikov, W. Ebeling, M.G. Velarde. Controlling electron transfer at the nano-scale by soliton-like excitations in two-dimensional nonlinear lattices. *Eur. Phys. J. B* **85**, 291, 2012; DOI: 10.1140/epjb/e2012-30276-x.
- [28] K.J. Donovan, E.G. Wilson. Demonstration of an ultra high mobility organic polymer, *Phil. Mag. B* 44, 9-29. (1981). Photocarrier creation in one dimension, *Phil. Mag. B* 44, 31-45 (1981).
- [29] V.D. Lakhno, N.S. Fialko, Long-range charge transfer in DNA, *Regular and Chaotic Dynamics* **7**, 299 –213, 2002.

- [30] A.P. Chetverikov, W. Ebeling, G. Röpke, M.G. Velarde. Hopping transport and stochastic dynamics of electrons in plasma layers. *Contr. Plasma Phys.* **51**, 814 – 829, 2011.
- [31] A.P. Chetverikov, W. Ebeling, M.G. Velarde. Soliton-like excitations and solectrons in two-dimensional nonlinear lattices. *Eur. Phys. J. B* **80**, 137 - 145, 2011.
- [32] F. Schweitzer, W. Ebeling, B. Tilch, Complex motion of Brownian particles with energy depots, *Phys. Rev. Lett.* **80**, 5044-5046, 1998.
- [33] J. Dunkel, W. Ebeling, S. Trigger, Active and passive Brownian motion of charged particles in two-dimensional plasma models, *Phys. Rev. E* **70**, 046406, 2003.
- [34] W. Ebeling, I. Sokolov, *Statistical thermodynamics and stochastic theory of nonequilibrium systems*, World Scientific, Singapore 2005.
- [35] A.A. Gogolin, Polaron transport in organic conductors, *Pisma v Zhety* **157**, 348–391, 1986.
- [36] A.A. Gogolin, Polaron transport in quasi-1d organic conductors, *Physics Reports* **157**, 348–391, 1988.
- [37] V.D. Lakhno, Davydov’s solitons in a nucleotide chain, *Int. J. Quant. Chem.* **110**, 127–137, 2010.
- [38] Y. Ono, A. Terai. Motion of charged soliton on polyacetylen due to electric field. *J.Phys.Soc.Japan* **59**, 2893–2904, 1990.

# One way to generate Lyapunov function for the chemical kinetic equations

E.V. Gasnikova

*Laboratory for Structural Methods of Data Analysis in Predictive Modeling, MIPT, Moscow, Russia*  
*e-mail address: evgenia.gasnikova@gmail.com*

Consider a macrosystem. This macrosystem can stay at different states described by the vector with the integer non-negative components. In the considered system at the random moments of time (chemical) “reactions” take place:  $\vec{n} \rightarrow \vec{n} - \vec{\alpha} + \vec{\beta}$ ,  $(\vec{\alpha}, \vec{\beta}) \in J$ .  $J$  — the set of all possible types of reactions (finite set). Let’s introduce following to M.A. Leontovich (1935) intensity of the reaction:

$$\lambda_{(\vec{\alpha}, \vec{\beta})}(\vec{n}) = \lambda_{(\vec{\alpha}, \vec{\beta})}(\vec{n} \rightarrow \vec{n} - \vec{\alpha} + \vec{\beta}) = M^{1 - \sum_i \alpha_i} K_{\vec{\beta}}^{\vec{\alpha}} \prod_{i: \alpha_i > 0} n_i \cdot \dots \cdot (n_i - \alpha_i + 1),$$

where  $K_{\vec{\beta}}^{\vec{\alpha}} \geq 0$  — a constant of reaction. It is often assumed that  $\sum_i n_i(t) \equiv M$ . So  $\lambda_{(\vec{\alpha}, \vec{\beta})}(\vec{n})$  — is a probability to the reaction  $\vec{n} \rightarrow \vec{n} - \vec{\alpha} + \vec{\beta}$  takes place in the unit of time. On the macro level this dynamic corresponds to the chemical kinetic (CK) principles. We assume that  $\dim \vec{n}$  and the number of the reaction  $|J|$  doesn’t depend on  $M$ . Note that (see [1])  $\langle \vec{\mu}, \vec{n}(t) \rangle \equiv \langle \vec{\mu}, \vec{n}(0) \rangle$  (inv) iff  $\vec{\mu}$  is orthogonal to  $\text{Lin} \left\{ \vec{\alpha} - \vec{\beta} \right\}_{(\vec{\alpha}, \vec{\beta}) \in J}$ .

Let at the  $t = 0$  for all  $i$  exists  $c_i(0) = \lim_{M \rightarrow \infty} n_i(0)/M > 0$ . Then for arbitrary  $t > 0$  and for all  $i$  exist determinate limits  $c_i(t) \stackrel{a.s.}{=} \lim_{M \rightarrow \infty} n_i(t)/M$ . Moreover,

$$\frac{dc_i}{dt} = \sum_{(\vec{\alpha}, \vec{\beta}) \in J} (\beta_i - \alpha_i) K_{\vec{\beta}}^{\vec{\alpha}} \vec{c}^{\vec{\alpha}}, \quad \vec{c}^{\vec{\alpha}} = \prod_j c_j^{\alpha_j}. \quad (\text{CK})$$

This statement is following from the results of Troter-Kurtz (1986) [2].

Considered stochastic chemical kinetic (in discrete time) we can represent as random walks on a graph  $G = (V_G, E_G)$ . Where  $G$  is a integer lattice in non-negative ortant in space of the dimension  $\dim \vec{n}$ . To say more precisely, in the hyperplane, defined by the (inv). Let’s designate the matrix of transitional probabilities  $P = \|p_{ij}\|$ , and stationary measure by  $\pi$ . Let’s introduce the following definitions:

$$h(G) = \inf_{S \subseteq V_G: \pi(S) \leq 1/2} P(S \rightarrow \bar{S} | S) = \min_{S \subseteq V_G: \pi(S) \leq 1/2} \frac{\sum_{(i,j) \in E_G: i \in S, j \in \bar{S}} \pi(i) p_{ij}}{\sum_{i \in S} \pi(i)}, \quad (\text{Cheeger constant})$$

$$T(i, \varepsilon) = \Theta \left( h(G)^2 \left( \ln(\pi(i)^{-1}) + \ln(\varepsilon^{-1}) \right) \right). \quad (\text{Mixing time})$$

Then (see [3])

$$\forall i \in V_G, t \geq T(i, \varepsilon) \rightarrow \|P^t(i, \cdot) - \pi(\cdot)\|_{TV} = \sum_j |P^t(i, j) - \pi(j)| \leq \varepsilon.$$

**Theorem.** *Let invariant measure can be represented in the form:*

$$\nu(\vec{n}) = M \exp(-M \cdot (H(\vec{n}/M) + o(1))), \quad M \gg 1, \quad (\text{IM})$$

with smooth function  $H(\vec{c})$ . Then

a) If  $\vec{\xi}(\vec{s}) = \arg \max_{\vec{\xi}} \left\{ \langle \vec{\ln s}, \vec{\xi} \rangle - H(\vec{\xi}) \right\}$  fulfilled Fermat's principle:  $\vec{\ln s} = \text{grad } H(\vec{\xi}(\vec{s}))$ , then full derivative according to the system (CK)  $dH(\vec{c})/dt|_{\vec{c}=\vec{\xi}(\vec{s})} \leq 0$ .

b) If  $H(\vec{c})$  is strictly convex then  $h(G) = O(M^{-1/2})$ .

*Scheme of the prove.* a) Let's introduce generating function [4]:

$$F(t, \vec{s}) = \sum_{\vec{n}} P(\vec{n}(t) = \vec{n}) \cdot \vec{s}^{\vec{n}}, \quad |\vec{s}| \leq \vec{1}, \quad \vec{s}^{\vec{n}} = s_1^{n_1} \cdot s_2^{n_2} \cdot \dots \quad (\text{GF})$$

This (GF) satisfies to the following quasi linear partition differential equation (PDE):

$$\frac{\partial F(t, \vec{s})}{\partial t} = \sum_{(\vec{\alpha}, \vec{\beta}) \in J} \left( \vec{s}^{\vec{\beta}} - \vec{s}^{\vec{\alpha}} \right) K_{\vec{\beta}}^{\vec{\alpha}} M^{1 - \sum_i \alpha_i} \frac{\partial^{\alpha_1 + \alpha_2 + \dots} F(t, \vec{s})}{\partial s_1^{\alpha_1} \cdot \partial s_2^{\alpha_2} \cdot \dots} \quad (\text{PDE})$$

Note, that if we take partition derivative  $\partial/\partial s_i$  from the both side of the equation (PDE), to divide (PDE) on  $M$  beforehand, and then put  $\vec{s} = (1, \dots, 1)^T$ , so we obtain in the limit  $M \rightarrow \infty$  (we assumed also that there exists the following limits  $\lim_{M \rightarrow \infty} n_i(0)/M$ ) the system (CK). From (IM) and (GF) we have:

$$F(\infty, \vec{s}) \approx M \int e^{M \left( \langle \vec{\ln s}, \vec{\xi} \rangle - H(\vec{\xi}) \right)} d\vec{\xi}.$$

Therefore [5], we have

$$M^{-(\alpha_1 + \alpha_2 + \dots)} \frac{\partial^{\alpha_1 + \alpha_2 + \dots} F(\infty, \vec{s})}{\partial s_1^{\alpha_1} \cdot \partial s_2^{\alpha_2} \cdot \dots} \approx \frac{\vec{\xi}(\vec{s})^{\vec{\alpha}}}{\vec{s}^{\vec{\alpha}}} C(\vec{s}, M),$$

where  $\vec{\xi}(\vec{s})$  is defined by the system  $\vec{\ln s} = \text{grad } H(\vec{\xi})$ , and function  $C(\cdot) > 0$  — doesn't depend on  $\vec{\alpha}$  and bounded uniformly on  $M$ . Hence,

$$\begin{aligned} 0 &\equiv \sum_{(\vec{\alpha}, \vec{\beta}) \in J} \left( \vec{s}^{\vec{\beta}} - \vec{s}^{\vec{\alpha}} \right) K_{\vec{\beta}}^{\vec{\alpha}} \frac{\vec{\xi}(\vec{s})^{\vec{\alpha}}}{\vec{s}^{\vec{\alpha}}} = \sum_{(\vec{\alpha}, \vec{\beta}) \in J} \left( e^{\langle \vec{\beta} - \vec{\alpha}, \text{grad } H(\vec{\xi}(\vec{s})) \rangle} - 1 \right) K_{\vec{\beta}}^{\vec{\alpha}} \frac{\vec{\xi}(\vec{s})^{\vec{\alpha}}}{\vec{s}^{\vec{\alpha}}} \geq \\ &\geq \sum_{(\vec{\alpha}, \vec{\beta}) \in J} \left\langle \vec{\beta} - \vec{\alpha}, \text{grad } H(\vec{\xi}(\vec{s})) \right\rangle K_{\vec{\beta}}^{\vec{\alpha}} \frac{\vec{\xi}(\vec{s})^{\vec{\alpha}}}{\vec{s}^{\vec{\alpha}}} = \frac{dH(\vec{c})}{dt} \Big|_{\vec{c}=\vec{\xi}(\vec{s})} \end{aligned}$$

— the complete derivative of the function  $H(\vec{c})$  according to the system (CK) at the point  $\vec{\xi}(\vec{s})$ .

- b) It is sufficient to notice that under the conditions of strictly convexity of  $H(\vec{c})$  the isoperimetric problem

$$\min_{S \subseteq V_G: \pi(S) \leq 1/2} \frac{\sum_{(i,j) \in E_G: i \in S, j \in \bar{S}} \pi(i) p_{ij}}{\sum_{i \in S} \pi(i)},$$

reduces to the following problem

$$\min_{S \subseteq V_G: \pi(S) \approx 1/2} \frac{\sum_{(i,j) \in E_G: i \in S, j \in \bar{S}} \pi(i) p_{ij}}{\sum_{i \in S} \pi(i)},$$

where the set  $S$  can be chosen as sphere (in subspace (inv)) in proper metric close to Euclidian with the center at the (unique) equilibrium. Equilibrium is determinate as argminimum  $H(\vec{c})$  over the set (inv). Since  $\dim(\text{inv}) \leq \dim \vec{n}$  doesn't depend on  $M$ , we have the desired estimation. □

**Consequence.** Let the condition (IM) is true. Attractor set of the system (CK) belongs to  $\text{Arg} \min_{\vec{c} \in (\text{inv})} H(\vec{c})$ . That is, at the large values of time the arbitrary trajectory of the system (CK) is closed enough to this set.

The author is partially supported by Laboratory for Structural Methods of Data Analysis in Predictive Modeling, MIPT, RF government grant, ag. 11.G34.31.0073 and by RFBR 11-01-00494-a, 12-01-33007 (program of supporting of leading youth collectives).

## References

- [1] Ya. G. Batishcheva and V. V. Vedenyapin. The 2-nd law of thermodynamics for chemical kinetics. *Matem. Mod.*, 17(8):106–110, 2005.
- [2] V. A. Malyshev, S. A. Pirogov, and A. N. Rybko. Random walks and chemical networks. *Mosc. Math. J.*, 4(2):441–453, 2004.
- [3] F. Chung. Laplacians and the cheeger inequality for directed graphs. *Annals of Combinatorics*, 9:1–19, 2005.
- [4] A. V. Kalinkin. Markov branching processes with interaction. *Uspekhi Mat. Nauk*, 57(2(344)):23–84, 2002.
- [5] M. V. Fedoruk. *Saddle Point Method*. Nauka, Moscow, 1977.

# Mathematical Models in Social Dynamics

M.A. Herrero

*Departamento de Matemática Aplicada, Facultad de Matemáticas, Universidad Complutense,  
28040 Madrid, Spain  
e-mail address: Miguel\_Herrero@mat.ucm.es*

## 1 Introduction

Living beings show a distinct tendency to gather into comparatively large groups of individuals, whose ability to interact increases as their internal structure becomes more complex. Such interaction, mediated by the exchange of communicating signals, turns out to be advantageous for community survival. Moreover, collective behaviour has a deep impact in the surrounding environment on the one hand, as well as on the structure of the community itself, whose evolution in time is often termed as social dynamics.

The analysis of the behaviours displayed by living societies leads at once to a number of relevant problems in different scientific fields. For instance, starting with simple organisms, it is widely assumed that the growth of large colonies of cyanobacteria in early Earth gave rise to a high oxygen production, which irreversibly changed the atmosphere of the planet and the nature of creatures that could live on it [1, 2]. Actually, ever since the chemical composition of our atmosphere needs to be kept under strict control, and suspicion is growing that human-induced climate change is seriously damaging such regulation [3].

Even simple organisms are able to exchange information and coordinate their behaviour through the use of appropriate signals. Consider for example the social amoeba *Dictyostellium discoideum* (Dd for short), a well-studied model in Developmental Biology (see <http://dictybase.org>). When food becomes scarce, Dd individuals enter a developmental stage which begins by their clustering into aggregating centres, following gradients of a chemical messenger (cAMP) that they themselves release (see [4] for a survey). As individual complexity increases, so does the nature of the signals exchanged and that of the patterns thus induced. It is well beyond the scope of this work to present a comparative analysis of social patterns for different types of organisms. The reader is instead referred to recent studies on bacteria [5, 6], plants [7] and insects [8] to learn more about particularly relevant examples. This note is concerned with some particular aspects of social dynamics in human populations, and more precisely with the use of suitable mathematical techniques to gain insight into those processes.

More precisely, we will analyse the impact of social and economical mobility on the dynamics, and particularly in the stability properties, of a human society structured in classes. No attempt will be made to present here a comprehensive discussion of such general problem. Instead, our goal consists in illustrating, by means of a few examples, both the scope and the limitations of a particular type of mathematical models (population dynamics) commonly used for that purpose. To that end, we will begin by recalling in Section 2 below a few results on the existence and stability of steady states for systems of differential equations when only partial information about the coefficients or the kinetics of those systems are available. We then discuss in Section 3 a model of social dynamics when social mobility is taken into account. Specifically, we shall examine the nature of local equilibria in two

different cases, which roughly speaking correspond to the absence and presence of criminals respectively. As will be observed there, the dynamics around such equilibria relies heavily on appropriate knowledge of the parameters involved, on which little information is in general available. This makes a strong case to exploit in this context the type of results sketched previously in Section 2, an approach that remains largely unexplored as yet. Finally, Section 4 contains a short discussion on results obtained and a few remarks about possible future directions.

## 2 A discussion on stability

The mathematical tools to be used in this work are those of population dynamics, as provided by the theory of continuous or discrete dynamical systems. The corresponding techniques, which roughly speaking derive from the study of systems of differential (or difference) equations, are well developed, and have proved their strength in a number of biological problems, most particularly in Ecology and related areas [9, 10]. In general, one is interested in the asymptotic behaviour (in space and time) of solutions of the equations considered, particular attention being paid to the existence of constant solutions (equilibrium states) and their stability properties. Roughly speaking, a roadmap to describe the dynamics of the corresponding system consists in identifying first its equilibrium states and then characterizing the local behaviour of nearby solutions. A second, and often more challenging step consist in describing the behaviour of solutions that may join such equilibria, approach (or escape) to (from) possible limit circles and exploring the possible location of attractors. Dependence of solutions on parameters is a relevant issue as well, particularly in what concerns the appearance and properties of bifurcations, where solutions undergo sharp changes in behaviour [11, 12].

Concerning parameter values, a first issue to be reckoned with is the fact that in many practical cases only partial information on such values is available. The question then arises of deriving significant information on solutions dynamics under such limitations. We shall briefly remark on that issue in our next paragraph.

### 2.1 Stability under uncertainty

We shall address here the following general question. What can be said about the number of equilibrium states (and their stability properties) of a dynamical system when only partial information about its coefficients is available? For instance, consider a linear system with constant coefficients:

$$\frac{dx_i}{dt} = \sum_{j=1}^n a_{ij}x_j; \quad i = 1, \dots, n \quad (1)$$

where for  $i, j = 1, \dots, n$ , the  $a_{i,j}$  are real numbers whose precise values are unknown. We say that a constant vector  $x^* = (x_1^*, \dots, x_n^*)$  is a steady (or equilibrium) state of (1) if it provides a solution to that system, so that:

$$\sum_{j=1}^n a_{ij}x_j^* = 0 \quad \text{for } i = 1, \dots, n \quad (2)$$

Notice that the origin  $(0, \dots, 0)$  is always a steady state for (1). Following [13], we may wonder if the stability of the origin can be determined merely from knowledge of the signs of the coefficients  $a_{ij}$ . This question is motivated by Ecology models, where each coefficient  $a_{i,j}$  represents an interaction from species  $j$  on species  $i$ , so that the impact of the former species into the latter is positive, negative or neutral depending on the cases  $a_{ij} > 0$ ,  $a_{ij} < 0$ ,  $a_{ij} = 0$  respectively, and the full matrix  $A = (a_{ij})$  provides a description of the thropic web

involving species  $x_1, \dots, x_n$ . The following Table taken from [14] provides a description of the meaning of the interaction coefficients in an ecological context

Effect of species $i$ on $j$ (sign $a_{ji}$ )	Effect of species $j$ on $i$ (sign $a_{ij}$ )			
		+	0	-
+	++	+0	+-	
0	0+	00	0-	
-	-+	-0	--	

which respectively correspond to commensalism (+0), mutualism or symbiosis (+,+), competition (-,-) and predator-prey interaction (+,-)

Concerning our stability question, some notation will be recalled. We say that the origin is asymptotically stable when  $Re \lambda < 0$  for any eigenvalue of  $A$ , i.e, for any solution of the algebraic equation  $\det(A - \lambda I) = 0$ . In this case, any solution of (1) which at some point passes close enough to the origin will eventually approach it as time passes. On the other hand, we say that  $A = (a_{ij})$  is qualitatively stable with respect to the origin (qualitatively stable for short) if the origin is asymptotically stable for any matrix  $A^* = (a_{ij}^*)$  whose coefficients have same signs as those in  $A$ . Interestingly enough, a matrix can be shown to be qualitatively stable under rather general assumptions on the signs of its coefficients. More precisely, the following result has been proved in [13] (see also [14]).

**Theorem A.** *The following are necessary and sufficient conditions for  $A = (a_{ij})$  to be qualitatively stable:*

- (i)  $a_{ij}a_{ji} \leq 0$  for  $i \neq j$ .
- (ii)  $i_1 \neq i_2 \neq \dots \neq i_n, a_{i_1 i_2} \neq 0, a_{i_2 i_3} \neq 0, \dots, a_{i_{m-1} i_m} \neq 0$  implies  $a_{i_m i_1} = 0$  for any  $m > 2$ .
- (iii)  $a_{ii} \leq 0$  for all  $i, a_{kk} \leq 0$  for some  $k, 1 \leq k \leq n$ .
- (iv)  $\det A \neq 0$ .

As observed in [14] a consequence of the previous Theorem is that matrix  $M_1$  below is qualitatively stable, whereas matrix  $M_2$  is not

$$M_1 = \begin{pmatrix} - & + & + & + \\ - & - & 0 & 0 \\ - & 0 & - & 0 \\ - & 0 & 0 & - \end{pmatrix} \quad M_2 = \begin{pmatrix} - & + & + & + \\ - & - & + & + \\ - & - & + & - \\ - & - & + & - \end{pmatrix}$$

Concerning Theorem A, a few remarks are in order. To begin with, there is a natural extension of that result to general autonomous systems of the type:

$$\frac{dx}{dt} = F(x) \quad (3)$$

where  $F = (f_1, \dots, f_n)$  and for any  $i = 1, \dots, n$   $f_i$  is a sufficiently smooth function. It is well known that if  $x^*$  is a steady state of (3), to the lowest order the small-amplitude perturbations around  $x^*$  satisfy a linear system given by:

$$a_{ij} = J_F(x^*) \quad (4)$$

where  $J_F$  is the jacobian matrix,  $J_F = \left( \frac{\partial f_i}{\partial x_j} \right) \equiv J_{ij}$ , evaluated at  $x = x^*$ .

Therefore, Theorem A is still relevant to discuss linear stability of steady states of (3). Notice however that care is required to derive information concerning stability with respect to large perturbations around equilibria of (3) from the study of linearized systems as (4). A similar remark applies to neutral stability (i.e. the case where  $\text{Re } \lambda_j = 0$  for some eigenvalue  $\lambda_j$ ) a particularly relevant case associated to the onset of oscillations, that cannot be discussed directly for system (3) from a mere analysis of (4). See [15] for more details on such issues.

## 2.2 How many equilibria are out there?

A significant question, both from theoretical and applied points of view, is that of estimating the number of possible steady states of systems like (1) or (3) when only partial information about their coefficients is available. Clearly, the complexity of solution dynamics increases with the number of such equilibria. One can roughly state that the larger the number of steady states, the larger also is the type of possible solution behaviours. In particular, new possibilities of heteroclinic (and also homoclinic) equilibria connections appear that would be absent otherwise. A system that has several stable steady states is usually called multistable. On the other hand, and keeping to a standard notation, we will say that a system is injective if  $F(x_1) = F(x_2)$  implies that  $x_1 = x_2$ . Obviously, multistability and injectivity are mutually excluding possibilities.

Let us consider injectivity first, and let us particularise to the case of one space dimension. Then a sufficient condition for injectivity is that  $F(x)$  be different from zero everywhere. It was conjectured in [16] that the corresponding condition in higher dimensions should be:

$$\det J_F(x) \neq 0 \quad \text{for all } x \quad (5)$$

However, this conjecture is not true in general. For instance, the function  $F$  given by:

$$F(x, y) = (e^{2x} - y^2 + 3, 4e^{2x}y - y^3) \quad (6)$$

is such that  $\det(J_F) > 0$  for any  $(x, y) \in \mathfrak{R}^2$  but  $F(0, 2) = F(0, -2) = 0$  (see [17]).

As a matter of fact, even if we restrict ourselves to polynomial nonlinearities in  $F(x)$ , the previous conjecture fails to hold for large polynomial degrees, although it is satisfied in the quadratic case [18]. We shall refrain here from presenting a detailed description of conditions ensuring injectivity, a subject that has attracted considerable attention in chemistry. The reader is instead referred to [19, 20] for that purpose.

Let us now turn our attention to multistability, and in particular to the simplest case of bistability, i.e. the existence of two different stable equilibria in a given dynamical system. In the latter case two different basins of attraction exist, each being located around any stable state, and if sufficiently pushed, trajectories can switch from one to the other. This allows for much richer dynamics than what can be found in injective systems. In particular, when coupled to additional restoring mechanisms, excitable systems may be generated. These constitute a paradigm in the study of biological models, since signals can propagate in an excitable medium without altering it in an irreversible manner [21, 22].

It is natural to expect that bistability will require of more stringent requirements than single stability does. As a matter of fact, bistability is usually achieved only within a restricted range of parameter values [23, 24]. At the evolutionary level, a particularly relevant, elementary mechanism to achieve bistability consists in the mutual interconnection of two single monotone systems, each of them being monostable, by means of positive feedback (cf. [25]).

### 3 Utopia: a mathematical model of social dynamics

We next describe, by means of a simple example, the way in which information about multistability in a dynamical system may be used to explore a model of social dynamics.

#### 3.1 Living in Utopia

To begin with, let us consider a toy model for Utopia, a free-from-criminals human society consisting only of industrious individuals. Following [26], which we refer to for further details, we consider a society divided into classes (subpopulations)  $X_i(t)$  with  $i = 1, \dots, n$ , according to their economic performance. Individuals in each class are assumed to equally contribute to the total wealth,  $W(t)$ . The latter is defined as follows:

$$W(t) = \sum_{i=1}^n W_i(t) \equiv \sum_{i=1}^n c_i X_i(t) \quad (7)$$

where  $W_i(t)$  is the wealth produced by the  $i$ th-class, and  $c_i > 0$  are proportionality constants characterising the economic performance within each class. For definiteness, we will assume  $c_i \leq c_{i+1}$  for any  $i$ .

There is social mobility in Utopia, and is governed by the following rules:

$$X_i'(t) = \alpha_{i-1} X_{i-1}(t) - (\alpha_i + \beta_i) X_i(t) + \beta_{i+1} X_{i+1}(t) \quad (8)$$

where  $\alpha_i$  (respectively  $\beta_i$ ) are the so-called promotion (respectively, relegation) parameters, not necessarily constants. Clearly, (8) has to be understood with the proviso that relegation (respectively, promotion) is not possible in the lowest (respectively, the highest) class.

The equilibrium distributions of (7) should thus satisfy the conditions:

$$\alpha_{i-1} X_{i-1}(t) - (\alpha_i + \beta_i) X_i(t) + \beta_{i+1} X_{i+1}(t) = 0 \quad (9)$$

Analysis of social dynamics in our model is particularly simple when promotion and relegation coefficients are constant. In this case there are two steady states, the trivial one,  $X(t) = 0$  and an explicit, non-trivial equilibrium (see equations (5), (6) in reference [26]). Not surprisingly, the situation becomes more complex when such coefficients are assumed to depend on  $W(t)$ . Suppose for instance that only three classes are present (so that  $i = 1, 2, 3$ ) and that the total population  $N$  remains constant in time. Upon suitable rescaling, both  $N$  and  $W(t)$  can be assumed to be less or equal than one. We next hypothesize that resistance to upward mobility increases as one moves towards higher classes. More precisely, let us select:

$$\alpha_i = W^i, \beta_{i+1} = 1 - W^{3-i} \quad \text{for } i = 1, 2 \quad (10)$$

A standard analysis now reveals that a wealthiest state ( $X_3 = N, X_1 = X_2 = 0$ ) always exist and is asymptotically stable if  $c_2 > 0$  and  $c_3 > 0$ ; other steady states may exist depending on the values of parameters in (7). An interesting case occurs when  $c_1 = 0$ , so that the lowest class does not contribute to the total wealth. Then bistability sets in. In particular, two stable equilibria can be identified: the wealthiest one (defined just as before), the poorest one, where  $X_1 = N, X_2 = X_3 = 0$ , and an unstable one, where nonnegative values for all three populations coexist. Furthermore, if we now let  $c_2$  tend to zero, so that only the richest class contributes to total wealth, both the unstable intermediate point and the wealthiest one coalesce into an unstable equilibria, and the only remaining stable state corresponds to the poorest one. In this manner a crisis appears that drives the whole society into poverty.

### 3.2 Criminals arrive at Utopia

We next consider the situation that arises when a part of the population, that will be termed as criminals for simplicity, decides to draw on social resources but to contribute little or nothing to global wealth. For modelling purposes, we represent this by introducing a criminal subpopulation  $Y(t)$ , and postulate the following rules:

- i) Criminal action is felt by means of a criminal rate  $K(t)$  given by:

$$K(t) = \sum_{i=1}^n \theta_i X_i(t) Y(t) \quad (11)$$

where the collision rate  $\theta_i$  measures the likelihood of interaction between  $Y(t)$  and the  $i^{\text{th}}$ -population  $X_i(t)$ . A possible choice for  $\theta_i$  may be:

$$\theta_i(t) = \frac{a_i}{b_i + X_i(t)},$$

where  $a_i, b_i$  are nonnegative.

- ii) Criminals arise from the lowest class only, so that their recruitment term is given by:

$$R(t) = kX_1(t)Y(t) \quad ; \quad k > 0 \quad (12)$$

while no clear dependence on the recruitment rate  $k$  and the global wealth seems to have been elucidated as yet, we may assume that

$$k = k_0 W(t) \quad \text{for some } k_0 > 0$$

- iii) In the absence of specific subpopulations in charge of fighting criminals, the dynamics of  $Y(t)$  is determined by recruitment, natural decay and interspecific competition:

$$Y'(t) = kW(t)Y(t) - \rho Y(t) - \gamma Y^2(t) \quad ; \quad \rho, \gamma > 0 \quad (13)$$

- iv) As a reaction against criminal action, a population  $G(t)$  (the guards) is introduced, whose growth is stimulated by criminal effects on the various social classes. Namely, we postulate:

$$G' = -qG + hY \sum_{i=1}^n \frac{a_i}{b_i + X_i} X_i - l \frac{YG}{M + Y} \quad (14)$$

where  $q, h, a_i, b_i$  ( $i = 1, \dots, n$ ),  $l$  and  $M$  are nonnegative parameters.

Bearing these assumptions in mind and following [26], the dynamics of the society under consideration can be described by the following set of equations:

$$\begin{aligned}
Y' &= kWX_1Y - \rho Y - \gamma Y^2 - \frac{mYG}{M+Y}, \\
G' &= -qG + hY \sum_{i=1}^n \frac{a_i}{b_i + X_i} X_i - l \frac{YG}{M+Y}, \\
J' &= \frac{mYG}{M+Y} - J, \\
X_1' &= -\alpha_1 X_1 + \beta_2 X_2 + \tau J - kWX_1Y, \\
X_i' &= \alpha_{i-1} X_{i-1} - (\alpha_i + \beta_i) X_i + \beta_{i+1} X_{i+1}; \quad i = 2, \dots, n-1, \\
X_n' &= \alpha_{n-1} X_{n-1} - \beta_n X_n
\end{aligned} \tag{15}$$

Notice that the last term in the right of the first equation has been introduced to describe criminal removal through guard action, and a new population  $J(t)$  (the prisoners) has been added to account for such criminals that have been temporarily neutralized by the guards. The last term in the second equation reflects in turns loses suffered by guards during their fight with criminals. To this system, an equation describing the evolution of the total wealth is to be added:

$$W' = \left( \sum_{i=1}^n c_i X_i - W \right) - \lambda Y W \sum_{i=1}^n \frac{a_i}{b_i + X_i} X_i - g(W)G \tag{16}$$

Note that the total reference wealth:

$$\bar{W} = \sum_{i=1}^n c_i X_i$$

corresponds to an equilibrium state of equation (15) when  $Y = G = J = 0$ , so that neither criminals nor guards are present.

A particular example might be useful to better understand the type of information that can be derived from models as (15), (16). Assume that only two classes are present, the guard population is constant (say,  $G = G_0$ ) and prisoners are ignored. Moreover, we assume that promotion and relegation coefficients are constant, and that the total population remains constant as well, so that:

$$X_1 + X_2 + Y = N$$

Supposing also  $g(W)$  to be linear, so that  $g(W) = gW$  for some constant  $g$ , the corresponding reduced system now reads as follows:

$$\begin{aligned}
X_1' &= -\alpha_1 X_1 + \beta_2 X_2 - kWX_1Y + \rho Y + \gamma Y^2 + \frac{mYG}{M+Y}, \\
X_2' &= \alpha_1 X_1 - \beta_2 X_2, \\
Y' &= kWX_1Y - \rho Y - \gamma Y^2 - \frac{mYG}{M+Y}, \\
W' &= c_1 X_1 + c_2 X_2 - W - \lambda Y W \left( \frac{a_2}{b_2 + X_2} \right) X_2 - gWG
\end{aligned} \tag{17}$$

We then normalize units to obtain  $N = \lambda = 1$ , and select a reference set of parameter values, namely:

$$\begin{aligned}
M = 1; \quad \rho = 0.1; \quad g = 0.1; \quad \alpha_2 = 1; \quad b_2 = 1; \quad m = 0.1; \\
c_1 = 0.1; \quad c_2 = 1; \quad g = 0.1; \quad \alpha_1 = 0.1; \quad \beta_2 = 0.01; \quad \gamma = 0
\end{aligned} \tag{18}$$

Under the previous assumptions, system (17), (18) has a free-from-criminals stationary state such that:

$$Y = 0, \quad X_1 \approx 0.091, \quad W \approx \frac{9.18}{10 + G} \quad (19)$$

To discuss the stability of such steady state, one has to compute the eigenvalues of the linearized matrix around that equilibrium, which is given by:

$$M \equiv \begin{pmatrix} -1 - 0.1G & -1 - \frac{4.372}{10+G} & -0.9 \\ 0 & \frac{0.835k}{10+G} - 0.01 - 0.1G & 0 \\ 0 & -\frac{0.835k}{10+G} + 0.1G & -0.11 \end{pmatrix} \quad (20)$$

A quick computation reveals that  $M$  has two negative eigenvalues. As to the third one, it is given by:

$$\lambda_3 = -\frac{-0.835k + 0.1 + 1.01G + 0.1G^2}{10 + G} \quad (21)$$

so that if either  $G$  is large enough or  $k$  is small enough,  $\lambda_3$  is negative and the equilibrium under consideration is asymptotically stable. We point out that if condition  $\lambda_3 < 0$  holds, the assumptions in Theorem A above are satisfied. As a matter of fact, such Theorem allows for an extensive screening of stability properties of steady states in (17) when only partial information about system parameters is available. We shall discuss this issue elsewhere, and continue here the analysis of our example under the parameter restrictions made in (18).

It is easy to check that  $\lambda_3 < 0$  provided that  $k < k_c$  for some positive value  $k = k_c(G)$ . Thus, if criminal recruitment is small enough, our model relaxes to a crimeless society whenever a fluctuation introduces a (sufficiently small) criminal population. Notice that a similar effect is obtained if we sufficiently increase the values of  $G$  (that is, the guards population), which in turns contributes to wealth depletion (see (19)). However, when  $k > k_c$ , the previous steady state is no longer stable. Roughly speaking, the corresponding society becomes criminal-prone, and in fact an additional steady state with  $Y > 0$  appears. The reader is referred to [26] for further discussion on the measures that can be taken to keep stable the steady state given in (20).

## 4 Concluding remarks

In the example just discussed we have shown how stability properties of a dynamical system translate into changes of social trends of the societies modelled by such systems. In particular, we have shown conditions under which unsocial behaviours tend to disappear as a consequence of definite actions: lowering the criminal recruitment rate (which can be made by social promotion measures) or increasing the strength of police corps (that is, by enhancing repression). Each of these alternatives can be characterised in terms of the parameters appearing in the system. Since parameter identification in this (and in many other) settings is far from being straightforward, the question naturally arises of taking advantage of results as those recalled in Section 2 to significantly extend the range of validity of the conclusions derived from analysis of systems like (17).

The previous remark applies to situation where parameters in the model system can be assumed to have precise, although largely unknown, constant values. However, in many cases the interaction rules among classes that are to be retained in a model are such that the corresponding interaction parameters cannot be taken as constant, but should instead be obtained as a result of deterministic or stochastic games. Indeed, game theory is a well-established tool in the study of population dynamics (see for instance [27]) and steady states (defined in a

generalised manner) can be obtained from repeated game playing [28]. A particularly simple (but relevant) example is provided by society models in the spirit of (17) where promotion and relegation among classes proceeds according to stochastic games where, for instance, cooperation within neighbouring classes is less favoured than that occurring between distant ones (see [29] for preliminary results in that direction).

Finally, concerning the asymptotic properties of the models to be considered, a key issue is that of obtaining early warnings for critical transitions that in this context may be interpreted as structural crisis. Some preliminary results have been obtained under rather strict assumptions on the nature of the models considered (cf [30]), and we intend to further explore elsewhere that issue in a general context, where interactions are determined from game-theoretical rules, and considerable uncertainty prevails on some aspects of the dynamics under consideration.

**Acknowledgements.** This work has been partially supported by MINECO Research Grant MTM2011-22656.

## References

- [1] B. Rasmussen, I. R. Fletcher, J. J. Brochs, and M. R. Kilburn. Reassessing the first appearance of eukaryotes and cyanobacteria. *Nature*, 455:1101–1104, 2008.
- [2] A. Lazcano and S. L. Miller. The origin and early evolution of life: prebiotic chemistry. the pre-rna world, and time. *Cell*, 85:793–798, 1996.
- [3] J. Lovelock. *Gaia: a new look at life on Earth*. Oxford University Press, 1995.
- [4] M. A. Herrero and L. Sastre. Models of aggregation in dictyostelium discoideum: on the track of spiral waves. *Networks and Heterogeneous Media*, 1(2):241–268, 2006.
- [5] J. W. Costerton, P. S. Stewart, and E. P. Greenberg. Bacterial biofilms: a common cause of persistent infections. *Science*, 284(5418):1318–1322, 1999.
- [6] L. Hall-Stoodley, J. W. Costerton, and P. Stoodley. Bacterial biofilms: from the natural environment to infectious diseases. *Nature Rev. Microbiol.*, 2:95–108, 2004.
- [7] M. Gagliano, M. Renton, N. Duvdevani, M. Timmins, and S. Mancuso. Out of sight but not out of mind: alternative means of communication in plants. *PLoS ONE*, 7(5):e37382, 2012. doi:10.1371/journal.pone.0037382.
- [8] C. Detrain and J. L. Deneubourg. Self-organized structures in a superorganism: do ants behave like molecules? *Phys. Life Rev.*, 3:162–187, 2008.
- [9] D. Neal. *Introduction to Population Biology*. Cambridge University Press, 2004.
- [10] M. A. Nowak and R. M. May. *Virus dynamics: mathematical principles of immunology and virology*. Oxford University Press, 2000.
- [11] D. K. Arrowsmith and C. M. Place. *An introduction to dynamical systems*. Cambridge University Press, 1994.
- [12] Y. Kuznetsov. *Elements of applied bifurcation theory*. Springer Appl. Math. Sci 112, 2004.
- [13] J. P. Quirk and R. Ruppert. Qualitative economics and the stability of equilibrium. *Rev. Econ. Stu.*, 32:311–326, 1965.
- [14] R. M. May. Qualitative stability in model ecosystems. *Ecology*, 54(3):638–641, 1973.
- [15] E. A. Coddington and N. Levinson. *Theory of ordinary differential equations*. Mc.Graw-Hill, 1955.
- [16] P. A. Samuelson. Prices of factors and goods in general equilibrium. *Rev. Econ. Stu.*, 21(1):1–20, 1953.

- [17] D. Gale and H. Nikaido. The jacobian matrix and global univalence of mappings. *Math. Ann.*, 159:81–93, 1965.
- [18] S. Oda and K. I. Yoshida. A short proof of the Jacobian conjecture in case of degree less or equal than two. *Compt. Rend. Acad. Sci. Paris*, 5(4):159–162, 1983.
- [19] B. L. Clarke. Stability of complex reaction networks. *Adv. Chem. Phys.*, 42:1–213, 1980.
- [20] G. Craciun and M. Feinberg. Multiple equilibria in complex chemical reaction networks I: the injectivity property. *SIAM J. Appl. Math.*, 65(5):1526–1546, 2005.
- [21] J. D. Murray. *Mathematical Biology*. Biomathematics series 19. Springer, 1991.
- [22] A. S. Mikhailov. *Foundations of Synergetics I*. Series in Synergetics. Springer, 1994.
- [23] E. M. Ozbudak, M. Thattai, H. N. Lim, B. I. Shraiman, and A. van Oudenaarden. Multistability in the lactose operon network of *Escherichia coli*. *Nature*, 427:737–740, 2004.
- [24] D. Angeli, J. E. Ferrell Jr, and E. D. Sontag. Detection of multistability, bifurcation and hysteresis in a large class of biological positive feedbacks systems. *Proc. Natl. Acad. Sci. USA*, 7:1822–1827, 2004.
- [25] E. D. Sontag. Monotone and near-monotone biochemical networks. *Syst. Synth. Biol.*, 1(2):59–87, 2007.
- [26] J. C. Nuño, M. A. Herrero, and M. Primicerio. A mathematical model of a criminal-prone society. *Disc. Cont. Dyn. Systems S*, 41:193–207, 2011.
- [27] J. Hofbauer and K. Sigmund. *Evolutionary games and population dynamics*. Cambridge University Press, 2002.
- [28] A. Sanchez and J. A. Cuesta. Altruism may arise from individual selection. *J. Theor. Biol.*, 235:233–240, 2005.
- [29] M. L. Bertotti and M. Delitala. On a discrete generalized kinetic approach for modelling persuader’s influence in opinion formation processes. *Math. Comput. Mod.*, 48:1107–1121, 2008.
- [30] M. Scheffer, J. Bascompte, W. A. Brock, V. Brovkin, S. R. Carpenter, V. Dakos, H. Held, E. H. van Nes, M. Rietkerk, and G. Sugihara. Early-warning signals for critical transitions. *Nature*, 416:53–59, 2009.

# “Locsitons” in self-interacting atomic nanolattices

A.E. Kaplan and S.N. Volkov

*Department of Electrical and Computer Engineering,  
Johns Hopkins University, Baltimore, MD 21218, USA*

## Abstract

We found that the major assumption of the Lorentz – Lorenz theory about uniformity of local fields in dense material does not hold in finite groups of atoms. Self-interaction of atomic lattices results in the uniformity being broken at sub-wavelength scale. The system then exhibits strong sub-wavelength stratification of local field and dipole polarization due to nanoscale excitation of so called “locsitons”, which give rise to size-related resonances and related large field enhancement in finite atomic lattices. At certain “magic” numbers of atoms in the array, the system may exhibit self-induced cancellation of resonant local-field suppression. In a 2D case, a similar effect gives rise to “magic shapes”; it also enables the formation of distinct vector locsiton patterns consisting of multiple vortices in the field distribution. We also studied nonlinear modes of locsitons and found optical bistability and hysteresis in the simplest and most fundamental case of two atoms. We briefly discuss potential applications of those effects.

A well known fact of the electrodynamics of continuous media is that the microscopic field acting upon atoms or molecules (known as the “local field”) is generally different from the macroscopic (average) field because of the dipole interaction between the particles comprising the medium. This difference is a central point of the classical theory of the local fields in dielectrics advanced by Lorentz and Lorenz [1]. An important, albeit implicit, assumption of that theory is that the local field remains virtually unchanged from atom to atom at distances much shorter than the wavelength of light  $\lambda$ . The theory is, therefore, essentially based on the so-called “mean-field approximation”.

Here we review our recent results [2–4] on the discovery of a host of new effects emerging in low-dimensional (1D and 2D) systems of resonantly excited two-level atoms with sufficiently strong dipole-dipole interactions. We have shown that in systems smaller than the wavelength of light, an excitation of the atomic dipole moments may become substantially *inhomogeneous*, forming strata and two-dimensional structures on a nanometer scale. Such behavior of the local field in a dielectric system is significantly different from the results of the Lorentz–Lorenz theory for the local fields; it gives rise to resonances defined by the system’s size and geometry and is capable of inducing a giant local-field enhancement. A saturation nonlinearity in two-level atoms may then cause optical bistability, in particular, in the simplest case when the system is comprised of two atoms only. We also predicted “magic” system sizes and geometries that, unlike the Lorentz model, do not result in a suppression of the local field in the system when the laser frequency is tuned to the resonance of the two-level atom.

Rapid advances in nanotechnology opened up possibilities to fabricate artificial systems of strongly interacting particles, whereby the assumption of the local-field uniformity would no longer be valid. It would be natural to presume that abandoning the mean-field approximation in the description of the local fields may result in a discovery of many new interesting

phenomena, just as going from the macroscopic Curie–Weiss theory to the Ising model significantly extended the ability of the theory to describe magnetic materials [5]. This does not, of course, mean that a complete analogy is to be expected in the descriptions of the local fields and magnetic media. In our case one could expect still more interesting discoveries, because the atomic electric dipoles induced by the local fields are driven by the incident electromagnetic wave, in contrast to the static magnetic dipoles in the Ising model. Another crucial distinctive feature of our work is that the systems under consideration are very small, less than the wavelength in size, while the majority of studies in the theory of magnetism focus on building a macroscopic, “thermodynamic”, description of the medium.

In our research [2–4] we demonstrated that taking into consideration significant spatial variations of the local field from atom to atom, on a scale much smaller than the wavelength, opens the way for describing many new effects in ordered systems of strongly interacting atoms, including giant local-field resonances, “magic” system sizes and geometries, the optical bistability and hysteresis. Of particular importance is that our research brings forward a totally new paradigm in the theory of light–matter interaction. Our calculations show that various field-related and array-related factors may disrupt a smooth variation of the local field from atom to atom, enabling nearly periodic strata or more complex patterns of induced dipole moments. They are most pronounced in one- and two-dimensional dielectric systems comprised of atoms, molecules, quantum dots, clusters, or other resonant particles. The resonant nature of the interaction between the particles allows to control the anisotropy and strength of the interaction. If the light wave in such a process propagates normally to the one- or two-dimensional lattice, we can then also eliminate wave propagation aspects of the problem.

In general, two major types of dipole strata emerge: short-wave, with a period of up to four interatomic distances, and long-wave strata. The strata can be interpreted as standing waves of local-field excitations, which we will hereafter call “locsitons”. The locsitons are electrostatic by nature and can have a very low group velocity. They may be classified as Frenkel excitons [6], because the electrons are bound to the atoms and there is no charge transfer in the systems under consideration.

In the first approximation, the phenomenon under consideration is linear in the external field, and the locsitons can be excited within a spectral band much broader than the atomic linewidth. It essentially amounts to a Rabi broadening of the spectral line of the resonant atom, which arises because of the strong interatomic interactions. The dipole strata can be controlled by adjusting the laser polarization and the dimensionless interatomic coupling parameter  $Q$  (see below), which depends, in turn, on the interatomic distance, on the dipole moment and spectral linewidth of the resonant transition in the atoms, and on the detuning of the laser frequency from the atomic resonance. At  $|Q| > Q_{\text{cr}} = O(1)$ , the smooth variation of the local field from atom to atom can be broken by boundaries, impurities, defects in the lattice, etc. A most striking manifestation of the effect is the emergence of large local-field resonances due to locsiton eigenmodes in finite arrays and lattices. Another interesting and unexpected phenomenon is an almost complete cancellation of the local-field suppression, if the laser frequency is tuned exactly to the atomic resonance and the system is made of a certain “magic” number of atoms. Moreover, in a system with the saturation nonlinearity, different types of optical bistability and hysteresis can emerge.

Our model is based on the dipole interaction between atoms. We can neglect retardation effects because of the small size of the system; therefore, similarly to the classical theory of the local fields [1], we will rely on the fact that the near-field of a dipole is predominantly quasistatic and nonradiative in nature. The frequency  $\omega$  of the incident laser radiation is close to the resonant frequency  $\omega_0$  of the atom, which we will approximate by a two-level

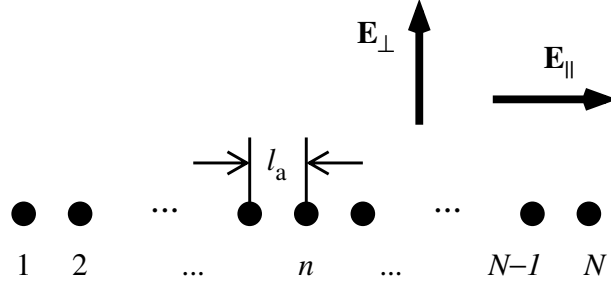


**Figure 1:** The geometry of the one-dimensional problem: the local field in an array of resonant atoms. The light wave propagates normally to the plane of the drawing.

system [7–9] with a transition dipole moment  $d_a$ . The local field acting upon an atom at a point  $\mathbf{r}$  can be represented as a sum of the field  $\mathbf{E}_{\text{in}}$  of the light wave incident on the system and the quasi-static contributions from all other dipoles (their coordinates being denoted as  $\mathbf{r}'$ ), which are induced by the local fields  $\mathbf{E}_{\text{L}}(\mathbf{r}')$ :

$$\mathbf{E}_{\text{L}}(\mathbf{r}) = \mathbf{E}_{\text{in}}(\mathbf{r}) - \frac{Q}{4} \sum_{\text{lattice}}^{\mathbf{r}' \neq \mathbf{r}} \frac{l_a^3}{|\mathbf{r}' - \mathbf{r}|^3} \times \frac{3\mathbf{u}[\mathbf{E}_{\text{L}}(\mathbf{r}') \cdot \mathbf{u}] - \mathbf{E}_{\text{L}}(\mathbf{r}')}{1 + |\mathbf{E}_{\text{L}}(\mathbf{r}')|^2/[E_{\text{sat}}^2(1 + \delta^2)]}, \quad (1)$$

where  $\mathbf{u}$  is the unit vector along  $\mathbf{r} - \mathbf{r}'$ ,  $\delta = T\Delta\omega = T(\omega - \omega_0)$  is the dimensionless detuning of the laser frequency from the atomic resonance,  $E_{\text{sat}}^2 = \hbar^2\epsilon/(|d_a|^2\tau T)$  is the saturation intensity of the two-level system. The dimensionless coupling parameter

$$Q = \frac{4|d_a|^2T}{\epsilon\hbar l_a^3(\delta + i)} \quad (2)$$

represents the strength of the dipole interaction between neighboring atoms; it depends on the transverse relaxation time  $T = 2/\Gamma$  of the two-level atom, whose homogeneous spectral linewidth is  $\Gamma$ , on its longitudinal relaxation time (excitation life time)  $\tau$ , and on a background dielectric constant  $\epsilon$ . We also assume that the interatomic distance  $l_a$  is large enough to prevent any overlap between atomic orbitals of neighboring atoms, so that  $l_a \gg |d_a|/e$ . This assumption is, in fact, also present in the standard Lorentz theory of the local fields [7–9], in which the interaction between the atoms and molecules is treated classically. Our approach radically departs from the standard Lorentz theory in that we do not imply any averaging of the local field over the neighboring sites of the crystalline lattice, which would reveal itself in the assumption that  $\mathbf{E}_{\text{L}}(\mathbf{r}) = \mathbf{E}_{\text{L}}(\mathbf{r}')$ , and we do not use an encapsulating sphere around the observation point, outside of which a continuous medium is assumed.

Large transition dipole moments in, e. g., alkali vapors,  $\text{CO}_2$ , narrow-band resonances in solids [11], quantum dots, clusters, etc., may significantly enhance the effects that we discovered. In many of these cases localitons can emerge with  $l_a$  as large as a few tens of nanometers. One should note that surface plasmons in metal-dielectric composites [12, 13] usually require a more sophisticated theoretical description involving long-range dipole interactions, so this case falls outside the scope of our report.

We first consider a simpler problem of finding the local field in a one-dimensional array of atoms lined up along the  $z$  axis with equal interatomic distances  $l_a$  (Fig. 1). The laser beam, which is incident normally to the array, is polarized either along the array ( $\mathbf{E}_{\text{in}} \parallel \hat{\mathbf{e}}_z$ ),

thus inducing atomic dipole moments that are parallel to the array axis, or perpendicular to the array ( $\mathbf{E}_{\text{in}} \perp \hat{\mathbf{e}}_z$ ), accordingly aligning the dipoles normally to the array and parallel to each other. In both cases we have  $\mathbf{E}_{\text{L}} \parallel \mathbf{E}_{\text{in}}$ , so the equations for the field are reduced to scalar ones. Using the dimensionless notation  $\mathcal{E}_n = [E_{\text{L}}(\mathbf{r}_n)/E_{\text{in}}]_{(p)}$ , where  $(p) = \parallel, \perp$  denotes the field polarization, we can write Eq. (1) for each polarization as

$$\mathcal{E}_n - \frac{\delta_{\text{R}}}{2(\delta + i)} \sum_{\text{chain}}^{j \neq n} \frac{\mathcal{E}_j/S}{|j-n|^3} = 1, \quad (3)$$

where  $1 \leq n, j \leq N$ ,

$$\delta_{\text{R}} = -4SF_{(p)} \frac{|d_{\text{a}}|^2 T}{\epsilon \hbar l_{\text{a}}^3}, \quad (4)$$

and the summation in Eq. (3) is performed over all atoms in the one-dimensional array (chain), resulting in the appearance of the factor  $S = \sum_{j=1}^{\infty} j^{-3} \approx 1.202$ . The factor  $F_{(p)}$  is defined by the field polarization,  $F_{\parallel} = 1$  and  $F_{\perp} = -1/2$ . In the near-neighbor approximation, similarly to the Ising model for magnetic media, the summation over all atoms in Eq. (3) may be replaced with a simpler sum,  $\mathcal{E}_{n-1} + \mathcal{E}_{n+1}$  (one can then set  $S = 1$ ). In both cases [i. e., both for the full summation in Eq. (3) and in the near-neighbor approximation] the results will be qualitatively similar. In the case of a two-atom system, discussed below, the two approaches naturally merge.

For  $N \rightarrow \infty$ , the solution of Eq. (3) can be found as a sum of a uniform ‘‘Lorentz’’ field,

$$\bar{\mathcal{E}} = \frac{\delta + i}{\delta - \delta_{\text{R}} + i}, \quad (5)$$

and wave contributions in the form  $\Delta \mathcal{E} \propto \exp(\pm iqn)$ . The wave number of each of these spatially oscillating solutions is  $q = 2\pi l_{\text{a}}/\Lambda$ , and the wavelength  $\Lambda$ , to be found later, is usually much shorter than the wavelength of the incident light. Here one may notice an analogy to the phonon theory [6], except that our case involves excitations of bound electrons, not mechanical vibrations of atomic nuclei. The solution of Eq. (3) is very anisotropic, with a pronounced dependence on the polarization of the incident wave. The homogeneous ‘‘Lorentz’’ component of the local field is significantly suppressed at the exact resonance, i. e., if the laser frequency is tuned to the frequency of the atomic transition,  $\delta = 0$ , and the dipole interaction between atoms is strong, so that  $|\delta_{\text{R}}| \gg 1$ :

$$|\bar{\mathcal{E}}_{\text{res}}|^2 = \frac{1}{1 + \delta_{\text{R}}^2} \ll 1. \quad (6)$$

In this case the field is, essentially, driven out from the system.  $|\bar{\mathcal{E}}|$  reaches its maximum at  $\delta = \delta_{\text{R}}$ ,

$$|\bar{\mathcal{E}}_{\text{peak}}|^2 = 1 + \delta_{\text{R}}^2 \gg 1. \quad (7)$$

The wave vectors  $q$  are found from the following dispersion relation:

$$\frac{1}{S} \sum_{n=1}^{\infty} \frac{\cos(nq)}{n^3} = \frac{\delta + i}{\delta_{\text{R}}}. \quad (8)$$

(In the near-neighbor approximation the whole l. h. s. of this equation may be replaced with  $\cos q$ .) Within our present model, we showed that spatially oscillating solutions emerge if  $|\delta_{\text{R}}| > 1$  within the following range of frequency detunings:  $1 > \delta/\delta_{\text{R}} > -3/4$ . (In the near-neighbor approximation this range widens:  $|\delta/\delta_{\text{R}}| < 1$ ). The dipole strata are especially

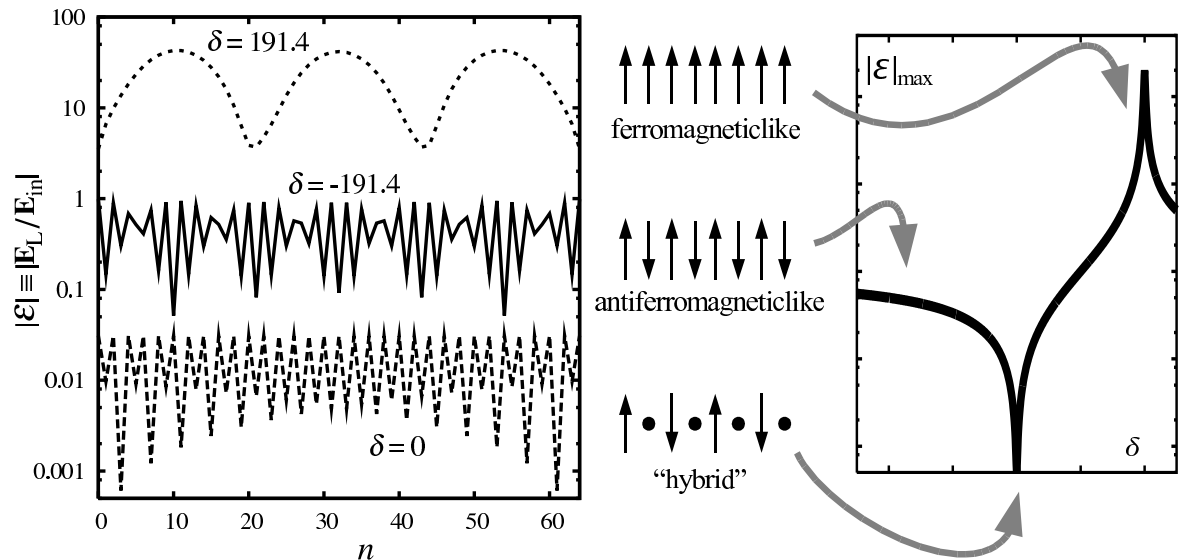


**Figure 2:** Strata patterns of excitation and local field in finite arrays, and their relations to the resonance tuning in the case of 64 atoms and  $\delta_R = 200$ .  $n$  is a sequential number of an atom in the array. Curves and patterns show long-wave, ferromagneticlike excitation near the Lorentz–Lorenz resonance (top curve in the left plot and top pattern in the center), counter-phase, antiferromagneticlike excitation near the anti-Lorentz edge of the band (middle curve and pattern), and hybrid excitation near the point of atomic resonance (bottom curve and pattern). Note that all the curves in the left plot show *absolute* normalized amplitudes of the local field. Since the fields are in general complex, their absolute amplitudes are positive, so the near-zero points in the schematic depiction of the “hybrid” mode actually correspond to the lowest points of the bottom curve in the left plot.

pronounced for  $|\delta_R| \gg 1$ . The strength of the dipole interaction between atoms may be gauged by the Rabi frequency  $\Omega_R = \delta_R/T$ , which essentially defines the position of the Lorentz resonance with respect to the atomic transition frequency. The Rabi frequency sets the width of the energy-spectrum band where locsitos can exist, so that at  $|\delta_R| \gg 1$  this width is  $\sim 2\hbar|\Omega_R| \gg \hbar\Gamma$ . Here we may draw some analogies with energy-spectrum bands in solids [6] and photonic crystals [14]. In the limit of  $1 - \delta/\delta_R \ll 1$  (i. e., on the band edge near the Lorentz resonance, where  $\delta \approx \delta_R$ ), “long-wave” locsitos emerge, with

$$q_{\text{LW}} \approx \sqrt{1 - \frac{\delta^2}{\delta_R^2}}, \quad (9a)$$

$$\Lambda_{\text{LW}} = \frac{2\pi l_a}{q_{\text{LW}}}. \quad (9b)$$

It is worth noting that their wavelength  $\Lambda_{\text{LW}}$  may be as large as  $2\pi l_a \delta_R$ , while remaining much shorter than the wavelength of the incident light wave. A typical example of such strata is presented in Fig. 2 (top curve). At the opposite edge of the locsiton frequency band (in the near-neighbor approximation it corresponds to  $1 + \delta/\delta_R \ll 1$ ) short-wave locsitos emerge, with  $q_{\text{SW}} \sim \pi$  and  $\Lambda_{\text{SW}}/2 \sim l_a$ , which is close to the shortest spatial oscillation wavelength possible in a discrete system.

As  $\Lambda_{\text{SW}}/2$  is generally not a multiple of  $l_a$ , the distribution of dipole moments and the corresponding local fields in the discrete array of atoms may be spatially modulated with a longer wavelength, much like in the case of two waves with close wave vectors. Such modulation is clearly visible in the middle curve in Fig. 2, where  $\Lambda_{\text{SW}}/2$  is quite close to  $l_a$ .

The case of the exact resonance of the incident wave with the atomic transition, for which  $\delta = 0$ , may be used to demarcate the locsiton frequency band into the regions with short-wave and long-wave locsitons. The boundary case, with  $\Lambda = 4l_a$ , is represented by the lower curve in Fig. 2.

To draw the analogy with phonons, we may note that the long-wave locsitons are counterparts of acoustic phonons, and the short-wave locsitons correspond to optical phonons. Another interesting analogy can be drawn with ferromagnetic or ferroelectric materials, which feature strong interaction between static magnetic or electric dipoles. Within this analogy, the locsitons with the longest wavelengths resemble ferromagnetics, while those with the shortest wavelengths resemble antiferromagnetics. A similar analogy may also be noticed in the difference between bistability regimes in these two extreme cases, which we will consider below for the simplest, two-atom, system.

Let us emphasize that this analogy between the locsitons and ferromagnetics or ferroelectrics is inevitably very limited. For example, at  $\delta = 0$  a hybrid configuration of a sort is formed by the induced atomic dipoles in the array,  $\uparrow \circ \downarrow \circ \uparrow \cdots$ , which corresponds to the lower curve in Fig. 2. Such hybrid configurations are only possible because of the dynamic nature of the atomic dipoles in our optical problem, and are unattainable with static dipoles. One could thus smoothly transform the dipole configuration in an array of atoms from a “ferromagneticlike” to an “antiferromagneticlike” by tuning the laser frequency from one locsiton band edge to the other, while going through all the different hybrid configurations in the process.

We have shown that a finite array of atoms should exhibit size-related resonances, which are somewhat similar to resonances in thin semimetal films [15], long organic molecules [16], or a common violin string. The main difference is that in our case the number of the resonances is limited by the number of atoms  $N$ . The linear system of equations (3) may be solved, for example, by using numerical matrix solvers for  $N \gg 1$ , while for small  $N$  the problem is amenable to analytic methods. Some results for the local field  $\mathbf{E}_L$  obtained using numerical methods are shown in Figs. 2–5.

We also applied the following simple approximation to achieve a better qualitative understanding of the numerical results. The solution for an infinite array of atoms can be used to approximate the solution for a finite array of  $N$  atoms as a sum of the uniform “Lorentz” solution  $\bar{\mathcal{E}}$  at  $N = \infty$  and spatially oscillating components  $\Delta \mathcal{E} \propto \exp(\pm iqn)$ , where the resonant locsiton wavenumber  $q$  and the resonant amplitude  $\Delta \mathcal{E}$  are found from appropriate boundary conditions for the local field at the ends of the array. If interaction between all atoms is taken into account, boundary conditions can only be approximated; however, we verified the precision of such approximation for locsitons with sufficiently long wavelengths by many numerical simulations.

In the near-neighbor approximation, the method described above provides an exact solution of the problem. In this solution, the half-wavelength  $\Lambda_1/2 = (N+1)l_a$  of the resonant locsiton with the longest wavelength is determined from the condition that the nodes of the local-field eigenmode lie beyond the end atoms of the array at the distances  $l_a$ , i. e.,  $\mathcal{E}_0 = \mathcal{E}_{N+1} = 0$ . The frequency resonances for the locsitons are defined by the frequency detuning  $\delta_k$  ( $0 < k \leq N$ ):

$$\delta_k = \delta_R \cos q_k, \quad (10a)$$

where

$$q_k = \frac{\pi k}{N+1}. \quad (10b)$$

The corresponding locsiton wavelength  $\Lambda_k = \Lambda_1/k$ . Due to symmetry considerations, only resonances with an odd  $k$  may be excited by an incident laser beam with a symmetric trans-

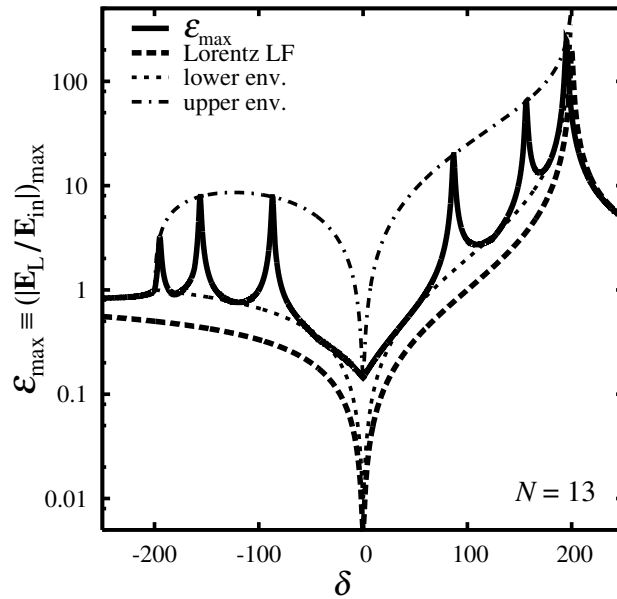


**Figure 3:** Locsiton resonances appearing in the dependence of the normalized maximum amplitude  $\mathcal{E}_{\max}$  of the local field on laser frequency detuning  $\delta$  in an array of  $N = 13$  atoms with  $\delta_R = 200$  (solid curve). For comparison, its upper and lower envelopes are shown along with the corresponding dependence obtained using the classical Lorentz theory for unbounded media (the dashed curve denoted ‘Lorentz theory’).

verse field profile, while resonances with an even  $k$  may be excited by a beam with an anti-symmetric profile. The solid curve in Fig. 3 depicts resonances of the maximum local field

$$\mathcal{E}_{\max} \equiv \max_{0 < n \leq N} |\mathcal{E}_n|$$

at the atoms in the array; the resonances are obtained in the near-neighbor approximation for a uniform distribution of the incident field along an array with  $N = 13$  and  $\delta_R = 200$ . The lower envelope for this curve is  $\mathcal{E}_{\text{low}}(\delta) \approx 2\bar{\mathcal{E}}$ , while the upper envelope, obtained in the near-neighbor approximation, is given by the following expression:

$$\mathcal{E}_{\text{up}} \approx \begin{cases} \bar{\mathcal{E}} \left( n_\delta + \frac{1}{n_\delta} \right) & \text{if } n_\delta \leq 1, \\ 2\bar{\mathcal{E}} & \text{if } n_\delta > 1, \end{cases} \quad (11a)$$

where

$$n_\delta = \frac{N+1}{2\sqrt{\delta_R^2 - \delta^2}}. \quad (11b)$$

As  $N$  increases, the resonances start merging and getting weaker as that number approaches  $N \sim \delta_R$ . However, even for large  $N$ , the lower envelope  $\mathcal{E}_{\text{low}}$  is still twice the local field  $\bar{\mathcal{E}}$  predicted by the classical Lorentz theory [see Eq. (5)].

For  $N = 3k - 1$ , where  $k$  is a natural number, the local-field amplitude  $\mathcal{E}_{\max}$ , which is obtained in the near-neighbor approximation, goes below  $\mathcal{E}_{\text{low}}$  at  $\delta = -\delta_R/2$ . For this frequency detuning  $\delta$ , the absolute value of the locsiton wave number  $|q| \approx 2\pi/3$ , and the spatial period of the locsiton is  $\Lambda = 3l_a$ . The long-wavelength modulations of the spatial profiles of the dipole moments and the local field in the array disappear in this case, because  $\Lambda$  becomes an integer of  $l_a$ . This results in an ‘antiresonance’ of a sort appearing in the

dependence of the local field  $\mathcal{E}_{\max}$  on  $\delta$ ; in other words, the locsiton in the array becomes suppressed.

Another important and unusual effect that we discovered is a cancellation of the resonant local-field suppression in an array consisting of a certain “magic” number of atoms [2, 3]. At the exact resonance of the laser radiation with the atomic transition (i. e., at  $\delta = 0$ ) and if  $\delta_{\text{R}}^2 \gg 1$ , the local field obtained from the Lorentz theory is “pushed out” of the system [see Eq. (6)]. We will call this effect the resonant local-field suppression; it is also present in finite arrays of atoms for most  $N$ . We found, however, that at certain “magic number”  $N$  this resonant suppression vanishes and the local field penetrates the system even at  $\delta = 0$ . In the near-neighbor approximation, the “magic” array sizes are  $N = km_{\text{mag}} + 1$ , where  $k$  is a natural number and  $m_{\text{mag}} = 4$ . The effect is most pronounced at  $N = 5$ , where the atomic dipoles line up as  $\uparrow \circ \downarrow \circ \uparrow$ , with the amplitudes of the dipoles and the local field reaching their maxima ( $\mathcal{E}_{\text{mag}} \approx 1/3$ ) at odd-numbered atoms, while almost vanishing at even-numbered atoms.

The “magic enhancement” of the local field (compared to the uniform, Lorentz, case) can be substantial:  $|\mathcal{E}_{\text{mag}}/\bar{\mathcal{E}}_{\text{res}}|^2 \approx \delta_{\text{R}}^2/9$ . In this effect, one of the resonant locsitons, whose frequency matches exactly that of the atomic transition, virtually compensates the resonant suppression of the local field in the system. The effect is also present if one accounts for interactions between all atoms in the array [see Eq. (3)], where  $m_{\text{mag}} = 13$ . While an interference of an evil spirit cannot be completely ruled out, we assume that the result stems from properties of the equation for the wave vector  $q$  of a locsiton in the array of atoms; this equation follows from Eq. (8) at  $\delta = 0$ :

$$\sum_{n=1}^{\infty} \frac{\cos(nq)}{n^3} = 0. \quad (12)$$

The smallest positive root  $q_1$  of Eq. (12) is such that  $q_1/\pi$  is very close to a rational number,  $(q_1/\pi)/(6/13) = 1.00026\dots$ , so that the locsiton wavelength  $\Lambda = 2\pi/q_1 \approx (13/3)l_{\text{a}}$ , and, thus, a multiple of  $\Lambda/2$  is close to a multiple of  $l_{\text{a}}$ . Therefore, the resonant local-field suppression is cancelled at  $N = 14$ , with the relative amplitude of the field becoming a substantial  $\mathcal{E}_{\text{mag}} \approx 2/15$ .

There is a semantic irony in that the local-field effects are actually due to nonlocal interactions between atoms. If the field of the incident wave is limited to a small spatial region, the local field can extend beyond this region; locsitons can propagate away from their origin. At the edges of the locsiton frequency band, i. e., at  $|\delta_{\text{R}}| > |\delta| \gg 1$ , the group velocity of a locsiton  $v_{\text{gr}} = l_{\text{a}}\sqrt{\Omega_{\text{R}}^2 - \Delta\omega^2}$  could be lower than the speed of sound in a solid. This effect can be useful, e. g., for designing nanometer-scale delay lines that could be used in molecular computers or integrated nanodevices for optical signal processing.

Aside from dipole strata, other, even more interesting structures emerge in two-dimensional lattices of resonant atoms [2, 4]. Let us consider, for example, a standing electromagnetic wave acting upon an equilateral triangular lattice of atoms, the wave being polarized perpendicular to the lattice plane. The interatomic distances are very small, of the order of a few nanometers, so that the external field can be regarded as uniform on a scale of a few tens, even hundreds, of atoms. We found that, at certain conditions, concentric dipole strata (Fig. 4) can emerge around a circular hole made by removing a few tens of atoms from the lattice; the amplitude of the strata decreases fast as the distance to the hole boundary increases. Even more interesting dipole configuration emerges if the laser radiation is incident normally to the lattice and polarized in the lattice plane. For better qualitative understanding of the local-field behavior in this case, we use the “near-ring approximation”, which is a modification of the near-neighbor approximation. In the near-ring approximation,

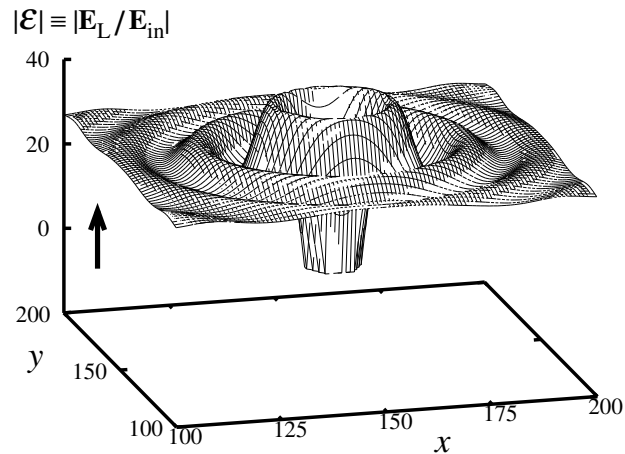


**Figure 4:** Localization of a locsiton in a two-dimensional triangular lattice of atoms around a hole with the diameter of 15 interatomic distances. The distribution of the local field  $\mathcal{E}$  in the system is shown for the case where the external field of the light wave is normal to the lattice plane,  $\delta = 100$ , and  $\tilde{\delta}_R = 69$ .

we consider interactions of each atom with its six immediate neighbors only, while assuming that the positions of the six atoms are evenly “spread” over a circle with the diameter of one interatomic distance  $l_a$ . Like in the one-dimensional case, we introduce a polarization-independent dimensionless parameter  $\tilde{\delta}_R$ , which differs from  $\delta_R$ , defined by Eq. (4), in that here we set  $SF_{(p)} = -1$ :

$$\tilde{\delta}_R = \frac{|d_a|^2 T}{\epsilon \hbar l_a^3}. \quad (13)$$

By comparing Eqs. (2) and (4), one may notice that  $Q = \tilde{\delta}_R / (\delta + i)$ . After replacing the summation in Eq. (1) by an integration over the “near ring” described above, we find a simple isotropic expression for the uniform Lorentz local field:

$$\bar{\mathbf{E}}_L = \frac{\mathbf{E}_{in}}{1 + (3/4)Q}. \quad (14)$$

It can be demonstrated that Eq. (14) remains valid not only in the near-ring approximation, but also in the context of more precise calculations, which account for the structure of the two-dimensional lattice of atoms and for the dependence of the solution on the direction of the locsiton wave vector  $\mathbf{q}$  within the first Brillouin zone. Like in the one-dimensional case, we look for the solution of Eq. (1) as a superposition of the Lorentz field  $\bar{\mathbf{E}}_L$  and plane-wave locsitons with the coordinate dependences  $\exp(\pm i\mathbf{q} \cdot \mathbf{r} / l_a)$ . Assuming that  $\mathbf{q}$  makes an angle  $\psi$  with the polarization direction of the incident laser radiation, we arrive at the following dispersion relation for two-dimensional locsitons (which is a good approximation for relatively long-wavelength locsitons):

$$1 + \frac{3}{4}Q[J_0(q) - 3J_2(q) \cos(2\psi)] = 0, \quad (15)$$

where  $J_n$  is the Bessel function of the first kind.

The near-ring approximation becomes insufficient for short-wavelength locsitons; a more detailed study is required in this case, which takes account of the symmetry of the triangular lattice of atoms and the respective Brillouin zone structure. We have shown that the solution in this more general case depends on the orientation of the incident laser polarization with

respect to the lattice. Let us denote the unit vector pointing from a given atom to one of its nearest neighbors as  $\mathbf{u}_K$  (this corresponds to the  $\Gamma K$  direction in the first Brillouin zone).

Let us consider four most interesting configurations, which are defined by different polarizations and orientations of the locsiton wave vector:

$$(a) \quad \mathbf{q} \perp \mathbf{E}_{\text{in}}, \mathbf{E}_{\text{in}} \parallel \mathbf{u}_K,$$

$$(b) \quad \mathbf{q} \perp \mathbf{E}_{\text{in}}, \mathbf{E}_{\text{in}} \perp \mathbf{u}_K,$$

$$(c) \quad \mathbf{q} \parallel \mathbf{E}_{\text{in}}, \mathbf{E}_{\text{in}} \parallel \mathbf{u}_K,$$

$$(d) \quad \mathbf{q} \parallel \mathbf{E}_{\text{in}}, \mathbf{E}_{\text{in}} \perp \mathbf{u}_K.$$

The respective dispersion relations in these four cases are found by us to be:

$$(a) \quad \cos \frac{q\sqrt{3}}{2} = 4(1 + Q^{-1}),$$

$$(b) \quad \cos \frac{q}{2} = \frac{1}{8}[5 \pm \sqrt{57 + 64Q^{-1}}],$$

$$(c) \quad \cos \frac{q}{2} = \frac{1}{16}[1 \pm \sqrt{1 + 128(1 - Q^{-1})}],$$

$$(d) \quad \cos \frac{q\sqrt{3}}{2} = \frac{2}{5}(1 - 2Q^{-1}).$$

The dipoles induced in a finite two-dimensional lattice form distinctive patterns if locsiton resonances emerge at the same  $Q$  in both dimensions. In the limit of long-wavelength locsitons ( $q \ll 1$ ) the dispersion relations in the cases (a) and (b) coincide with each other and with the result obtained in the near-ring approximation [see Eq. (15)]. In these two cases,  $\psi = \pi/2$  and  $Q \approx -4/3$ , while

$$q_a^2 \approx q_b^2 \approx q_{\text{ring}}^2 \approx -\frac{32}{3} \left( \frac{3}{4} + \frac{1}{Q} \right). \quad (16)$$

In a similar manner, one obtains approximate solutions for the cases (c) and (d), for which  $\psi = 0$ :

$$q_c^3 \approx q_d^2 \approx q_{\text{ring}}^2 \approx \frac{32}{15} \left( \frac{3}{4} + \frac{1}{Q} \right). \quad (17)$$

By combining the cases (a) and (b) or the cases (c) and (d), we can achieve simultaneous resonances in both directions in the lattice, if the lattice is approximately square in shape. Resonances of the same order are hereby attained for locsitons with wave vectors pointing in the two orthogonal directions; a sufficient ‘‘squareness’’ of the two-dimensional triangular lattice can be achieved by choosing the lattice size (i. e., the numbers of atoms in the two directions). Locsitons with shorter wavelengths and wave vectors pointing in different directions will also be present, but they will not significantly affect the emerging dipole pattern, because of their nonresonant nature.

An interference of locsitons in a two-dimensional lattice of atoms [2, 4] can produce many different dipole excitation patterns and strata. Some of them are reminiscent to ‘‘quantum carpets’’ [17]. Fig. 5 depicts vector patterns that are formed by the atomic dipoles induced by the local field. The atoms are arranged in a  $48 \times 56$  equilateral triangular lattice, which results in approximately equal sides of the lattice patch. The field of the incident electromagnetic wave is uniform and polarized along the diagonal of the lattice patch. The

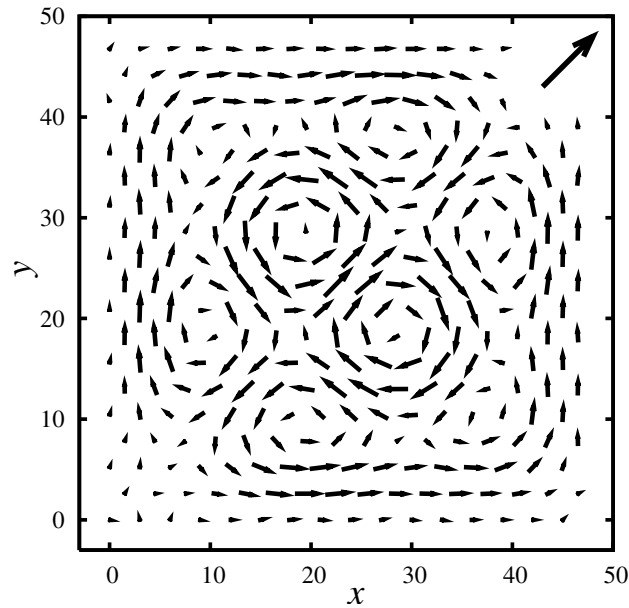


**Figure 5:** Vortices in the distribution of the local field  $\mathcal{E}$  in a nearly square patch of a two-dimensional triangular lattice of atoms at  $\delta = -1000$  and  $\tilde{\delta}_R = 1316.5$ . To avoid overcrowding of the plot, only one of each nine dipoles is shown. The incident light wave is polarized in the lattice plane along the diagonal of the lattice patch, its field is shown with a big arrow.

frequency of the incident wave is so chosen that the third resonance (in the order of increasing wavenumbers, counting only those resonances allowed by the symmetry of the problem) is excited in each dimension; at least six distinct vortices of the local field are visible. Fig. 5 shows the imaginary parts of the complex field amplitudes, because they are dominant for each of the resonant locsitions.

Finite two-dimensional lattices and other similar systems of resonant atoms produce especially interesting examples of cancellation of the resonant local-field suppression. Unlike in the one-dimensional arrays of atoms, the “restoration” of the local field in such systems at  $\delta = 0$ , compared to that in the uniform, Lorentz, case, can be more complete (up to 100%). The two-dimensional “magic shapes” of atoms have the same “cabbalistic” streak as in the one-dimensional case. For example, in the near-neighbor approximation, the effect is most pronounced only in a system of  $N = 13$  atoms arranged as an equilateral six-point star with an atom at the center, for which the maximum restoration of the local field is reached,  $\mathcal{E}_{\max} \approx 1.02$ . The directions and relative amplitudes of the local field at the atoms in this system are shown in Fig. 6 for  $\mathbf{E}_{\text{in}} \parallel \mathbf{u}_K$ . One can see from the picture that the local field is concentrated on the outermost atoms and the one at the center, while the local field at the inner hexagon of atoms is almost completely suppressed. Any symmetry distortion in this system of strongly interacting atoms (e. g., by attaching a foreign atom or molecule to it) would break the balance of the local fields in the system and bring back the resonant suppression of the local field, which is cancelled in the symmetric “magic system”. This effect may be used for designing nanometer-scale sensors for detecting various biological molecules, etc.

Sufficiently strong electromagnetic field applied to the system of strongly interacting atoms can bring about nonlinear local-field effects, e. g., solitons. A detailed consideration of many and varied interesting effects of this kind falls out of the scope of the present report. It worth noting, however, that some nonlinear effects, such as the optical bistability and hysteresis, are possible even in the steady-state regime considered here, where the

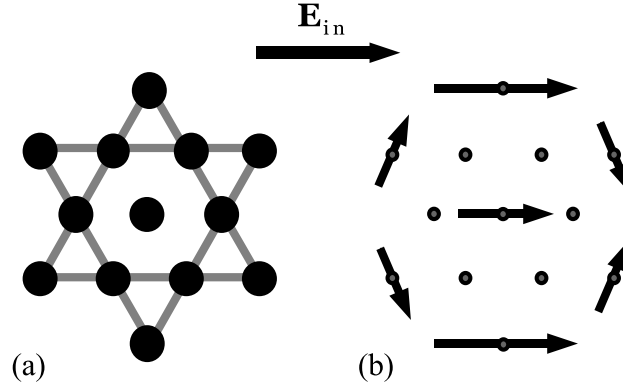


**Figure 6:** (a) The geometry of a “magic system” of 13 resonant atoms; (b) the local-field distribution in the system.

amplitude of the incident electromagnetic wave is constant. The optical bistability for the uniform, Lorentz, local field in an unbounded medium was predicted in [18] and experimentally observed later in [19]. However, the possibility of bistability and multistability for short-wavelength locsitons, whose local field is highly nonuniform in space, has not been discussed in the literature. We found that this effect is possible even in the ultimately simple system of two two-level atoms with the saturation nonlinearity and a strong dipole interaction. This system also provides the most dramatic example of a self-induced local-field nonuniformity.

We will describe the two-atom system using Eqs. (3) and (4) with  $S = 1$ . Depending on the orientation of the local and external fields  $\mathbf{E}_L \parallel \mathbf{E}_{in}$  either perpendicular or parallel to the line connecting the two atoms, Eq. (4) will include either  $F_{\perp}$  or  $F_{\parallel}$ , respectively. We will introduce dimensionless amplitudes of the local field on both atoms,  $Y_j = E_j/E_{sat}$ , where  $j = 1, 2$ , and the dimensionless field of the incident wave,  $X = E_{in}/E_{sat}$ , by normalizing the amplitudes of these fields to the saturation field  $E_{sat}$  of the two-level system. With this new notation, the system of equations for the local fields takes the following form:

$$Y_1 = X + \frac{\delta_{R2}(\delta - i)Y_2}{1 + \delta^2 + |Y_2|^2}, \quad (18a)$$

$$Y_2 = X + \frac{\delta_{R2}(\delta - i)Y_1}{1 + \delta^2 + |Y_1|^2}, \quad (18b)$$

where  $\delta_{R2} \equiv \delta_R/2 > 0$ . Equations (18) give rise to two types of solutions, or two different modes, for the local field in the system. A solution of the first type is similar to the uniform Lorentz solution for an infinite array of atoms, in which the local fields at the two atoms oscillate in phase. In this case the system of equations (18) leads to a cubic equation with respect to  $|\bar{Y}|^2$ , which is readily solved or analyzed with the help of a plot, Fig. 7. For  $|\delta_{R2}| \gg 1$ , the onset of the bistability and hysteresis for  $\bar{Y}$  occurs at the detuning  $\delta \approx \delta_{R2}$  of the laser frequency from the frequency of the two-level transition, with  $\delta_{R2} - \delta > \sqrt{3}$ . In this case, the threshold field of the incident wave  $X_{thr} \approx [(2/\sqrt{3})^3/\delta_{R2}]^{1/2} \ll 1$ , i. e., it may be significantly below the saturation field  $E_{sat}$  of the two-level system.

In the case of antiphase oscillations of the local fields, a multistable solution of the second type is, in fact, a limiting case of a short-wave locsiton which emerges at the opposite edge of the locsiton band at  $\delta \approx -\delta_{R2}$ . In the limit of  $|X| \ll \delta_{R2}$ , aside from the uniform, Lorentz, local field  $\bar{Y} \approx X/2$ , we found a nonuniform solution

$$Y_{1,2} = \bar{Y} \pm s, \quad (19a)$$

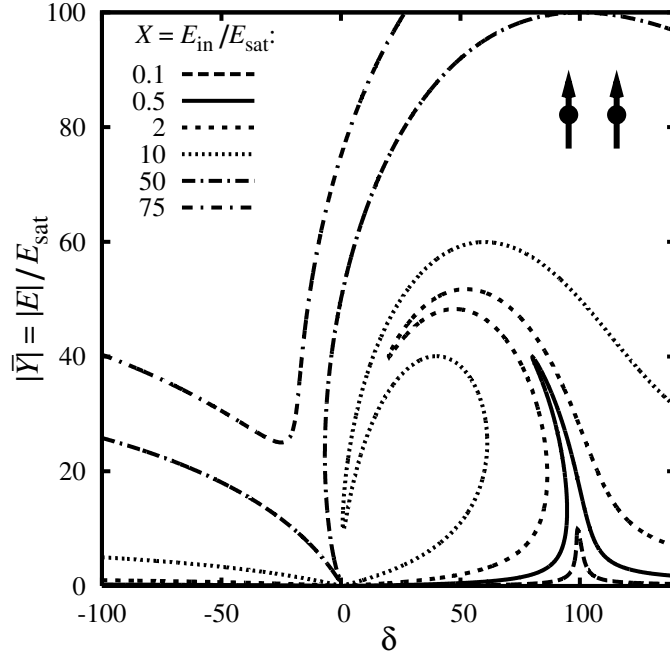


**Figure 7:** Optical bistability and hysteresis in a system of two resonant atoms with the saturation nonlinearity. The dependencies of the normalized local-field amplitude  $|\bar{Y}|$  on the frequency detuning  $\delta$  are shown for  $\delta_{R2} = 100$  and different normalized field amplitudes  $X$  of the incident wave.

where

$$s = \frac{\sigma}{\sqrt{2}}(\sqrt{1 \mp R} - i\sqrt{1 \pm R}), \quad (19b)$$

$$\sigma = \sqrt{\delta_{R2}(\delta_{R2} + \delta) - 2\bar{Y}^2 \pm \bar{Y}^2 R}, \quad (19c)$$

$$R = \sqrt{1 - \frac{\delta_{R2}^2}{\bar{Y}^4}}. \quad (19d)$$

The choice of the signs in Eqs. (19b) and (19c) is independent on the choice of the sign in Eq. (19a). In Eq. (19a) one of the possible choices for the  $\pm$  sign corresponds to  $Y_1$  and the other one corresponds to  $Y_2$ , which enables two different solutions, depending on the signs chosen. A similar property gives rise to the split-fork bistability for counterpropagating waves in a ring resonator [20]. The necessary conditions for the second-type multistable solution for the local field are  $\delta_{R2} + \delta > \sqrt{3}$  and  $X^2 > 4\delta_{R2}$ . Three branches of the solution are seen in Fig. 8 near the bistability threshold: two stable branches given by Eqs. (19) and one unstable “Lorentz” solution  $\bar{Y}$ . At  $\delta_{R2} + \delta > 2$  there exist five different branches of the solution, but only two of them are stable. The antiphase oscillations of the dipole moments of the two atoms, which are represented by the term  $\pm s$  in Eq. (19a), could be likened to a pair of spins, one of which is aligned and the other one is counter-aligned with the applied magnetic field.

Turning back to the above-mentioned similarities between the local-field behavior in a system of atoms and the behavior of spins in magnetic materials, we must emphasize that our research is focused on the effects that are characteristic of fairly small systems of atoms, while studies of magnetic phenomena are typically aimed at finding averaged, “thermodynamic”, properties of sufficiently large systems. It is possible that our approach, which allowed us to predict giant resonances, “magic” numbers and shapes of atoms, etc., may allow one to expose similar effects in nanometer-scale magnetic systems.

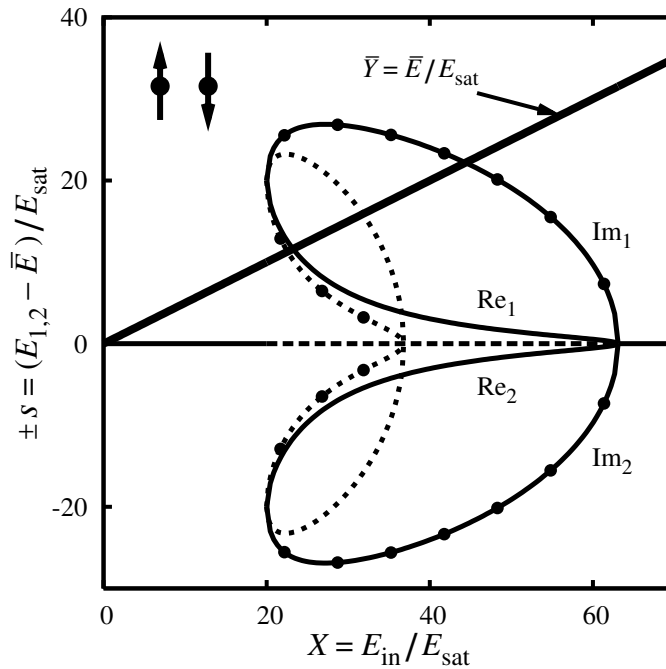


**Figure 8:** Optical bistability in a system of two resonant atoms with the saturation nonlinearity at  $\delta_{R2} = 100$  and  $\delta_{R2} + \delta = 10$ . The thicker solid line represents the average uniform (“Lorentz”) solution, the curves show the dependencies of the “nonuniform components” of our solution on the normalized field amplitude  $X$  of the incident wave. The solid and dashed curves correspond to the stable and unstable regimes, respectively; the real parts of the solutions are shown with the curves marked with filled circles, the imaginary parts are shown with the unmarked curves.

The internal structure of locsitons and dipole strata emerges at a nanometer scale, with many interesting effects involving drastic changes of the local field even between neighboring atoms, i. e., at distances of the order of a few nanometers or less. Optical methods are ill suited for resolving such small systems, so that the x-ray or electron-energy-loss spectroscopies as well as an observation of the size-related optical resonances predicted by us may become more promising methods to detect locsitons experimentally.

It must be noted that locsitons and dipole nanostrata may open up fresh opportunities in designing elements for molecular computers and other nanodevices [21]. The significant advantage of locsitons as compared to electrons in semiconductors and metals is that no electric current or charge transfer is required for locsitons to emerge. This advantage might aid in reducing sizes of computer logic elements, since current semiconductor technology suffers from heat-related problems on a scale below 10 nm.

Locsitons might be put into service both in passive elements (e. g., for data transmission or in delay lines) and active elements (switches or logic elements). Locsiton-based nanodevices could thus supplement the list of alternative nanotechnologies including plasmonics [22, 23], which is substantially based on surface plasmons [12, 13], and spintronics [24]. Another application of locsitons could be in nanosensors for biological molecules and other particles and impurities. Such a nanosensor may be built out of resonant receptor molecules, which can selectively bind target molecules or particles; otherwise, receptor molecules may be attached to particles with an optical resonance. By arranging the molecules in a “magic shape”, the nanosensor may be designed so that the locsiton in the system is not suppressed even at the exact resonance of the laser radiation with the constituent molecules; at the same time, the locsiton will be suppressed whenever a target biological molecule attaches to the

nanosensor.

Even more exciting opportunities open up in arrays and lattices of atoms with inverse population of the resonant quantum transition; this inverse population may be created by an appropriate (e. g., optical) pumping. Such systems may open up the way to controlling locsitions, amplifying them, and even generating coherent locsitions with a “locsiton laser” of a sort (a “locster”).

In conclusion, we demonstrated that dipole nanostrata and short-wave excitations of the local field (locsitions) can be brought about in arrays and lattices of strongly interacting atoms, including a two-atom system, by the action of a laser radiation with a frequency close to that of the atomic resonance. Locsitionic effects include giant size-related resonances of the local field, the cancellation of the resonant local-field suppression in the system at certain “magic” shapes and numbers of atoms, and also optical bistability and hysteresis.

This research was supported by the US Air Force Office of Scientific Research (AFOSR). One of us (AEK) is grateful to the organizers of ICENet2012 conference, G.T. Guria and K.I. Agladze, for their invitation to attend the conference.

## References

- [1] M. Born and E. Wolf, *Principles of Optics*, (Pergamon, Oxford, 1980), Chapter 2 and references therein.
- [2] A. E. Kaplan and S. N. Volkov, *Phys. Rev. Lett.* **101**, 133902 (2008).
- [3] A. E. Kaplan and S. N. Volkov, *Phys. Rev. A* **79**, 053834 (2009);
- [4] S. N. Volkov and A. E. Kaplan, *Phys. Rev. A* **81**, 043801 (2010).
- [5] A. Aharoni, *Introduction to the Theory of Ferromagnetism* (Oxford Univ. Press, Oxford, 2001).
- [6] C. Kittel, *Introduction to Solid State Physics* (Wiley, New York, 1996).
- [7] C. M. Bowden and J. P. Dowling, *Phys. Rev. A* **47**, 1247 (1993);
- [8] J. J. Maki, M. S. Malcuit, J. E. Sipe, and R. W. Boyd, *Phys. Rev. Lett.* **67**, 972 (1991);
- [9] V. S. Butylkin, A. E. Kaplan, and Yu. G. Khronopulo, *Sov. Phys. JETP* **32**, 501 (1971).
- [10] L. D. Landau and E. M. Lifshitz, *The Classical Theory of Fields* (Butterworth, New York, 1980).
- [11] D. G. Steel and S. C. Rand, *Phys. Rev. Lett.* **55**, 2285 (1985).
- [12] V. M. Shalaev, W. Cai, U. K. Chettiar, H.-K. Yuan, A. K. Sarychev, V. P. Drachev, and A. V. Kildishev, *Opt. Lett.* **30**, 3356 (2005);
- [13] V. A. Markel and A. K. Sarychev, *Phys. Rev. B* **75**, 085426 (2007).
- [14] E. Yablonovitch, *Phys. Rev. Lett.* **58**, 2059 (1987).
- [15] V. B. Sandomirskii, *Sov. Phys. JETP* **25**, 101 (1967).
- [16] V. Chernyak, S. N. Volkov, and S. Mukamel, *Phys. Rev. Lett.* **86**, 995 (2001).
- [17] A. E. Kaplan, I. Marzoli, W. E. Lamb Jr., and W. P. Schleich, *Phys. Rev. A* **61**, 032101 (2000).
- [18] C. M. Bowden and C. C. Sung, *Phys. Rev. A* **19**, 2392 (1979).
- [19] M. P. Hehlen, H. U. Güdel, Q. Shu, J. Rai, S. Rai, and S. C. Rand, *Phys. Rev. Lett.* **73**, 1103 (1994).
- [20] A. E. Kaplan and P. Meystre, *Opt. Commun.* **40**, 229 (1982).
- [21] J. R. Heath and M. A. Ratner, *Phys. Today* (May 2003), p. 43.

- [22] W. A. Murray and W. L. Barnes, *Adv. Mater.* **19**, 3771 (2007);
- [23] Y. Fainman, K. Tetz, R. Rokitski, and L. Pang, *Optics and Photonics News*, **7**, 24 (2006).
- [24] I. Žutić, J. Fabian, and S. Das Sarma, *Rev. Mod. Phys.* **76**, 323 (2004).

# From macro- to nano-systems and back in search of the primary cause and control of aging

A. V. Khalyavkin<sup>1,2,\*</sup>

<sup>1</sup>*Institute of Biochemical Physics of RAS, Moscow, Russia*

<sup>2</sup>*Institute for Systems Analysis of RAS, Moscow, Russia*

\**e-mail address: ab3711@mail.sitek.net*

## Introduction

I fully agree with the existent opinion that resolving the big problem connected with the multidimensional nature of protein functions in time, space and context is a key to revolutionizing health care and that a deep understanding of complex biological systems will lead to new ways of preventing/treating many diseases and perhaps even aging. But despite the fact that the pursuit of cellular-molecular and genetic causes of aging receives substantial attention and financial support today, the efforts were insufficient yet to distinctly clarify the picture. Because, when interconnected, cross-talking, and cooperating components of such large system as an whole organism function like a single unit, they have rather new characteristics that are not detected in the study of these parts separately (phenomenon of emergence). For this reason, our understanding of the primary cause and control of aging is still limited. I give here a brief overview of our current knowledge of this problem and describe how a better understanding of some phenomenological peculiarities of macro-systems in different environment might lead us to the development of useful approaches to the origin of aging and its control.

## Senescence as enigma

Almost all tissues in adult organisms are continuously degraded and become rebuilt at the cellular and/or molecular level. With aging, this delicate balance becomes shifted in favor of degradation along with deceleration of protein and cell turnover. These events can render the bodies less reliable, more frail and prone to age-related morbidity and mortality - the main features of senescence. The reason of such imbalance and turnover deceleration constitutes the central question of gerontology.

The concept of homeostenosis implies that a functional aging organism still try to maintain health promoting homeostasis and overall resistance but become increasingly vulnerable to stress and illness because of a step by step reduction of physiologic reserve. That is to say, the concept of homeostenosis points out on the regular and fatal age-dependent shrinkage of phase space for normal homeostatic control. But what is the primary cause for triggering homeostenosis and senescence? Unfortunately the basic reason of this reduction in homeostasis capability remains enigmatic and up to now [1] the following classic statement of G. Williams remains topical — “It is indeed remarkable that after the seemingly miraculous feat of morphogenesis a complex metazoan organism should be unable to perform the much simpler task of merely maintaining what is already formed” [2].

## Is senescence stochastic or programmed?

There are two main and opposite concepts concerning the origin and inevitability of natural senescence. Sometimes a combination of these concepts also is used [3]. In accordance with the *programmed aging* similar to the genetic program of development from a zygote up to a mature organism, senescence is likewise programmed (e.g., via repression of telomerase gene) to facilitate the turnover of generations, which is necessary for survival of a population. From the point of view of the *stochastic aging*, there is no built-in program of senescence; there is only a program of development. After its end, the mature organism could be self-maintained for a limitless time. But the repairing efficiency (e.g., damages from free radicals) must be always less than 100% (in accordance with the accepted postulates of the stochastic aging theory). It is worth to mention that the interventions based on these concepts fail to extend natural lifespan, but only life expectancy [4, 5].

Moreover, the attractive hypothesis that aging might be caused by shrinkage of chromosome tips (telomeres) has rejected now even by its author [6]. He has recently put forth a new proposal based on hypothetical entities called “redosomes” [6].

A quite different, but popular as well, free radical theory of aging has also failed to explain nonpathological senescence [7–10]. The current view posits that continuous superoxide and hydrogen peroxide formation is essential for normal cell function as the second messengers and is not a direct cause of senescence [9]. Therefore, uncontrolled antioxidant treatment may inhibit important cell functions and thus may be dangerous. For example, significant life-span extensions tend to be observed in experiments only when the control flies are phenotypically [7] or genotypically [8] relatively short-lived, suggesting that bolstering antioxidant defenses is not effective in the case of normal aging [7, 8] and can even reduce standard life span [7, 10]. So the primary cause of nonpathological senescence is still unknown.

On the other hand, the evidence is currently accumulating that many age-related changes in cells and organs are quite reversible [11–14] and that the normal somatic cell lines are potentially immortal like cancer or germ-line cells [15]. In this connection “the efforts of evolutionists-gerontologists should probably be directed at clarifying the question of why the organism consisting of potentially immortal cells gets old” [16].

## Cellular background of non-senescence

Indeed, the well-known and famous Hayflick’s effect [17] — the gradually loss of the replicative capacity in fibroblasts and other cells *in vitro* is most likely a manifestation of cellular maturation and terminal differentiation but not of the true senescence of cells [18, 19]. The limitless proliferative potential which somatic stem-like cells are thought to possess [15] is clearly revealed by means of *in vitro* restoration of the stem cell supporting microenvironment, or by removing differentiating stimuli from the cell culture, or by adding differentiating inhibitors to cultural medium [15], and so forth. The same effect can be achieved by the constitutive expression of proto-oncogenes, which encode the nuclear immortalization proteins of the MYC type [20] and some others. The important function of these proteins is the blocking of cellular differentiation [21–23]. The decade later there are the same results, obtained by means of telomerase constitutive expression [24, 25] and the same plausible explanation of it via differentiation blocking [26–28]. The foregoing proves that anti-aging processes can, in principle, successfully counteract cellular deterioration and shows the essential futility of attempting to search the aging primary causes by purely cytological methods at the cellular level.

This conclusion takes us to the position of Carrel [29], who has suggested a century ago that in certain conditions a cell population can exist outside an organism for an unlimited

period, and that the primary causes of organism senescence are located outside cells. Now even old proponent of intracellular sources of aging [30] recognized recently “that at present the aging of multicellular organisms cannot be satisfactorily explained with the help of cytogerontological studies’ data” [31]. Some researchers also agree with the view that the aging of the whole animal is more a function of breakdown in integrative mechanisms than of primary changes in individual cells [15, 32–34]. Even age-related alterations of non-dividing long-life cells, such as neurons or cardiomyocytes, not connected with their maturation and differentiation, may be a consequence of senescence, and not its primary cause. Why, in this case, does an organism hypothetically composed of potentially non-senescent cellular population age?

### **System approach to an aging origin**

The system approach application is rather useful for understanding of the causes and mechanisms of aging because the organism represents a supercomplex system, consisting of a hierarchy of cooperating subsystems. The functioning of subsystems is subordinated to general purposes and is coordinated and managed by the control systems of the individual. For this reason, an organism functions as a single unit. The steady disturbances in the coordination of the activity of subsystems can result in aging. A.A. Bogdanov, the grandfather of a general theory of systems, identified a “system divergence” (an increasing of subsystems’ noncoordination) as the main cause of an aging in the 1920s. It is quite possible that inadequate interaction of an environment and an organism is the main reason of such noncoordination [15, 34]. Many findings have been published regarding both cellular and population aging that are compatible with this approach. The normal cells do not exist in isolation in the body, and their functions are regulated by out-of-cells factors. The levels and activities of most of these factors are highly dependent on the current response of living being to external challenges. Evolutionary biology forecasts that organisms always should be adapted in the best way for an ecological niche that is habitual for them.

### **Environmental influences on aging and longevity**

The detection and processing of environmental cues just as the adequate response to these signals are crucial for the survival of the individual. It is thus not surprising that a large number of different tissues and organs belonging to physiological systems are adjusted to the most probable range of natural environmental pressure characterizing selected ecological niche. This is because organism reacts as a whole on a set of external influences by means of certain changes in numerous regulatory systems at the physiological levels as well as via some changes in signal transduction pathways at the cellular level. Part of such changes may, in principle, modify the aging pattern according to concrete circumstances. For this reason study of natural aging process by means of observation or investigation of animals in captivity as well as human beings in protected conditions would be both artificial and potentially misleading [35, 36].

Nevertheless, environmental influences on aging pattern are often underestimated. In fact, most studies of aging are conducted in humans and domestic or laboratory animals, i.e. in conditions where artificial environment protection is applied. This yields changes in physiology and behavior, which set up organism’s state unobserved in wild life [35, 36]. It might be possible that such state is less adequate to the evolutionary adjusted genetic construction of an organism. In natural niches, physiological homeostasis of organisms may be better regulated. One may hypothesize that in natural environment the aging rate may be significantly lower. Stress resistance may also be substantially higher than in captivity despite the fact that life expectancy in habitat is essentially lower than that in laboratory

conditions due to high external mortality. An analysis of the facts taken as a whole shows that they are compatible with the hypothesis that living conditions exist which are conducive to a significant deceleration (theoretically to a rate of zero) of the human aging process [15, 34, 37, 38].

Let us take into account the influence of all external factors that induce organisms to function in one physiological regimen or another, exactly as an enzymes activity has a bell-shaped dependence on temperature, pH, and so forth. Such bell-shaped [39] and U-shaped [40] regularities prevail in nature. Therefore, one can assume that the control system of a potentially non-senescent organism is able to sustain a physiological regimen of complete self-maintenance not in any circumstances but only within a certain range of changes in the total external conditions known as “environmental pressure”. Self-maintenance will be incomplete outside the zone of adequate environmental pressure. The reserve capacity of organism will start to diminish, and it will begin to age. But individuals “strive” to occupy positions in ecological niches with minimal environmental pressure so as to minimize extrinsic mortality and to maximize survivability and life expectancy, despite the onset of senescence, an age-related increase in mortality rate, and decrease in longevity records. In support of this line of arguments are the following facts. It is common knowledge that reducing below a critical level the values both in the concentration of nutrients in the habitat of amoebae and the water temperature in an aquarium with hydras leads to the senescence of these potentially non-senescent creatures [3, 35]. That is to say, that by changing external conditions one can cause primitive non-senescent organism to age [3, 15, 35]. Therefore, the possibility that the same cause may lie at the base of human senescence should not be discounted; the more so because it is supported by the correlation between parameters of mortality statistics for different countries, the populations of which live in varying climatic, social and economic conditions. This correlation is similar to the mortality pattern for populations of potentially non-senescent organisms, which age in circumstances preventing, to varying extents, the complete self-maintenance of the organisms. Thus, lowering environmental pressures beyond the critical threshold must result in senescence, which is statistically expressed in age-related rise in mortality rate. It is worth mentioning that the mortality pattern [15, 41] for species with a life history that incorporates repeated reproduction is compatible with this concept.

### **Simplest model of aging emergence**

Here is a simple model explaining inevitable aging in some non-adequate ambience even with a perfect design of potentially non-senescent organism. The model based on the extension of Gompertz’s differential equation  $dM/M = a dt$  for an age-dependent increment in mortality rate  $M$  (i.e., relative dying rate of cohort) connected with an increment of age  $t$  by means of introducing to initial equation an additional term, namely  $b dp(t)$  [37, 42]. This term takes into consideration an increment/decrement in mortality rate connected with the alterations in total external conditions (“environmental pressure”) in which the population exists. And  $p$  is the most probable value of this fluctuating environmental pressure in relative units. Then the proved assumption was made that Gompertz’s kinetic parameter  $a$  (rate of aging) is not a phenomenological constant but depends on  $p$ . Because the effectiveness of self-maintenance processes may depend not only on the structural and/or functional peculiarities of an organism but also on the external conditions in which it exists. A linear approximation of this dependence in pessimal conditions ( $p < 1$ ) is  $a = A[1 - p(t)]$ . That is a new modified equation will be rewritten as  $dM/M = A[1 - p(t)]dt + bdp(t)$ . General solution of this differential equation in case of  $dp/dt \neq 0$  (significant and irregular trends in  $p$  values) should be different from exponential growth in rate of mortality described by

Gompertz formula  $M(t) = M_0 e^{at}$ . But in case of quasi-stable  $p$  (average  $p \approx const$ ) the solution is like Gompertzian  $M(t, p) = M(0, 1) e^{-b(1-p) + A(1-p)t}$ . Because  $a = A(1-p)$ , then to a set of different quasi-constant  $p$  corresponds a set of kinetic parameters of  $a$  and the previous formula should be rewritten as

$$M(t, a) = [M(0, 0) e^{-aT}] e^{at}$$

Because  $M_0 = M(0, 0) e^{-aT}$ , then it resembles an existent relationship between two Gompertzian parameters  $M_0$  and  $a$ :  $\ln M_0 = \ln M - aT$ . That is to say, though value  $p$ , which characterized the total external conditions, is hard to determine and evaluate nevertheless its simultaneous influence on both parameter  $M_0$  and parameter  $a$  allows us to exclude it and consider only measurable parameters of mortality statistics such as Gompertzian  $M_0$  and  $a$  and their relationship. Good enough negative relationship between these parameters (rate of aging parameter  $a$  and initial rate of mortality  $M_0$ ) allows us to extrapolate the values of these parameters out of the range of available statistical data (e.g.  $a \rightarrow 0$ ) in order to make some plausible assumptions on the origin of aging in potentially ageless organisms. It is a very important point because the most reliable data of both human mortality statistics and of domestic and laboratory animal's death statistics reveal the feature of their aging in highly protected/unnatural conditions, and to overcome this situation the external control of aging is possible [12, 13, 15, 34, 37].

## Discussion

External factors affect organisms' vital activities resulting in higher or lower induction of self-maintenance to a more or less effective degree. We consider Gompertz's two-parameter mortality rate and assume that these parameters depend on a third parameter,  $p$ , representing environmental pressure (total external influences). Biological consideration allows for the conclusion that a range of environmental conditions (parameter  $p$ ) exists corresponding to an adequate level of vital activity. Therefore, a reasonable amount of environmental pressure plays a stimulating role for organism's functioning and within this range an organism can function optimally and completely renew itself thus remaining non-senescent. However, this range of environmental pressure is not optimal for survival because the environment induces a heavy death toll among such populations. In other words, the mortality rate of these organisms is high for environmental reasons (extrinsic mortality) [15, 38]. To reduce this mortality the organism will favor a less aggressive environment. It thus compromises by sacrificing optimal functioning (complete renewal) for the benefits of the less aggressive environment. As a result, the organism's self-renewal becomes incomplete, and senescence generates an age-related increase in mortality rate. This age-related mortality increase is compensated for by a more significant decline in mortality due to external (environmental) causes. The optimal balance is kept by evolutionary forces, which optimize the average fitness of a population of organisms. Taking this into account, one can assume that in the compromised situation the Gompertzian exponential parameter (which reflects the contribution of the rate of aging) must decline as environmental pressure increases. At the same time, the age-independent part of Gompertz's mortality rate (another Gompertzian parameter) must increase when the environmental pressure increases. Thus there is distinctly reciprocal relationship between these two parameters, which has been repeatedly observed for human beings, primates, rats and flies since 1960 [41, 43]. This relationship is quite similar to the mortality pattern for populations of potentially non-senescent organisms, which grow old under external conditions that prevent their complete self-maintenance [15, 34, 37, 44]. So we suggest that natural, nonpathological senescence may be caused by an inadequate interaction of the organism with its environment.

## Conclusion

Bernard Strehler prophetically said: “There is no inherent property of cells or of meta-zoan organization which by itself precludes their organization into perpetually functioning and self-replenishing individuals” [43]. It is clear today that the normal somatic cell lines are potentially immortal, like cancer cells and germ-line cells. New findings also paradoxically highlight the capability of old mitochondria, precursor cells, tissues, and organs to rejuvenation during the vital activity at appropriate conditions [12–14, 34]. These and other findings can lead to a point at which the age-related changes in the most parts of a body are not the cause, but the effect of organism’s aging. *In vivo* and *in vitro* observations suggest that adequate stimuli can ameliorate the state of different biological units. Moreover, many findings are compatible with the possibility of an entirely extrinsic cause of normal cellular aging. I have extended this principle to the level of the whole organism and offer the hypothesis in which emergence of senescence is not a result of the action of a program or stochastic events, but rather is the consequence of functioning in evolutionary and environmentally inadequate conditions. The signals from these habitats induce the incomplete self-maintenance regimen of organism’s control systems as well as the organism itself. Modification of some components of the control system can readjust its parameters, as in the nematode whose lifespan can be prolonged 10-fold in artificial laboratory conditions [45]. It is possible that a similar result can be attained by means of specific modulation of external signals.

Our current understanding both mortality patterns’ regularities and fundamental features of cellular functions, when combined with our understanding of the results of environmental influences, makes full aging control potentially possible.

## References

- [1] L. A. K. Milewski. The evolution of aging. *Biosci. Horizons*, 3:77–84, 2010.
- [2] G. C. Williams. Pleiotropy, natural selection, and the evolution of senescence. *Evolution*, 11:398–411, 1957.
- [3] M. Lamb. *Biology of Ageing*. Blackie, Glasgow & London, 1977.
- [4] A. Tomás-Loba, I. Flores, P. J. Fernández-Marcos, et al. Telomerase reverse transcriptase delays aging in cancer-resistant mice. *Cell*, 235:609–622, 2008.
- [5] V. N. Anisimov, L. E. Bakeeva, P. A. Egormin, et al. Mitochondria-targeted plastoquinone derivatives as tools to interrupt execution of the aging program. 5. SkQ1 prolongs lifespan and prevents development of traits of senescence. *Biochemistry (Mosc)*, 73:1329–1342, 2008.
- [6] A. M. Olovnikov. The redosome hypothesis of aging and the control of biological time during development. *Biochemistry (Mosc)*, 68:2–33, 2003.
- [7] D. M. Izmailov and L. K. Obukhova. Geroprotector efficiency depends on viability control population: life span investigation in *D. melanogaster*. *Mech. Ageing Dev*, 13:155–164, 1996.
- [8] W. C. Orr and R. S. Sohal. Does overexpression of Cu,Zn-SOD extend life span in *Drosophila melanogaster*? *Exp. Gerontol.*, 38:227–230, 2003.
- [9] A. W. Linnane and H. Eastwood. Cellular redox regulation and prooxidant signaling systems. A new perspective on the free radical theory of aging. *Ann. N.Y. Ac. Sci.*, 1067:47–55, 2006.
- [10] A. C. Bayne, R. J. Mockett, W. C. Orr, and R. S. Sohal. Enhanced catabolism of mitochondrial superoxide/hydrogen peroxide and aging in transgenic *Drosophila*. *Biochem. J.*, 391:277–284, 2005.
- [11] A. V. Blokhin and A. V. Khalyavkin. Influence of long-term limitation of cell proliferation on the cell cycle duration. *Cell Prolif.*, 28:431–435, 1995.

- [12] A. V. Khalyavkin and A. I. Yashin. Inadequate intensity of various components of total environmental signals can lead to natural aging. *Ann. N.Y. Acad. Sci.*, 1067:45–46, 2006.
- [13] A. V. Khalyavkin and A. I. Yashin. Nonpathological senescence arises from unsuitable external influences. *Ann. N.Y. Acad. Sci.*, 1119:306–309, 2007.
- [14] T.A. Rando and H. Y. Chang. Aging, rejuvenation, and epigenetic reprogramming: resetting the aging clock. *Cell*, 20:46–57, 2012.
- [15] A. V. Khalyavkin. Influence of environment on the mortality pattern of potentially non-senescent organisms. General approach and comparison with real populations. *Adv. Gerontol.*, 2:46–49, 2001.
- [16] V. V. Frolkis and K. K. Muradian. *Life Span Prolongation*. CRC Press, Boca Raton, 1991.
- [17] L. Hayflick. The limited *in vitro* lifetime of human diploid cell strains. *Exp. Cell Res.*, 37:614–636, 1965.
- [18] E. Bell, L. F. Marek, D. S. Levinstone, et al. Loss of division potential *in vitro*: aging or differentiation? *Science*, 202:1158–1163, 1978.
- [19] K. Kontermann and K. Bayreuther. The cellular aging of rat fibroblasts *in vitro* is a differentiation process. *Gerontology*, 25:261–274, 1979.
- [20] M. Schwab and J. M. Bishop. Sustained expression of the human protooncogene MYC N rescued rat embryo cells from senescence. *PNAS*, 85:9585–9589, 1988.
- [21] J. A. Coppola and M. D. Cole. Constitutive c-myc oncogene expression blocks mouse erythroleukemia cell differentiation but not commitment. *Nature*, 320:760–763, 1986.
- [22] E. Dmitrovsky, W. M. Kuehl, G. F. Hollis, et al. Expression of transfected human c-myc oncogene inhibits differentiation of a mouse erythroleukemia cell line. *Nature*, 322:748–750, 1986.
- [23] E. V. Prochownik and J. Kukowska. Deregulated expression of c-myc by murine erythroleukemia cells prevents differentiation. *Nature*, 322:848–850, 1986.
- [24] A. G. Bodnar, M. Ouellette, M. Frolkis, et al. Extension of life-span by introduction of telomerase into normal human cells. *Science*, 279:349–352, 1998.
- [25] H. Vaziri and S. Benchimol. Reconstitution of telomerase activity in normal human cells leads to elongation of telomeres and extended replicative life span. *Curr. Biol.*, 8:279–282, 1998.
- [26] H. W. Sharma, J. A. Sokoloski, J. R. Perez, et al. Differentiation of immortal cells inhibits telomerase activity. *PNAS*, 92:12343–12346, 1995.
- [27] P. A. Kruk, A. S. Balajee, K. S. Rao, and V. A. Bohr. Telomere reduction and telomerase inactivation during neuronal cell differentiation. *Biochem. Biophys. Res. Comm.*, 224:487–492, 1996.
- [28] W. Zhang, M. A. Piatyszek, T. Kobayashi, et al. Telomerase activity in human acute myelogenous leukemia: inhibition of telomerase activity by differentiation-inducing agents. *Clin. Cancer Res.*, 2:799–803, 1996.
- [29] A. J. Carrel. On the permanent life of tissues outside of the organism. *J. Exp. Med.*, 15:516–528, 1912.
- [30] A. N. Khokhlov. Stationary cell cultures as a tool for gerontological studies. *Ann. N. Y. Acad. Sci.*, 663:475–476, 1992.
- [31] A. N. Khokhlov. From Carrel to Hayflick and back, or what we got from the 100-year cytogerontological studies. *Biophysics (Moscow)*, 55:859–864, 2010.
- [32] N. W. Shock. System integration. In *Handbook of the Biology of Aging*, pages 639–666. Van Nostrand Reinhold, New York, 1977.
- [33] R. J. Rosen. Feedforward and global system failure: a general mechanism for senescence. *J. Theor. Biol.*, 74:579–590, 1978.

- [34] A. V. Khalyavkin. The updated view concerning the possibility growing old without senescence. *Rejuvenation Res.*, 13:319–321, 2010.
- [35] A. Comfort. *The Biology of Senescence*. Elsevier, New York, 1979.
- [36] H. Gershon and D. Gershon. Critical assessment of paradigms in aging research. *Exp. Gerontol.*, 36:1035–1048, 2001.
- [37] A. V. Khalyavkin. One approach to the control of life span. In *Problems in the Biology of Aging*, pages 49–55. Nauka, Moscow, 1983. in Russian.
- [38] R. M. Seymour and C. P. Doncaster. Density dependence triggers runaway selection of reduced senescence. *PLoS Comput Biol.*, 3(12):e256, Dec 2007.
- [39] D. J. Clancy, D. Gems, L. G. Harshman, et al. Extension of life-span by loss of CHICO, a Drosophila insulin receptor substrate protein. *Science*, 292:104–106, 2001.
- [40] M. M. Vilenchik and A. G. Knudson. Inverse radiation dose-rate effects on somatic and germ-line mutations and DNA damage rates. *PNAS*, 97:5381–5386, 2000.
- [41] B. L. Strehler and A. S. Mildvan. General theory of mortality and aging. *Science*, 132:14–21, 1960.
- [42] A.V. Khalyavkin and A.I. Yashin. Senescence: The role of a control signals. In *Gerontology in silico. The emergence of a new discipline. Mathematical models, analysis of data and numerical experiments.*, pages 114–147. Binom, Moscow, 2007. in Russian.
- [43] B. L. Strehler. *Time, Cells, and Aging*. Academic Press, New York, 1962.
- [44] A. V. Khalyavkin. Experimental indications of the possibility of approaching to the ageless modes vital activity. In *Mechanisms of the Aging Process*, pages 53–60. Nauka, Moscow, 1989. in Russian.
- [45] S. Ayyadevara, R. Alla, J. J. Thaden, and R. J. Shmookler Reis. Remarkable longevity and stress resistance of nematode PI3K-null mutants. *Aging Cell*, 7:13–22, 2008.

# Computational Model of Blood Flow Optimization in Lower Extremities during Intensive Exercise

A.S. Kholodov<sup>1,2</sup>, S.S. Simakov<sup>1,\*</sup>, Y.N. Soe<sup>1</sup> and T.M. Gamilov<sup>1</sup>

<sup>1</sup>*Moscow Institute of Physics and Technology, Dolgoprudny, Russia*

<sup>2</sup>*Institute of Computer Aided Design, RAS, Moscow, Russia*

\**e-mail address: simakov@crec.mipt.ru*

## 1 Introduction

The scientific study of blood flow through human circulatory system has been the subject of scientific re-search for a couple of centuries. It is a complex problem due to the complicated structure of blood vessels and the blood itself. The experimental studies are very useful for the diagnosis of cardiovascular diseases and other practical applications. Unfortunately, experiments are usually expensive and have technical limitations. That's why mathematical models are so important in studying human circulatory system. They help to predict the consequences of different impacts on human body and calculate various blood parameters.

We use 1D network dynamical model of systemic circulation [1, 2] et. al. in this work that is briefly presented in the beginning. It provides adequate and detailed enough description for the blood flow in the heart, major large arteries and veins of hands and legs. We introduce new method of model validation and identification by comparing calculated and experimental values of the pulse wave velocity (PWV) [3, 4]. We use PWV index in this work to specify model parameters more adequate for specific cases of trained athletes [5, 6].

The work is focused on extending this model with mathematical model of skeletal-muscle pumping that is described in the second part. The skeletal-muscle pump is an effect of the group of skeletal muscles during exercise providing additional pressure to the blood flowing to the heart from extremities. Such pumping is especially important in the veins of the legs during walking and running. Numerical simulations are presented showing blood flow redistribution during intensive exercise. Basing on the purely mechanical approach we conclude that effective blood flow through lower extremities during intensive running can be optimized by the stride frequency that depends on the cardiovascular network morphological properties.

## 2 1D-model of systemic circulation

In this work we used network dynamical model of closed circulation [1, 2] et. al. taking into account systemic arteries and veins. The model is based on the model of viscous incompressible fluid flow through the network of elastic tubes. Such flow in every vessel is described in terms of mass and momentum balance equations

$$\frac{\partial S_k}{\partial t} + \frac{\partial(S_k u_k)}{\partial x} = 0 \quad (1)$$

$$\frac{\partial u_k}{\partial t} + \frac{\partial(u_k^2/2 + p_k/\rho_k)}{\partial x} = f_{fr}(S_k, u_k, S_k^0) + \alpha_k g \quad (2)$$

where  $k$  — index of the vessel;  $t$  — time;  $x$  — distance along the vessel counted from the junction point;  $\rho$  — blood density;  $S_k(t, x)$  — vessels's cross-section area;  $S_k^0$  — unstressed cross-sectional area;  $u_k(t, x)$  — linear velocity averaged over the cross-section;  $p_k$  — blood pressure;  $\alpha_k g$  — force of gravity ( $\alpha_k$  — orientation of the vessel toward vertical);  $f_{fr}(S_k, u_k, S_k^0)$  — friction force

$$f_{fr}(S_k, u_k, S_k^0) = -\frac{4\pi\mu u_k}{S_k^2} \left( \frac{S_k}{S_k^0} + \frac{S_k^0}{S_k} \right) \quad (3)$$

$\mu$  — blood viscosity.

We suppose that the networks of the arteries and veins have the same structure. The full network of systemic circulation is composed of joining these two networks by virtual vessels having averaged properties corresponding to the terminal circulation. General scheme of the network used in this work is shown at fig. 1. Vessels and the heart are connected at junction points of three types: vessel-heart, several vessels of the same type (arteries or veins), virtual vessel connecting large terminal artery and vein. As a result peripheral circulation is described in this model by virtual terminal vessels. Some averaging procedures required to identify their properties corresponding to some macro region of the capillary bed.

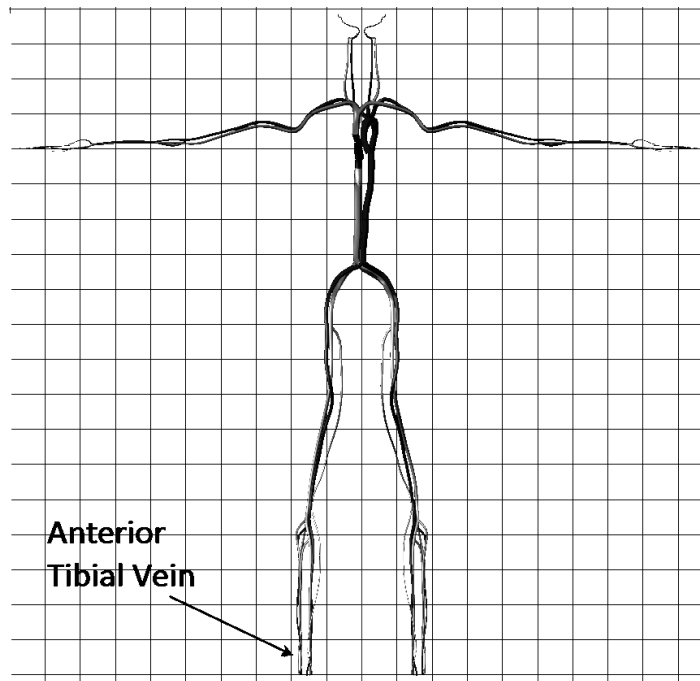


**Figure 1:** The scheme of arterial and venous vessel networks.

To close the set (1), (2) it is necessary to take into account the wall-state equation providing elastic response of the vessel's wall to pressure gradient between “internal” blood pressure and “external” pressure from surrounding tissues

$$p_k - p_{*k} = \rho c_k^2 f_k(S_k) \quad (4)$$

where

$$f_k(S_k) = \begin{cases} \exp(S_k/S_k^0 - 1) - 1, & S_k > S_k^0 \\ \ln(S_k/S_k^0), & S_k \leq S_k^0 \end{cases} \quad (5)$$

$p_{*k}$  — pressure in the tissues surrounding the vessel. Parameter  $c_k$  has a physical meaning of PWV in unstressed vessel. In the simulations concerning intensive muscle-pumping we set it according to the data for professional athletes [5, 6].

### 3 The model of skeletal-muscle pump

Exact simulation of muscle pump work is an enormous task. We derive muscle pumping in the scope of a few assumptions. The force compressing the vessel is directed perpendicularly to the vessel's axis. It allows to consider muscle pumping as external pressure  $p_{*k}$  in (4). To evaluate this pressure we consider muscle as a cylinder holding the weight of a human body. According to [7]

$$p_{*k} \sim \frac{mg}{S} \frac{\sigma}{1-\sigma} \quad (6)$$

where  $m$  — mass of the body;  $S$  — muscle cross-section;  $g$  — gravity constant;  $\sigma$  — muscle Poisson ratio. For a professional sprinter we evaluate  $p_{*k}$  as  $10 \text{ kPa}$ .

Walking and running are periodical processes. Hence, they should be simulated by a periodic function. The period  $T$  equals the time needed to perform two complete strides. Thus, stride frequency can be computed as

$$\nu = 2/T \quad (7)$$

and external pressure can be given by

$$p_{*k} = \frac{P_{\max}}{2} \left[ 1 + \sin \left( \frac{2\pi t}{T} + \Phi \right) \right] \quad (8)$$

where  $P_{\max} = 10 \text{ kPa}$ ;  $\Phi$  — phase (for the vessels of the left leg we set  $\Phi_l = 0$  and for the right —  $\Phi_r = \pi/2$ ).

Major veins of the legs have the valves preventing the backward blood flow. The mechanism of valves functioning is shown on fig. 2

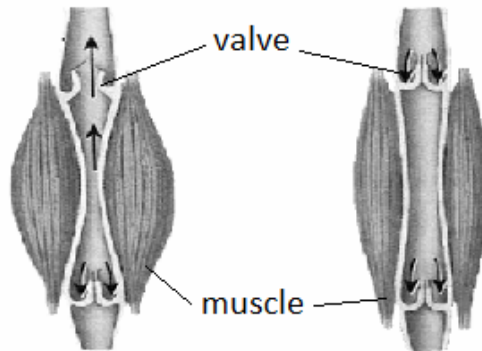


**Figure 2:** Venous valves.

We propose to simulate this feature by modifying friction force for the negative values of blood velocity

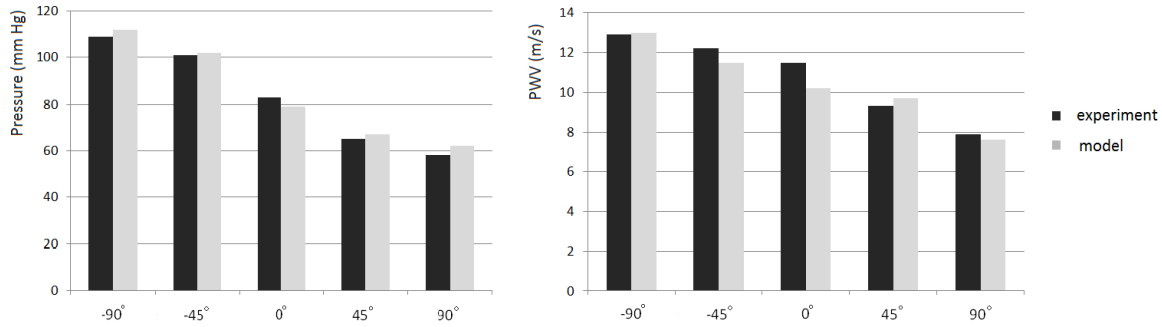
$$F_{fr} = \begin{cases} f_{fr}(s, u), & u > 0 \\ A, & u < 0 \end{cases}, A \gg 1 \quad (9)$$

where  $f_{fr}(s, u)$  is a force used in general non-valved vessel (3);  $A$  — a barrier which is a great positive value totally preventing backward flow.

## 4 Results

### 4.1 Model validation

Developed model was identified, tested and validated by different methods described in [1, 2] et. al. In this work we also validate the model by comparison integral PWV obtained in experiments [4] and computed by our model. Results are depicted at fig. 3.



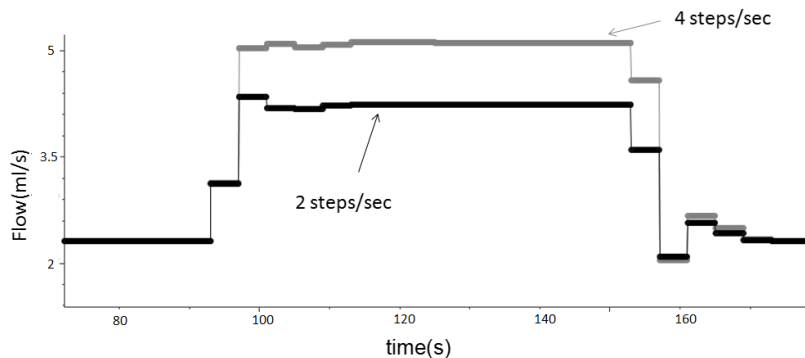
**Figure 3:** Blood pressure and PWV in arm arteries at different arm positions.

Fig. 3 shows that blood pressure and PWV in brachial artery drops as the angle between the arm and horizontal level increased. It validates our model as far as PWVs obtained from numerical simulations are in good correspondence with experimental data [4].

### 4.2 Skeletal-muscle pump

The key feature in blood supply of extremities during intensive exercise is muscle pumping. In order to simulate blood flow in the legs during intensive exercise a series of numerical simulations were carried out. In each simulation we considered the network (fig. 1) to be at rest (zero stride frequency) for the first 90 sec. External pressure (8) were added to (5) in the equation set (1)-(5) corresponded to the leg veins for the next 70 sec for particular stride frequency. Pressure amplitude was gradually increased to its maximum value within the first 10 seconds of this period due to numerical stability limitations.

During these simulations we observed anterior tibial vein (fig. 1) blood flow averaged over the 4 cardiac cycles. Thus, fig. 4 has a stair-step shape. The results of two simulations are shown at fig. 4. They correspond to the stride frequency of 2 and 4 steps per sec.



**Figure 4:** Blood flow during muscle pumping.

From fig. 4 we conclude that increase of the stride frequency results in increase of the average blood flow that results in increased muscles oxygen supply and thus energy production.

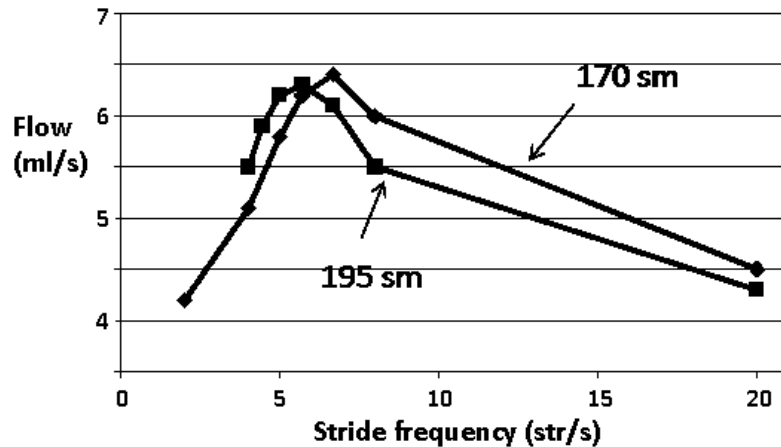


**Figure 5:** Optimal stride frequency for two networks (170 cm and 195 cm in height).

Further stride frequency increase reveals an optimal value giving the highest increase in average blood flow through the leg vessels. Our simulations showed that this optimal frequency depends on the vessel's length. Networks with longer vessels demonstrate lower optimal frequency while networks with short vessels produce a higher one. Further we assume correlation between the network length and the height of a human. Effect is demonstrated at fig. 5 where two networks were uniformly scaled to fit 170 cm and 195 cm in height. We observe optimal stride frequency of 7.5 and 6 strides per sec for these cases.

In order to validate these results we tried to use specific network that was reproduced to fit Usain Bolt's (gold medal in 100 meters sprint in Beijing 2008 Olympiad) height. Elastic properties of the vessels were adjusted corresponding to professional athletes PWV measurements [6]. Using described above technique we simulate Usain Bolt's optimal stride frequency that is presented on fig. 6. The result is compared to the actual stride frequency demonstrated by Usain Bolt during his gold medal run. This value was calculated from Beijing Olympiad video. Obviously fig. 6 shows very good coincidence between our prediction

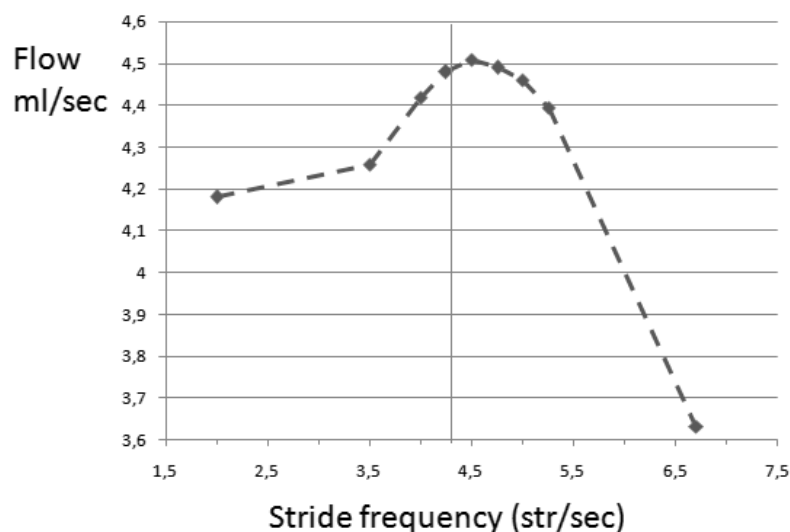


**Figure 6:** Blood flow vs stride frequency; vertical line — Usain Bolt's stride frequency during his 100 m runs in Beijing 2008.

and actual result that is within 5% accuracy.

## 5 Discussion

In this work we extending previous global dynamical model [1, 2] et. al. with muscle pumping model that allows us to simulate average blood flow in lower extremities under intensive exercise. In a set of numerical experiments we observe optimal stride frequency providing maximum average blood flow in the vessels of lower extremities. The further increase of the strides results in decrease of the average blood flow. We suppose this decrease may be accounted for the decrease of period  $T/2$  in (8) during muscles relaxation that becomes insufficient to provide appropriate venous filling.

Numerical simulations presented in this work show that optimal stride frequency depends on the total length of the network. This idea approved by the fact that taller sprinters demonstrate lower stride frequency during competitions. We also validate this result by comparing Usain Bolt stride frequency demonstrated during his 100 meter runs in Beijing 2008 and simulated optimal stride frequency that coincides within 5% accuracy.

It should be mentioned that actual value of the average blood flow is not accessed in this study. Exact quantitative value of average blood flow prediction requires a great number of patient-specific parameters to be measured (cardiac output, vessels structure and property, muscle pump function, pressure amplitude et. al.) that are unavailable in our situation. It also important that numerical optimal stride frequency was computed basing on the 10 seconds acceleration and 70 seconds running time that is caused by numerical stability limitations. Actual 100 meters distance was completed by Usain Bolt within 10 seconds. Thus, extensive future study required to validate proposed method more precisely. This future work would include sprinters, stayers and marathoners.

**Acknowledgements** The work was partially supported by the grants RFBR 11-01-00855-a and MK 2719.2012.9.

## References

- [1] A. S. Kholodov. Some dynamical models of external breathing and blood circulation regarding to their interaction and substances transfer. In O. M. Belotserkovsky and A. S. Kholodov, editors, *Computer Models and Medicine Progress*, pages 127–163. Nauka, Moscow, 2001.
- [2] S. S. Simakov and A. S. Kholodov. Computational study of oxygen concentration in human blood under low frequency disturbances. *Math. Mod. Comp. Sim.*, 1(2):283–295, 2009.
- [3] I. B. Wilkinson, J. R. Cockcroft, and D. J. Webb. Pulse waveanalysis and arterial stiffness. *J. Cardiovasc. Pharmacol*, 32:S33–7, 1998.
- [4] D. Zheng and A. Murray. Non-invasive quantification of peripheral arterial volume distensibility and its non-linear relationship with arterial pressure. *J Biomech*, 42:1032–1037, 2009.
- [5] T. Otsuki, S. Maeda, M. Iemitsu, and Y. Saito. Relationship between arterial stiffness and athletic training programs in young adult men. *Am J Hypertens*, 20:967–963, 2007.
- [6] R. Sala, C. Rossel, and P. Encinas. The continuum of pulse wave velocity from young elite athletes to uncontrolled older patients with resistant hypertension. *J. Hypertens*, 28:19.216, 2010.
- [7] L. D. Landay and E. M. Lifshitz. *Theory of Elasticity*. Elsevier, Oxford, 3rd edition, 1986.

# Russian interbank networks: main characteristics and stability with respect to contagion

A.V. Leonidov<sup>1</sup> and E.L. Romyantsev<sup>2,\*</sup>

<sup>1</sup>*P.N. Lebedev Physical Institute, MIPT and ITEP, Moscow*

<sup>2</sup>*MIPT*

\**settlemen@mail.ru*

## Abstract

Systemic risks characterizing the Russian overnight interbank market from the network point of view are analyzed.

## Introduction

The continuing financial crisis has focused particular attention on systemic risks related to interbank networks. The corresponding literature includes papers analyzing real interbank networks [1–3], theoretical discussions and modelling [4, 5] and discussion of prudential measures [6]. At the conceptual level the research in this area is based on a theory of complex networks, see e.g. [7–9].

The main goal of the present study is to examine the structure of the Russian interbank network and the corresponding systemic risks related to possible default of one of the banks and the volume of contagion triggered by this event.

In our analysis we use the data on overnight interbank transactions of 767 banks from August 1 2011 till November 3 2011. The choice was made in such a way that each bank had at least one transaction within the considered time period. Only transactions corresponding to borrowing (lending) money without any collateral were taken into account.

## Network structure

Let us turn to a more detailed description of the global properties of the Russian interbank network. As has been already mentioned, the database includes all 767 banks having at least one transaction within the considered period of 69 days.

The network of interbank interactions is defined as follows. The nodes of a network stand for banks. A (directed) link between two nodes describes an interbank interaction involving two parties, a borrower and a lender. In what follows we use a standard definition where a link is directed from a borrower to a lender. In network terms lending money to a counterparty creates an outgoing link and borrowing money - an incoming one. In addition, each link is characterized by an amount of money borrowed (lent). An interbank network is thus fully characterized by a directed weighted graph  $G^W = (N, W)$ , where  $N$  is the number of the nodes and  $W = \{w_{ij}\}$  is the  $N \times N$  matrix of interbank exposures where  $w_{ij} > 0$  is a total obligation of the bank  $i$  to the bank  $j$ .

Let first analyze the gross geometrical features of the interbank network under consideration.

The simplest characteristics of a network is a probability  $p$  of having a link which, for a network with  $N$  vertices and  $K$  links can be estimated as

$$p = \frac{2K}{N(N-1)} \quad (1)$$

For the Russian interbank network under consideration the average value of  $p$  is  $\langle p \rangle \sim 0.0037$ .

Another important characteristics of a graph is a clustering coefficient  $C$  which<sup>1</sup> can conveniently be defined as a ratio of a number of actually existing links between the  $z$  nearest neighbors of a vertex and their total possible number  $z(z-1)/2$ . It is clear that for a totally random graph one has  $C = p$ . For the network under consideration the averaged clustering coefficients for incoming and outgoing clusters  $C^{In} = 0.035$  and  $C^{Out} = 0.012$  respectively showing a significant amount of clustering.

Let us now turn to the global characteristics of the trading pattern corresponding to a characteristic interbank network. The simplest characteristics of an overall activity is the mean number of banks that are active or, equivalently, the mean number of banks that are passive on a given day. The corresponding values are 470 and 297 respectively, so that on a typical day we have a network of 470 active banks. These latter can be active in a different fashion. At two opposite poles are pure lenders, i.e. vertices with incoming links only - on average, 299 vertices per day and pure borrowers, i.e. vertices with outgoing links only - on average, 92 vertices. The remaining 79 vertices serve as connectors between borrowers and lenders, i.e. borrow and lend at the same time. A more detailed description of an average daily "in-out" pattern is presented in the Table 1. The columns in Table 1 correspond to an

**Table 1:** Interbank market structure

Condition	$k = 0$	$k > 0$	$k > 2$	$k > 10$
In	389 (14)	378 (14)	126 (9)	14 (3)
Out	596 (8)	171 (8)	82 (5)	29 (3)
Only In	297 (15)	299 (14)	82 (8)	2 (1)
Only Out	297 (15)	92 (8)	29 (4)	5 (2)

average daily number of vertices of given type (In, Out, etc.) satisfying certain conditions. In parentheses we show the corresponding standard deviations.

As has been already mentioned, the systemic risk associated with an interbank network refers to propagation of defaults triggered by the default of one or several banks (vertices) and propagating along outgoing links. In this context the properties of the Russian interbank market characterized by the Table 1 lead us to the following observations:

1. The number of pure lenders is almost twice as large as that of pure borrowers. This feature creates specific systemic risks because a default of any borrower may lead to defaults of several lenders.
2. Of special interest are those 29 banks which are characterized by large ( $k_{out} > 10$ ) values of their out-degree. These banks are clearly especially important sources of systemic risk. Let us note that these banks accumulate 63% of the total systemic debt.

<sup>1</sup>For simplicity in computing  $C$  we treat the graph as an undirected one.

3. Let us also point at those 14 banks that have more than 10 incoming links. From the network perspective these banks play a role of hubs absorbing potential shocks due to their loan's diversification. These banks control 37% of the total loan.

An important generic feature of a directed network are the probability distributions  $P(k^{\text{in}})$  and  $P(k^{\text{out}})$  for the number of incoming and outgoing links for a vertex. The majority of networks discussed in the literature, see e.g. [7–9], are the so-called scale-free ones, i.e. have powerlike tails  $P(k) \sim \text{const}/k^\gamma$ . The corresponding marginal in- and out- degree distributions for the Russian interbank market are shown in Figs. 1 and 2 respectively. We see that the network is scale-free for both distributions with  $\gamma^{\text{in}} = 1.92$  and  $\gamma^{\text{out}} = 2.64$ .

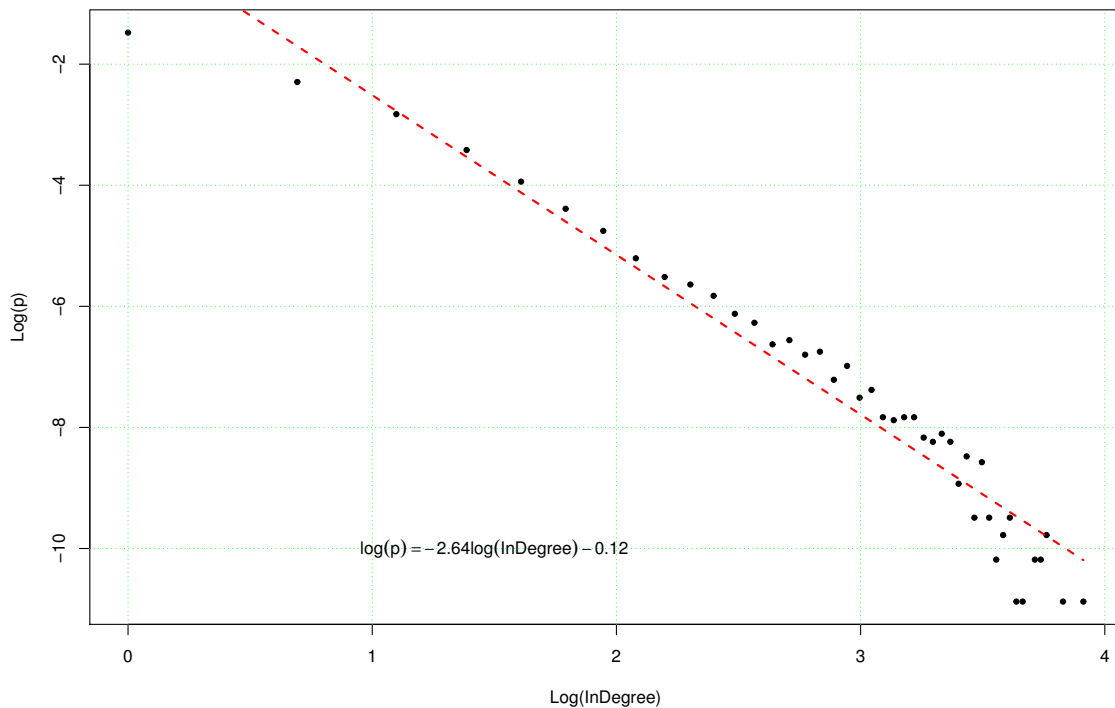


**Figure 1:** Marginal in- degree distribution.

Propagation of contagion in a network is crucially dependent on its connectivity. The simplest corresponding characteristic is an average number of in- and out- links  $z_2^{\text{in}}$  and  $z_2^{\text{out}}$  of the nearest neighbors of a vertex. The bigger are  $z_2^{\text{in}}$  and  $z_2^{\text{out}}$  in comparison with the mean number of in- and out- links for a vertex  $z_1 = z_1^{\text{in}} = z_1^{\text{out}}$ , the easier is contagion propagation along the corresponding cluster. For the Russian interbank network we have  $z_1 = 1.41$ ,  $z_2^{\text{in}} = 9$  and  $z_2^{\text{out}} = 28$ . This the condition  $z_2/z_1 > 2$  for an existence of a giant component holds both for in- and out- clusters.

A more detailed information on the network connectivity is given by a conditional probability distribution  $P(k_2^{\text{in}}, k_2^{\text{out}} | k_1^{\text{in}}, k_1^{\text{out}})$  characterizing probability for a nearest neighbor of a vertex with  $k_1^{\text{in}}$  incoming and  $k_1^{\text{out}}$  outgoing to have  $k_2^{\text{in}}$  and  $k_2^{\text{out}}$  incoming and outgoing links respectively. In Fig. 3 we show two lowest moments of its marginal distributions, namely  $\langle k_2^{\text{out}} \rangle (k_1^{\text{out}})$ , Fig. 3 (a), and  $\langle k_2^{\text{in}} \rangle (k_1^{\text{out}})$ , Fig. 3 (b). Both plots show pronounced assortativity at small  $k_1^{\text{out}}$  for both  $k_2^{\text{in}}$  and  $k_2^{\text{out}}$ .

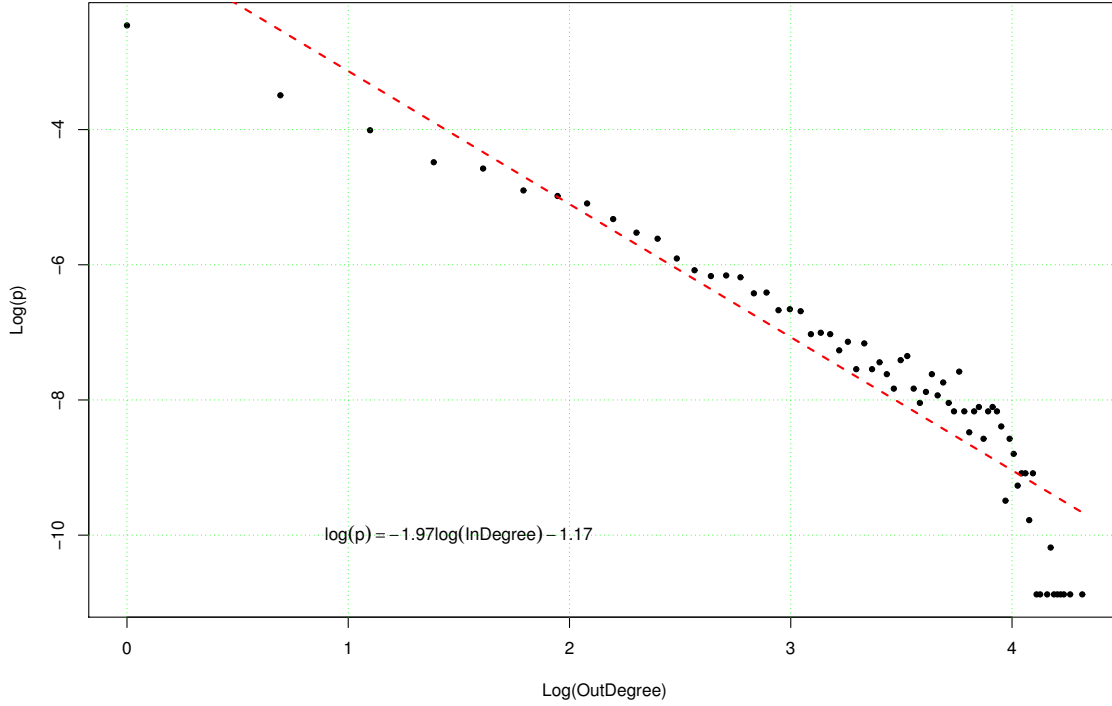


**Figure 2:** Marginal out- degree distributions.

## Contagion effect

Let us start with formulating the model of default contagion spreading in a bank network we are using in the present study. The original source of risk are banks (vertices) that have loans and default on their payment. The banks immediately affected by such a default are the nearest neighbors of this vertex reachable via outgoing links attached to it. If one of the nearest neighbors also defaults, the process can spread further. A probability of infection depends on the number of incoming and outgoing links of a vertex. In the present study we use a simple stylized model of bank balance sheets from [5]. However, at difference with the analysis of [5] and similarly to [3], we are working with the real day-by-day topologies of the interbank market. In this model a representative bank has a simple balance sheet structure with interbank and illiquid assets on the assets side and capital, deposits and interbank obligations on the liabilities side shown in Fig. 4. The corresponding condition for the bank  $i$  to be solvent is

$$(1 - \phi)A_i^{IB} + qA_i^M - L_i^{IB} - D_i > 0, \quad (2)$$

where  $A_i^{IB}$  denotes interbank assets of bank  $i$ ,  $A_i^M$  – its illiquid assets,  $L_i^{IB}$  – its interbank liabilities,  $\phi$  is a fraction of banks having obligations with respect to bank  $i$  that have defaulted, and  $q$  is the discount for fire-selling illiquid assets. It is assumed that interbank claims and liabilities of a particular bank are uniformly distributed across its borrowers and creditors so that  $\phi = \frac{1}{j_i}$  where  $j_i$  is the number of borrowers. This assumption highlights an importance of the incoming degree for each bank as reflecting its risk diversification. Banks with a high value of the incoming degree have lower probability to go bankrupt due to contagion effect. At the same time banks with a high value of the outgoing degree can be the sources of contagion. For simplicity neglect the fire discount, i.e. assume  $q = 1$  in Eq. 2. Therefore one

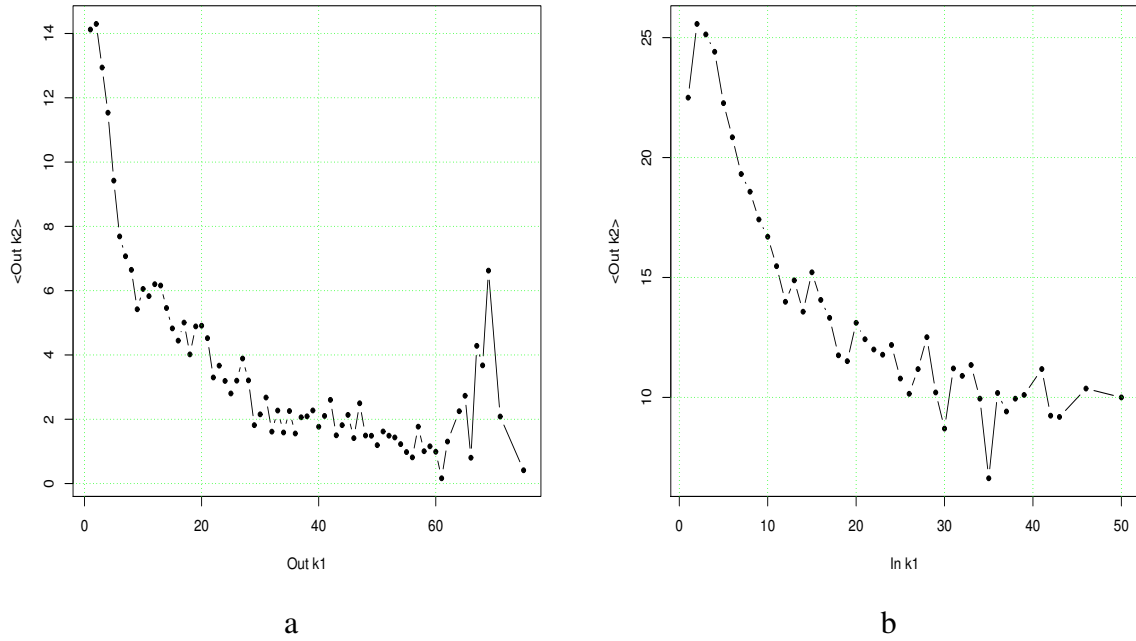


**Figure 3:** Out-in (a) and out-out (b) degree correlations

Assets	Liabilities
Interbank credits	Capital
	Interbank liabilities
Illiquid assets	Deposits

**Figure 4:** Simplified balance sheet

can rewrite the solvency condition 2 as follows:

$$\frac{K_i}{A_i^{IB}} > \frac{1}{j_i}, \quad (3)$$

where the capital buffer  $K_i$  is defined as

$$K_i = A_i^{IB} + qA_i^M - L_i^{IB} - D_i \quad (4)$$

Our main goal will be to study the impact of the capital buffer size on the number of banks which default due to contagion. The procedure we use is as follows:

1. We set the values of relevant parameters. We assume that  $A_i^{IB}$  makes 20% of the balance sheet and study a range of capital buffer values from 4 to 10 % of the balance sheet.
2. Taking real structure of the overnight interbank market we default each bank and determine the size of the default cluster by checking, using Eq. 3, whether some of its

nearest neighbors that can be reached from the defaulted vertex via outgoing links are infected, etc. For each initial bank  $i$  a default cluster for is the number of banks defaulted due to the default of  $i$  as a result of contagion process.

3. Finally, for each value of the capital buffer we calculate an average over default cluster.

The results of this simulation are presented in Figs. 5 and 6 in which probability distribution of default cluster sizes (Fig. 5) and a dependence of the average default cluster on the value of capital buffer (Fig. 6) are shown. From the distribution in Fig. 5 we can make

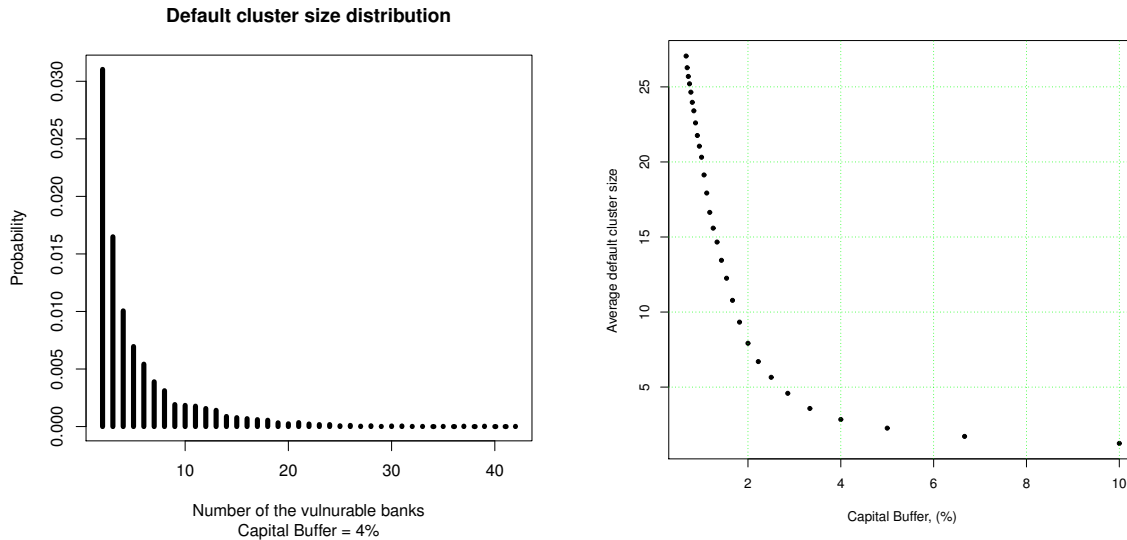


**Figure 5:** Probability distribution for cluster size, Capital Buffer = 4%.

**Figure 6:** Average size of default cluster as a function of a capital buffer.

quantitative statements on the significance of systemic network-related risks. For example, for the capital buffer size of 4% of total balance sheet there is a 1% probability for more than 8 banks go bankrupt. The main conclusion that can be drawn from Fig. 6 is that the average default cluster size is rapidly decaying with growing capital buffer.

## Conclusion

In this study we have analyzed some systemic network-related properties of the Russian overnight interbank market. A detailed analysis will be published in [10].

## References

- [1] M. Eslinger, A. Leher, M. Summer. *Risk Assessment for Banking Systems* Management Science 52 (9): 1301-1314, 2006
- [2] C. Upper, A. Worms. *Estimating Bilateral Exposures in the German Interbank Market: Is there a Danger of Contagion?* Economic Research Centre of the Deutsche Bundesbank, Discussion paper 09/02, February 2009
- [3] E.B. e Santos, R. Cont. *The Brazilian Interbank Network Structure and Systemic Risk*. Banco Central do Brasil, Working Paper Series 219, October 2010
- [4] A. G. Haldane. *Rethinking the Financial Network*. Speech delivered at the Financial Student Association, Amsterdam, April 2009, available at <http://www.bankofengland.co.uk/publications/Documents/speeches/2009/speech386.pdf>.

- 
- [5] P. Gai, S. Kapadia. *Contagion in financial networks*. Proceedings of the Royal Society of London A446 (2020), 2401-2423, 2010
- [6] Basel Committee on Banking Supervision. *Models and tools for macroprudential analysis*. Working Paper No. 21, May 2012.
- [7] R. Albert, A.-L. Barabasi. *Statistical Mechanics of Complex Networks*. Rev. Mod. Phys. 74 (2002), 47-97
- [8] S. N. Dorogovtsev, J.F.F. Mendes. *Evolution of networks*. Adv. Phys. 51 (2002), 1079
- [9] S. Boccaletti, V. Latora, Y. Moreno, M. Chavez, D.-U. Hwang. *Complex Networks: Structure and Dynamics*. Physics Reports, No 424 (2006), p. 175-308.
- [10] A.V. Leonidov, E.L. Rumyantsev, in preparation

# Mathematics for some classes of networks

V. A. Malyshev, A. A. Zamyatin

*Moscow State University, Moscow, Russia*  
*e-mail address: malyshev2@yahoo.com*

Network (as a general notion) is not a mathematical object - there is no even any definition. However, there is a lot of good rigorous mathematics for well-defined classes of networks. In sections 1-3 we give a short overview of classes of networks which interested the authors for some time. In section 4 we consider in detail a new class of networks, related to markets with many agents.

## 1 Random field dynamics on a fixed graph

The basic element of most networks is a graph  $G$  with the set  $V = V(G)$  of vertices and the set  $L = L(G)$  of links (lines, edges). Second basic element is a function  $s = f(v) : V \rightarrow S$  with values in some space  $S$ . The elements of  $S$  may be called marks, spins, field values, queues etc. The function  $f$  is subjected to random dynamics.

Simplest example is (an earlier stuff) random walks on graph, where  $f = 0$  everywhere except one point where the particle is situated. This is related to electric networks, see for example [6].

In general there are two different situations. First one is a local continuous time Markov dynamics given by infinitesimal transitions. Classical reference is [9], mostly such processes model stochastic dynamics of particles or spins. The latter are related to Gibbs random fields (invariant measures for this dynamics) on graphs, see [10] and references therein.

**Queuing, communication and transportation networks** The simplest case is when the particles jump (from one node to another) freely without seeing each other, the only interaction is only through queues at the nodes, where they spend some time. There are two main theories concerning such class of networks:

1. Most popular - Jackson network (1963) and its generalizations (Gordon-Newell, BCMP). This theory gives explicit formulas for the stationary distribution and is the origin of many other analytical results. One of the applications is to describe jams and phase transitions in communication [11] and transportation [12] networks.
2. Stability theory (1968-1995) exhibits in many cases of large time qualitative behavior. If the walking clients are identical then it is described by random walks in orthants and strongly uses It uses Lyapounov functions, Euler scaling (fluid approximation), ergodic theory of dynamical systems and Lyapounov exponents, see [13]. If the walking clients can be of finite number of types then the corresponding theory [4] is the union of the one type case and the theory of random grammars (see below).

For more sophisticated restrictions - network protocols (TCP etc.) - there are many partial results but no comparable (deeply elaborated) mathematical theories.

**Chemical kinetics - mean field Markov chain**

Mean field network means that there is no specified local structure on the graph. Example of such theory is the chemical kinetics. It describes the following situation. Molecular types are indexed by  $V$ ,  $n_v$  - number of molecules of type  $v$

$$n_1 + \dots + n_{|V|} = N$$

There are also reaction types  $r = 1, 2, \dots, R$ , formally - multigraph defined by finite number of equations

$$\sum_v s_{vr} M_v = 0$$

where  $M_v$  - molecule of type  $v$ ,  $s_{vr}$  - stoichiometric coefficients of molecule type  $v$  in reaction of type  $r$ , negative for substrates, positive for products. Reaction rates (continuous time Markov chain) are given by

$$\lambda_r = A_r \prod_{v: s_{vr} < 0} n^{-s_{vr}}$$

for the jump (transition)

$$n_v \rightarrow n_v + s_{vr}, v \in V$$

To get ODE of **classical chemical kinetics**

$$\frac{dc_v}{dt} = \sum_r Q_{vr}(c_1, \dots, c_{|V|})$$

for some polynomials  $Q_r$ , in the limit  $N \rightarrow \infty$

$$c_v(t) = \lim \frac{n_v^{(N)}(t)}{N}$$

one uses canonical scaling of reaction rates

$$A_r = a_r N^{s_r+1}, s_r = \sum_{v: s_{vr} < 0} s_{vr}$$

To deduce **chemical thermodynamics** is more difficult [14], one should, together with molecular types  $v$ , introduce more degrees of freedom: kinetic energy  $T_{v,i}$  and internal energy  $K_{v,i}$  of  $i$ -th molecule of type  $v$ . Also, one should define more complicated mean field dynamics - introduce energy mechanism in reactions. As there is kinetic energy - there should be Newtonian movement, and the dynamics become mixed: **local + mean field**. Molecule move freely (as in ideal gas) but kinetic energies randomly interchange with internal energies.

**Network homeostasis [15]** Network is defined by

1. large graph  $G$  of compartments, this graph  $G$  has metrics and the boundary,
2. in any compartment chemical kinetics is defined, that is there are molecules with chemical reactions,
3. there is transport of molecules between compartments
4. there is input and output of molecules on the boundary

Under some conditions (the main is that reactions are unary) it is possible to prove that **far from the boundary there is equilibrium** - concentrations almost do not change with change of input.

## 2 Dynamics of graphs and of marked graph

Earlier the science of random graphs considered mainly the properties of graphs with fixed number of vertices and/or random number (for example Bernoulli) of edges, see for example [6, 8, 18, 19]. The simplest dynamics (appending edge by edge) appeared already in [7], see also [3]. What more general dynamics on graphs one should study? First of all, it is more reasonable to consider evolution of marked graphs. Most general dynamics of marked graphs (local random dynamics of a graph, jointly with a field on it) is called random graph grammars [1, 2, 5] and [21, 22]. It appears to be quite natural in connection with the emerging new physical theories [16, 17, 25] and social networks [20]. Namely, if eventually the local space-time appears to be discrete, then the most natural language for it is a graph with some physical fields on it. The dynamics of the space time is local. The example is the following.

**Macrodimension of a graph - invariant of local dynamics** We consider infinite (countable) graphs  $G$ . Let  $O_n(v)$  be the neighborhood of vertex  $v$  of radius  $n$ . Put

$$D_n(v) = \frac{\ln |O_n(v)|}{\ln n}, \bar{D}(v) = \limsup_{n \rightarrow \infty} D_n(v), \underline{D}(v) = \liminf_{n \rightarrow \infty} D_n(v)$$

If for all  $v$

$$\bar{D}(v) = \underline{D}(v) = D_S$$

then  $D_S$  is called **scaling macrodimension** of graph  $G$ . For example any homogeneous lattice in euclidean space  $R^d$  has scaling macrodimension  $D_S = d$ . Note that there are many other definitions of variants of macrodimension: connectivity, Hausdorff, entropy, inductive macrodimension.

Denote  $\mathbf{G}_M$  the class of connected graphs where each vertex has degree  $\leq M$ . Let  $U$  - any **local dynamics** (graph grammar).

There is the following result [16]. If for some sufficiently large  $M$   $U$  leaves the **class  $\mathbf{G}_M$  invariant** and the corresponding Markov chain is **locally reversible** then the scaling macrodimension is an invariant.

Local reversibility means that Kolmogorov cycle criteria relations

$$a_{i_1 i_2} \dots a_{i_L i_1} = 1, a_{ij} = \frac{\lambda_{ij}}{\lambda_{ji}}$$

follow from such relations of bounded length.

**Random graph grammars** Consider words  $\alpha = x_1 \dots x_N$  (ordered sequences of symbols), where  $x_N$  belongs to some finite alphabet  $A$ . Grammar is defined by the list  $Sub$  of productions (allowed substitution types)

$$S_j : \alpha_j \rightarrow \beta_j, j = 1, \dots, S$$

Random grammar includes also positive numbers  $\lambda_j$  (rates). That is at time interval  $(t, t + dt)$  in the word  $\alpha(t)$  any subword  $\alpha_j$  is independently replaced by  $\beta_j$  with probability  $\lambda_j dt$  (continuous time Markov chain).

For **graph grammar**  $\alpha(t)$  are marked graphs,  $\alpha_j, \beta_j$  are (small) connected marked graphs. Thus,  $\alpha_j$  is deleted from the graph and  $\beta_j$  is pasted instead (some restrictions needed of course). Note that ordinary grammar is a particular case, corresponding to linear marked graphs.

One of the problems - invariant measure and conserved characteristics with respect to given graph grammar dynamics was considered in [12, 21, 22].

### 3 Quantum Graph Grammar

What is quantum graph [26]. Consider Hilbert space  $l_2(\{G\})$  with (orthonormal) basis  $e_G$ , enumerated by finite graphs  $G$ . Or by finite marked graphs if the set of marks is finite. First example is linear marked graphs - **quantum words**.

To define quantum dynamics assume that if  $a_j = (\alpha_i \rightarrow \beta_i) \in Sub$  then also inverse substitution  $a_j^* = (\beta_i \rightarrow \alpha_i) \in Sub$ . Denote  $S_j(k)$  the substitution  $S_j$  applied to subword of the word  $\alpha$  starting on  $k$ -th symbol of the word  $\alpha$ . Introduce the Hamiltonian

$$\sum_{j=1}^{|Sub|} \sum_{k=1}^{\infty} (\lambda_j a_j(k) + \lambda_j^* a_j^*(k))$$

The first simple result is: this Hamiltonian is selfadjoint in  $l_2(\{G\})$ , that is the quantum evolution is well-defined.

**Gibbs and Quantum Spaces**  $\mathbf{G}$  - class of finite graphs with a function  $f : V \rightarrow R$ , called spin graphs  $(G, f)$ ,  $\mathbf{G}_N$  - class of such spin graphs of radius  $\leq D$ . Potential is defined as some function  $\Phi : \mathbf{G}_D \rightarrow R$ . Hamiltonian  $H : \mathbf{G} \rightarrow R$  is

$$H((G, f)) = \sum \Phi(\gamma)$$

where the sum over all sub spin subgraphs of  $(G, f)$ . Partition function

$$Z_N = \sum_{(G, f) \in \mathbf{G}_N} \exp(-\beta H(G, f))$$

Gibbs measure on  $\mathbf{G}_{f, N}$

$$\mu_N(G, f) = Z_N^{-1} \exp(-\beta H(G, f))$$

There are many results-examples (by physicists and mathematicians) related to “quantum gravity”, see for example [17, 25] and references therein.

### 4 Trading network as Boltzmann mechanics of communicating vessels

Standard financial mathematics considers games of one or small number of players against the chance (random market). Recently, a new approach (called multi-agent models) appeared which considers the games of many players against each other. This theory is at the starting point and its models are mainly **mean-field** models.

In this section some **local** models are considered where there are many players and many financial or trading instruments. Our model develops simpler models of ([23, 24]). The model resembles communication and transportation networks - the main difference is that the nodes have special dynamical values (moving boundaries, or real prices). The clients have also their own subjective prices and their interaction (transaction) with the nodes depend on these prices. This model does not describe any real situation (and any other existing multi-agent model as well) but we hope that some features of this model will be useful for future more realistic models.

**Free one-phase Boltzmann dynamics** Consider the phase space  $\mathbf{S} = I \times I_0$ , where  $I \subset R$  is an infinite interval and  $I_0 = [-V_0, V_0]$ ,  $0 < V_0 < \infty$ . On  $\mathbf{S}$  at any time  $t \geq 0$  a random locally finite configuration  $\{(x_i(t), v_i(t))\}$  of particles is given with coordinates  $x_i \in I$  and velocities  $v_i \in I_0$ . Assume that this configuration at any time  $t$  has distribution  $P_t$  with one-particle correlation function  $f(x, v, t)$  defined so that for any subset  $A \subset \mathbf{S}$  of the phase space

$$E \#\{i : (x_i, v_i) \in A\} = \int_A f(x, v, t) dx dv$$

One can have in mind Poisson measure  $P_0$  at time  $t = 0$ . Any particle moves always with its initial velocity, independently of other particles. Also there is Poisson income flow of particles from exterior with rate  $\lambda(x, v, t)$ , that is during time interval  $[t, t + dt]$  the mean number of incoming particles to the cell  $[x, x + dx] \times [v, v + dv]$  of the phase space is  $\lambda(x, v, t) dx dv dt$ . Assume moreover that each particle can die (disappear) with exponential distribution having rate  $\mu(x, v, t)$ . This means that during time  $dt$   $\mu(x, v, t) dx dv dt$  particles leave the cell  $dx dv$ .

Remind that we assume boundedness of velocities, that is

$$f(x, v, t) = \lambda(x, v, t) = \mu(x, v, t) = 0, |v| \geq V_0$$

**Lemma 1** For any  $x \in I$  and  $t < \frac{d(x, \partial I)}{V_0}$ , where  $d(x, \partial I)$  is the distance of the point  $x$  from the boundary of  $I$ , the standard linear Boltzmann equation holds

$$\frac{\partial f}{\partial t} + v \frac{\partial f}{\partial x} = -\mu(x, v, t) f(x, v, t) + \lambda(x, v, t) \quad (1)$$

This is trivial for  $\mu = \lambda = 0$ . In fact, for small  $\delta > 0$  we have

$$f(x, v, t + \delta) = f(x - v\delta, v, t) \quad (2)$$

if  $x$  is not on the boundary of  $I$  and  $\delta$  is sufficiently small. Subtracting  $f(x, v, t)$  from both parts of this equality, dividing by  $\delta$  and taking the limit  $\delta \rightarrow 0$ , we have

$$\frac{\partial f}{\partial t} + v \frac{\partial f}{\partial x} = 0 \quad (3)$$

The unique solution of the Cauchy problem for (3) is

$$f(x, v, t) = f(x - vt, v, 0)$$

If there  $\lambda \neq 0, \mu = \mu(x, v) \neq 0$  then it is also easy to see that the equation (1) holds. Note that if  $\lambda = 0$  and  $\mu$  does not depend on  $t$ , there is also explicit solution, see section XI.12 in [27]

$$f(x, v, t) = f(x - vt, v, 0) \exp\left(\int_0^t \mu(x - vs, v) ds\right)$$

**Two phases — particle dynamics** We shall define two types of dynamics — particle dynamics and continuum media dynamics.

In the particle dynamics ( $\pm$ )-phases consist of ( $\pm$ )-particles so that each ( $-$ )-particle is to the left of any ( $+$ )-particle. Denote  $b(t) \in R$  (boundary between phases) the coordinate of the leftmost ( $+$ )-particle. Then for  $x \geq b(t)$  there is ( $+$ )-phase and for  $x < b(t)$  there is ( $-$ )-phase. Particles move, as above, with their own velocities until a ( $-$ )-minus particle reaches the point  $b(t)$ , then it disappears together with the ( $+$ )-particle at  $b(t)$  and the point  $b(t)$  jumps to the coordinate of the new leftmost ( $+$ )-particle. After this, the process proceeds similarly.

Random configurations of particles are defined by the correlation functions  $f_{\pm}(x, v, t)$  correspondingly. Assume that also the functions  $\lambda_{\pm}(r, t), \mu_{\pm}(r, t), r \geq 0$ , are defined, smooth on  $R_+$  and zero if  $r \geq R_0$  for some  $0 < R_0 < \infty$ .

The dynamics of one point correlation functions  $f_{\pm}(x, v, t)$  for  $x \neq b(t)$ , that is on  $(b(t), \infty)$  and  $(-\infty, b(t))$  correspondingly, is given by the equations (already non-linear as  $b(t)$  is unknown)

$$\frac{\partial f_{\pm}}{\partial t} + v \frac{\partial f_{\pm}}{\partial x} = -\mu_{\pm}(x - b(t), v, t) f_{\pm}(x, v, t) + \lambda_{\pm}(x - b(t), v, t) \quad (4)$$

This means that we assume that arrivals and departures depend only on the distance  $r = |x - b(t)|$ .

Thus two phases add reactions between particles of different phases. The following interpretation is useful. We consider one instrument (**stocks, futures, houses or other real estate** etc.). There are two types of traders - (+)-particles correspond to **sellers** and (-)-particles to **buyers**,  $x_i$  are subjective prices comfortable for the trader  $i$ . Collision between particles corresponds to transaction, after this both leave the market. In more general cases it will be possible that they do not leave the market (see below).

We consider here a particular case when for some constant velocities  $v_{\pm}$  and for any  $t$

$$f_{\pm}(x, v, t) = \rho_{\pm}(x, t) \delta(v - v_{\pm})$$

For this to hold at any time  $t$  it is sufficient to demand that this holds for  $t = 0$ . *Initial conditions* are defined by the initial densities  $\rho_{\pm}(r, 0)$ . The velocities  $v_{\pm}$  can be interpreted as averaged velocities for sellers and buyers correspondingly.

**Two phases — fluid dynamics** It can occur that under some scaling the defined particle dynamics tends to some kind of **continuous (fluid) picture**, see [23], but we shall not pursue this way here. Instead, we consider continuous densities of (+)-masses and (-)-masses and shall define their dynamics directly. We assume that at each time  $t$  there exists point  $b(t)$  - boundary between phases. There are two phases with initial densities  $\rho_{+}(r, 0), \rho_{-}(r, 0)$  where

$$r = r(t) = |x - b(t)| = \pm(x - b(t))$$

correspondingly. Phases move with velocities  $v_{\pm}$  correspondingly. Collision of plus and minus masses (at the point  $b(t)$ ) leads to their cancellation in equal amount. There is more realistic possibility - to make the cancellation proportional to the current price, but we do not consider this possibility here.

We obtain equations for the triple  $(b(t), \rho_{+}(r, t), \rho_{-}(r, t))$  similarly to the way how the equations of continuum mechanics are derived in the textbooks, that is using conservation laws. Here there is only one - mass conservation law.

First of all, obtain the equation for the boundary. Assume  $b(t)$  smooth and put  $\beta = \frac{db(t)}{dt}$ . Then for time  $dt$  the amount of positive mass, reaching the boundary will be

$$\begin{aligned} M_{+}(\beta, t)dt &= \int_{v-\beta < 0} \int_{r < (-v+\beta)dt} f_{+}(r, v, t)dv + o(dt) = \\ &dt \int_{v-\beta < 0} f_{+}(0, v, t)(-v + \beta)dv + o(dt) \end{aligned}$$

In fact, income and outcome give the contribution  $o(dt)$ . Similarly for negative mass

$$\begin{aligned} M_{-}(\beta, t)dt &= \int_{v-\beta > 0} \int_{r < (v-\beta)dt} f_{-}(r, v, t)dv + o(dt) = \\ &dt \int_{v-\beta > 0} f_{-}(0, v, t)(v - \beta)dv + o(dt) \end{aligned}$$

**Lemma 2** For any  $t$  there exists unique  $\beta = \beta(t)$  such that

$$M_{+}(\beta, t) = M_{-}(\beta, t) \tag{5}$$

In fact, consider the equation with respect to  $\beta$

$$\int_{v-\beta < 0} f_+(0, v, t)(-v + \beta) dv = \int_{v-\beta > 0} f_-(0, v, t)(v - \beta) dv$$

Then if  $\beta$  increases, then the right-hand side increases and the left-hand side decreases.

We can rewrite the equation (5) in our case

$$\rho_+(0, t)(-v_+ + \beta(t)) = \rho_-(0, t)(v_- - \beta(t)) \quad (6)$$

from where we can get  $\beta(t)$

$$\beta(t) = \frac{\rho_+(0, t)v_+ + \rho_-(0, t)v_-}{\rho_+(0, t) + \rho_-(0, t)} \quad (7)$$

Now we should write the equations for the densities. For  $\rho_+(r, t)$  we get

$$\begin{aligned} \rho_+(r, t + \Delta t) &= \rho_+(r - (v_+ - \beta(t))\Delta t, t) - \mu_+(r, t)\rho_+(r, t)\Delta t + \lambda_+(r, t)\Delta t + o(\Delta t) = \\ &= \rho_+(r, t) - (v_+ - \beta(t))\frac{\partial \rho_+(r, t)}{\partial r}\Delta t - \mu_+(r, t)\rho_+(r, t)\Delta t + \lambda_+(r, t)\Delta t + o(\Delta t) \end{aligned}$$

In the limit  $\Delta t \rightarrow 0$

$$\frac{\partial \rho_+(r, t)}{\partial t} = -(v_+ - \beta(t))\frac{\partial \rho_+(r, t)}{\partial r} - \mu_+(r, t)\rho_+(r, t) + \lambda_+(r, t) \quad (8)$$

Similarly  $\rho_-(r, t)$ :

$$\begin{aligned} \rho_-(r, t + \Delta t) &= \rho_-(r + (v_- - \beta(t))\Delta t, t) - \mu_-(r, t)\rho_-(r, t)\Delta t + \lambda_-(r, t)\Delta t + o(\Delta t) \\ \frac{\partial \rho_-(r, t)}{\partial t} &= (v_- - \beta(t))\frac{\partial \rho_-(r, t)}{\partial r} - \mu_-(r, t)\rho_-(r, t) + \lambda_-(r, t) \end{aligned} \quad (9)$$

It would be nice to prove accurately that the solution of equations (6,8,9) exists for any  $t \geq 0$  and is unique, but we did not try to do this.

**Fixed points and stationary points** Assume that the functions  $\lambda_{\pm}(r) = \lambda_{\pm}(r, t)$  and  $\mu_{\pm}(r) = \mu_{\pm}(r, t)$  do not depend on  $t$  (remind that they were assumed to have compact support). Denote

$$\begin{aligned} \gamma_{cr}^{(+)} &= -v_+^{-1} \int_0^{\infty} \lambda_+(x) \exp\left(\frac{1}{v_+} \int_0^x \mu_+(y) dy\right) dx, \quad \gamma_{cr}^{(-)} = \\ &= v_-^{-1} \int_0^{\infty} \lambda_-(x) \exp\left(-\frac{1}{v_-} \int_0^x \mu_-(y) dy\right) dx \end{aligned}$$

and

$$\gamma_{cr} = \max\left(\gamma_{cr}^{(+)}, \frac{v_- \gamma_{cr}^{(-)}}{-v_+}\right)$$

We define the fixed point of our dynamics by the conditions:  $\beta(t) = 0$  and  $\rho_{\pm}(r, t)$  do not depend on time. Alternatively the fixed points are defined as any solutions of the stationary version

$$\rho_+(0)v_+ + \rho_-(0)v_- = 0 \quad (10)$$

$$-v_+ \frac{\partial \rho_+(r)}{\partial r} - \mu_+(r) \rho_+(r) + \lambda_+(r) = 0 \quad (11)$$

$$v_- \frac{\partial \rho_-(r)}{\partial r} - \mu_-(r) \rho_-(r) + \lambda_-(r) = 0 \quad (12)$$

of the system (6,8,9). We will prove that there exists a family of fixed points depending on a real parameter.

Similarly, we call stationary point any solution of the system of equations (6,8,9), where  $\beta = \beta(t)$  and the densities do not depend on  $t$ . We shall prove that there is a family of stationary points depending on two real parameters.

We say that a fixed (or stationary) point has finite mass if

$$\int_0^\infty \rho_\pm(r) dr < \infty$$

**Theorem 3** *Let the parameters  $\lambda_\pm(r), \mu_\pm(r)$  and  $v_\pm$  be fixed. Then*

1. *For any value of the parameter  $\gamma_+ = \rho_+(0)$  there is at most one fixed point. For  $\gamma_+ < \gamma_{cr}$  there is no any fixed point. For  $\gamma_+ \geq \gamma_{cr}$  there exists exactly one fixed point defined by*

$$\rho_+(r) = e^{-\frac{1}{v_+} \int_0^r \mu_+(x) dx} \left( \rho_+(0) + v_+^{-1} \int_0^r \lambda_+(x) e^{\frac{1}{v_+} \int_0^x \mu_+(y) dy} dx \right) \quad (13)$$

$$\rho_-(r) = v_-^{-1} e^{\frac{1}{v_-} \int_0^r \mu_-(x) dx} \left( -v_+ \rho_+(0) - \int_0^r \lambda_-(x) e^{-\frac{1}{v_-} \int_0^x \mu_-(y) dy} dx \right) \quad (14)$$

2. *The fixed point has finite mass if  $\gamma_{cr}^{(+)} = \gamma_{cr}^{(-)}$*
3. *For any  $\gamma_+, \gamma_-$  such that*

$$\gamma_+ = \rho_+(0) \geq \gamma_{cr}^{(+)}, \quad \gamma_- = \rho_-(0) \geq \gamma_{cr}^{(-)}$$

*there is exactly one fixed point. Then the densities are defined by formulas (13,14) and the boundary velocity is*

$$\beta = \frac{\rho_+(0)v_+ + \rho_-(0)v_-}{\rho_+(0) + \rho_-(0)}$$

4. *Stationary point has finite mass iff  $\gamma_+ = \gamma_{cr}^{(+)}, \gamma_- = \gamma_{cr}^{(-)}$ .*

**Proof.** Solving equations (8,9) we get for any  $r > 0$  equations (13) and (14). Note that, by equations (14) and (13), densities  $\rho_-(r), \rho_+(r)$  are positive iff  $\gamma_+ \geq \gamma_{cr}^{(+)}, \gamma_- \geq \gamma_{cr}^{(-)}$ . Taking into account equation (10) we get the first assertion of the theorem.

For the stationary points the densities are again defined by equations (13) and (14). We have two conditions for them to be non-negative. Then the boundary will move with constant velocity defined from equation (7).

**More complicated one market model** Note that collision of masses of two phases create total annihilation flow

$$v(t) = (v_- - \beta(t))\rho_-(0,t) = -(v_+ - \beta(t))\rho_+(0,t)$$

of the disappearing ( $\pm$ )-particles. Here we assume that a part of annihilating particles does not disappear but can transform to particles of the other phase jumping from the collision point 0 to some point  $r$ . On the language of continuous media this means that there are output flows of mass  $v(+, -, r, t)$  and  $v(-, +, r, t)$  such that

$$\int_0^\infty p(+, -, r, t)dr \leq 1, \int_0^\infty p(-, +, r, t)dr \leq 1$$

where

$$p(+, -, r, t) = \frac{v(+, -, r, t)}{v(t)}, p(-, +, r, t) = \frac{v(-, +, r, t)}{v(t)}$$

For such model we have the system of three equations

$$\begin{aligned} \beta(t) &= \frac{v_- \rho_-(0,t) + v_+ \rho_+(0,t)}{\rho_-(0,t) + \rho_+(0,t)} \\ \frac{\partial \rho_+(r,t)}{\partial t} &= -(v_+ - \beta(t)) \frac{\partial \rho_+(r,t)}{\partial r} - \mu_+(r,t) \rho_+(r,t) + \lambda_+(r,t) + \\ &\quad + (v_- - \beta(t)) \rho_-(0,t) p(-, +, r, t) \\ \frac{\partial \rho_-(r,t)}{\partial t} &= (v_- - \beta(t)) \frac{\partial \rho_-(r,t)}{\partial r} - \mu_-(r,t) \rho_-(r,t) + \lambda_-(r,t) - \\ &\quad - (v_+ - \beta(t)) \rho_+(0,t) p(+, -, r, t) \end{aligned} \quad (15)$$

We again assume that the functions  $\mu_\pm(r,t), \lambda_\pm(r,t), p(-, +, r, t), p(+, -, r, t)$  do not depend on  $t$  and have compact support. Introduce the functions

$$F_+(x) = -\frac{1}{v_+} \int_0^x \mu_+(y)dy, F_-(x) = \frac{1}{v_-} \int_0^x \mu_-(y)dy$$

Denote

$$\alpha_{-+} = \int_0^\infty p(-, +, x) \exp(-F_+(x)) dx, \alpha_{+-} = \int_0^\infty p(+, -, x) \exp(-F_-(x)) dx$$

and assume that  $\alpha_{-+}, \alpha_{+-} < 1$ . Define

$$\hat{\gamma}_{cr} = \max \left( \frac{\gamma_{cr}^{(+)}}{1 - \alpha_{-+}}, \frac{v_- \gamma_{cr}^{(-)}}{-v_+(1 - \alpha_{+-})} \right)$$

**Theorem 4** Let the parameters  $\lambda_\pm(r), \mu_\pm(r), p(-, +, r, t), p(+, -, r, t)$  and  $v_\pm$  be given. Then

1. For any value of the parameter  $\gamma_+ = \rho_+(0)$  there is at most one fixed point. For  $\gamma_+ < \hat{\gamma}_{cr}$  there is no any fixed point. For  $\gamma_+ \geq \hat{\gamma}_{cr}$  there exists exactly one fixed point. It is

$$\begin{aligned} \rho_+(r) &= e^{F_+(r)} \left( \rho_+(0) + v_+^{-1} \int_0^r (\lambda_+(x) - v_+ \rho_+(0)) p(-, +, x) e^{-F_+(x)} dx \right) \\ \rho_-(r) &= v_-^{-1} e^{F_-(r)} \left( -v_+ \rho_+(0) - \int_0^r (\lambda_-(x) - v_+ \rho_+(0)) p(+, -, x) e^{-F_-(x)} dx \right) \end{aligned}$$

2. *There is a unique stationary point with finite mass. It is*

$$\rho_+(r) = e^{F_+(r)} \left( \rho_+(0) + v_+^{-1} \int_0^r (\lambda_+(x) + (v_- - \beta)\rho_-(0)p(-, +, x)) e^{-F_+(x)} dx \right)$$

$$\rho_-(r) = e^{F_-(r)} \left( \rho_-(0) - v_-^{-1} \int_0^r (\lambda_-(x) - (v_+ - \beta)\rho_+(0)p(+, -, x)) e^{-F_-(x)} dx \right)$$

and we denote

$$\rho_+(0) = \frac{-v_+ \gamma_{cr}^{(+)}}{-v_+(1 - \alpha_{-+}) - \beta \alpha_{-+}}$$

$$\rho_-(0) = \frac{v_- \gamma_{cr}^{(-)}}{v_-(1 - \alpha_{+-}) + \beta \alpha_{+-}}$$

where  $\beta$  is a root (belonging to the interval  $(v_+, v_-)$ ) of quadratic equation (23). It exists and is unique.

*Proof.* 1. Similarly to the first part of theorem 3.

2. As follows from system (15) the equations for the stationary points are

$$\begin{aligned} 0 &= (v_- - \beta)\rho_-(0) + (v_+ - \beta)\rho_+(0) \\ 0 &= -v_+ \frac{\partial \rho_+(r)}{\partial r} - \mu_+(r)\rho_+(r) + \lambda_+(r) + (v_- - \beta)\rho_-(0)p(-, +, r) \\ 0 &= v_- \frac{\partial \rho_-(r)}{\partial r} - \mu_-(r)\rho_-(r) + \lambda_-(r) - (v_+ - \beta)\rho_+(0)p(+, -, r) \end{aligned} \quad (16)$$

Solving these linear first order equations we get

$$\rho_+(r) = e^{F_+(r)} \left( \rho_+(0) + v_+^{-1} \int_0^r (\lambda_+(x) + (v_- - \beta)\rho_-(0)p(-, +, x)) e^{-F_+(x)} dx \right) \quad (17)$$

$$\rho_-(r) = e^{F_-(r)} \left( \rho_-(0) - v_-^{-1} \int_0^r (\lambda_-(x) - (v_+ - \beta)\rho_+(0)p(+, -, x)) e^{-F_-(x)} dx \right) \quad (18)$$

We are looking for a stationary point with finite mass such that

$$\int_0^\infty \rho_\pm(r) dr < \infty \quad (19)$$

Then by (17), (18), (19), (16), a stationary point is uniquely defined by three parameters  $\gamma_\pm = \rho_\pm(0)$ ,  $\beta$  which satisfy the following equations

$$\begin{aligned} -v_+ \gamma_+ &= -v_+ \gamma_{cr}^{(+)} + (v_- - \beta)\gamma_- \alpha_{-+} \\ v_- \gamma_- &= v_- \gamma_{cr}^{(-)} - (v_+ - \beta)\gamma_+ \alpha_{+-} \\ (v_- - \beta)\gamma_- &= -(v_+ - \beta)\gamma_+ \end{aligned} \quad (20)$$

where  $\beta \in (v_+, v_-)$ . We show that this system has a unique solution. Using the third equation of the system, we get from the first two

$$\gamma_+ = \frac{-v_+ \gamma_{cr}^{(+)}}{-v_+(1 - \alpha_{-+}) - \beta \alpha_{-+}} \quad (21)$$

$$\gamma_- = \frac{v_- \gamma_{cr}^{(-)}}{v_- (1 - \alpha_{+-}) + \beta \alpha_{+-}} \quad (22)$$

Substituting these expressions to the third one we come to the quadratic equation with respect to  $\beta$ :

$$(\sigma_+ \alpha_{+-} - \sigma_- \alpha_{-+})(-v_+ + \beta)(v_- - \beta) + (\sigma_- v_+ - \sigma_+ v_-) \beta - v_+ v_- (\sigma_- - \sigma_+) = 0 \quad (23)$$

where, for shortness, we denote  $\sigma_+ = -v_+ \gamma_{cr}^{(+)}$ ,  $\sigma_- = v_- \gamma_{cr}^{(-)}$ .

Consider first the case when  $\sigma_+ \alpha_{+-} - \sigma_- \alpha_{-+} \neq 0$ . Note that the boundary velocity should satisfy  $v_+ < \beta < v_-$ . One can show easily that there is always one root of the equation in the interval  $v_+ < \beta < v_-$ . Now one should verify that  $\gamma_+, \gamma_-$ , defined by (21) and (22) are non-negative. By (21) (22) one of the values  $\gamma_+, \gamma_-$  is always positive. Then by the third equation of the system (20) also the other value is positive as  $v_- - \beta, -v_+ + \beta > 0$ . Thus there exists the unique fixed point satisfying (17), (22), (21) (22).

Is  $\sigma_+ \alpha_{+-} - \sigma_- \alpha_{-+} = 0$ , we have a linear equation with respect to  $\beta$ , we gives

$$\beta = \frac{\sigma_- - \sigma_+}{\sigma_- v_-^{-1} - \sigma_+ v_+^{-1}}$$

and from (21) (22) we get  $\gamma_+ = \sigma_+ v_+^{-1}$  and  $\gamma_- = \sigma_- v_-^{-1}$ . In this case also a stationary point exists and is unique.

**Networks with many markets** Let us call the previous model an elementary market. A network is a set  $V$  of elementary markets with similar parameters and variables indexed by  $m \in V$

$$v_{\pm,m}, \lambda_{\pm,m}(r,t), \mu_{\pm,m}(r,t), \rho_{\pm,m}(r,t), b_m(t), \beta_m(t)$$

There are also other parameters interconnecting the markets. Denote  $v_{+,m}(t)$  ( $v_{-,m}(t)$ ) the total annihilation flow of ( $\pm$ )-particles from the market  $m$ . As they are equal we denote  $v_m(t) = v_{+,m}(t) = v_{-,m}(t)$ . Let

$$v_{k,m}(+,+,r,t), v_{k,m}(+,-,r,t), v_{k,m}(-,+,r,t), v_{k,m}(-,+,r,t)$$

be the parts of these annihilation flows of ( $\pm$ )-particles, that after the transaction on the market  $m$ , become ( $\mp$ )-particles on the market  $k$  with the coordinate  $r$ . Denote

$$p_{km}(\pm, \pm, r, t) = \frac{v_{k,m}(\pm, \pm, r, t)}{v_m(t)}$$

We mean that  $p_{km}(+,+,r,t) = p_{km}(-,-,r,t) \equiv 0$ . Then for any  $k$  and  $t$  the conditions

$$\sum_{m \in V} \int_0^\infty p_{km}(+,-,r,t) dr \leq 1, \quad \sum_{m \in V} \int_0^\infty (p_{km}(-,+,r,t) dr \leq 1$$

should hold. Denote by  $|V|$  the cardinality of the set  $V$ . We have then the following system of  $3|V|$  equations:

$$\begin{aligned}\beta_m(t) &= \frac{v_{-,m}\rho_{-,m}(0,t) + v_{+,m}\rho_{+,m}(0,t)}{\rho_{+,m}(0,t) + \rho_{-,m}(0,t)} \\ \frac{\partial \rho_{+,m}(r,t)}{\partial t} &= -(v_{+,m} - \beta_m(t)) \frac{\partial \rho_{+,m}(r,t)}{\partial r} - \mu_{+,m}(r,t)\rho_{+,m}(r,t) + \lambda_{+,m}(r,t) \\ &\quad + \sum_{k \in V} (v_{-,k} - \beta_k(t))\rho_{-,k}(0,t)p_{km}(-,+,r,t) \\ \frac{\partial \rho_{-,m}(r,t)}{\partial t} &= (v_{-,m} - \beta_m(t)) \frac{\partial \rho_{-,m}(r,t)}{\partial r} - \mu_{-,m}(r,t)\rho_{-,m}(r,t) + \lambda_{-,m}(r,t) \\ &\quad - \sum_{k \in V} (v_{+,k} - \beta_k(t))\rho_{+,k}(0,t)p_{km}(+,-,r,t)\end{aligned}$$

**Fixed points** Again we assume  $\lambda_{\pm,m}(r,t), \mu_{\pm,m}(r,t), p_{km}(\pm, \pm, r, t)$  do not depend on  $t$  and have a compact support. Put

$$\begin{aligned}F_+^{(m)}(x) &= -v_{+,m}^{-1} \int_0^x \mu_{+,m}(y) dy, \quad F_-^{(m)}(x) = v_{-,m}^{-1} \int_0^x \mu_{-,m}(y) dy \\ \hat{\lambda}_{+,m} &= \int_0^\infty \lambda_{+,m}(x) e^{-F_+^{(m)}(x)} dx, \quad \hat{\lambda}_{-,m} = \int_0^\infty \lambda_{-,m}(x) e^{-F_-^{(m)}(x)} dx \\ \alpha_{km}(-,+) &= \int_0^\infty p_{km}(-,+,x) e^{-F_+^{(m)}(x)} dx, \quad \alpha_{km}(+,-) = \int_0^\infty p_{km}(+,-,x) e^{-F_-^{(m)}(x)} dx\end{aligned}\tag{24}$$

for  $k, m \in V$ .

Define matrices  $A_{-+}, A_{+-}$  with elements  $\alpha_{km}(-,+) \alpha_{km}(+,-)$ , where  $k, m \in V$ , and assume, that they have the following property:

$$\forall k \sum_{m \in V} \alpha_{km}(\pm, \pm) \leq 1, \quad \exists k_0 \sum_{m \in V} \alpha_{km}(\pm, \pm) < 1\tag{25}$$

For two vectors  $a = (a_i)$  and  $b = (b_i)$  we shall write  $a \geq b$  ( $a > b$ ) if  $a_i \geq b_i$  ( $a_i > b_i$ ) for all coordinates. Consider the following system of inequalities with respect  $\bar{s}$

$$\bar{s}(E - A_{-+}) \geq \bar{\lambda}_+, \quad \bar{s}(E - A_{+-}) \geq \bar{\lambda}_-\tag{26}$$

where  $E$  is the identity matrix and  $\bar{\lambda}_\pm$  are vectors with coordinates  $\hat{\lambda}_{\pm,m}$  defined by (24). We say that this system has a positive solution if there is vector  $\bar{s}$  with positive coordinates satisfying both inequalities in (26). Generally, this system may not have a positive solution. If one of the matrices  $A_{-+}, A_{+-}$  is diagonal or zero the set of positive solutions is nonempty.

**Theorem 5** Each solution  $\bar{s} = (s_m, m \in V) > 0$  of the system (26) uniquely defines the fixed point as follows:

$$\begin{aligned}\rho_{+,m}(r) &= -v_{+,m}^{-1} e^{F_+^{(m)}(r)} \left( s_m - \int_0^r \left( \lambda_{+,m}(x) + \sum_{k \in V} s_k p_{km}(-,+,x) \right) e^{-F_+^{(m)}(x)} dx \right) \\ \rho_{-,m}(r) &= v_{-,m}^{-1} e^{F_-^{(m)}(r)} \left( s_m - \int_0^r \left( \lambda_{-,m}(x) + \sum_{k \in V} s_k p_{km}(+,-,x) \right) e^{-F_-^{(m)}(x)} dx \right)\end{aligned}$$

If the set of positive solutions of system (26) is empty there is no any fixed point.

Proof. The fixed points satisfy the system consisting of  $3|V|$  equation:

$$\begin{aligned} 0 &= v_{-,m}\rho_{-,m}(0,t) + v_{+,m}\rho_{+,m}(0,t) \\ 0 &= -v_{+,m}\frac{\partial\rho_{+,m}(r)}{\partial r} - \mu_{+,m}(r)\rho_{+,m}(r) + \lambda_{+,m}(r) + \sum_{k\in V} v_{-,k}\rho_{-,k}(0)p_{km}(-,+,r) \quad (27) \\ 0 &= v_{-,m}\frac{\partial\rho_{-,m}(r)}{\partial r} - \mu_{-,m}(r)\rho_{-,m}(r) + \lambda_{-,m}(r) - \sum_{k\in V} v_{+,k}\rho_{+,k}(0)p_{km}(+,-,r) \end{aligned}$$

Solving first order linear differential equations we get

$$\rho_{+,m}(r) = e^{F_+^{(m)}(r)} \left( \rho_{+,m}(0) + v_{+,m}^{-1} \int_0^r (\lambda_{+,m}(x) + \sum_{k\in V} v_{-,k}\rho_{-,k}(0)p_{km}(-,+,x)) e^{-F_+^{(m)}(x)} dx \right) \quad (28)$$

$$\rho_{-,m}(r) = e^{F_-^{(m)}(r)} \left( \rho_{-,m}(0) - v_{-,m}^{-1} \int_0^r (\lambda_{-,m}(x) - \sum_{k\in V} v_{+,k}\rho_{+,k}(0)p_{km}(+,-,x)) e^{-F_-^{(m)}(x)} dx \right) \quad (29)$$

for  $m \in V$ .

Using equations  $0 = v_{-,m}\rho_{-,m}(0) + v_{+,m}\rho_{+,m}(0)$ , we conclude that solutions (28), (29) are uniquely defined by parameters  $s_m = -v_{+,m}\rho_{+,m}(0)$ ,  $m \in V$ , and one can write

$$\rho_{+,m}(r) = -v_{+,m}^{-1} e^{F_+^{(m)}(r)} \left( s_m - \int_0^r \left( \lambda_{+,m}(x) + \sum_{k\in V} s_k p_{km}(-,+,x) \right) e^{-F_+^{(m)}(x)} dx \right) \quad (30)$$

$$\rho_{-,m}(r) = v_{-,m}^{-1} e^{F_-^{(m)}(r)} \left( s_m - \int_0^r \left( \lambda_{-,m}(x) + \sum_{k\in V} s_k p_{km}(+,-,x) \right) e^{-F_-^{(m)}(x)} dx \right) \quad (31)$$

Whereas the densities (30), (31) are nonnegative for all  $r \geq 0$  the following conditions must be satisfied

$$s_m \geq \hat{\lambda}_{+,m} + \sum_{k\in V} s_k \alpha_{km}(-,+) \quad (32)$$

$$s_m \geq \hat{\lambda}_{-,m} + \sum_{k\in V} s_k \alpha_{km}(+,-) \quad (33)$$

for all  $m \in V$ . These inequalities are equivalent to system (26).

So the fixed points exist iff there exist positive solutions of system (26).

## References

- [1] A. Rosenfeld. Picture Languages. Acad. Press. 1979.
- [2] A. Habel. Hyperedge Replacement: Grammars and Languages. Lecture Notes in Computer Science, v. 643, 1992. Springer Verlag.
- [3] E.M.Palmer. Graphical Evolution. Wiley. 1985.
- [4] V.A.Malyshev. Interacting Strings of Symbols. Russian Math. Surveys, 1997, v.52, No. 2, 59-86.
- [5] V.A.Malyshev. Random Grammars. Russian Math. Reviews, 1998, No. 2, pp.
- [6] B. Bollobas. Random Graphs.1985. Academic Press.
- [7] P. Erdos, A. Renyi. On the evolution of random graphs. Bull. Inst. Int. Statist. Tokyo, 1961, v. 38,343-347.
- [8] M. Karonski. Random Graphs. In Handbook of Combinatorics, vol. 1 (Eds. R. Graham,M. Grotchel, L. Lovasz). 1995, Elsevier.

- [9] Th. Liggett. *Interacting Particle Systems*. 1985. Springer.
- [10] V. A. Malyshev, R. A. Minlos. *Gibbs random fields*. 1991. Kluwer.
- [11] V. Malyshev, A. Yakovlev. Condensation in Large Closed Jackson Networks. *Annals of Applied Probability*, 1996, v.6, No. 1, pp. 92-115.
- [12] A. Zamyatin, V. Malyshev. Introduction to stochastic models of transportation flows. In the book “Introduction to mathematical modelling of transportation flows”, 2010, Moscow, pp. 247-287.
- [13] V. Malyshev. Networks and dynamical systems *Adv. Appl. Prob.*, 1993, v. 25, 140-175.
- [14] V. Malyshev. Microscopic Models of Chemical Thermodynamics, 2005, *J. Stat., Physics*, 119, No. 5/6, pp. 997-1026.
- [15] V. Malyshev, A. Manita, A. Zamyatin. Homeostasis phenomena in chemical reaction networks. *Probability theory and applications*, 2006, v. 51, pp. 793-802.
- [16] V. Malyshev. Macrodimension is an invariant of local dynamics. *Probability theory and applications*, 2000, 45, No.2, 368-374.
- [17] V. Malyshev. Gibbs and quantum discrete spaces. *Russian Math. Surveys*, 2001, v. 56, No. 5, pp. 117-172.
- [18] S. Janson, T. Luczak, A. Ruchinski. *Random Graphs*. 2000. Wiley.
- [19] V. Kolchin. *Random Graphs*. 2004. Moscow.
- [20] R. Pasto-Sattoras, M. Rubi, A. Diaz-Guilera (Eds.) *Statistical Mechanics of Complex Networks*. Lecture Notes in Physics. 2003, Springer.
- [21] V. Malyshev. Random graphs and Graph Grammars. *Discrete Mathematics and its applications*, 1998, v. 8. No. 3, 247-262.
- [22] V. Malyshev. Random Infinite Spin Graph Evolution. In “On Dobrushin’s way. From Probability Theory to Statistical Physics AMS Publications, v. 198, 2000, pp. 157-167.
- [23] V. A. Malyshev, A.D. Manita. Dynamics of phase boundary with particle annihilation. *Markov Processes and Related Fields*, 2009, v. 15, No. 4, 575-584.
- [24] V. A. Malyshev, A.D. Manita, A. A. Zamyatin. Explicit asymptotic velocity of the boundary between particles and antiparticles. *ISRN Mathematical Physics*, 2012.
- [25] V. Malyshev. Combinatorics and probability of maps In “Asymptotic Combinatorics with Applications to Mathematical Physics”, Kluwer, 2002, pp. 71-95.
- [26] V. Malyshev. Quantum Evolution of Words. *Theoretical Computer Science*, 2002, v. 273, pp. 263-269.
- [27] M. Reed, B. Simon. *Methods of Mathematical Physics*, v. 3, 1979. Academic Press.

# Spatial-Temporal Patterns Arising in Active Media in the Vicinity of the Wave Bifurcation

A.A. Polezhaev and M.Yu. Borina

*P.N. Lebedev Physical Institute of the Russian Academy of Sciences  
Leninskiy prospekt, 53, 119991, Moscow, Russia  
e-mail address: apol@lpi.ru*

## Abstract

Diffusion instability is a reason for different spatial-temporal patterns observed in physical, chemical and biological systems. Two types of diffusion instability are known: Turing and wave ones. While Turing instability is responsible for stationary nonuniform patterns, wave instability gives rise to a great variety of spatial-temporal regimes. Here we discuss patterns which may arise in the vicinity of the wave bifurcation. Investigation of a set of amplitude equations, describing interaction of several modes which became unstable due to the wave bifurcation, is carried out. It is shown that as a result of competition between modes, depending on the value of the parameter defining the strength of interaction, only two regimes are possible: either quasi one-dimensional travelling waves (there exists only one nonzero mode) or standing waves (all the modes are nonzero). This result is supported by numerical experiments for the Gierer-Meinhardt model modified by addition of one more equation for the second fast diffusing inhibitor. We suggest a possible mechanism for the transition from standing waves with a wavelength  $\lambda_{SW}$  to traveling waves with a half wavelength:  $\lambda_{TW} \cong \lambda_{SW}/2$ . This phenomenon was observed in the Belousov-Zhabotinsky reaction dispersed in a water-in-oil aerosol OT/Span-20 microemulsion. The problem is solved in a spatially one-dimensional case using amplitude equations approach. We demonstrate that a transition is possible under certain conditions. We obtain conditions for the mode coupling strength parameters, under which the scenario of transition from a standing wave to a half-period traveling wave, observed experimentally, is realized. The results of theoretical analysis are confirmed by numerical simulations.

## 1 Introduction

Spatial-temporal self-organization has long been the subject of both experimental and theoretical investigations [1–3]. So far not only autowaves and dissipative structures are discovered [4–7] but such new types of patterns as antispirals, wave packets, segmented waves, oscillons — localized oscillating spots and others. All this variety of patterns was observed in particular in Belousov-Zhabotinsky reaction proceeding in microemulsion (BZ–AOT system) [8]. Now it is common knowledge that diffusion can cause instability of the uniform state in a spatially distributed system. It was first demonstrated by Turing in his classical paper [9], published in 1952. Due to diffusion in a reacting system the uniform state may become unstable for the waves with wave vectors from a certain range. There are two possibilities: either for these wave vectors one of the real eigenvalues of the linearized problem becomes positive, or a pair of complex conjugate eigenvalues acquires a positive real part. The first case is well known as the Turing instability and it usually results in formation of

stationary non-uniform patterns. It was employed in numerous models of biological morphogenesis (for examples, see [10]). The second case is studied not so well though it can lead to a variety of patterns, which were discovered experimentally by Vanag et al. [8] in Belousov-Zhabotinsky microemulsion (BZ–AOT) system.

While the Turing bifurcation may occur already in a two variable reaction-diffusion model, the wave instability needs at least three equations. In the paper [11] we obtained the conditions for the wave instability in a three-variable reaction diffusion model, which follow from linear analysis, and formulated qualitative properties of the system for it to occur. Here we discuss patterns which may arise in the vicinity of the wave bifurcation. First we consider patterns which arise due to polymodal interaction right after the wave bifurcation and obtain the conditions for them to occur. Then we suggest the scenario of transition from standing waves to travelling waves with the half-wavelength observed in experiments [12].

## 2 Spatio-temporal patterns in a multidimensional active medium caused by polymodal interaction near the wave bifurcation

### 2.1 Analytical treatment

In the vicinity of the wave bifurcation, as a rule, only two types of structures are observed: traveling and standing waves. In this case, an effective method for studying such patterns is the construction and subsequent investigation of amplitude equations [13, 14]. However, the situation is complicated by the fact that in multidimensional space degeneracy in the directions takes place, and a lot of unstable modes (in the case of an unbounded domain — infinitely many) participate in pattern formation. In the bounded region only the modes which meet the boundary conditions contribute to the pattern. Then the amplitude equations for interacting unstable modes may be presented in the form:

$$\partial_t \tilde{A}_k = \tilde{A}_k - (1 - ic_1) \tilde{A}_k |\tilde{A}_k|^2 - h(1 - ic_2) \tilde{A}_k \cdot \sum_{j=1, j \neq k}^N |\tilde{A}_j|^2, \quad k \in \overline{1, N}. \quad (1)$$

Here  $\tilde{A}_j$  are complex amplitudes of modes corresponding to equal in length but different in direction wave vectors becoming unstable due to the wave bifurcation. If we present  $\tilde{A}_j$  in the form  $\tilde{A}_j = A_j e^{i\varphi_j}$ , where  $A_j = |\tilde{A}_j|$ , for real magnitudes of amplitudes  $A_j$  we obtain the following equations:

$$\partial_t A_i = A_i - A_i^3 - A_i \cdot h \sum_{j=1, j \neq i}^N A_j^2, \quad i \in \overline{1, N}. \quad (2)$$

It can be easily shown that Eqns. (2) have  $2^N$  stationary states of the form (with the account of subscripts permutation)

$$A_i^{st} = \begin{cases} \frac{1}{\sqrt{1 + (p-1)h}}, & i \in \overline{1, p}, \\ 0, & i \in \overline{p+1, N}, \end{cases} \quad (3)$$

where  $p$  is an integer from the segment  $\overline{0, N}$ .

To investigate stability of these states we linearize Eqns. (2) near each of the points:

$$\begin{cases} \delta\dot{A}_i = \frac{2}{1+(p-1)h} \left( -\delta A_i - h \sum_{j=1, j \neq i}^p \delta A_j \right), & i \in \overline{1, p}, \\ \delta\dot{A}_i = \frac{(1-h)}{1+(p-1)h} \delta A_i, & i \in \overline{p+1, N}. \end{cases} \quad (4)$$

Assuming small deviations from the stationary point  $\delta A_i$  and  $\delta A_j$  to be proportional to  $\exp\left(\frac{\lambda t}{1+(p-1)h}\right)$ , we substitute them into the set (4) and obtain the characteristic equation which after some manipulations is reduced to the form:

$$[\lambda + 2(1+(p-1)h)][\lambda - 2(h-1)]^{p-1} [\lambda - (1-h)]^{N-p} = 0.$$

Solution of this equation results in the following set of eigenvalues for the point specified by Eqn. (3):

$$\lambda_k = \begin{cases} -2(1+(p-1)h), & i = 1 \\ 2(h-1), & k \in \overline{2, p} \\ 1-h, & k \in \overline{p+1, N} \end{cases} \quad (5)$$

Analysis of these eigenvalues shows that of all the stationary states only few are stable, depending on the value of the single parameter  $h$ , which we consider positive. Namely, we arrive at the following

**Theorem.** *If  $h \in (1, \infty)$  then the system (1) has  $N$  stable stationary states such that only one of the amplitudes is nonzero and its magnitude equals unity, while all the others are zero. If  $h \in (0, 1)$  then all the amplitudes are nonzero and have the same magnitudes equal to  $1/\sqrt{1+(N-1)h}$ . All other stationary points are unstable for any  $h$ .*

Thus from this theorem it follows that depending on the strength of competition between the modes, determined by the parameter  $h$ , only two regimes are possible: if the competition is strong, wave bifurcation results in a quasi one-dimensional travelling wave, while for low competition all the modes survive and a complex standing wave arises. All intermediate regimes in the system (1) are impossible near the wave bifurcation.

## 2.2 Numerical simulations

This general result was numerically verified on the example of the Gierer-Meinhardt model [15] expanded by the third equation corresponding to another rapidly diffusing inhibitor. This was done due to the fact that in a two-variable model a wave bifurcation is impossible contrary to the Turing bifurcation [11]. The very choice of the model is quite arbitrary and is only determined by its possibility to demonstrate wave instability.

$$\begin{cases} \partial_t u = \left( \rho + \frac{u^2}{v} - \mu u - cu + dw \right) \Omega + D_1 \nabla^2 u, \\ \partial_t v = u^2 - v + D_2 \nabla^2 v, \\ \partial_t w = cu - dw + D_3 \nabla^2 w. \end{cases} \quad (6)$$

These equations have one stationary point:  $u_0 = \frac{\rho+1}{\mu}$ ,  $v_0 = \left(\frac{\rho+1}{\mu}\right)^2$ ,  $w_0 = \frac{c(\rho+1)}{d\mu}$ .

Linearizing Eqns. (6) near the stationary point and applying the conditions for the wave bifurcation formulated in [11] we determine the boundary of the wave instability in the parameter plane  $(\mu, \Omega)$  for all other parameters fixed (Fig. 1). Then we obtain amplitude equations near this boundary and thus establish the relation between the kinetic parameters of

the model (6) and the parameter  $h$  responsible for the strength of competition between the modes. Thus we determine the domains of existence for both travelling and standing waves in the parameter plain  $\mu, \Omega$  shown in Fig. 1.

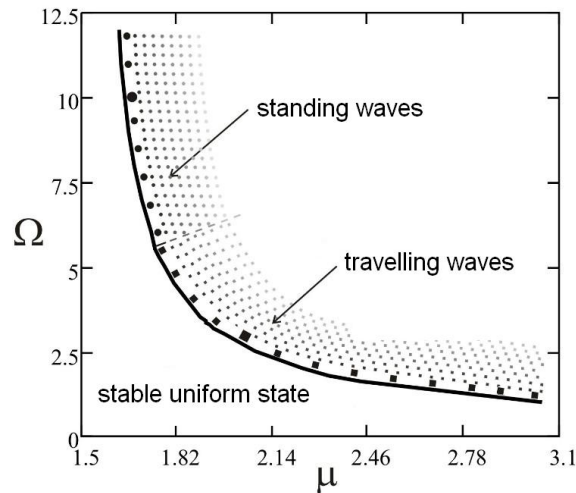


**Figure 1:** The parameter plane  $(\mu, \Omega)$  of the model (6). Solid line corresponds to the wave bifurcation. The domains corresponding to standing and travelling waves are shown. In the same figure the results of numerical simulations are presented where circles and squares are for standing and travelling waves correspondingly. Larger symbols represent the combinations of parameters for the examples given below.

Numerical simulations presented in Figs. 2 and 3 for the parameters of the model (5) corresponding to  $h > 1$  ( $h < 1$ ) demonstrate travelling waves formation (standing waves respectively), as is predicted by the above analysis. The corresponding parameters are designated by larger symbols in Fig. 1.

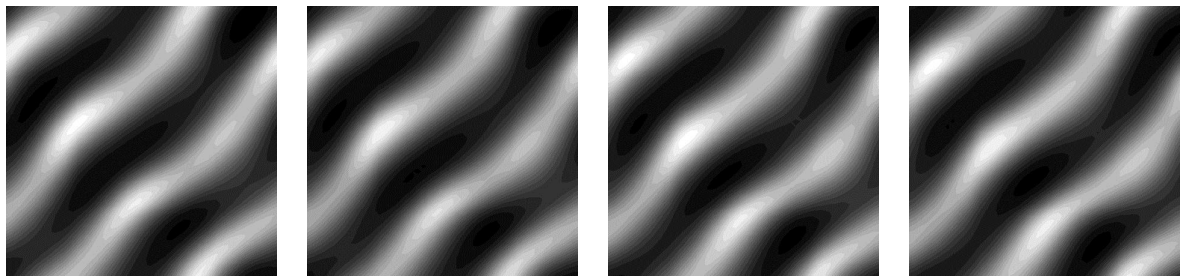


**Figure 2:** Travelling waves in the model (6) for the following moments of time:  $t = t_0$ ,  $t = t_0 + 10\Delta$ ,  $t = t_0 + 20\Delta$ ,  $t = t_0 + 30\Delta$ , where  $t_0 = 530$  and  $\Delta = 0.192$  — integration step. Parameters of the model:  $\rho = 0.23$ ,  $\mu = 2$ ,  $\Omega = 3$ ,  $c = 1$ ,  $d = 1$ ,  $D_1 = 1$ ,  $D_2 = 1$ ,  $D_3 = 50$ . Domain size  $150 \times 150$ .

### 3 Mechanism of switching from standing to traveling waves accompanied by halving of the wavelength

The transition between standing waves (SW) and traveling waves (TW) in active media of different nature is a well-known phenomenon. In most cases studied to date, regardless of the nature of the medium, the wavelength remains unchanged during such transition [16–19]. However experimental evidence was reported [12] for a SW–TW transition in which the

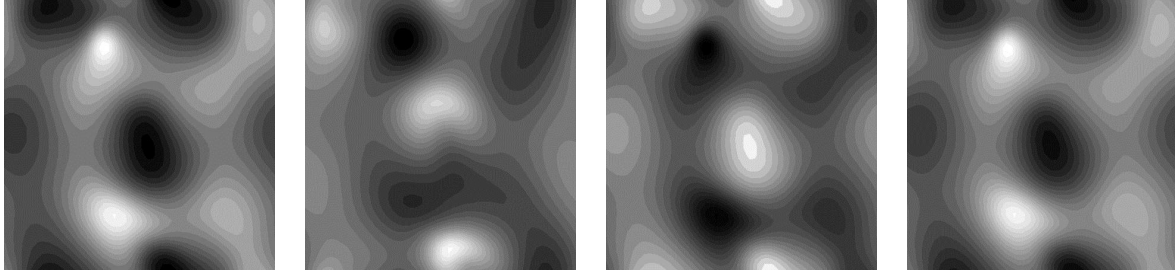


**Figure 3:** Standing waves in the model (6) for the following moments of time:  $t = t_0$ ,  $t = t_0 + 12\Delta$ ,  $t = t_0 + 23\Delta$ ,  $t = t_0 + 46\Delta$ , where  $t_0 = 1755$  and  $\Delta = 0.032$  — integration step. Parameters of the model:  $\rho = 0.23$ ,  $\mu = 1.65$ ,  $\Omega = 10$ ,  $c = 1$ ,  $d = 1$ ,  $D_1 = 1$ ,  $D_2 = 1$ ,  $D_3 = 50$  Domain size  $100 \times 100$ .

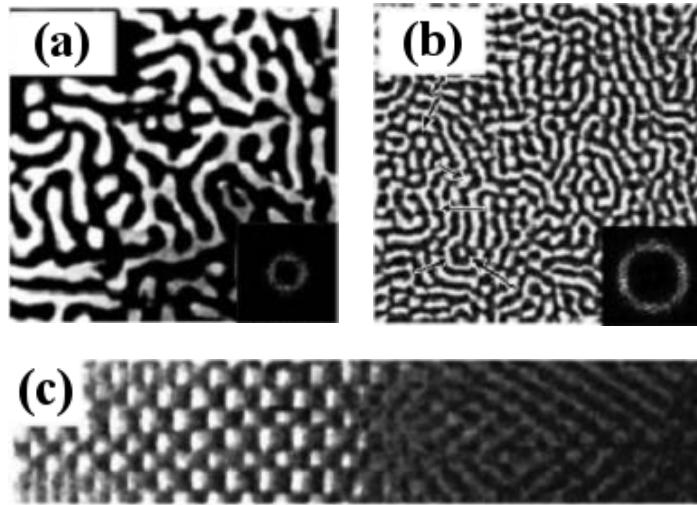


**Figure 4:** Snapshots of (a) standing waves and (b) traveling waves found in the BZ–AOT system. (c) Space-time plot ( $0.6 \text{ mm} \times 20 \text{ min}$ , time increases from left to right) for SW–TW transition [12].

wave number doubles (Fig. 4). This phenomenon was observed in the Belousov-Zhabotinsky reaction dispersed in a water-in-oil aerosol OT/Span-20 microemulsion.

We suggest a possible mechanism for the transition from standing waves with a wavelength  $\lambda_{SW}$  to traveling waves with a half wavelength:  $\lambda_{TW} \cong \lambda_{SW}/2$ . The problem is solved in a spatially one-dimensional case using amplitude equations approach. We demonstrate that the transition is possible under the following conditions:

1. A standing wave is excited by a supercritical wave bifurcation.

The wave can be presented in the form  $u_1(r, t) = \tilde{A}_1 e^{i(\omega t + kr)} + \tilde{A}_2 e^{i(\omega t - kr)}$ , where  $\tilde{A}_1, \tilde{A}_2$  are complex amplitudes of the modes with equal in length but opposite in direction wave vectors  $\pm k$  and the same frequency  $\omega$  which became unstable due to the wave bifurcation. Near the bifurcation the dynamics of interacting modes can be described by the following set of equations of the Ginzburg-Landau type:

$$\begin{cases} \tilde{\dot{A}}_1 = \tilde{A}_1 - (1 - ic_1)\tilde{A}_1 |\tilde{A}_1|^2 - h_1(1 - ic_2)\tilde{A}_1 |\tilde{A}_2|^2, \\ \tilde{\dot{A}}_2 = \tilde{A}_2 - (1 - ic_1)\tilde{A}_2 |\tilde{A}_2|^2 - h_1(1 - ic_2)\tilde{A}_2 |\tilde{A}_1|^2. \end{cases} \quad (7)$$

In these equations spatial dispersion of modes is not taken into account and thus there are no spatial derivatives. It is quite justified if a bounded domain is considered [14].

In equations (7), as was shown in the previous section, depending on the parameter

$h_1$  corresponding to the strength of competition between modes two regimes are possible either standing or travelling wave. For the standing wave to be formed this parameter should be small:  $h_1 \in (0, 1)$ . In this case the modes coexist having the same amplitudes  $|\tilde{A}_i| = 1/\sqrt{1+h_1}$ .

2. We assume that a wave  $u_2(r, t) = \tilde{B}_1 e^{i(w_2 t + 2kr)} + \tilde{B}_2 e^{i(w_2 - 2kr)}$  with a twofold wave number  $2k$  related to a standing wave and frequency  $w_2$  is stable, but can be excited in a rigid manner due to a subcritical bifurcation. In this case in the corresponding amplitude equations we should take into account besides cubic terms also terms of the fifth power:

$$\begin{cases} \dot{\tilde{B}}_1 = -\alpha \tilde{B}_1 + (1 - id_1) \tilde{B}_1 |\tilde{B}_1|^2 - (1 - id_3) \beta \cdot \tilde{B}_1 |\tilde{B}_1|^4 - h_2 (1 - id_2) \tilde{B}_1 |\tilde{B}_2|^2, \\ \dot{\tilde{B}}_2 = -\alpha \tilde{B}_2 + (1 - id_1) \tilde{B}_2 |\tilde{B}_2|^2 - (1 - id_3) \beta \cdot \tilde{B}_2 |\tilde{B}_2|^4 - h_2 (1 - id_2) \tilde{B}_2 |\tilde{B}_1|^2, \end{cases} \quad (8)$$

where  $\alpha, \beta$  are positive constants. The coefficient  $h_2$  corresponds to the strength of interacting modes. It can be shown that when  $h_2$  is sufficiently large:  $h_2 > 1 - 4\alpha\beta$ , one of the modes will suppress the other and a standing wave will be formed.

3. There is a resonance between the first and the second waves, namely, the wave with a twofold wave number has also a duplicated frequency:  $w_2 = 2w$ . The dispersion curves of the system for which the resonance conditions are met are illustrated in Fig. 5.

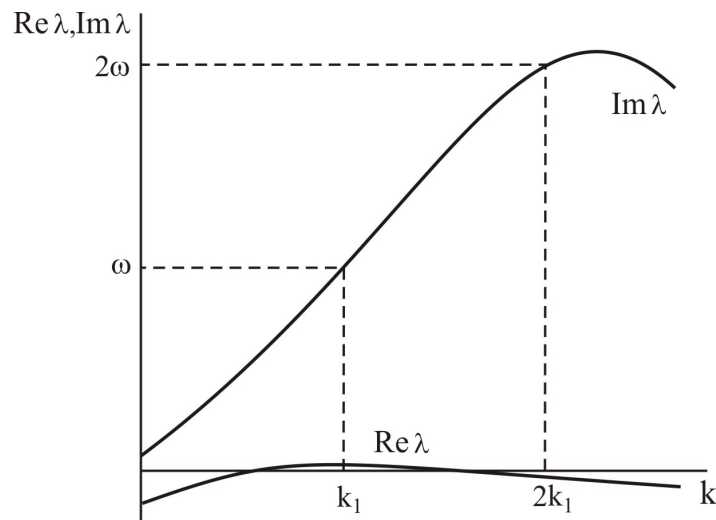


**Figure 5:** Dispersion curves of the system for which the resonance conditions are met: the wave with a twofold wave number has also a duplicated frequency

In terms of amplitude equations this resonance means that besides the conventional cubic terms describing interaction between the modes there is also a term, proportional to the square of the first mode amplitude in the equation for the second mode.

Then the solution of the original kinetic model which is to describe the phenomenon may be sought in the form

$$u(r, t) = A_1 e^{i(wt+kr)} + A_2 e^{i(wt-kr)} + B_1 e^{i(2wt+2kr)} + B_2 e^{i(2wt-2kr)} \quad (9)$$

The set of the corresponding amplitude equations after rescaling and transition to real magnitudes of the amplitudes is the following:

$$\begin{cases} \frac{dA_1}{dt} = A_1 - A_1^3 - h_1 A_2^2 A_1 - \delta_1 (B_1^2 + B_2^2) A_1, \\ \frac{dA_2}{dt} = A_2 - A_2^3 - h_1 A_1^2 A_2 - \delta_1 (B_1^2 + B_2^2) A_2, \\ \frac{dB_1}{dt} = -\alpha B_1 + B_1^3 - \beta B_1^5 - h_2 B_2^2 B_1 - \delta_2 (A_1^2 + A_2^2) B_1 + \sigma \cos \psi_1(t) A_1^2, \\ \frac{dB_2}{dt} = -\alpha B_2 + B_2^3 - \beta B_2^5 - h_2 B_1^2 B_2 - \delta_2 (A_1^2 + A_2^2) B_2 + \sigma \cos \psi_2(t) A_2^2, \end{cases} \quad (10)$$

In terms of these equations the transition from standing to traveling waves with wavelength halving may be explained in the following way. If  $h_1 < 1$  then initial perturbation results in standing wave formation with a wavelength  $\lambda_{SW}$ . However when the amplitudes  $A_i$  have grown they excite in a certain moment of time when  $\cos \psi_i(t) = 1$  ( $\psi_i$  are slowly varying phase shifts) the second pair of modes with a half wavelength due to quadratic terms if the coefficient  $\sigma$  is sufficiently large, namely  $\sigma > \frac{1+h_1}{25\beta} \left( 20\beta\alpha' - 3 + \sqrt{9 - 20\beta\alpha'} \sqrt{\frac{3 - \sqrt{9 - 20\beta\alpha'}}{10\beta}} \right)$ , where  $\alpha' = \alpha + 2\delta_2/(1 + h_1)$ . If  $\delta_2$  is large enough and  $h_2 > 1 - 4\alpha\beta > 0$ , competition between all the four modes results in extinction of three of them and survival of either  $B_1$  or  $B_2$ . It means that the transition to the travelling wave with wavelength halving has occurred. Evolution of the amplitudes in time obtained by numerical solution of Eqns. (10) is presented in Fig. 6. The space-time plot of the function  $u(r, t)$  (9) is given in Fig. 7 which looks similar to the experimental graph (Fig. 4(c)).

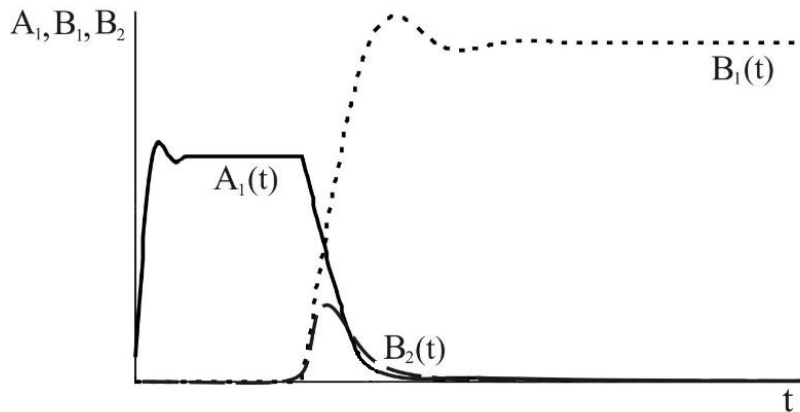


**Figure 6:** Evolution of the amplitudes  $A_1$ ,  $B_1$  and  $B_2$  obtained by numerical solution of Eqns. (10)

## 4 Conclusion

In the present paper we considered patterns formed near the boundary of the wave bifurcation. This case is adequately treated by amplitude equations of the Ginzburg-Landau type. First we have shown that though in multidimensional space a lot of modes contribute to pattern formation, in fact the variety of possible patterns is very limited: either there is a standing wave with rather complicated spatial structure (all of the modes survive) for low intermodal competition, or there is a quasi one-dimensional travelling wave for strong competition. In fact it means that having just a snapshot of the pattern we can immediately say whether we deal with a standing or travelling wave.

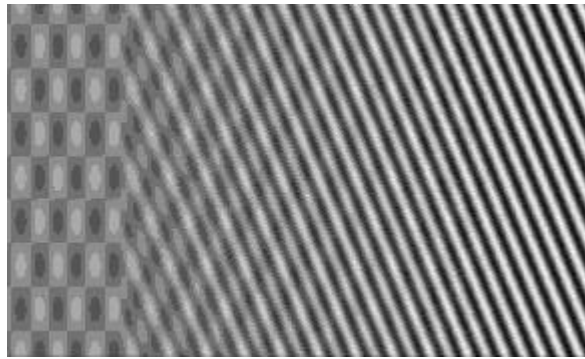


**Figure 7:** Space-time plot  $u(r,t)$  of the transition from standing to travelling wave obtained for Eqns. (7).

In the second part of the paper we suggested a possible mechanism for a rather nontrivial phenomenon observed in experiment: the transition from standing waves to travelling waves with the half-wavelength, based on the hypothesis of a kind of resonance between the unstable mode, responsible for the standing wave, and the rigidly excited mode with a twofold wave number. Though, from the point of view of the theory of dynamical systems, this situation is noncoarse, it is possible that due to the drift of parameters in a real experimental system such resonance may occur, resulting in the observed transition.

**Acknowledgment** This work was partly supported by grant 11-01-00392 from the Russian Foundation of Basic Research.

## References

- [1] G. Nicolis and I. Prigogine. *Self-organization in Nonequilibrium Systems*. Wiley, New York, 1977.
- [2] I. Prigogine. *From Being To Becoming*. Freeman, San Francisco, 1980.
- [3] H. Haken. *Synergetics, an Introduction: Nonequilibrium Phase Transitions and Self-Organization in Physics, Chemistry, and Biology*. Springer-Verlag, Berlin, 1978.
- [4] V. Castets, E. Dulos, J. Boissonade, and P. D. Kepper. Experimental evidence of a sustained standing turing-type nonequilibrium chemical pattern. *Phys. Rev. Lett.*, 64:2953–2956, 1990.
- [5] R. J. Fields and M. Burger. *Oscillations and Travelling Waves in Chemical Systems*. Wiley, New York, 1985.
- [6] R. Kapral and K. Showalter. *Chemical Waves and Patterns*. Kluwer, Dordrecht, 1995.
- [7] A. M. Zhabotinsky. A history of chemical oscillations and waves. *Chaos*, 1:379–386, 1991.
- [8] V. K. Vanag. Waves and patterns in reaction–diffusion systems. Belousov–Zhabotinsky reaction in water-in-oil microemulsions. *Physics-Uspekhi*, 47(9):923–941, 2004.
- [9] A. M. Turing. The chemical basis of morphogenesis. *Philosophical Transactions of the Royal Society of London. Series B, Biological Sciences*, 237(641):37–72, 1952.
- [10] J. D. Murray. *Mathematical Biology*. Springer-Verlag, Berlin, 1989.
- [11] M. Yu. Borina and A. A. Polezhaev. Diffusion instability in a three-variable reaction-diffusion model. *Computer research and modeling*, 3(2):135–146, 2011. In Russian.
- [12] A. Kaminaga, V. K. Vanag, and I. R. Epstein. Wavelength halving in a transition between standing waves and traveling waves. *Phys. Rev. Lett.*, 95(5):058302, 2005.

- 
- [13] Y. Kuramoto. *Chemical Oscillations, Waves, and Turbulence*. Springer-Verlag, Berlin, 1984.
- [14] G. Nicolis. *Introduction to Nonlinear Science*. Cambridge University Press, 1995.
- [15] A. Gierer and H. Meinhardt. A theory of biological pattern formation. *Kibernetik*, 12:30–39, 1972.
- [16] K. Boronska and L. S. Tuckerman. Standing and travelling waves in cylindrical rayleigh-benard convection. *J. Fluid Mech.*, 559:279–298, 2006.
- [17] A. E. Deane, E. Knobloch, and J. Toomre. Traveling waves and chaos in thermosolutal convection. *Phys. Rev. E*, 36:2862–2869, 1987.
- [18] I. Rehberg, S. Rasenat, J. Fineberg, M. de la Torre Juarez, and V. Steinberg. Temporal modulation of traveling waves. *Phys. Rev. Lett.*, 61:2449–2452, 1988.
- [19] B. Marts and A. L. Lin. Transition from traveling to standing waves in the 4:1 resonant belousov-zhabotinsky reaction. *Phys. Rev. E*, 77:026211, 2008.

# Threshold activation of intravascular fibrin polymerization and gel formation under intensive blood flow conditions. Theoretical analysis.

A.S. Rukhlenko<sup>1,\*</sup>, K.E. Zlobina<sup>2</sup> and G.Th. Guria<sup>1,2</sup>

<sup>1</sup>*Moscow Institute of Physics and Technology, Dolgoprudny, Russia*

<sup>2</sup>*National Research Centre for Haematology, Moscow, Russia*

\**e-mail address: aleksey.rukhlenko@gmail.com*

## 1 Introduction

It is commonly accepted that platelets as well as serine proteases participating in biochemical reactions of fibrin production play an essential role in the development of intravascular blood coagulation [1–3]. At the same time, in the initiation of intravascular blood coagulation an important role belongs to the condition of vessel walls (including their impairment by ulcers or sclerosis and the state of endothelium) [4–9].

According to current scientific views, the initiation of the intravascular coagulation processes may occur either as a result of the disruption of vessel wall barrier properties [5, 10, 11], or due to the activation of platelets in the shear flows (mainly near the vessel wall) where the shear rate exceeds  $\sim 5400 \text{ s}^{-1}$  [12–14].

Within the scope of this work, we focus only on the situations of blood flow in which shear rate does not exceed  $\sim 10^3 \text{ s}^{-1}$ . Therefore, hydrodynamical activation of platelets will not be taken into consideration in this research.

Main attention will be paid to intravascular coagulation initiated by procoagulants that infiltrate into the blood flow when endothelium barrier properties are diminished due to the intensification of wall shear stress [15–18].

Within the approach suggested, the permeability of endothelium layer will be assumed to depend on the wall shear stress in a threshold manner. The highest stresses in blood vessels normally occur in the areas of greater stenosis narrowing, which appear, for instance, due to the local formation of atherosclerotic plaques. This is precisely the reason why the starting centers of above-threshold stimulation of thrombus formation are usually associated with the location of atherosclerotic plaques in the vessels [15–18].

The role of pro-coagulant factors that enter blood flow from atherosclerotic plaques is mostly performed by the products of inflammatory processes that take place in the plaques [19, 20]. Regardless of procoagulant's biochemical nature, we consider all substances of that type as pro-coagulants in cases when they can serve as primary activators of blood coagulation [21, 22].

The threshold activation of the blood coagulation system (BCS) cascade of reactions manifests itself by means of a self-accelerated production in the blood flow of a range of key biochemical agents — serine proteinases (factors IIa (thrombin), Xa, VIIIa, Va etc.), among which the central role is played by thrombin. In this work, thrombin generation and its distribution in the vessel was taken into consideration within scope of phenomenological model [21–25]. The biological significance of thrombin is dealt with its catalytic ability to

convert fibrinogen molecules (present in the blood in inactive form) into fibrin-monomers capable of fast precipitous polymerization.

The formation of a fibrin polymer network in the blood flow can change the flow pattern even up to complete stoppage of blood flow.

The main aim of this work was to develop a description of the mass transfer processes involving the formation of fibrin thrombi in vessels having variable crosssection of the lumen. The study of the relevant problems within the framework of the suggested approach allowed us to reveal several typical scenarios of intravascular clot formation, as well as to build parametrical diagrams of the blood liquid state stability in intense flows.

The results obtained probably have some value in the discussion of indications for stenting procedures practically used for the vessel remodeling in patients.

## 2 Model description

### 2.1 Geometry

Blood vessel with stenosis (atherosclerotic plaque) on its lower wall was considered in a two-dimensional approximation (see fig. 1). Vessel walls were supposed to be rigid.

The form of stenosed vessel wall was approximated by formula:

$$f(x) = L_y(1-s)e^{-\frac{x^2}{2d^2}}, \quad (1)$$

where  $L_y$  denotes vessel width,  $H$  denotes vessel minimal width,  $s = (H/L_y) \in (0; 1)$  reflects relative size of minimal lumen, and  $d$  corresponds to stenosis width (see fig. 1).

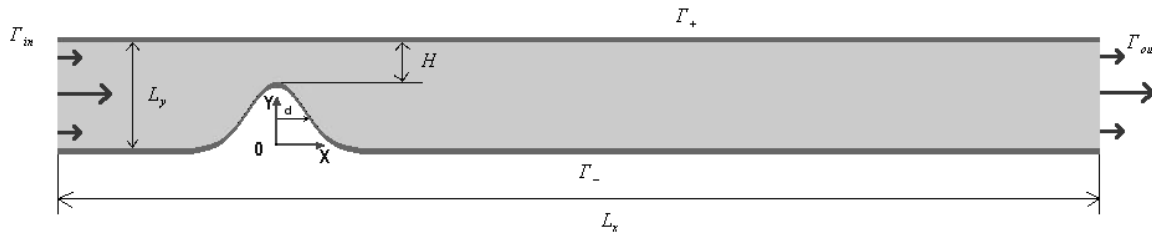


**Figure 1:** Vessel's fragment geometry.  $L_x$ ,  $L_y$  and  $H$  correspond to vessel length, width and minimal vessel width.  $\Gamma_+$  and  $\Gamma_-$  refer to upper and lower vessel walls respectively.  $\Gamma_{in}$  and  $\Gamma_{out}$  denote inlet and outlet boundaries respectively.

### 2.2 Governing equations

Blood was supposed to be a Newtonian fluid with viscosity  $\nu$  and density  $\rho$ . Hemodynamics was described by means of modified Navier-Stokes equations:

$$\frac{\partial \vec{V}}{\partial t} + (\vec{V}, \vec{\nabla}) \vec{V} = -\frac{1}{\rho} \vec{\nabla} p + \nu \nabla^2 \vec{V} - \alpha_p(M_1, M_2) \nu \vec{V} \quad (2)$$

$$(\vec{\nabla}, \vec{V}) = 0, \quad (3)$$

where  $t$  denotes time,  $\vec{\nabla}$  is well-known Hamilton's operator,  $\alpha_p(M_1, M_2)$  describes filtration resistance of fibrin polymer network (in case it is formed),  $M_1$  and  $M_2$  refer to statistical moments of fibrin polydisperse system (see below)<sup>1</sup>.

<sup>1</sup>The polymer structure formed was considered as a porous media with a specific (non-constant) Darcy coefficient. The value of Darcy coefficient depended on the state of polydisperse macromolecule fibrin system.

The kinetics of blood coagulation reactions was described in the framework of the phenomenological model [21–24]:

$$\frac{\partial u}{\partial t} = -k_d u - \nabla \cdot (\vec{V}u - D_u \nabla u) \quad (4)$$

$$\frac{\partial \theta}{\partial t} = k_u u + \frac{\alpha \theta^2}{\theta + \theta_0} - \chi_1 \theta - \gamma \theta \varphi - \nabla \cdot (\vec{V}\theta - D_\theta \nabla \theta) \quad (5)$$

$$\frac{\partial \varphi}{\partial t} = \beta \theta \left(1 - \frac{\varphi}{c}\right) \left(1 + \left(\frac{\varphi}{\varphi_0}\right)^2\right) - \chi_2 \varphi - \nabla \cdot (\vec{V}\varphi - D_\varphi \nabla \varphi) \quad (6)$$

$$\frac{\partial F_g}{\partial t} = -k_g F_g \theta - \varepsilon_g (F_g - F_g^0) - \nabla \cdot (\vec{V}F_g - D_g \nabla F_g) \quad (7)$$

$$\frac{\partial M_1}{\partial t} = k_g F_g \theta - k_r M_1 - \nabla \cdot (b_p \vec{V}M_1 - D_f \nabla M_1) \quad (8)$$

$$\frac{\partial M_2}{\partial t} = k_g F_g \theta + 4k_p (M_2 + M_1)^2 - \frac{k_b}{3} \left(\frac{M_2^2}{M_1} - M_1\right) - k_r M_2 - \nabla \cdot (b_p \vec{V}M_2 - D_f \nabla M_2), \quad (9)$$

where  $u$  denotes the concentration of the primary activator of blood coagulation,  $\theta$  and  $\varphi$  denote concentrations of the activator (thrombin) and the inhibitor of biochemical network of blood coagulation reactions (see [26, 27] and [21]),  $F_g$  corresponds to fibrinogen (fibrin precursor) concentration.  $M_1$  and  $M_2$  are first and second fibrin moments that are defined through the concentration of  $k$ -meres of fibrin  $F_k$  as [21]:

$$M_n = \sum_{k=1}^{\infty} k^n F_k, \quad n = 1, 2. \quad (10)$$

It is well-known that  $M_1$  reflects the total amount of fibrin-monomer molecules in all polymerized and unpolymerized forms in the considered element of volume, while the ratio  $M_2/M_1$  determines weight-averaged molecular weight [28, 29]  $M_w$  of fibrin polymer molecules in the system considered [30]:

$$M_w = \sum_{k=1}^{\infty} m_0 k \cdot w_k = m_0 \frac{M_2}{M_1}, \quad (11)$$

where  $m_0$  denotes the molecular weight of fibrin-monomer and  $w_k = \frac{kF_k}{\left(\sum_{m=1}^{\infty} mF_m\right)}$  corresponds to the weight fraction of  $k$ -meres in the system. The weight-averaged number of fibrin-monomers in polymer molecules of fibrin  $N_w$  could be expressed as:

$$N_w = \frac{M_w}{m_0} = \frac{M_2}{M_1}. \quad (12)$$

We assumed that with the increase in the polymer chains length they will become less and less transportable by the flow. To take into account this circumstance, a special term  $b_p$  has been introduced into equations (8)-(9) as a coefficient of polymer chains transport by the flow (see [23–25] for details).

We believe that the system equations (2)-(9) can correctly describe the early stages of intravascular coagulation processes, that is, the situations in which the loss of stability of the blood liquid state triggers the bulk chain processes of generation of fibrin-monomer molecules followed by their polymerization. The dynamics of fibrin-polymer microemboli formation has several stages [31, 32]. The early stage, nucleation, is followed by the stage

of emboli growth up to the size comparable to the mean distance between them. Next comes the stage when neighbouring fibrin-polymer clots start to overlap, that is, an essential interaction between them is established. During later stages, the system evolution results in gel formation in the vessel under consideration.

In this work, it will be assumed that during all the listed stages of coagulation the blood density undergoes no changes. Unlike the density, the kinetic coefficients  $\nu$ ,  $\alpha_p$ ,  $D_f$  and  $b_p$  undergo an essential change during the stage-to-stage transition. It was assumed that during the fibrin-polymer clots nucleation the value of blood viscosity  $\nu$  is equal to the initial value, the filtration resistance  $\alpha_p$  is taken to be negligibly small, and the coefficient of polymer chains transport by the flow  $b_p$  and the diffusion coefficient  $D_f$  are adequately represented by the expressions:

$$b_p = 1 \quad (13)$$

$$D_f = D/N_w \quad (14)$$

where  $D$  is the fibrin-monomer diffusion coefficient.

When the growing polymer clusters begin to mutually overlap, the process is commonly termed as the formation of a semi-diluted polymer solution [33, 34]. The following inequation serves as a criterion of a semi-diluted polymer solution formation:

$$N_w \geq N_w^s \quad (15)$$

where  $N_w^s$  is the weight-averaged number of fibrin monomer molecules in polymer coils at the appearance of semi-diluted conditions.

Fulfillment of these conditions actually implies that functional dependences of the listed coefficients  $\nu$ ,  $\alpha_p$ ,  $D_f$  and  $b_p$  on statistical moments  $M_1$  and  $M_2$  begin to change.

In the present work, the description of the dependences of the kinetic coefficient  $s$  on the moments of the distribution of a fibrin molecule polydispersional system employed asymptotic expressions that in the limitary cases turn into well-known in polymer physics expressions. The actual form of the respective dependences is given below (see [23–25] for details):

$$\alpha_p = k_{num} N_a^2 M_1^2 K^2 l_0^4 \cdot (1 - b_p) \quad (16)$$

$$D_f = D \cdot \frac{1}{N_w} \cdot \frac{1}{1 + N_w/N_w^s} \quad (17)$$

$$b_p = \frac{1}{1 + N_w/N_w^s} \quad (18)$$

where  $N_a$  is the Avogadro number,  $k_{num} = 10^{-24} \text{ mole}^2 / (nM^2 \cdot \text{cm}^6)$  is the coefficient for the conversion of length dimensions.

The work mainly focused on the early stages of fibrin gel formation in the blood flow. Therefore it was assumed that when the mean length of polymer chains  $N_w$  exceeds the characteristic value of the half-dilution condition  $N_w^s$  by two or more orders ( $N_w = 10^2 \cdot N_w^s$ ), a sufficiently “mature” gel is formed, and the research of its further evolution remains outside the scope of this work’s objectives<sup>2</sup>

<sup>2</sup>It should be noted that adopting of this assumption lets to avoid us analysis of the singular solutions of equations, describing the dynamics of statistical moments  $M_1$  and  $M_2$ , i.e. the situations when  $M_2$  blows up [35].

### 2.3 Boundary and initial conditions

Poiseuille's conditions were applied at the left boundary of the considered area  $\Gamma_{in}$ :

$$V_x|_{\Gamma_{in}} = \frac{4V_0}{L_y^2}y(L_y - y) \quad (19)$$

$$V_y|_{\Gamma_{in}} = 0 \quad (20)$$

Pressure on the outlet boundary was assumed to be equal to zero:

$$p|_{\Gamma_{out}} = 0 \quad (21)$$

The no-slip conditions were satisfied at the boundaries  $\Gamma_+$  and  $\Gamma_-$ .

The values of  $u$ ,  $\theta$ ,  $\phi$ ,  $M_1$  and  $M_2$  on  $\Gamma_{in}$  were supposed to be equal to zero, while  $F_g$  concentration on  $\Gamma_{in}$  was assumed to be equal to initial fibrinogen concentration  $F_g^0$ . On the vessel outlet  $\Gamma_{out}$  the zero-gradient conditions were used for all chemicals.

Vessel walls were supposed to be impermeable for all chemicals but the primary activator. This means that for  $\theta$ ,  $\phi$ ,  $F_g$ ,  $M_1$  and  $M_2$  the zero-gradient boundary conditions were set on  $\Gamma_+$  and  $\Gamma_-$ . The upper (non-stenosed) vessel was supposed to be impermeable for  $u$ . To describe the process of primary activator infiltration into the blood flow through the lower (stenosed) vessel wall the following boundary condition was used for  $u$  on  $\Gamma_-$ :

$$-D \left. \frac{\partial u}{\partial \vec{n}} \right|_{\Gamma_-} = \mu(|\gamma_{sh}|) (u_0 - u|_{\Gamma_-}) \quad (22)$$

where operator  $\left. \frac{\partial}{\partial \vec{n}} \right|_{\Gamma_-}$  denotes the space derivative normal to  $\Gamma_-$ ,  $u_0$  denotes primary activator concentration under the vessel wall, and  $u|_{\Gamma_-}$  corresponds to the concentration of primary activator in the blood flow near the lower vessel wall ( $\Gamma_-$ ).

**Table 1:** Parameter values

Parameter	Value	Refs.	Parameter	Value	Refs.
$\alpha$	$3.33 \cdot 10^{-2} s^{-1}$	[21, 22]	$k_b$	$1.67 \cdot 10^{-3} s^{-1}$	[21, 22]
$\theta_0$	$5 nM$	[21, 22]	$n_0$	$10^{10} cm^{-3}$	[36]
$\chi_1$	$8.33 \cdot 10^{-4} s^{-1}$	[21, 22]	$F_g^0$	$9 \cdot 10^3 nM$	[21, 22]
$\gamma$	$8.33 \cdot 10^{-2} (nM \cdot s)^{-1}$	[21, 22]	$D_u$	$3 \cdot 10^{-7} cm^2/s$	[21, 22]
$\beta$	$2.5 \cdot 10^{-5} s^{-1}$	[21, 22]	$D_\phi$	$3 \cdot 10^{-7} cm^2/s$	[21, 22]
$c$	$5 nM$	[21, 22]	$D_\theta$	$3 \cdot 10^{-7} cm^2/s$	[21, 22]
$\epsilon_g$	$1.66 \cdot 10^{-6} s^{-1}$	[21, 22]	$D_g$	$3 \cdot 10^{-7} cm^2/s$	[21, 22]
$\phi_0$	$0.05 nM$	[21, 22]	$D$	$3 \cdot 10^{-7} cm^2/s$	[21, 22]
$\chi_2$	$0.35 nM$	[21, 22]	$k_d$	$1.66 \cdot 10^{-6} s^{-1}$	[21, 22]
$k_g$	$5 \cdot 10^{-6} (nM \cdot s)^{-1}$	[21, 22]	$k_u$	$1.66 \cdot 10^1 s^{-1}$	[21, 22]
$k_p$	$2.5 \cdot 10^{-4} (nM \cdot s)^{-1}$	[21, 22]	$k_r$	$1.67 \cdot 10^{-2} s^{-1}$	[21, 22]
$\gamma_1$	$10 dyn/cm^2$	[15, 16, 18]	$\mu_1$	$2 \cdot 10^{-12} cm/s$	[23, 24]
$\gamma_2$	$20 dyn/cm^2$	[15, 16, 18]	$u_0$	$100 nM$	[23, 24]
$\nu$	$5 \cdot 10^{-2} cm^2/s$	[36]	$\rho$	$1 g/cm^3$	[36]
$L_x$	$7.5 cm$		$L_y$	$1 cm$	
$K$	$10$	[37]	$l_0$	$1.5 \cdot 10^{-6} cm$	[37, 38]
$N_a$	$6.02 \cdot 10^{23} mol^{-1}$				

The permeability  $\mu$  of the lower vessel wall  $\Gamma_-$  depended on wall shear stress  $\gamma_{sh}$  in a piecewise-linear manner:

$$\mu = \begin{cases} \mu_1, & |\gamma_{sh}| \leq \gamma_1 \\ \frac{|\gamma_{sh}| - \gamma_1}{\gamma_2 - \gamma_1} (\mu_2 - \mu_1) + \mu_1, & \gamma_1 < |\gamma_{sh}| < \gamma_2, \\ \mu_2, & |\gamma_{sh}| \geq \gamma_2 \end{cases} \quad (23)$$

where  $\mu_1$  denotes the permeability of vessel wall for sub-threshold wall shear stress values, and  $\mu_2$  corresponds to the permeability for over-threshold ones.

At the initial moment  $t = 0$  all variables but  $F_g$  were assumed to be equal to zero in the interior part of calculation domain while  $F_g$  was assumed to be equal to  $F_g^0$ . The  $\vec{V}$  and  $p$  fields were assumed to be equal to their stationary values in the given boundary conditions (i.e. stationary flow).

The values of all parameters used in numerical calculations are presented in the Table 1 (see [23, 24]).

### 3 Results

#### 3.1 Early stages of thrombi formation processes. Typical scenarios

Numerical simulation of the model described above opened the possibility to calculate spatio-temporal distribution of  $M_1$ ,  $M_2$ ,  $N_w$ , etc<sup>3</sup>. in the vessel. Some scenarios are shown in figures 2, 3 and 4. The gray color scale at these figures represents weight-average number of fibrin monomers in polymer chains  $N_w$  (see eqn. (12)). The maximum of the scale (white color) is  $N_w^s$  (see eqn. (15))<sup>4</sup>. This means that white color represents clots while grey shades represent microthrombi with different lengths of polymer chains.

There is a recirculation zone behind the atherosclerotic plaque in all investigated scenarios (see figures 2, 3 and 4). In the present work only the thrombus formation events taking place in recirculation zone were investigated. Within the scope of the presented approach we found 3 typical scenarios of thrombus formation events. In scenarios 1 and 2, a solid massive thrombus is formed as the result of blood coagulation system activation (see figures 2d and 3d). In contrast, the result of the activation of coagulation system in scenario 3 is a floating friable structure without a sharp border (see fig. 4c). It can be seen from fig. 4c, the floating structure has a long “tail” of microthrombi clouds downstream.

Numerical simulations have shown that in all scenarios early stages of coagulation processes development are the same. The nucleation of a macroscopic thrombus always happens in the region of reattachment point (see figures 2a, 3a and 4a). Then the stage of macroscopic fibre-like structure formation comes (see figures 2b, 3b and 4b). The direction of the growth of the fibre-like structure is determined by the separatrix line, which divides the core of the flow from the recirculation zone.

After that, there are three possible types of system behavior depending on the parameter values:

- fibre structure successively thickens (see fig. 2c) and a solid thrombus is formed in the recirculation zone (see fig. 2d);
- after some time of fibre structure growth the gelation front splitting happens (see fig. 3c) and solid thrombus in the recirculation zone is formed (see fig. 3d) as a result of a two-side clot growth;

<sup>3</sup>Numerical methods, used in analysis of presented model are described in [23–25].

<sup>4</sup>Note that  $N_w$  can be greater than  $N_w^s$ .

- formation of a floating friable structure takes place (see fig. 4c).

### 3.2 Threshold-like activation of thrombus formation process

Numerical simulations not only revealed the typical patterns of blood clot formation, but also allowed us to build parametric diagrams of blood liquid state stability. Using our mathematical model we investigated the influence of blood flow rate, vessel wall permeability and the shape of atherosclerotic plaque on threshold activation of blood coagulation processes.

Blood flow rate is characterized by a dimensionless parameter — Reynolds number:

$$Re = \frac{V_0 L_y}{\nu} \quad (24)$$

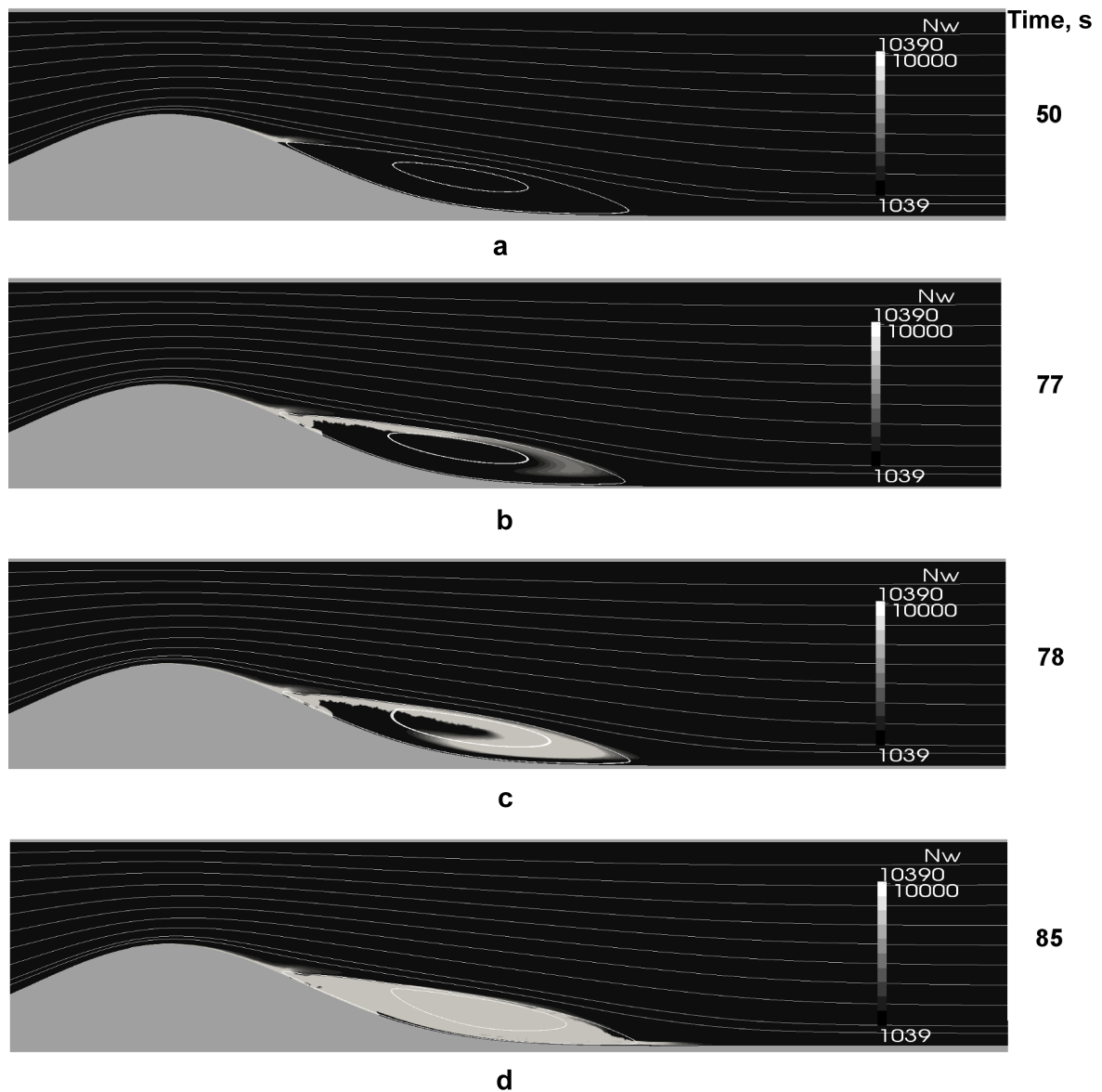


**Figure 2:** Scenario 1, solid thrombus formation through 1-side gelation front. Gray-scale map of  $N_w$  distribution in the vessel, white areas are places of fibrin gel formation ( $N_w \geq N_w^{pol}$ ). a-d are successive stages of the process: a — thrombus nucleation, b — formation of fibre-like fibrin structure, c — fibre-like structure thickening, d — solid thrombus.  $Re = 130$ ,  $s = 0.5$ ,  $\tilde{d} = 0.5$ ,  $\tilde{\mu}_2 = 9.5$ .

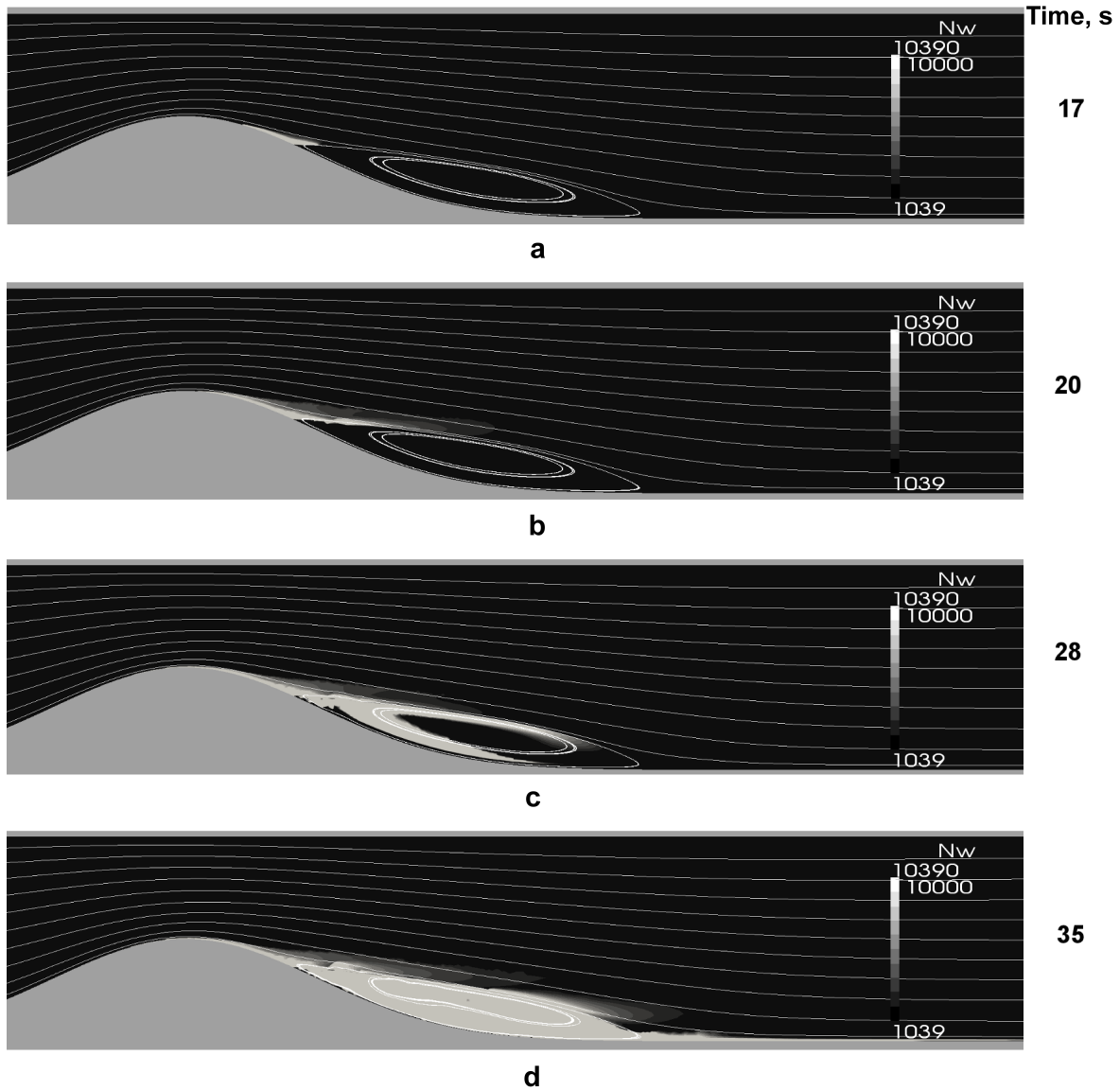


**Figure 3:** Scenario 2, solid thrombus formation through 2-side gelation front. Gray-scale map of  $N_w$  distribution in the vessel, white areas are the places of fibrin gel formation ( $N_w \geq N_w^{pol}$ ). a-d are successive stages of the process: a — thrombus nucleation, b — formation of fibre-like fibrin structure, c — two-side gelation front, d — solid thrombus.  $Re = 130$ ,  $s = 0.5$ ,  $\tilde{d} = 0.5$ ,  $\tilde{\mu}_2 = 95$ .

Vessel wall permeability may be characterized by dimensionless maximal vessel wall permeability:

$$\tilde{\mu}_2 = \mu_2 u_0 \cdot \frac{k_u}{L_y (\alpha - \chi_1)^2 \theta_0} \quad (25)$$

The parametric diagram of blood coagulation system regimes is presented in fig. 5. Parametric plane  $(Re, \tilde{\mu}_2)$  is divided in two main zones denoted as “I” and “II”. When the representative point is located in zone “I” the system evolves to stationary state with  $N_w < N_w^{pol}$ . This means that only formation of micro-thrombi (see [22]) takes place in the system. When the representative point is located in zone “II”  $N_w$  reaches and exceeds  $N_w^{pol}$  at some moment of time, that means that fibrin gelation, i.e. formation of macroscopic thrombi, occurs.

Figure 5 shows that the region where thrombus formation starts has a form of a “tongue”

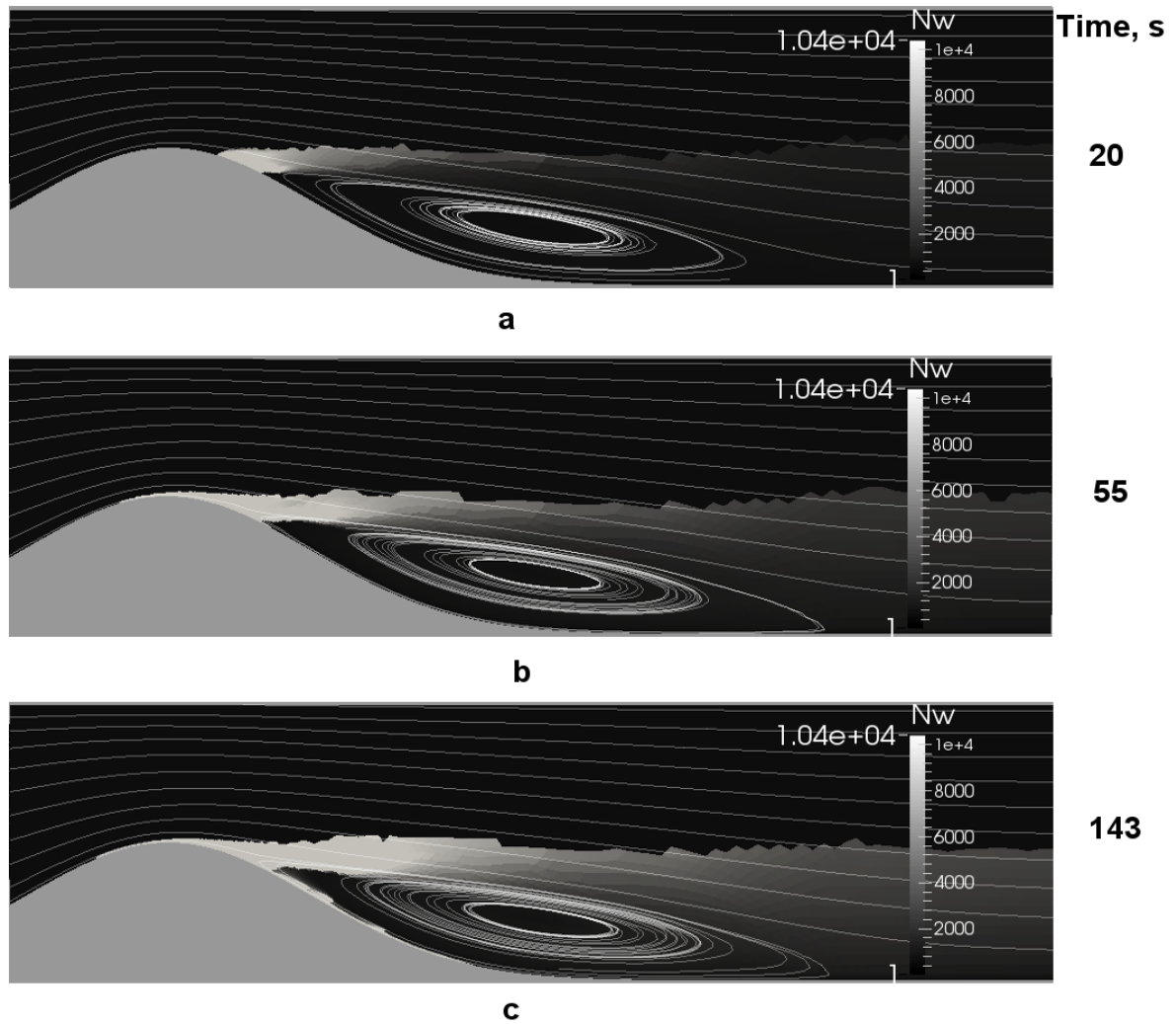


**Figure 4:** Scenario 3, floating fibrin structure formation. Gray-scale map of  $N_w$  distribution in the vessel, white areas are the places of fibrin gel formation ( $N_w \geq N_w^{pol}$ ). a-c are successive stages of the process: a — thrombus nucleation, b — formation of fibre-like fibrin structure, c — thick and friable floating fibrin structure.  $Re = 200$ ,  $s = 0.5$ ,  $\tilde{d} = 0.5$ ,  $\tilde{\mu}_2 = 9.5$ .

and that the range of Reynolds number values where it happens is limited both above and below. For any  $\tilde{\mu}_2 > \tilde{\mu}_2^{min}$  two thresholds of hydrodynamic activation of blood coagulation exist.

For example, if we follow the horizontal line with arrows in figure 5, the first threshold is at  $Re = Re_1$ : if  $Re < Re_1$ , the value of wall shear stress is less than  $\gamma_1$  and primary activator  $u$  doesn't appear in blood flow; otherwise fibrin clot is formed. The second threshold is at  $Re = Re_2$ : if  $Re > Re_2$ , convective flow washes coagulation substances away, otherwise thrombus formation starts.

This means that both increasing and decreasing of blood flow intensity may lead to thrombi formation, depending upon initial conditions.

In figure 5 one can see a vertical line  $Re = Re_{\gamma_2}$ . This value of Reynolds number corresponds to wall shear stress equal to  $\gamma_2$  that means that vessel wall permeability  $\mu = \mu_2$  (see eqn. (23)). In other words, it is the intensity of blood flow that leads to the plaque rupture.

Some part of zone “I” is on the right side of  $Re = Re_{\gamma_2}$  in fig. 5, that means that in spite of plaque rupture thrombi formation doesn't occur. This type of system behavior may be

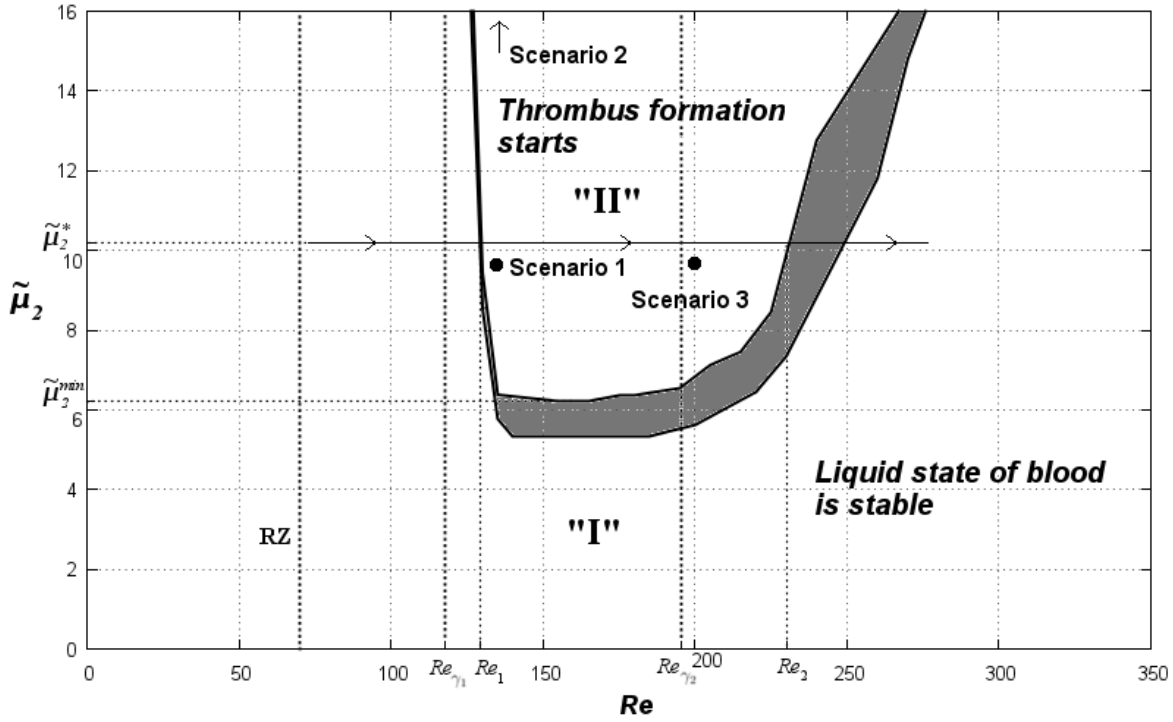


**Figure 5:** Parametric diagram of blood coagulation system regimes. This diagram describes the influence of the vessel wall permeability  $\tilde{\mu}_2$  and blood flow rate  $Re$  on thrombi formation threshold. Grey ribbon between zones “I” and “II” is a region where it is difficult to detect whether the point belongs to zone “I” or “II”. Parameter values:  $s = 0.5$ ,  $\tilde{d} = 0.5$ .

associated with asymptotic plaque rupture [39, 40].

It was found that in the vicinity of the border between zones “I” and “II” the following scaling law is valid for the nucleation time  $T^*$  (given constant  $Re$ ):

$$(\tilde{\mu}_2 - \tilde{\mu}_2^{crit})T^{*3} = C_1 = const, \quad (26)$$

where  $\tilde{\mu}_2^{crit}$  is specific value of  $\tilde{\mu}_2$ , located in the “grey” area (see fig. 5), and  $C_1$  is a value independent on  $\tilde{\mu}_2$ .

It was also shown that in the vicinity of the left border of zone “II” the following scaling law is valid (given constant  $\tilde{\mu}_2$ ):

$$(Re - Re_{crit})T^{*3} = C_2 = const \quad (27)$$

where  $Re_{crit}$  is the specific value of  $Re$ , located in the “grey” area (see fig. 5), and  $C_2$  is the value independent on Reynolds number ( $Re$ ).

In other words, it appeared that in the vicinity of the liquid state stability border the clot nucleation time grows up to infinity (see (26)-(27)). This result can be compared with the results of the theory of first-order transitions, where similar scaling laws connecting the extent of supersaturation with the nucleation time exist [41, 42].

To investigate the influence of stenosis shape on blood coagulation threshold the  $(s, Re, \tilde{d})$  parametric plane was scanned (see fig. 6), given the constant  $\tilde{\mu}_2$ . The dimensionless parameter  $\tilde{d}$  characterizes the width of the atherosclerotic plaque:

$$\tilde{d} = d/L_y \quad (28)$$

It appeared that the surface dividing the sub- and superthreshold regimes of blood coagulation system is saddle-like. For a chosen value of  $\tilde{\mu}_2$  the section of this surface by the  $\tilde{d} = 0.4$  plane crosses the saddle-point (see fig. 6b). It can be clearly seen that the Reynolds number range where macroscopic thrombus formation takes place for  $0.2 < s < 0.4$  is significantly wider than for  $0.6 < s < 0.8$ .

## 4 Discussion

In this work the blood coagulation system hydrodynamical activation conditions and the characteristic scenarios of the early stages of thrombi formation processes in stenosed vessels were investigated. Intravascular activation of blood coagulation processes was assumed to be caused by primary pro-coagulants that infiltrated into the blood flow through the vessel wall from adjacent tissues.

Clearly, the mathematical description of intravascular blood coagulation processes was oversimplified in the present work. The model suggested only took into consideration the biochemical part of the haemostasis system. It was taken into account that the processes of the hydrodynamical activation of the platelet-based part of the haemostasis system take place at the values of shear rate far exceeding those analysed in the present work<sup>5</sup>.

Naturally, the range of thrombi-based emergency situations is far wider. Therefore a correct evaluation of the platelets' role is also of considerable interest. Attempts to develop relevant mathematical models had taken place several times [43–51]. However, for the moment only a description of platelet aggregation processes in small intensity flows ( $Re \ll 1$ )<sup>6</sup> can be considered as more or less successful [47–50].

The main distinctive feature of the model presented and employed in this work (in contrast to the ones in earlier works [52–60]) is that it takes into the consideration the dependence of the vessel wall permeability on the shear stress in intense blood flow. It seems that such effects have been mathematically described for the first time.

Another important feature of the model suggested is the introduction of the dependence of kinetic parameters ( $b_p, D_f, \alpha_p$ ) on the statistical moments  $M_1$  and  $M_2$  that characterize the development of fibrin polymerization processes during blood coagulation. The expressions used in the work are of an asymptotic nature. They were drawn from the application of scaling approaches [34] and the technique of composite asymptotic expansions [61] to the description of the processes of fibrin polymerization in the processes of mass transport.

In this work we neglected the change of blood viscosity during thrombi formation. Proper assessment of the role of viscoelastic rheological effects [62] in the process of intravascular thrombi formation is a task for further research work in this field.

Numerical calculations have shown that in the framework of presented boundary conditions the formation of fibre-like structures in the post-stenotic area always precedes the development of massive voluminous clot formation processes. The fibre-like structures always started to grow from the reattachment point of the recirculation zone (see fig. 2-4). That is, the nucleation center of macroscopic thrombus formation is determined by the topologic properties of the flow.

The obtained results show that the growth of fibrin fibres may lead either to the formation of localized thrombi (see fig. 2 and 3) or to the formation of friable fibrin polymer structures flatter in the flow (see fig. 4). Localized thrombi formation normally takes place in less intense flows than the formation of floating structures. In intense flows, alongside with the formation of floating structures, the formation and spreading downstream the flow of multiple fibrin microemboli takes place. It seems that such finely dispersed “dust” may

<sup>5</sup>In the present work, the inequation  $\dot{\gamma} \leq 10^3 \text{ s}^{-1}$  was valid at all times.

<sup>6</sup>In the so-called Stokes approximation.

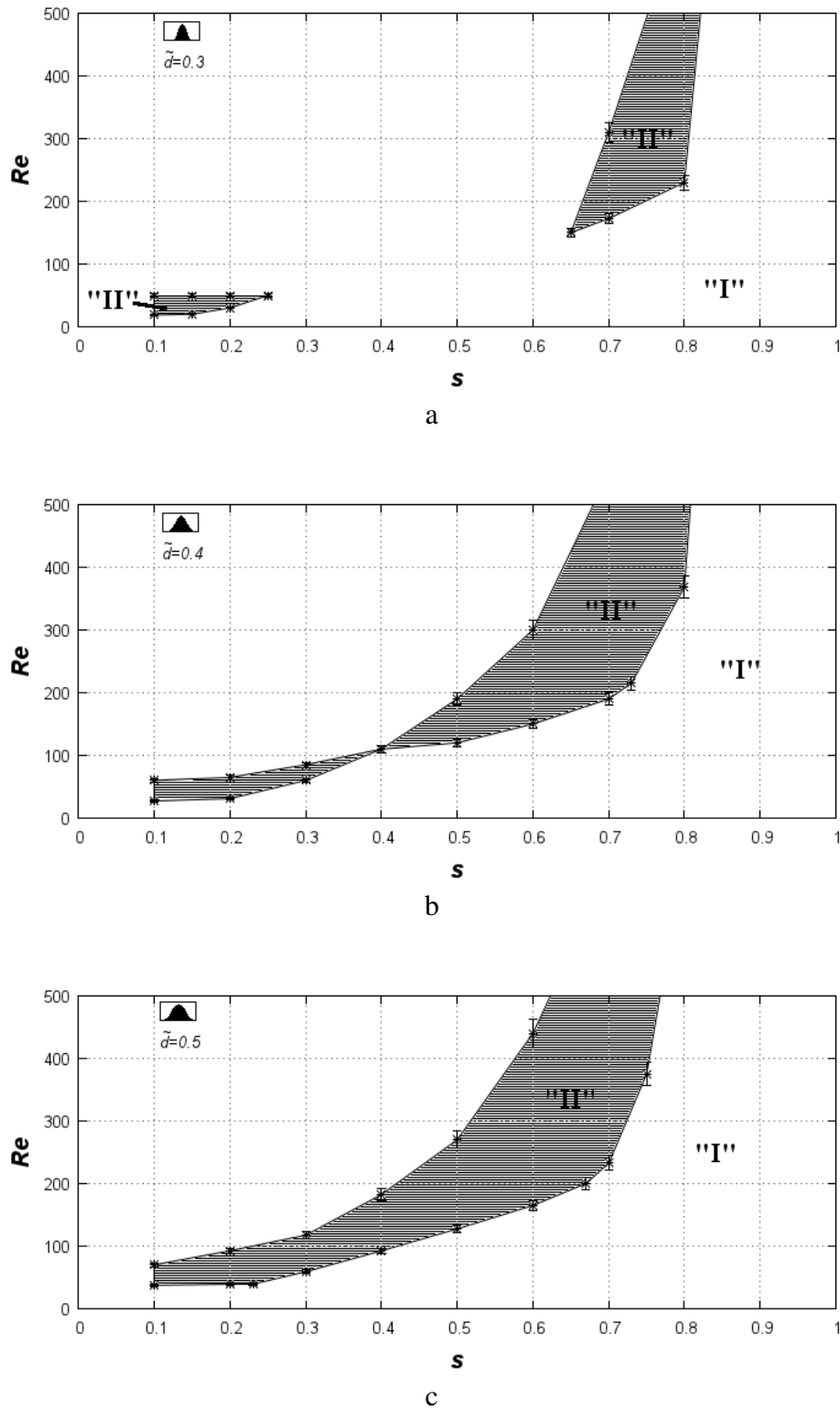


**Figure 6:** Sections of blood coagulation stability surface by the planes  $\tilde{d} = const$  in the  $(s, Re, \tilde{d})$  space,  $\tilde{\mu}_2 = 19$ . a:  $\tilde{d} = 0.3$ , b:  $\tilde{d} = 0.4$ , c:  $\tilde{d} = 0.5$ .

cause blood microcirculation disorders in organs situated more distally from the observed thrombi formation center.

In view of the notions listed above, it becomes clear why friable structures can be observed in the area adjacent to the right border of the “tongue” of blood liquid state stability loss (see fig. 5).

It is worth mention that the existence of some dependence of the threshold of coagulation system activation on the form of the plaque seems natural. At the same time, the character of that dependence obtained in the present work seems contrintuitive. In fact, the performed numerical calculations have shown (see fig. 6) that the plaques most dangerous with respect to thrombus formation are not the largest ones. The analysis of this phenomenon has shown that at high degrees of stenosis ( $s < 0.3$ ) the effect of convective diminishing of procoagulants concentration may dominate over the effect of vessel wall permeability increase. The higher stenosis values ( $s < 0.1$ ) may cause substantial changes in the flow topology, leading to a suppression of thrombus formation as well.

According to our calculations, the most thrombogenic plaques should occlude only 20–40% of the vessel lumen ( $0.6 < s < 0.8$ ). In the light of the result it seems that the “worldwide-accepted values” that serve as indications for stenting vessels of patients exposed to atherothrombosis risk should be critically re-assessed [63–65].

The present work was partially supported by ISTC grant #3744.

## References

- [1] K. P. Rentrop. Thrombi in acute coronary syndromes: Revisited and revised. *Circulation*, 101:1619–1626, 2000.
- [2] V. Fuster, J. J. Badimon, and J. H. Chesebro. Atherothrombosis: mechanisms and clinical therapeutic approaches. *Vasc Med*, 3:231–239, 1998.
- [3] Z. M. Ruggeri. Platelets in atherothrombosis. *Nature Medicine*, 8(11):1227–1234, 2002.
- [4] M. J. Davies. The pathophysiology of acute coronary syndromes. *Heart*, 83:361–366, 2000.
- [5] V. W. M. van Hinsbergh. Endothelium — role in regulation of coagulation and inflammation. *Semin Immunopathol*, 34:93–106, 2012.
- [6] L. Badimon, R. F. Storey, and G. Vilahur. Update on lipids, inflammation and atherothrombosis. *Thrombosis and Haemostasis*, 105 (Suppl 1):S34–S42, 2011.
- [7] U. Sadat, Z. Teng, and J. H. Gillard. Biomechanical structural stresses of atherosclerotic plaques. *Expert Rev. Cardiovasc. Ther.*, 8(10):1469–1481, 2010.
- [8] G. C. Makris, A. N. Nicolaidis, X. Y. Xu, and G. Geroulakos. Introduction to the biomechanics of carotid plaque pathogenesis and rupture: review of the clinical evidence. *The British Journal of Radiology*, 83:729–735, 2010.
- [9] V. P. Shirinskii. The role of light-chain myosin kinase in endothelial barrier functions and the prospects for use of its inhibitors in impaired vascular permeability. *Cardiologicheskyy vestnik*, 1(XIII):39–42, 2006.
- [10] K. K. Wu and P. Thiagarajan. Role of endothelium in thrombosis and hemostasis. *Annu. Rev. Med.*, 47:315–331, 1996.
- [11] P. K. Shah. Inflammation and plaque vulnerability. *Cardiovasc Drugs Ther*, 23:31–40, 2009.
- [12] Z. M. Ruggeri. Mechanisms of shear-induced platelet adhesion and aggregation. *Thromb. Haemost.*, 70(1):119–123, 1993.

- [13] B. R. Alevriadou, J. L. Moake, N. A. Turner, Z. M. Ruggeri, B. J. Folie, M. D. Phillips, A. B. Schreiber, M. E. Hrinca, and L. V. McIntire. Real-time analysis of shear-dependent thrombus formation and its blockade by inhibitors of von Willebrand factor binding to platelets. *Blood*, 81(5):1263–1276, 1993.
- [14] Z. M. Ruggeri, J. N. Orje, R. Habermann, A. B. Federici, and A. J. Reininger. Activation-independent platelet adhesion and aggregation under elevated shear stress. *Blood*, 108:1903–1910, 2006.
- [15] J. M. Tarbell. Shear stress and the endothelial transport barrier. *Cardiovascular Research*, 87(2):320–330, July 15 2010.
- [16] C. J. Slager, J. J. Wentzel, F. J. H. Gijssen, A. Thury, A. C. van der Wal, J. A. Schaar, and P. W. Serruys. The role of shear stress in the destabilization of vulnerable plaques and related therapeutic implications. *Nat Clin Pract Cardiovasc Med*, 2(9):456–464, 2005.
- [17] Y. Fukumoto, T. Hiro, T. Fujii, G. Hashimoto, T. Fujimura, J. Yamada, T. Okamura, and M. Matsuzaki. Localized elevation of shear stress is related to coronary plaque rupture. *JACC*, 51(6):645–650, 2008.
- [18] S. D. Gertz and W. C. Roberts. Hemodynamic shear force in rupture of coronary arterial atherosclerotic plaques. *The American Journal Of Cardiology*, 66:1368–1372, 1990.
- [19] R. Ross. Atherosclerosis — an inflammatory disease. *N. Engl. J. Med.*, 340:115–126, 1999.
- [20] M. T. Davies. Stability and instability two faces of coronary atherosclerosis. *Circulation*, 90:2013–2019, 1994.
- [21] G. Th. Guria, M. A. Herrero, and K. E. Zlobina. A mathematical model of blood coagulation induced by activation sources. *Discr Cont Dyn Syst A*, 25(1):175–194, 2009.
- [22] G. T. Guria, M. A. Herrero, and K. E. Zlobina. Ultrasound detection of externally induced microthrombi cloud formation: a theoretical study. *Journal of Engineering Mathematics*, 66(1-3):293–310, 2010.
- [23] A. S. Rukhlenko, O. A. Dudchenko, K. E. Zlobina, and G. Th. Guria. Threshold activation of blood coagulation as a result of elevated wall shear stress. *Proceedings of MIPT*, 4(2):192–201, 2012.
- [24] A. S. Rukhlenko, K. E. Zlobina, and G. Th. Guria. Hydrodynamical activation of blood coagulation in stenosed vessels. Theoretical analysis. *Computer Research and Modeling*, 4(1):155–183, 2012.
- [25] A. S. Rukhlenko. *Mathematical modeling of thrombus formation processes in intensive blood flow conditions*. PhD thesis, MIPT, Dolgoprudny, 2013.
- [26] F. I. Ataulakhanov and G. T. Guria. Spatial aspects of human blood clotting dynamics I. Hypothesis. *Biophysics*, 39(1):89–96, 1994.
- [27] F. I. Ataulakhanov, G. T. Guria, and A. YU. Safroshkina. Spatial aspects of human blood clotting dynamics II. Phenomenological model. *Biophysics*, 39(1):97–104, 1994.
- [28] M. V. Volkenstein. *Molecular biophysics*. Academic press, New York, 1977.
- [29] G. Strobl. *The Physics of Polymers. Concepts for Understanding Their Structures and Behavior*. Springer-Verlag Berlin Heidelberg, 3rd edition, 2007.
- [30] S. K. Friedlander. *Smoke, Dust, and Haze: Fundamentals of Aerosol Dynamics*. Oxford, 2000.
- [31] S. Uzlova, K. Guria, and G.Th. Guria. Acoustic determination of early stages of intravascular blood coagulation. *Philos Trans R Soc A*, 366:3649–3661, 2008.
- [32] S. G. Uzlova, K. G. Guria, A. A. Shevelev, S. A. Vasiliev, and G.Th. Guria. Acoustically detectable intravascular microemboli as precursors of postoperative complications. *Bulletin of Bakoulev Scientific Center for Cardiovascular Surgery*, (6):55–64, 2008. In Russian.
- [33] M. Doi and S. F. Edwards. *The Theory of Polymer Dynamics*. International series of monographs on physics. Oxford University Press, 1988.

- [34] P. G. de Gennes. *Scaling Concepts in Polymer Physics*. G - Reference, Information and Interdisciplinary Subjects Series. Cornell University Press, 1979.
- [35] M. A. Herrero. Mathematical models of aggregation: the role of explicit solutions. *Progress in nonlinear differential equations and their applications*, 63:309–318, 2005.
- [36] R. F. Schmidt and G. Thews. *Human Physiology*. Springer-Verlag, New York, 1989.
- [37] John W. Weisel. Fibrinogen and fibrin. In David A. D. Parry and John M. Squire, editors, *Fibrous Proteins: Coiled-Coils, Collagen and Elastomers*, volume 70 of *Advances in Protein Chemistry*, pages 247–299. Academic Press, 2005.
- [38] L. Bachmann, W. W. Schmittfiumian, R. Hammel, and K. Lederer. Size and shape of fibrinogen. 1. electron-microscopy of hydrated molecule. *Makromol Chem-Macromol Chem Phys*, 176(9):2603–2618, 1975.
- [39] Tobias Saam, Jianming Cai, Lin Ma, You-Quan Cai, Marina S. Ferguson, Nayak L. Polissar, Thomas S. Hatsukami, and Chun Yuan. Comparison of symptomatic and asymptomatic atherosclerotic carotid plaque features with in vivo mr imaging. *Radiology*, 240(2):464–472, August 2006.
- [40] Y. Sato, K. Hatakeyama, K. Marutsuka, and Y. Asada. Incidence of asymptomatic coronary thrombosis and plaque disruption: comparison of non-cardiac and cardiac deaths among autopsy cases. *Thromb Res*, 124(1):19–23, May 2009.
- [41] I. M. Lifshitz and V. V. Slyozov. The kinetics of precipitation from supersaturated solid solutions. *J. Phys. Chem. Solids*, 19:35–50, 1961.
- [42] V. V. Slezov. *Kinetics of First-Order Phase Transitions*. John Wiley & Sons, 2009.
- [43] D. M. Wootton, C. P. Markou, S. R. Hanson, and D. N. Ku. A mechanistic model of acute platelet accumulation in thrombogenic stenoses. *Annals of Biomedical Engineering*, 29:321–329, 2001.
- [44] B. J. Folie and L. V. McIntire. Mathematical analysis of mural thrombogenesis. concentration profiles of platelet-activating agents and effects of viscous shear flow. *Biophysical Journal*, 56:1121–1141, 1989.
- [45] Z. Xu, N. Chen, M. M. Kamocka, E. D. Rosen, and M. Alber. A multiscale model of thrombus development. *J. R. Soc. Interface*, 5:705–722, 2008.
- [46] C. Q. Xu, Y. J. Zeng, and H. Gregersen. Dynamic model of the role of platelets in the blood coagulation system. *Medical Engineering & Physics*, 24:587–593, 2002.
- [47] A. L. Fogelson and R. D. Guy. Platelet-wall interactions in continuum models of platelet thrombosis: formulation and numerical solution. *Mathematical Medicine and Biology*, 21:293–334, 2004.
- [48] A. L. Fogelson and R. D. Guy. Immersed-boundary-type models of intravascular platelet aggregation. *Comput. Methods Appl. Mech. Engrg.*, 2007.
- [49] A. L. Kuharsky and A. L. Fogelson. Surface-mediated control of blood coagulation: The role of binding site densities and platelet deposition. *Biophysical Journal*, 80:1050–1074, 2001.
- [50] K. Leiderman and A. L. Fogelson. Grow with the flow: a spatial-temporal model of platelet deposition and blood coagulation under flow. *Mathematical Medicine and Biology*, 28(1):47–84, 2011.
- [51] S. L. Diamond, J. Purvis, M. Chatterjee, and M. H. Flamm. Systems biology of platelet-vessel wall interactions. *Frontiers in Physiology*, 4:1–9, 2013.
- [52] R. D. Guy, A. L. Fogelson, and J. P. Keener. Fibrin gel formation in a shear flow. *Math. Med. Biol.*, 24(1):111–130, 2007.
- [53] A. P. Guzevatykh, A. I. Lobanov, and G. Th. Guria. Thershold intervacular blood coagulation as a result of stenosis development. *Mathematical modeling*, 12(4):39–60, 200.

- [54] A. L. Chulichkov, A. V. Nikolaev, A. I. Lobanov, and G. T. Guria. Threshold activation of blood coagulation and thrombus growth under flow conditions. *Mathematical modeling*, 12(3):76–95, 2000.
- [55] M. Anand, K. Rajagopal, and K. R. Rajagopal. A model incorporating some of the mechanical and biochemical factors underlying clot formation and dissolution in flowing blood. *J. of Theoretical Medicine*, 5:183–218, 2003.
- [56] M. Anand, K. Rajagopal, and K. R. Rajagopal. A model for the formation and lysis of blood clots. *Pathophysiol. Haemost. Thromb.*, 34:109–120, 2005.
- [57] A. I. Lobanov and T. K. Starozhilova. Effect of convective flow on formation of two-dimensional structures in the model of blood coagulation. *Phystech Journal*, 3(2):96–105, 1997.
- [58] A. I. Lobanov and T. K. Starozhilova. The effect of convective flows on blood coagulation processes. *Pathophysiol Haemost Thromb*, 34:121–134, 2005.
- [59] M. K. Runyon, C. J. Kastrup, B. L. Johnson-Kerner, G. Thuong, Van Ha, and R. F. Ismagilov. Effects of shear rate on propagation of blood clotting determined using microfluidics and numerical simulations. *JACS*, 130(11):3458–3464, 2008.
- [60] K. B. Neeves, D. A.R. Illing, and S. L. Diamond. Thrombin flux and wall shear rate regulate fibrin fiber deposition state during polymerization under flow. *Biophysical Journal*, 98(7):1344–1352, 2010.
- [61] A. H. Nayfeh. *Perturbation Methods*. Physics textbook. Wiley, 2008.
- [62] A. Ya. Malkin. The state of the art in the rheology of polymers: Achievements and challenges. *Polymer Science, Ser. A*, 51(1):80–102, 2009.
- [63] E. Eeckhout et al. Indications for intracoronary stent placement: the European view. *European Heart Journal*, 20(14):1014–1019, 1999.
- [64] Bates et al. ACCF/SCAI/SVMB/SIR/ASITN 2007 Clinical Expert Consensus Document on Carotid Stenting. *Journal of the American College of Cardiology*, 49(1):126–170, 2007.
- [65] Patel et al. ACCF/SCAI/STS/AATS/AHA/ASNC/HFSA/SCCT 2012 Appropriate Use Criteria for Coronary Revascularization Focused Update. *Journal of the American College of Cardiology*, 59(9):857–881, 2012.

## Index of Authors

—/ <b>A</b> /—	
Agladze, K.I. ....	1
Agladze, N.N. ....	1
—/ <b>B</b> /—	
Barkley, D. ....	8
Biktashev, V.N. ....	8
Biktasheva, I.V. ....	8
Bordyugov, G.V. ....	8
Borina, M.Yu. ....	104
—/ <b>C</b> /—	
Chetverikov, A.P. ....	28
—/ <b>D</b> /—	
Dierckx, H. ....	8
Doronina, N.I. ....	1
Dudchenko, O.A. ....	19
—/ <b>E</b> /—	
Ebeling, W. ....	28
—/ <b>F</b> /—	
Foulkes, A.J. ....	8
—/ <b>G</b> /—	
Gamilov, T.M. ....	77
Gasnikova, E.V. ....	40
Guria, G.Th. ....	19, 113
—/ <b>H</b> /—	
Herrero, M.A. ....	43
—/ <b>K</b> /—	
Kaplan, A.E. ....	53
Khalyavkin, A.V. ....	69
Kholodov, A.S. ....	77
—/ <b>L</b> /—	
Leonidov, A.V. ....	83
—/ <b>M</b> /—	
Malyshev, V.A. ....	90
Morgan, S.W. ....	8
—/ <b>P</b> /—	
Plank, G. ....	8
Polezhaev, A.A. ....	104
—/ <b>R</b> /—	
Rukhlenko, A.S. ....	113
Rumyantsev, E.L. ....	83
—/ <b>S</b> /—	
Sarvazyan, N.A. ....	8
Selsil, O. ....	8
Simakov, S.S. ....	77
Soe, Y.N. ....	77
—/ <b>V</b> /—	
Velarde, M.G. ....	28
Vershelde, H. ....	8
Volkov, S.N. ....	53
—/ <b>Z</b> /—	
Zamyatin, A.A. ....	90
Zlobina, K.E. ....	113

*Научное издание*

**Proceedings of the International Conference  
“Instabilities and Control of Excitable Networks:  
From Macro- to Nano-Systems”**

**Труды международной конференции  
«Неустойчивости в возбудимых сетях и возможности  
управления ими:  
от макро- к нано-системам»**

Редакционно-издательская группа:  
К.Е. Злобина, А.Р. Гагарина, О.А. Дудченко

Компьютерная верстка:  
А.С. Рухленко

Дизайн обложки:  
И.А. Романец, А.Н. Юнусова

